

# **COMSAT**

## **Technical Review**

Volume 21 Number 1, Spring 1991

# COMSAT TECHNICAL REVIEW

Volume 21 Number 1, Spring 1991

<i>Advisory Board</i>	Joel R. Alper Joseph V. Charyk John V. Evans John. S. Hannon
<i>Editorial Board</i>	Richard A. Arndt, <i>Chairman</i> S. Joseph Campanella Dattakumar M. Chitre William L. Cook Calvin B. Cotner Allen D. Dayton Russell J. Fang Ramesh K. Gupta Michael A. Hulley Edmund Jurkiewicz Ivor N. Knight Alfred A. Norcott Hans J. Weiss Amir I. Zaghloul
<i>Past Editors</i>	Pier L. Bargellini, 1971–1983 Geoffrey Hyde, 1984–1988
<i>Editorial Staff</i>	MANAGING EDITOR Margaret B. Jacocks TECHNICAL EDITOR Barbara J. Wassell PRODUCTION Barbara J. Wassell Virginia M. Ingram N. Kay Flesher Ladd Morse CIRCULATION Merilee J. Worsey

COMSAT TECHNICAL REVIEW is published by the Communications Satellite Corporation (COMSAT). Subscriptions, which include the two issues published for a calendar year, are: one year, \$20 U.S.; two years, \$35; three years, \$50; single copies, \$12; article reprints, \$3. Overseas airmail delivery is available at an additional cost of \$18 per year. Make checks payable to COMSAT and address to Records Department, Communications Satellite Corporation, 22300 Comsat Drive, Clarksburg, MD 20871-9475, U.S.A.

ISSN 0095-9669

© COMMUNICATIONS SATELLITE CORPORATION 1991  
COMSAT IS A TRADE MARK AND SERVICE MARK  
OF THE COMMUNICATIONS SATELLITE CORPORATION

- 1 EDITORIAL NOTE  
**S. B. Bennett AND G. Hyde**

## *INTELSAT VI: Spacecraft Design*

- 5 INTELSAT VI SPACECRAFT BUS DESIGN  
**L. R. Dest, J-P. Bouchez, V. R. Serafini, M. Schaviatello AND K. J. Volkert**
- 57 ATTITUDE AND PAYLOAD CONTROL SYSTEM FOR INTELSAT VI  
**L. I. Slafer AND V. L. Seidenstucker**
- 101 INTELSAT VI COMMUNICATIONS SUBSYSTEM DESIGN  
**G. N. Horvai, L. A. Argyle, T. L. Ellena, R. R. Persinger AND C. E. Mahle**
- 149 THE INTELSAT VI ANTENNA SYSTEM  
**R. R. Persinger, S. O. Lane, M. F. Caulfield AND A. I. Zaghloul**
- 191 INTELSAT VI ON-BOARD SS-TDMA SUBSYSTEM DESIGN AND PERFORMANCE  
**R. K. Gupta, J. N. Narayanan, A. M. Nakamura, F. T. Assal AND B. Gibson**

## *Non-INTELSAT VI Papers*

- 227 HIGH-EFFICIENCY SINGLE RIDGED 16-WAY RADIAL POWER COMBINER  
**M. Oz, B. D. Geller, P. K. Cline AND I. Yogev**
- 253 TRANSLATIONS OF ABSTRACTS  
FRENCH 253 SPANISH 256
- 259 AUTHOR INDEX, CTR 1990
- 261 INDEX OF 1990 PUBLICATIONS BY COMSAT AUTHORS
- 267 PAPERS SCHEDULED FOR PUBLICATION IN THE CTR INTELSAT VI SERIES

## **Editorial Note**

S. B. BENNETT, Guest Editor, INTELSAT  
G. HYDE, Associate Guest Editor, COMSAT

This is the second volume of the *COMSAT Technical Review* (CTR) dedicated to the INTELSAT VI satellite and system. Because of the importance and complexity of the INTELSAT VI satellite and its associated system operation, three volumes of CTR are needed to fully document the process leading to its very successful implementation. These volumes cover the subject from concept, through design and test, to in-orbit operation. Related fourth and fifth volumes will address system applications and the implementation of satellite-switched time-division multiple access (SS-TDMA). Compilation of these volumes is a joint effort of COMSAT and INTELSAT, including co-editors from each organization.

The first volume in the CTR INTELSAT VI series\* described the overall development process, as well as system planning, specification of the spacecraft bus and communications payload, and the design for SS-TDMA and FDMA services.

This second volume focuses on the design of the INTELSAT VI spacecraft and its communications payload. The first paper deals with design of the spacecraft bus, including the spun and despun sections, structures, thermal control, mechanical design, deployment mechanisms, power subsystem, telemetry and command, propellant systems, and beacon tracker subsystem. The second paper covers the attitude and payload control system, including descriptions of the design and performance of the microprocessor-based control system, despun platform pointing control, active nutation stabilization, fault protection, and control autonomy.

A design overview and description of the communications payload are provided in a third paper, with emphasis on the receivers, filters, switch networks, and power amplifiers. Paper four details the design, implementation, and testing of the antenna system, including the C-band dual-polarized, hemi/zone transmit and receive antennas; the east and west steerable Ku-band spot beam antennas; the C-band dual-polarized global coverage horns; the antennas used for telemetry, command, and beacon on-station; and the omnidirectional antennas used for telemetry and command in transfer orbit. The last paper in this volume discusses the design and implementation of the

---

\*Refer to pages 267 through 271 of this issue for a listing of the papers scheduled for publication in this series. Papers on other topics are also included.

on-board SS-TDMA package, including the switching system, the digital control unit, timing control, and operation.

The third volume in the INTELSAT VI series will cover a wide range of topics, including measures taken to ensure a reliable satellite; the launch, deployment, and in-orbit testing phases; and operation of the satellite in orbit. Presented in a related fourth volume on the INTELSAT system and applications will be papers on earth station considerations, as well as on digital, video, and other modulation coding techniques used in the INTELSAT VI era. The fifth volume will be devoted to describing all aspects of the SS-TDMA system, which was first used for commercial purposes on INTELSAT VI.

The editors trust that this comprehensive treatment of the INTELSAT VI system will prove useful to future system planners. The papers in this and subsequent volumes are the result of a major effort by a large group of authors from COMSAT, INTELSAT, and Hughes Aircraft Corporation, and we congratulate them on their substantial achievement.



*Simon B. Bennett received a B.E.E. from City College of New York in 1959 and an M.E.E. from New York University in 1961. His career, which spans the entire history of communications satellites, began with work on the first TELSTAR satellite program at Bell Telephone Laboratories from 1959 to 1963. He continued in this field at COMSAT from 1961 to 1974, where he contributed to the success of satellite programs from Early Bird to INTELSAT IV. Since 1974 he has been at INTELSAT, where he has been manager of spacecraft programs, directed systems planning studies, and managed the operation of INTELSAT's 15-satellite fleet (including the INTELSAT VI series). He is currently Assistant to the Vice President for Engineering and Research.*

*Geoffrey Hyde received a B.A.Sc. in engineering physics and an M.A.Sc. in electrical engineering from the University of Toronto in 1953 and 1959, respectively, and a Ph.D. in electrical engineering from the University of Pennsylvania, Philadelphia, in 1967. Prior to joining COMSAT Laboratories in July 1968, he worked on antennas, microwaves, and propagation at RCA, Moorestown, NJ, and at Avro Aircraft Company and Sinclair Radio Labs in Canada.*



*At COMSAT prior to 1974, Dr. Hyde was concerned with the development of the torus antenna, a general antenna analysis computer program (GAP), and related areas of endeavor. In February 1974 he became Manager of the Propagation Studies Department, where his work included a wide variety of efforts in propagation measurement and analysis. In 1980 he joined the staff of the Director, COMSAT Laboratories, and in 1984 became Assistant to the Director. His duties included coordination of the COMSAT R&D programs, coordination of ITU activities at COMSAT Laboratories, and editorship of the COMSAT Technical Review. In June 1989 he retired, and is currently a consultant to COMSAT Laboratories.*

*Dr. Hyde is a member of URSI Commissions B and F, and the AIAA, and is a Registered Professional Engineer in Ontario, Canada. His honors include David Sarnoff Fellowships (1965 and 1966), Fellow of the IEEE (1987), and the IEEE G-AP award for best paper, 1968 (jointly with Dr. Roy C. Spencer).*

## ***INTELSAT VI spacecraft bus design***

L. R. DEST, J-P. BOUCHEZ, V. R. SERAFINI, M. SCHAVIETELLO,  
AND K. J. VOLKERT

(Manuscript received October 18, 1990)

### ***Abstract***

The spin-stabilized INTELSAT VI spacecraft bus is described, including overall design requirements and individual subsystems. The satellite weighs approximately 4,500 kg at launch, has a beginning-of-life mass of 2,570 kg, and an end-of-life dry mass of 1,905 kg. It is composed of spun and despun sections connected by a bearing and power transfer assembly. The despun section structure supports the communications payload (repeater and antennas) and provides the command and telemetry and thermal control functions. The spun section includes the attitude control, power, propulsion, and thermal subsystems. Deployable appendages, including antennas and a telescoping solar panel, are implemented by multiple mechanisms.

### ***Introduction***

The spacecraft design that evolved to meet the INTELSAT VI specifications [1] was considerably different than the conceptual spacecraft designs INTELSAT (supported by COMSAT Laboratories) generated [2] prior to release of the request for proposals for INTELSAT VI in 1980. Because of the significant power necessary to support the defined INTELSAT VI payload, the stringent antenna pointing performance required to meet the hemi/zone antenna specifications, a 10-year design lifetime, and launch vehicle mass and volume constraints, it was assumed that only a contemporary three-axis-stabilized spacecraft would be suitable. Quite surprisingly, Hughes Aircraft Company (HAC) proposed a scaled-up version of a spin-stabilized spacecraft that combined concepts dating back to the early 1970s (which had been included in the TACSAT and INTELSAT IV/IV-A designs) with newer technology employed on the HAC LEASAT "widebody" Shuttle Transportation System

(STS) optimized design and the telescoping solar array developed for the small HAC HS-376 domestic satellites. This mixing of older fundamental technologies with unproven concepts such as large deployable antennas on a spin-stabilized spacecraft, in conjunction with spacecraft vehicle dynamics that challenged some prior analytical assessments (none of which had ever been demonstrated in space), gave rise to substantial reservations during the proposal technical evaluation phase in 1981. In terms of the design approach to handling the evolution of technology and the size required for the INTELSAT VI concept, the Ford Aerospace proposal involving scaling up of the INTELSAT V design was initially favored; however, the HAC design concept intrigued the engineers. Hundreds of hours were spent assessing each significant obstacle involved in the HAC technical approach. In the end, while the INTELSAT V derivative approach was assessed to have the preferred lower risk, the HAC INTELSAT VI design was found to be technically acceptable, and in many ways more technically sophisticated. The contract was awarded to HAC in April 1982.

Such a sophisticated spacecraft design provided numerous engineering difficulties, which in turn led to design and test problems that had to be resolved. The INTELSAT VI spacecraft design significantly challenged HAC (the world's largest commercial satellite manufacturer), HAC's large international team, and the INTELSAT and COMSAT technical teams. The sheer size (Figure 1) of INTELSAT VI overwhelmed all earlier spacecraft and presented difficulties that were unforeseen.

Ultimately, the INTELSAT VI spacecraft has proven to be as fundamental, sophisticated, and challenging as the technical evaluators had assessed in 1981. The design lifetime of the satellite is 10 years, with an orbital maneuver lifetime of between 13 and 15 years, depending on the launch vehicle capability. Its in-orbit performance has far exceeded the INTELSAT VI requirements for power, antenna pointing, and stationkeeping lifetime, and it is expected to provide INTELSAT with communications capacity into the 21st century.

### **Spacecraft bus design**

INTELSAT VI was the largest spin-stabilized commercial satellite ever launched. Its spacecraft bus is divided into spun and despun sections connected by a bearing and power transfer assembly (BAPTA), as shown in Figure 2. During launch, the two sections are locked together at their periphery to minimize load transfer through the bearing assembly. On-orbit, the solar panel is deployed first, followed by the communications antennas. The on-orbit configuration is depicted in Figure 3, and important spacecraft characteristics are summarized in Table 1 [3].

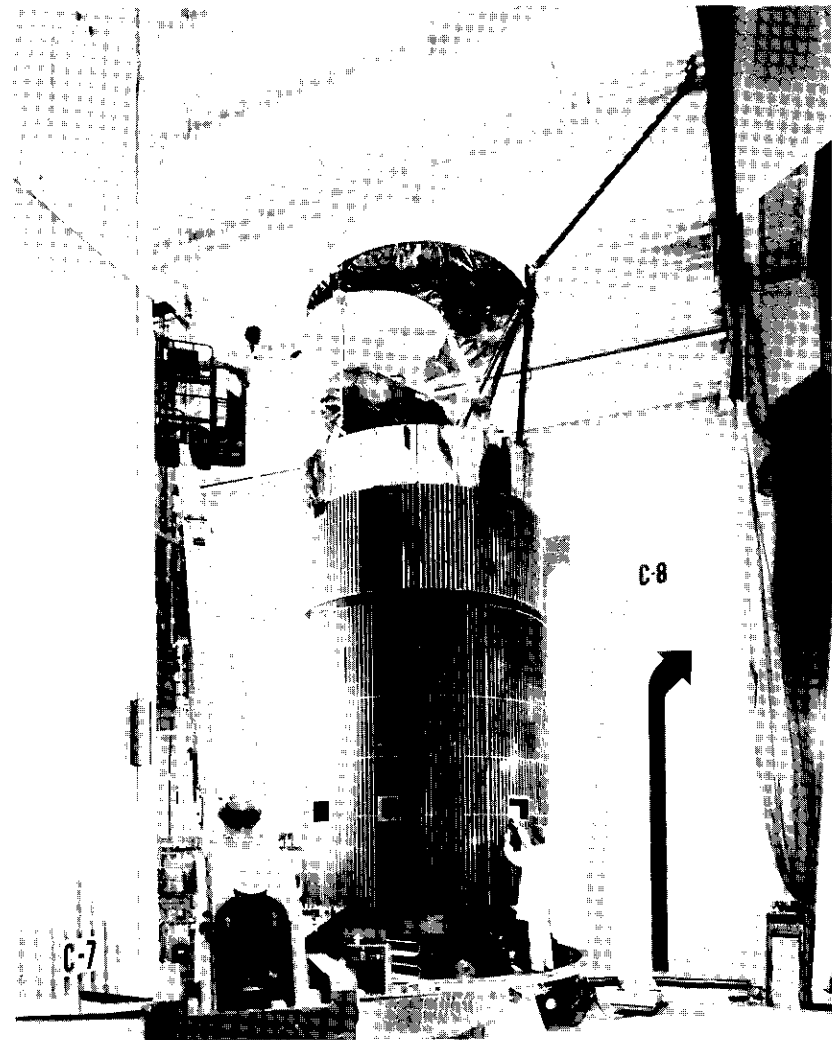


Figure 1. *The INTELSAT VI Spacecraft*  
(photo courtesy of HAC)

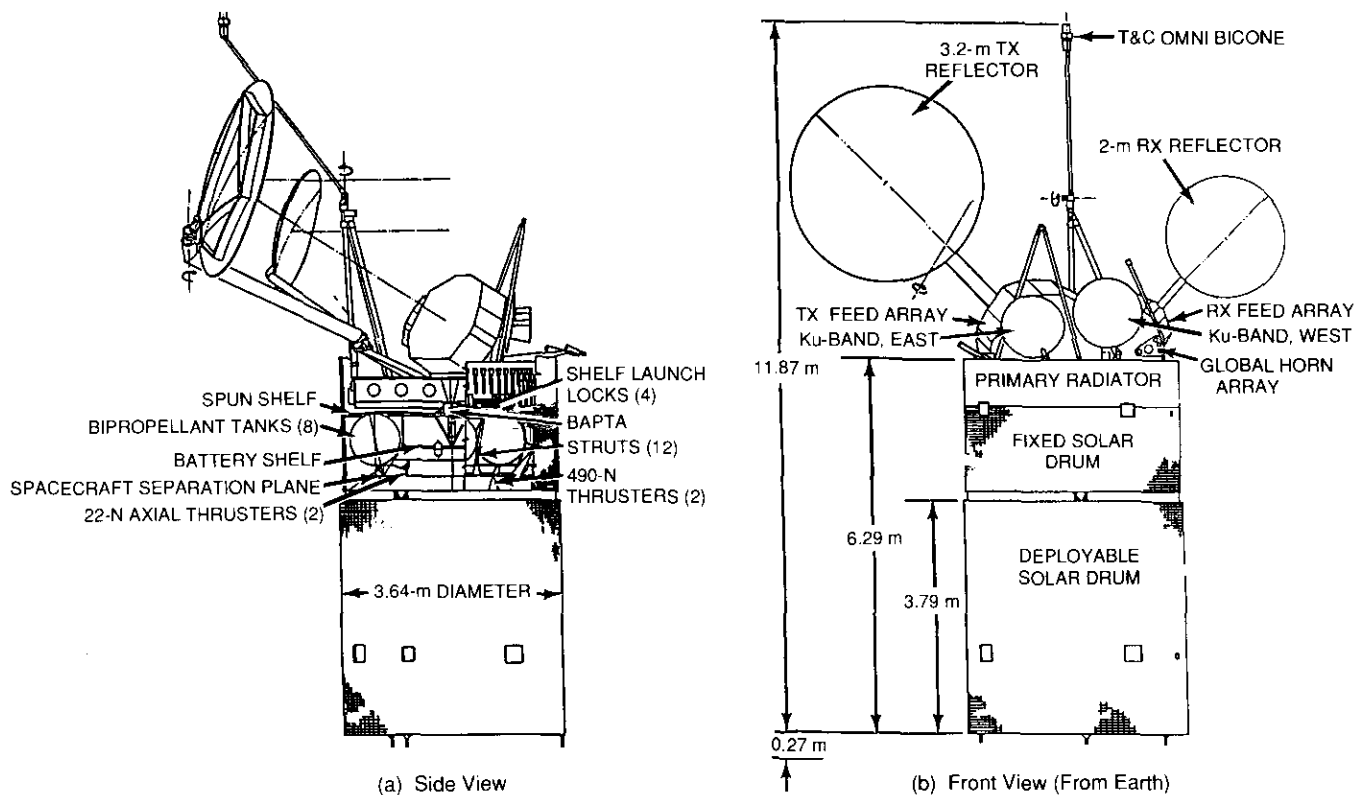


Figure 2. General Configuration Overview

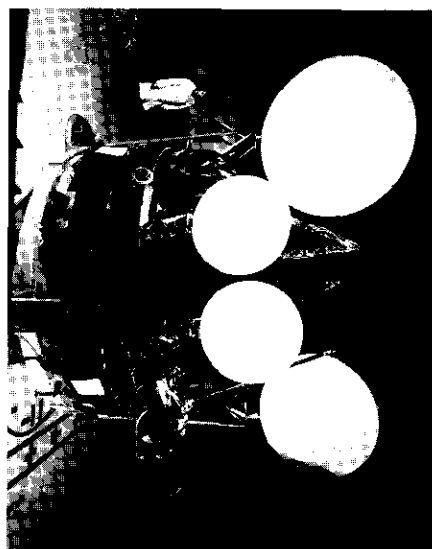


Figure 3. INTELSAT VI Antenna On-Orbit Configuration (photo courtesy of HAC)

TABLE 1. SPACECRAFT DESIGN AND PERFORMANCE CHARACTERISTICS

Size (mm)		
Spacecraft Diameter (max)		3,639
Solar Drum Height		
Forward (fixed)		2,159
Aft (deployable)		3,970
Overall Height		
Ariane 4 (including adapter)		6,414
Titan (including perigee motor)		8,284
Transfer Orbit (omni deployed)		7,228
On-Station		11,838
Mass (kg) (extended mission)		
Launch Vehicle Payload		
Titan	13,371*	4,286
Ariane		
Separated Mass	4,607	4,216
On-Station Mass, BOL	2,563	2,577
Spacecraft Dry Mass	1,901	1,906

\* Including perigee stage.

Stabilization	
Transfer Orbit	Stable spinner
On-Station	Gyrostabil

Stationkeeping Performance (limit)	
Longitude	±0.10°
Latitude	±0.10°

The spun section consists of the spun structure, solar panel assembly, aft thermal barrier, bus electronic equipment, and liquid bipropellant subsystem (LBS). A central shear tube provides a common interface for attachment to both the Ariane 4 and Titan adapters, as well as a convenient mounting surface for the propulsion lines and components. The eight liquid propellant tanks are located for direct mounting to the aft shear tube ring to minimize the interaction of their loads with the main structure. The spun shelf provides structural support for the solar panels and spun electronic units, including the attitude control electronics (ACE), power control electronics, telemetry and command units, and the squib and solenoid driver units. Additionally, four 22-newton-thrust radial thrusters are mounted on the spun shelf with their nozzles aimed through cutouts in the solar panel. Two 22-N axial thrusters and two 490-N apogee thrusters are mounted at the aft end of the spacecraft. Thermal control of the nickel-hydrogen (Ni/H<sub>2</sub>) battery is achieved by mounting the cells on a shelf within the aft portion of the shear tube to provide a low-temperature-biased environment.

The solar panel assembly is fabricated of lightweight Kevlar honeycomb. The fixed panel uses K4-3/4 cells for better temperature control of the bus subsystems, while the aft (telescoping) panel uses K7 cells for higher power output. Mirrored radiators on the solar panel provide radial heat rejection, thus minimizing back-radiation and shadowing from the extensive despun antenna farm.

The despun section (Figure 4) consists of the antenna subsystem and support structure, the despun forward barrier, and the despun shelf. The C-band reflectors and feeds are supported on the despun shelf by graphite/epoxy tube structures, which provide the required stiffness and thermal stability. The Ku-band antennas (with their feeds) and the global horn assembly are mounted on bracketry that is tied directly to the shelf. The despun shelf has a flat circular section, a cylindrical rim, and a narrow annular shelf which can be expanded for growth. The units that dissipate the greatest amount of heat (traveling wave tube amplifiers [TWTAs] and solid-state power amplifiers [SSPAs]) are mounted on the outside surface of the rim shelf for proximity to the mirror radiator on the solar panel. The forward side of the circular shelf contains the output multiplexers, the beacon tracker subsystem, and the beacon transmitters. The aft side is reserved for units requiring RF isolation, such as the input multiplexers, switch matrices, receivers, and telemetry and command hardware. The overall arrangement provides easy access for integration and testing of the repeater hardware.

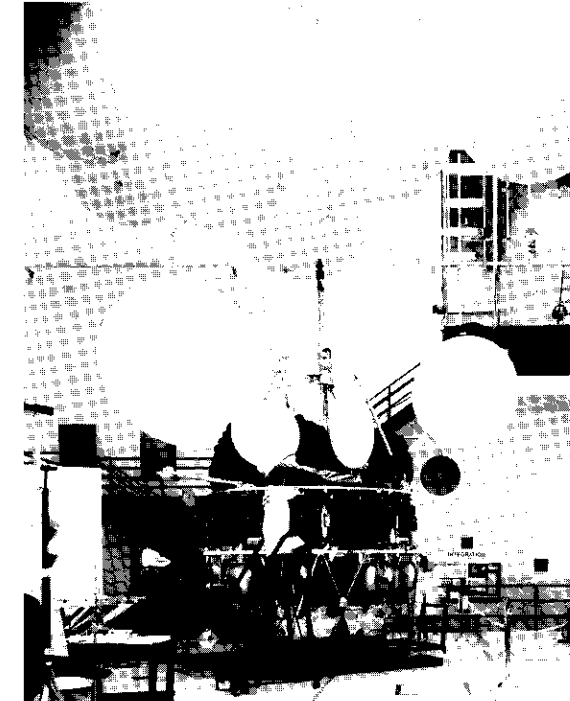


Figure 4. *INTELSAT VI Despun Section*  
(photo courtesy of HAC)

#### **Telemetry and command subsystem**

The INTELSAT VI telemetry and command subsystem (Figure 5) consists of an RF segment and a digital segment. The RF segment provides communications between the satellite and ground stations by receiving and demodulating commands and ranging tones and by transmitting telemetry and ranging signals. The digital segment decodes and executes the commands and collects and processes the telemetry and ranging data for transmission.

In the RF portion of the subsystem, commands are received during transfer orbit, and on-station, by the dual-mode toroidal beam command bicone antenna, which provides separate outputs for the redundant command receivers. The command carriers are transferred via coaxial lines to the 15-dB switch

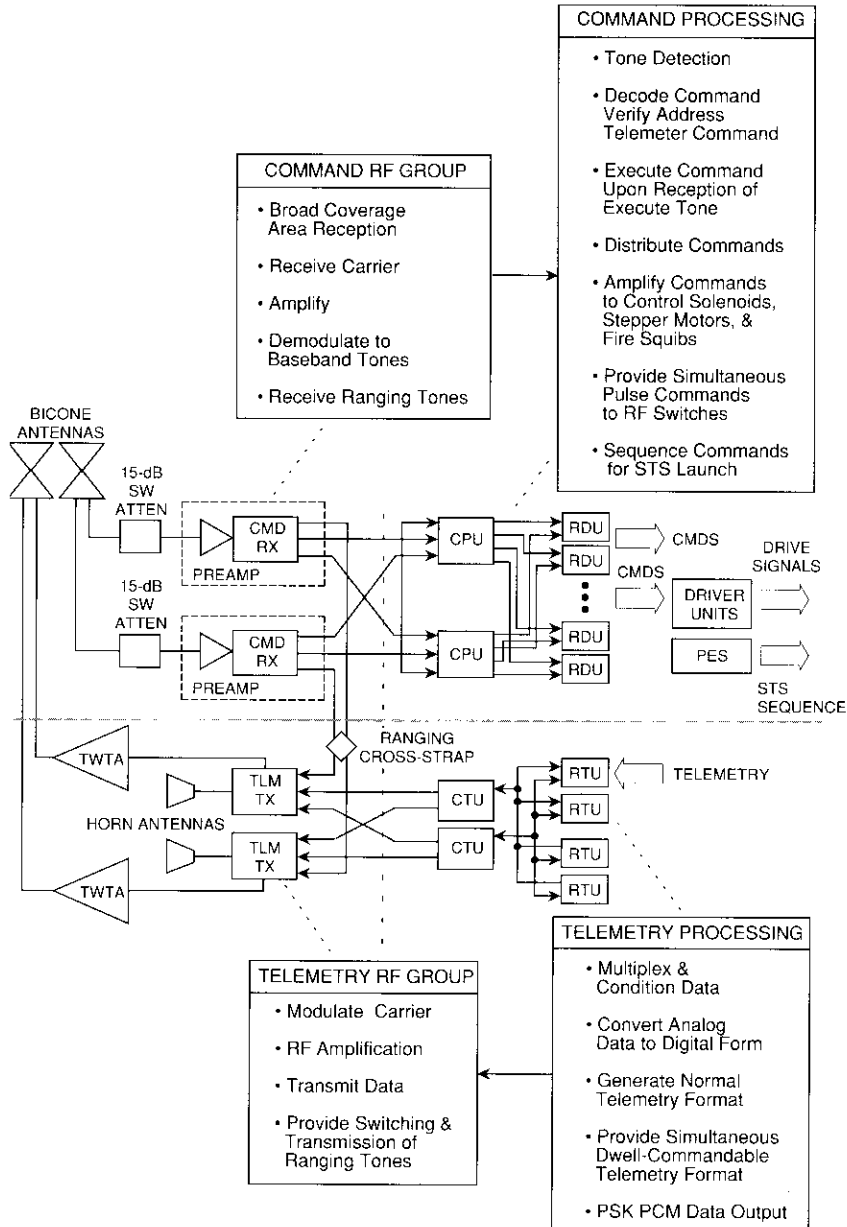


Figure 5. Telemetry and Command Subsystem

attenuators and then to the command receivers, where the command and ranging tones are demodulated. The receivers have three output ports: two connected to the redundant command processor units (CPUs), and a third which is used for ranging. A cross-connect switch allows ranging to be performed with either command receiver and either telemetry transmitter.

Each transmitter accepts input signals from the two redundant central telemetry units (CTUs) and from the ranging cross-connect switch. The signals are summed and then phase-modulated onto the telemetry carriers. The transmitter uses status signals from the CTUs to adjust the modulation index to accommodate any combination of normal, ranging, or dwell data. During transfer orbit, the telemetry RF signals are radiated by the toroidal beam telemetry bicone antenna using spare TWTAs from the zone 4 repeater. The omnidirectional bicone antenna provides broad toroidal coverage, with a beamwidth of  $\pm 20^\circ$  about the plane normal to the spin axis. On-station, the outputs of the transmitters are transferred to the global beam horn antennas. For normal on-station operation, each telemetry transmitter directly feeds a  $\pm 20^\circ$  conical global beam horn antenna.

The telemetry and command digital segment uses a central and remote unit architecture to provide flexibility, as well as block redundancy and cross-strapping for reliability. The use of multiple remote units allows their placement near the spacecraft units to be served, thus reducing the amount and complexity of cabling required. The telemetry subsystem provides a dwell mode for close examination of time-varying parameters such as nutation accelerometer output or despin motor current. The CTU can dwell on one to eight different telemetry measurements at one time, selectable by ground command. By configuring the telemetry subsystem via command, dwell-mode telemetry, normal telemetry, and ranging can be obtained simultaneously without using the redundant telemetry transmitter. The command and driver units were designed for compatibility with NASA's SRS safety requirements. Pyrotechnic devices, propulsion valves, and stepper motors are controlled by high-performance hybrid drivers. Each hybrid package contains input buffers and current-limiting for all squib driver outputs. These hybrids form the basis for all power driver units, including those for squibs, valves, stepper motors, and the perigee stage.

The digital command subsystem (Figure 6) is used to control the operation of the spacecraft. It consists of two redundant CPUs, 16 redundant remote decoder units (RDUs), and eight driver units. Each redundant unit is powered by separate spacecraft buses. Negative threshold voltage command interfaces provide high noise immunity and benign failure modes. There are 768 redundant commands on the despun side and 256 on the spun side, for a total of

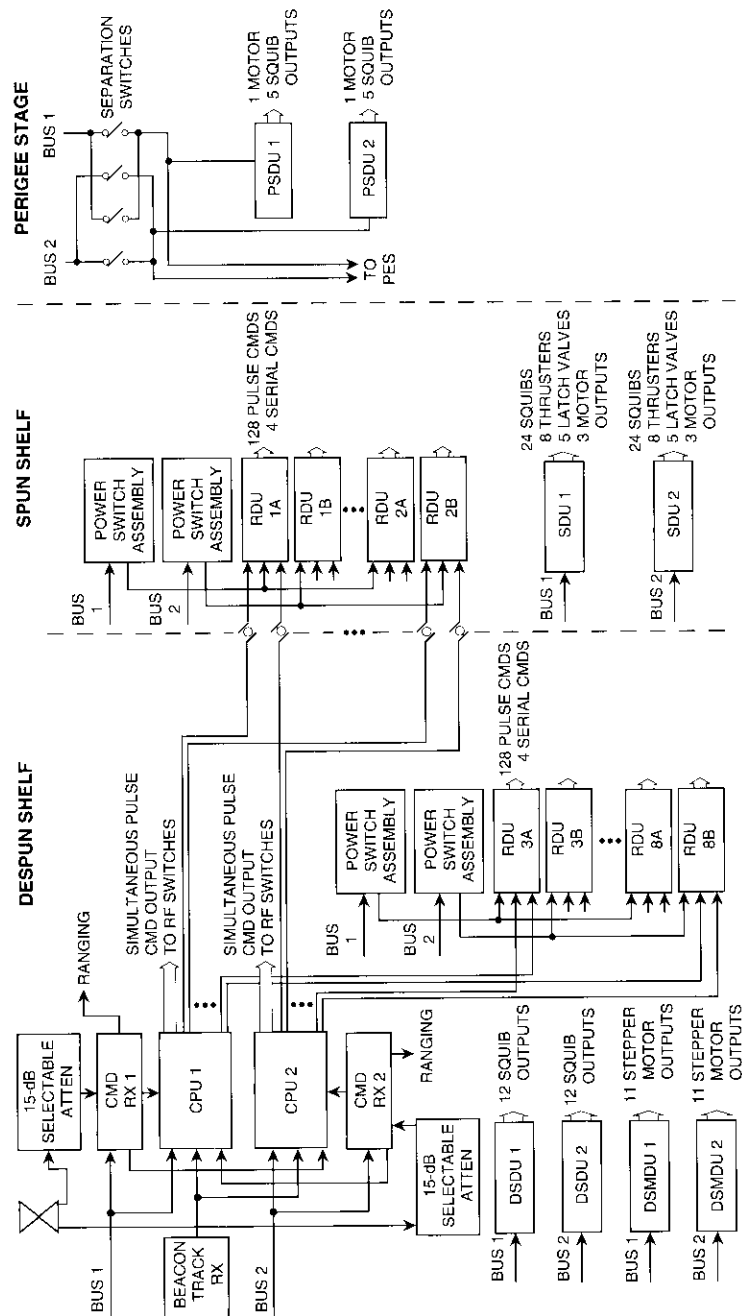


Figure 6. Digital Command Subsystem

1,024. In addition, there are 24 redundant serial commands on the despun side and eight on the spun side. The command subsystem also has the capability to issue simultaneous pulse commands to configure RF switches.

The CPU receives instructions from the command receivers and directs them to the selected RDU, which outputs a pulse or serial data to the user. Each CPU receives instructions from both command receivers as a series of one, zero, and execute tones transmitted as digital return-to-zero (RZ) tones. A two-part command structure (Figure 7) provides maximum flexibility in controlling execution durations, minimizes hardware complexity, and avoids the risk of excessively long execute pulses caused by bit errors. Part 1 of the command specifies the spacecraft address and command number. To execute the command, a brief part 2 is transmitted which checks the spacecraft address and enables the real-time execute tone circuits. The execute pulse can be of any duration and may be sent repeatedly for multiple executions if desired.

The input stage to the CPU (*i.e.*, the demodulator) consists of two groups of three tone filters (one, zero, and execute tones), one for each command receiver. The output of the tone filters is summed, and the result is a pulse code modulated (PCM)-RZ data stream delivered to the digital section of the CPU.

The output of the CPU demodulator contains the up-link command format, consisting of two parts and an execute tone. A complete part 1 command sequence is made up of at least 53 bits. Any number of zeros may precede the first 10-bit introduction sequence. After an entire part 1 command message (43 bits) is received, the command can be verified via telemetry. Part 2 consists of a minimum of 19 bits and is used to enable the CPU output to the appropriate RDU upon request of an execute tone. Telemetry verification of part 2 is also available in the telemetry format. After verification, an execute tone must be sent to execute the command.

Drivers are provided on the spacecraft to fire squibs, power stepper motors, power the perigee stage safe and arm motor, and activate thrusters and latch valves. These functions are provided in four driver units: the perigee stage driver unit (PSDU), the despun stepper motor driver unit (DSMDU), the spun driver unit (SDU), and the despun squib driver unit (DSDU). All units provide bus-redundant outputs to each load; thus all functions are retained in the event of a bus failure. Each unit protects against load or unit short circuits by providing a combination of either parallel fuse assemblies, electronic circuit breakers, or active current limiting. Each unit contains two independently commandable relays in series for all critical functions to prevent undesirable output due to component or command failures.

The digital telemetry subsystem (Figure 8) continuously samples, conditions, and formats measurements of spacecraft status, attitude, and



performance as required for control and fault isolation. It consists of two redundant CTUS and four pairs of redundant remote telemetry units (RTUS). Redundant units are powered from separate main power buses.

The telemetry subsystem also transmits spacecraft data for ground evaluation. The normal-mode telemetry minor frame consists of 256 8-bit words, while the major frame comprises 32 minor frames with 32 words subcommutated to the full depth of 32 minor frames. An independent dwell capability allows accelerated sampling of from one to eight selected measurements without interference with normal telemetry. There are 768 redundant telemetry inputs on the despun side and 256 on the spun side.

Operation of the telemetry subsystem is controlled by the CTUS, each of which has the normal telemetry format stored in programmable read-only memory (PROM). The CTUS provide a dwell mode which permits ground-controlled dwelling on from one to eight different measurements without interfering with normal telemetry. Because of the high sample rate of the telemetry subsystem and the processing performed by the ACE unit, there is no need for real-time FM channels to augment the digital data.

CTU outputs to the telemetry transmitter include separate normal and dwell data streams, plus control signals to select the desired combinations of signals for transmission to the ground. The CTU-to-transmitter interface is fully cross-strapped.

The RTUS are controlled via 32-bit instructions transmitted on redundant supervisory data buses. When addressed, an RTU acquires the requested analog and serial data from one of 256 input multiplexer channels and sends its response on one of the reply buses. Any required analog-to-digital conversion or bilevel threshold detection is performed in the RTU. Each RTU accepts the following five types of data:

- *Serial Digital*: in 8-bit bytes.
- *Analog*: scaled 0 to 5.12 V.
- *Conditioned Analog*: identical to analog, except a precision 1-mA current is provided to the user.
- *Bilevel*: binary inputs read in groups of eight.
- *Conditioned Bilevel*: bilevel inputs with a 1-mA conditioning current provided to the user.

#### Attitude control subsystem

The attitude determination and control subsystem (ADCS) collects attitude data, provides a facility for thruster control, and ultimately serves to keep the despun compartment oriented properly relative to earth so that the antennas are correctly positioned for service (Figure 9). Maintaining the orientation of

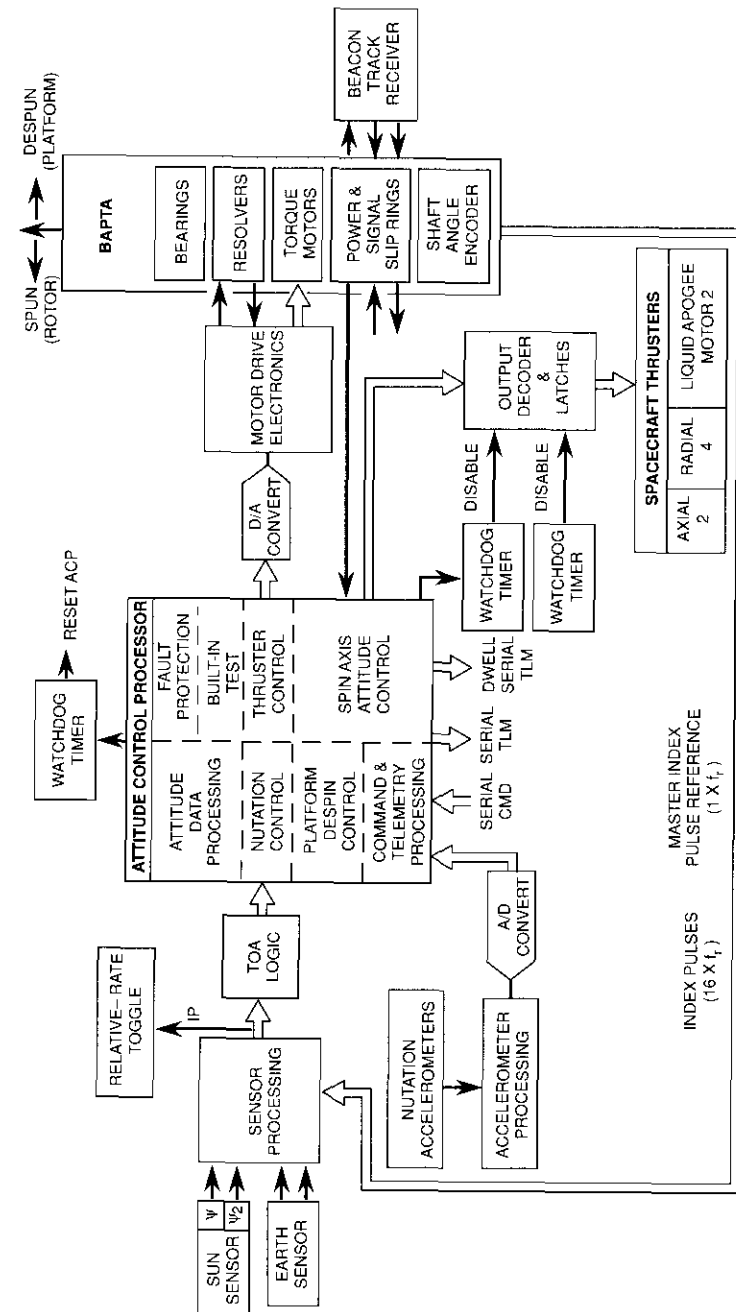


Figure 9. Attitude Determination and Control Subsystem

the payload involves orbital corrections, control of platform azimuth angle (pitch), spin axis attitude correction (nominally orbit normal), and spin axis stability (nutation and wobble). These functions are performed autonomously, with the exception of orbital and wobble corrections, which require earth-based calculations and commanding.

The microprocessor-based ADCS is implemented entirely in the spun section using processing electronics, sensors, and actuators. All processing electronics are packaged together in the ACE unit, and two units are provided for redundancy. There are four types of sensors: four earth sensors (two scan an earth chord in the northern hemisphere, two scan the southern hemisphere); one sun sensor unit (containing four independent sensors); two collocated nutation accelerometers; and a group of four shaft angle encoders incorporated into the BAPTA which monitor spun-to-despun relative phase. The actuators are LBS thrusters and pair-redundant despin torque motors within the BAPTA.

Platform azimuth control is accomplished by a continuously operating digital control system within the ACE which employs the despin motor as actuator.

Spin axis attitude control continually estimates spin axis precession due to solar pressure and autonomously corrects this attitude by pulsing an axial 22-N thruster.

Nutation damping is accomplished by thruster-active nutation control (TANC) and despin torque-active nutation damper (DAND) control functions. DAND produces despin torque in proportion to accelerometer excitation, while TANC produces thruster pulses when accelerometer excitation exceeds a threshold. A perigee active nutation control (PANC) capability is provided for commercial Titan-launched spacecraft.

The ACE provides thruster control throughout the duration of a maneuver, based on a few commands which parametrically specify the maneuver. Attitude control commands may be stored for execution and deferred up to 74 days. These functions minimize the need for real-time operation of the LBS for stationkeeping. Stored command processing is valuable for other purposes, including eclipse sensor switching and periodic updating of parameters.

Additional details on the ADCS are provided in a companion paper by Slafer and Seidenstucker [4].

### **Liquid bipropellant subsystem**

The INTELSAT VI spacecraft propulsion subsystem is a fully integrated, pressure-fed LBS which provides the combined energy for both the apogee maneuver functions and the transfer orbit and in-orbit reaction control func-

tions. The LBS uses the hypergolic liquid propellant combination consisting of equal volumes of nitrogen tetroxide for oxidizer and monomethyl hydrazine for fuel, with a mass mixture ratio of 1.65:1. This combination eliminates the need for an ignition system usually associated with a liquid propellant rocket propulsion system. Figure 10 is a schematic representation of the LBS, while Table 2 lists the components of the subsystem.

The thrusters are positioned on the spacecraft to provide impulse for spin rate control, transfer orbit control, apogee injection, precession, orbit trim, automatic nutation control, north-south and east-west stationkeeping, station change, and deorbit control. Two liquid apogee motors (LAMs) provide a nominal rocket engine thrust of 490 N each and are used for the apogee maneuver and spacecraft reorientation functions during the transfer orbit phase of the mission. They can also be used for perigee velocity augmentation if required. The LAMs are located in the aft end of the spacecraft and are used in the steady-state mode (continuous firing) for apogee maneuver firings (AMFs), and in the pulse mode for reorientation maneuvers.

Six reaction control thrusters (RCTs) provide a nominal rocket engine thrust of 22 N each and are used for transfer orbit and on-orbit spacecraft reaction control functions. Two of the RCTs are used in the axial position and are located at the aft end of the spacecraft, 180° apart, along with the LAMs. They are used for corrections requiring small repeatable impulse bits in the main thrust axis, attitude control thrust, and north-south stationkeeping maneuvers. The four other RCTs are located radially on the spun shelf and fire through cutouts in the solar panel(s). They are used for spin control (spin-up and spin-down) and east-west maneuvers. Because the majority of on-orbit propellant is used by the axial RCTs, these RCTs have a nozzle expansion area ratio of 300:1 to maximize specific impulse performance. The radial RCTs have an area ratio of 150:1 to optimize their installation on the shelf.

Eight spherical propellant supply tanks (PSTs) are used to store the two propellant loads: four for oxidizer and four for fuel. They are symmetrically located around the thrust tube to maintain transverse inertial balance. Surface tension or other propellant management devices (for propellant orientation and positive expulsion of gas-free liquids to the LAM and RCTs) are unnecessary on a spin-stabilized spacecraft.

Other major components of the LBS are as follows:

- Two high-pressure tanks (symmetrically located 180° apart) to store the helium gas used for propellant tank pressurization.
- Series-redundant pressure regulators to regulate the high-pressure helium pressurant to the propellant supply tanks.



- Twenty fill and drain valves (FDVs)/test ports for propellant and pressurant servicing and for checkout testing of the LBS.
- Pressurant and propellant filters, and associated lines and fittings (plumbing), for transfer of gas and propellants between the components.

The pressurant control components (except for the pressurant service valves) are mounted on a separate panel so that the entire subassembly can be assembled and tested independently of the LBS. The LBS FDVs used for servicing are located on separate panels to facilitate access during loading of the liquid propellants and the high-pressure helium pressurant gas. These FDVs/test ports, along with others located throughout the LBS, are also used to perform the various preflight testing, checkout, and transducer calibration operations necessary to verify the leak and functional integrity of the LBS throughout the various processing cycles of the spacecraft, and prior to propellant and pressurant loading at the launch site.

Numerous pressure and temperature transducers are incorporated in the LBS to monitor satisfactory operation of the subsystem during the mission. One high-pressure transducer on the helium tank manifold allows monitoring of the high-pressure helium supply, while four low-pressure transducers on the propellant tank gas manifolds permit continuous monitoring of propellant tank pressures. Also incorporated in the propellant supply system are four delta-pressure transducers to accurately assess the propellant remaining during the mission lifetime. Centrifugal forces created by the spinning spacecraft environment provide liquid orientation of the propellants at the propellant tank outlet ports without the need for propellant management devices. The centrifugal force field also allows the delta-pressure transducers to measure the difference between the effective liquid head pressure and the pressurization pressure in the tanks, thus enabling calculation of the remaining propellant masses.

The LAMs and RCTs have temperature sensors located on the injectors and valves so that critical thruster operations can be monitored in real time during various maneuvers. The PSTs also incorporate sensors to monitor the temperature of the various tanks.

#### REDUNDANCY AND FAILURE PROTECTION

The LBS incorporates all-welded construction to minimize long-term leakage, and extensive redundancy to ensure high mission reliability. The six RCTs are arranged into two functionally redundant groups (thruster sets) that can be separately isolated in the event of an RCT valve leak, without affecting mission life. The eight propellant supply tanks are divided into two functionally inde-

pendent half-systems, connected and controlled by various pyro valves and latch valves in the pressurant and propellant subsystems, respectively. This arrangement allows all the propellant to be used by either of the two functionally redundant thruster sets—either of which can complete the entire mission without compromise. That is, the PSTs and the functionally redundant (half-system) thruster groups are arranged so that each half-system can perform all propulsion functions required for spacecraft operation in both transfer and synchronous orbits, using the whole propellant load from the other half-system.

The half-systems are interconnected by electrically actuated, torque-motor-driven interconnect latch valves such that the half-systems can be isolated from each other. The system is designed to be operated with the interconnect latch valves closed throughout the mission life. These valves are opened only if it becomes necessary to transfer propellant from one half-system to the other. The two thruster groups also incorporate electrically actuated, torque-motor-driven isolation latch valves in the oxidizer and fuel supply lines that allow shutoff of either group or set. These valves are arranged so that closing the shutoff latch valves of one group will still allow completion of any desired maneuver by the redundant group. The fuel and oxidizer tanks can also be isolated on the pressurant side to prevent unwanted propellant migration.

Additional failure protection is provided by the following:

- Redundant NASA-standard initiators for each pyro valve
- Pressurant and propellant filters upstream of the pressure regulators and thruster groups
- Dual series-redundant pressure regulators to protect against regulator failure
- Dual series-redundant check valves to prevent mixing of oxidizer and fuel propellant vapors during the orbit insertion maneuver phase
- Redundant valve drivers for all propellant and pressurant control valves.

Each RCT incorporates an oxidizer valve and a fuel valve, each containing dual seats (series-redundant) and dual (redundant) electrical actuation coils. The LAMs have single-seat, single-coil propellant valves (one for oxidizer and one for fuel) with a latch valve upstream of each to provide redundancy for a failed-open or leaky LAM propellant valve.

#### LBS OPERATION

In the pre-launch configuration, all latch valves are closed and all pyro valves are in the normal position (NO PVs are open and NC PVs are closed). During pre-launch and boost phases, no valves are actuated. The NC PV (GSV1)

located upstream of the pressure regulator (PR1) isolates the high-pressure helium supply from the rest of the system and prevents operation of the series-redundant pressure regulators. The NC PVs downstream of the pressure regulators (FSV3, 4, 6, and 8, and OSV3, 4, 6, and 8) in the pressurization manifolds prevent mixing of the oxidizer and fuel propellant vapors which are present in the propellant tanks. The anti-migration, three-way NC PVs (FSV6 and 8, and OSV6 and 8) also prevent propellant transfer between manifolded PSTs (FTK1 and 2, FTK3 and 4, OTK1 and 2, and OTK3 and 4). The RCT and LAM isolation latch valves (FLV2, 3, 4, and 5, and OLV2, 3, 4, and 5) are closed to provide additional anti-leak redundancy to the LAMS and RCT valves during the launch/boost phase.

The sequence and manner of initiating LBS operation differ slightly, depending on whether the launch vehicle employs a perigee stage. For commercial Titan launches involving a perigee stage, initial LBS activation is performed remotely by a timer on board the perigee stage called the post-ejection sequencer (PES). The PES is initialized upon separation of the perigee stage from stage 2 of the commercial Titan. For Ariane launches not requiring a perigee stage, LBS activation commands are issued by ground command.

The first sequence of commands to initiate operation involves the opening of the propellant isolation latch valves (FLV2 through 5 and OLV2 through 5). This allows the propellants to flow from the propellant tanks, under the initial pre-launch-pad pressure (propellant tank ullage pressure), to the inlets of the RCT valves and LAM valves. Initial operation of the LBS takes place in a pressure blowdown (unregulated) mode for the spin control maneuvers, and for the PANC maneuvers if required. Two radial spin-up RCTs (RSU1 and RSU2), operated concurrently, provide a balanced torquing for initial spacecraft spin-up; however, it is possible to spin-up the spacecraft with just one radial RCT (RSU1 or RSU2). The RCTs operate in the steady-state (continuous firing) mode for spin-up and spin-down maneuvers. If PANC is required when using a perigee stage, the LAMS are utilized in the pulse mode under pressure blowdown conditions.

Following perigee firings (or just prior to the apogee maneuver phase in the case of a nonperigee stage), the LBS is activated to the pressure regulation mode by first opening the high-pressure helium gas isolation NC PV (GSV1). This allows the high-pressure gas to enter the pressure regulator(s) and establishes regulated operation. The PSTs of one of the half-systems (FTK1 and 2 and OTK3 and 4) are then pressurized to regulated pressure by opening the pressurization isolation NC PVs (FSV6 and OSV6). Following pressure stabilization, the interconnect valves between the two half-systems (FLV1 and OLV1) are opened to prime the interconnect lines, and then closed after a predeter-

mined time interval. The final step in the LBS activation sequence is to pressurize the remaining half-system (FTK3 and 4 and OTK1 and 2) to regulated pressure by opening NC PVs (FSV8 and OSV8). After this final propellant tank pressurization and pressure stabilization, the LBS is fully operational in the regulated pressure mode.

To circularize the geosynchronous transfer orbit, the two LAMS are fired in a sequence of several continuous steady-state burns (AMFs). Prior to each AMF, the spacecraft must be reoriented to the precise AMF attitude by a series of pulse firings utilizing one of the LAMS. (This reorientation maneuver can also be accomplished with the axial RCTs). Depending on various initial conditions, the final AMF may transition from the pressure-regulated mode into the pressure blowdown mode during the burn. This occurs when the high-pressure helium supply is expended and the pressure regulator(s) go into a fully open (nonregulation) condition.

Following the last AMF and final reorientation maneuvers with the LAMS, the LAMS are isolated from the propellant supply by closing the LAM isolation latch valves (FLV4 and 5 and OLV4 and 5) to provide additional insurance against losing any propellant because of a leak in one or more of the LAM valves during the remaining orbital life. Some time after LAM isolation, depending on mission considerations, the two helium pressurant isolation NO PVs (FSV1 and OSV1) are closed. This operation permanently isolates the pressurant supply from the PSTs and also isolates the oxidizer side from the fuel side to prevent any mixing of propellant vapors during the remainder of the mission. The LBS is now in the pressure blowdown mode, which is used for the rest of the mission. Based on the mixture ratio and propellant utilization during the earlier mission phases, the sequence of firing OFV1 and OSV1 can be staggered to rebalance the pressure in the PSTs in order to vary the mission mixture ratio for the on-orbit phase.

### **Power subsystem**

The electrical power subsystem for INTELSAT VI (Figure 11) is designed as a dual-redundant system with two separate electrical buses, each supported in sunlight by a three-element silicon solar cell array, with a Ni/H<sub>2</sub> battery for transitory load peaks and eclipse operation. Table 3 gives the broad characteristics of the subsystem. The design life of the subsystem is 10 years, with all degradable parts tested to 15 years.

The total power source capability is approximately 2,500 W at beginning of life (BOL) to support a power load of approximately 1,950 W. Figure 12 presents a summary of the power sources and loads, and Figure 13 depicts the INTELSAT VI power budget.

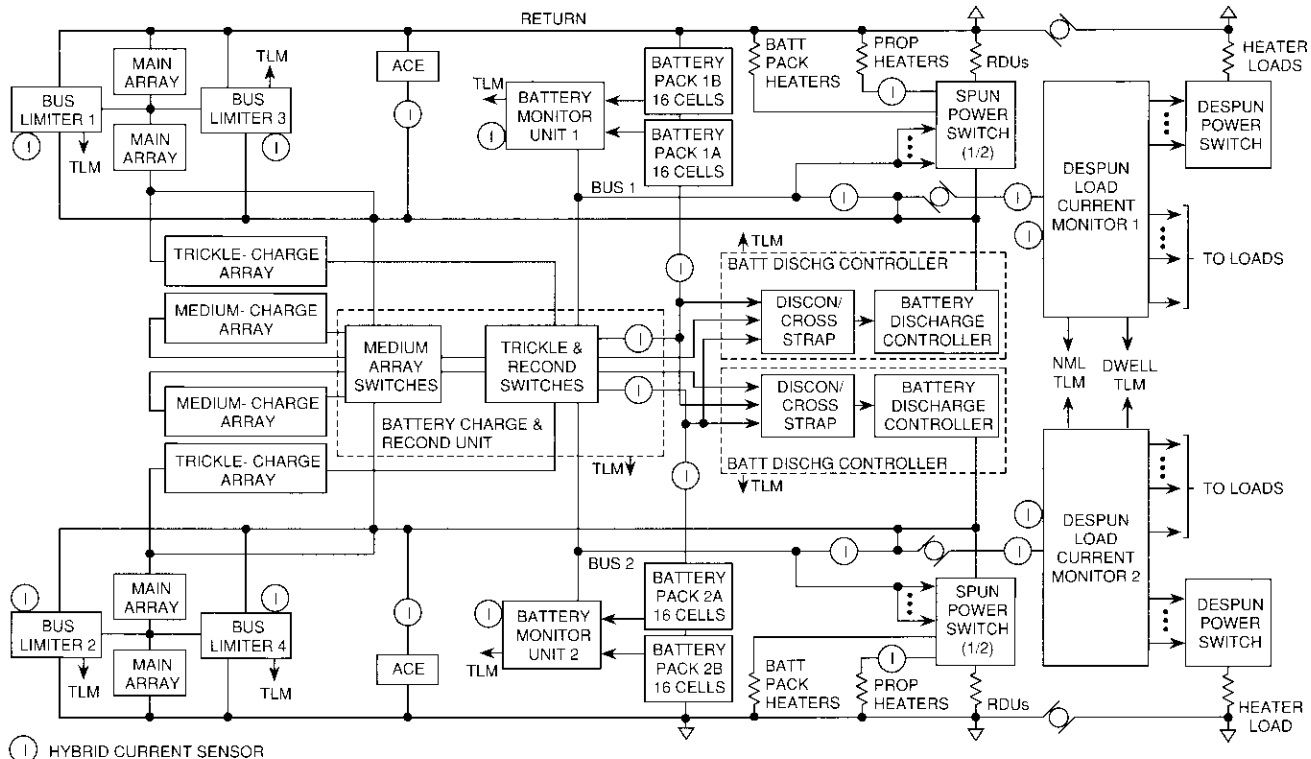


Figure 11. Power Subsystem

TABLE 3. POWER SUBSYSTEM CHARACTERISTICS AND PERFORMANCE

CHARACTERISTIC	VALUE
<b>Bus Voltage</b>	
Sunlight Operation	30.0 + 0.8 - 0.5 VDC
Eclipse Operation	28.9 + 0.25 - 0.3 VDC
Post-Eclipse Transient	42.5 V (max)
<b>Main Solar Array</b>	
Power Capability, min., EOL	2,123 W
Winter Solstice	2,205 W
Autumn Equinox	2,205 W
Power Margin, EOL,	260 W (13.8%)
Winter Solstice	221 W (11.1%)
Autumn Equinox	
<b>Battery Charge Rates</b>	
Trickle for Summer Solstice	
BOL	C/70
EOL	C/88
High Rate for Autumn Equinox	
BOL	C/7
EOL	C/10
Max. Recharge Time for 2 Batteries	≤ 20 hr
<b>Batteries</b>	
Number	2
Cells/Battery	32
Ah Rating, Each Battery	48.0
Maximum Depth of Discharge (FOL, one cell failed)	72%
Cell Type	Ni/H <sub>2</sub>
<b>Battery Discharge Controller</b>	
Efficiency	91%
Design Configuration	Redundant buck discharge controller per bus
<b>TWT-A Shutoff Voltage</b>	
Bus Voltage	26.1 + 0.5 V
Battery Monitoring and Failure Protection Characteristics	Individual cell voltage telemetry; battery cell pressure; cell bypass diodes

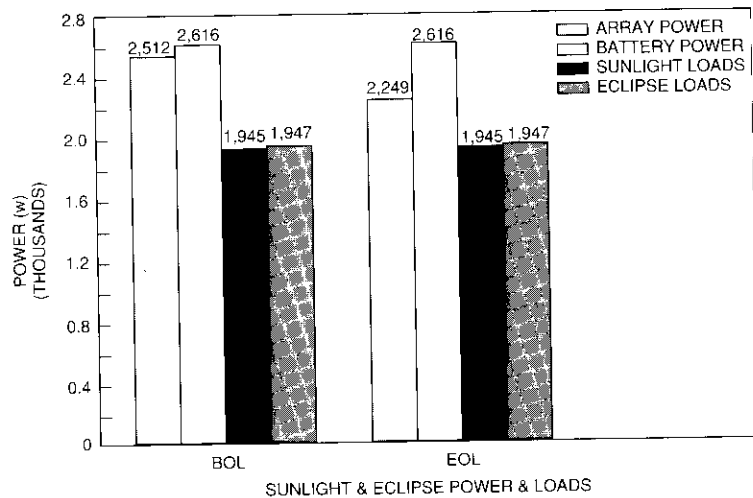


Figure 12. INTELSAT VI Available Power vs Loads

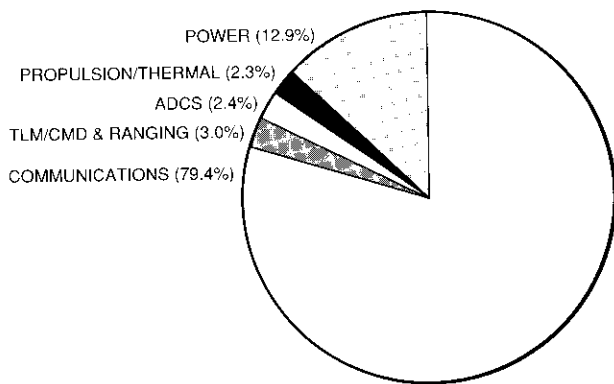


Figure 13. INTELSAT VI Power Budget

Figures 14 and 15 show details of the solar array supporting the bus. Approximately 60 percent of power comes from a telescopically deployed array, and the remainder from the main body array. Solar power is provided by a fixed body-mounted panel and a cylindrical telescoping panel (Figure 16). This arrangement features convenient growth capability, compact stowage, and optimized selection of distinct solar cell types for fixed and deployable sections. Conventional K7 solar cells are used on the cylinder. On

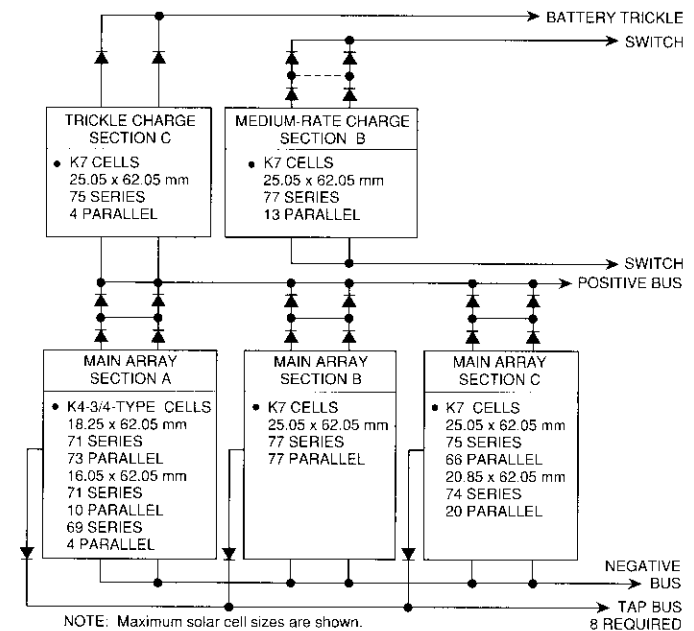


Figure 14. Solar Array for One of Two Identical Buses

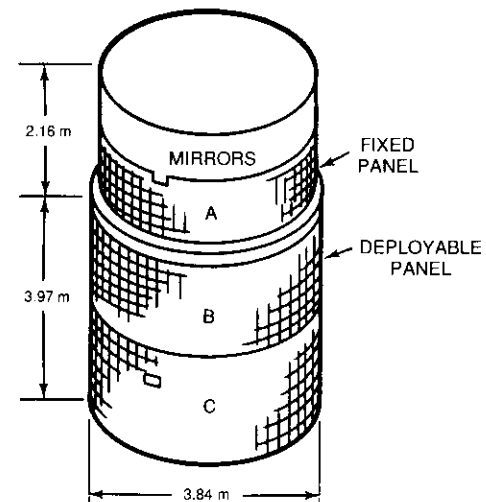


Figure 15. Solar Panel Configuration

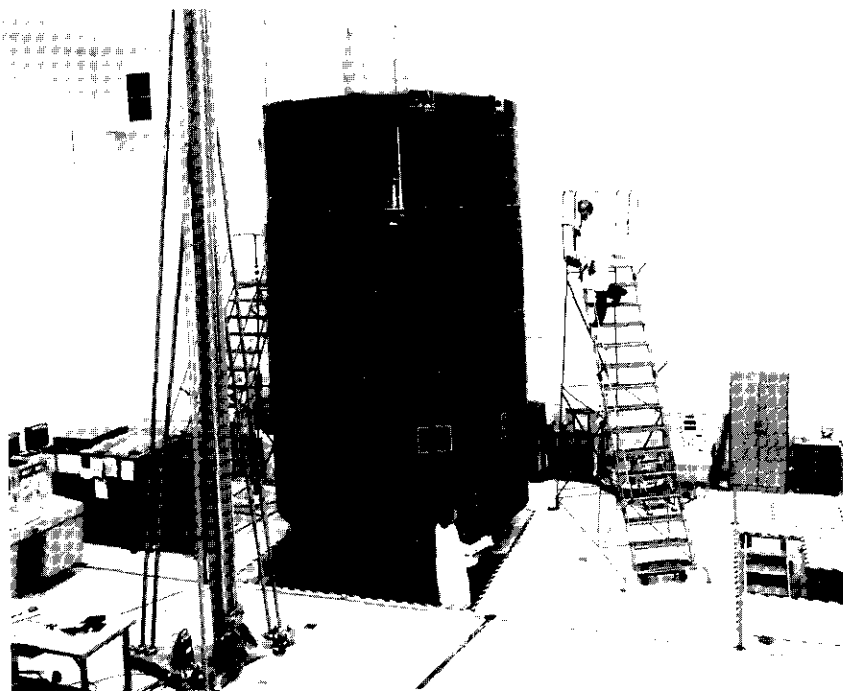


Figure 16. *INTELSAT VI Solar Cell Arrays*  
(photo courtesy of HAC)

the fixed panel, K4-3/4 cells are used because of their lower solar absorptance, which results in lower solar panel temperature. The characteristics of the solar cells are summarized in Table 4.

The Ni/H<sub>2</sub> batteries (Figure 17) are mounted on a platform at the aft end of the spacecraft body, permitting heat dissipation to space. This approach to integrating the batteries into the spacecraft maximizes battery thermal control capability. As a result, considerable leverage exists in the design to achieve optimum battery temperatures, and the excess thermal dissipation capability of this arrangement can accommodate battery growth. A modular battery discharge controller contains two controller circuits packaged in a single chassis for each of the two spacecraft buses. Battery cell characteristics are shown in Figure 18 and summarized in Table 5.

As noted above, the power subsystem is centrally preregulated, with two independent buses, and is controlled under steady-state conditions to between 28.9 and 30.8 V. The preregulated bus reduces voltage stress on units and permits the use of series-type regulators for most loads. The 28.9-V minimum

TABLE 4. SOLAR CELL CHARACTERISTICS

CHARACTERISTIC	FIXED-PANEL CELL (AFG-Telefunken)	DEPLOYABLE-PANEL CELL (Spectrolab, Inc.)
Size (mm)	18.35 × 62.05 and 16.05 × 62.05	25.05 × 62.05 and 20.85 × 62.05
Thickness (μm)	175	200
Material	Silicon	Silicon
Base Resistivity (Ω-cm/type)	10/N/P	10/N/P
Front Junction Depth (μm)	0.2	0.2
Back Surface Field	No	Yes
Back Surface Reflector	Yes	Yes
Contact Metalization	TiPdAg	TiPdAg
Front Contact Width (cm)	0.06	0.06
Cell Front Surface	Polished	Textured
Antireflective Coating	TiOx	TiOx Al <sub>2</sub> O <sub>3</sub>
Cover Type	CMX microsheet with antireflective coating	CMX microsheet with antireflective coating
Cover Thickness (μm)	210	210
Cover Adhesive	DC 93-500	DC 93-500

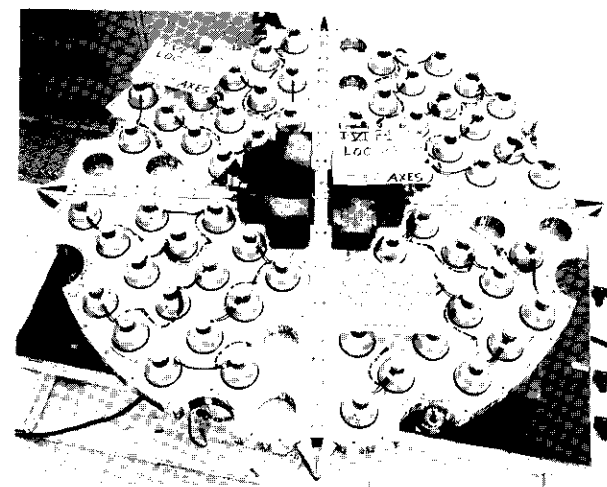


Figure 17. *INTELSAT VI Ni/H<sub>2</sub> Battery Pack*  
(photo courtesy of HAC)

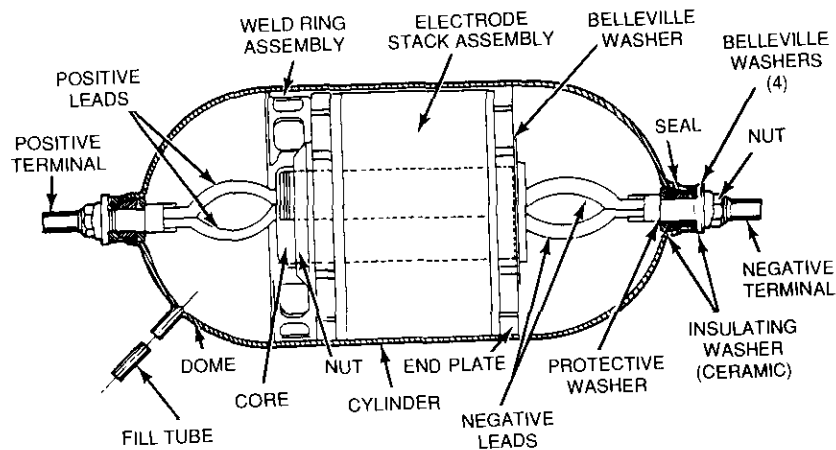


Figure 18.  $Ni/H_2$  Basic Cell Cross-Section

TABLE 5.  $Ni/H_2$  BATTERY FEATURES

FEATURE	DESCRIPTION
Negative Electrode	Photochemically etched nickel substrate; porous Teflon membrane; PT black catalyst; TFE binder
Positive Electrode	Nickel screen substrate; sintered carbonyl nickel powder plaque
Separator	Dual-layer Zircar
Gas Screen	Monofilament polypropylene screen
Wall Wick	Zirconium-oxide coating on cylinder and dome
Cell Type	Cylindrical pressure vessel
Cell Diameter	89 mm
Cell Capacity, 20°C	46.8 Ah
Cells/Pack	16
Packs/Battery	2
Battery/Spacecraft	2
No. Temperature Sensors/Pack	5, including 1 used only for launch
No. Pressure Sensors/Pack	6

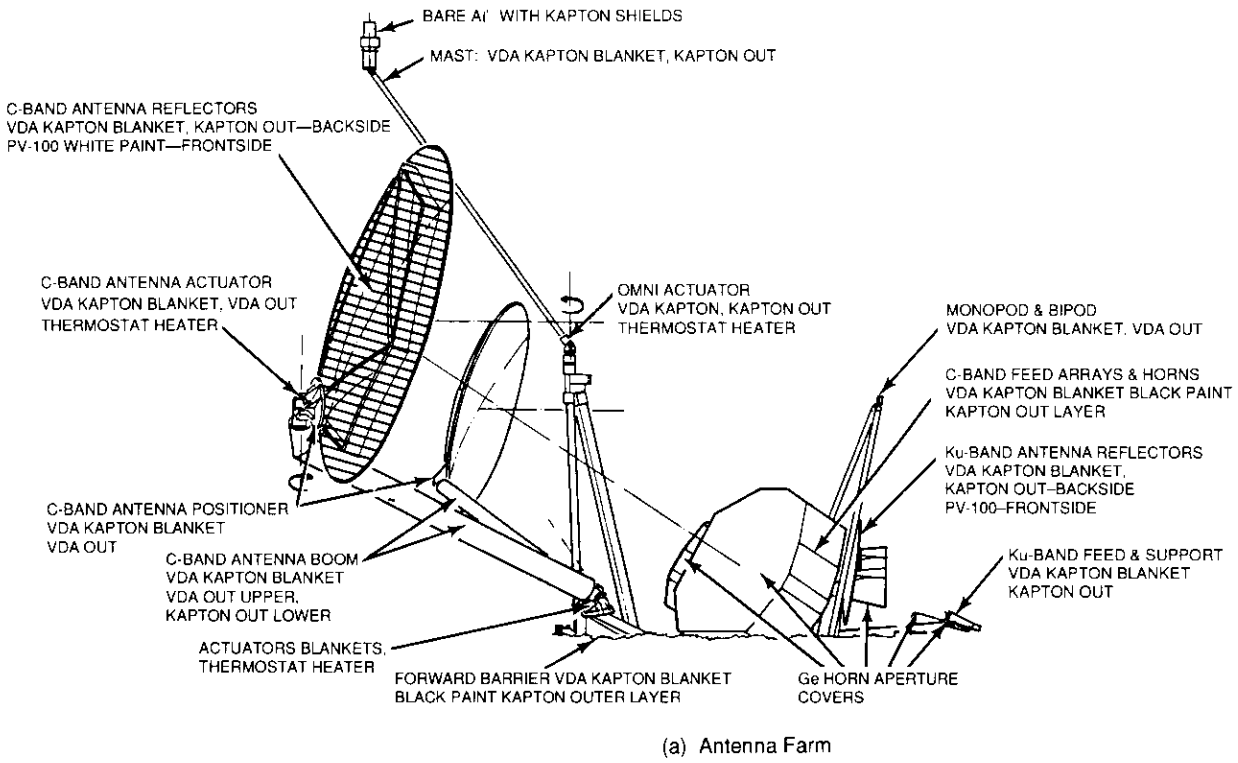
bus voltage is maintained by the battery discharge controller, while the 30.8-V maximum steady-state voltage is controlled by shunt limiters attached to tap points within the series length of the solar cell strings. In sunlight, the solar panel furnishes current directly at bus voltage. During eclipse, the battery automatically supplies current through a battery discharge controller, which translates the battery output from an average of 38 V to the 28.9-V bus. Battery charge current is passively controlled by switching a selected number of solar cell strings from the main 28-V array directly to the battery.

Power for operation in sunlight is derived from the cylindrical solar cell arrays. During eclipse season, the battery is recharged by dedicated battery charge arrays which can be switched to supplement the bus for end-of-life (EOL) solstice operation. Battery recharge can be performed at a high rate ( $C/7$  BOL) on each battery successively, or more normally at a mid-rate ( $C/16$  BOL) on each battery simultaneously. A trickle-charge rate of  $C/70$  BOL is used outside of eclipse and recharge operation. Battery reconditioning is performed prior to each eclipse season. While parallel operation of the buses is not possible on this spacecraft, limited flexibility is available to isolate either battery from both the bus and the charge arrays while supporting both buses with the second battery. Parallel operation of the batteries in an emergency is also possible. During normal operation in sunlight, bus voltage is maintained by four sets of redundant voltage regulators. During eclipse operation, the voltage is maintained by the battery discharge controller.

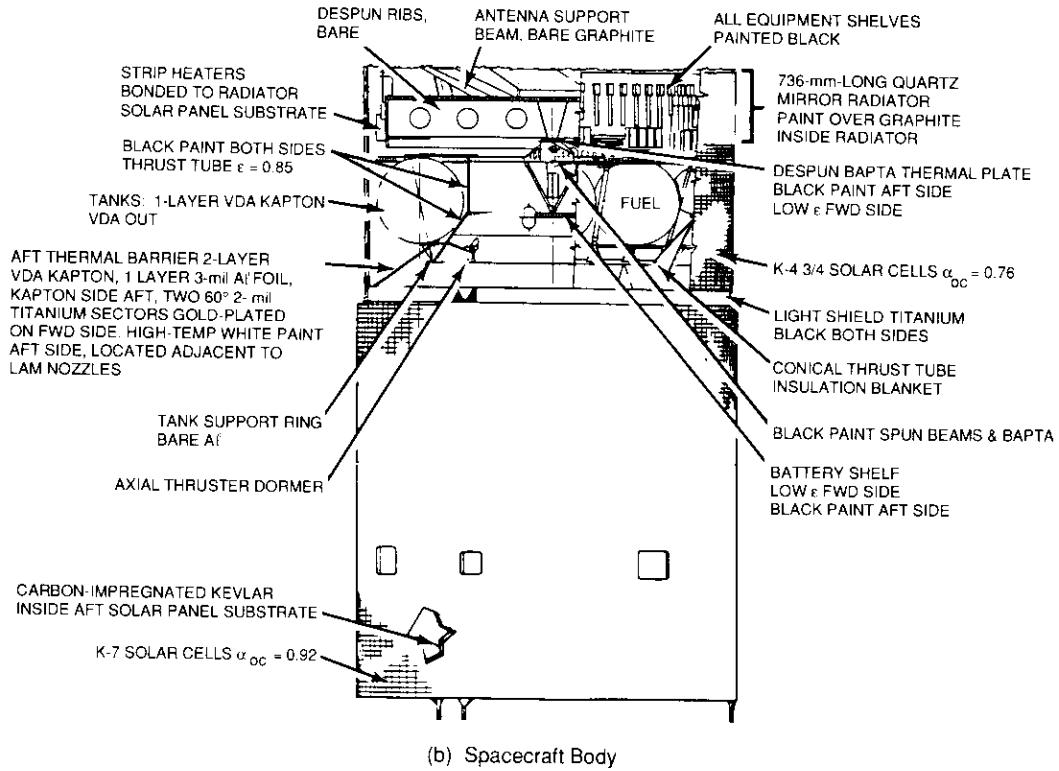
#### Thermal control subsystem

The INTELSAT VI spacecraft thermal control subsystem employs a conservative design similar to that used on past HAC and INTELSAT spacecraft. Its major features are illustrated in Figure 19. The design is passive, relying on superinsulation blankets to reduce heat loss, and a dedicated radiator to control and radiate the internally dissipated energy to space. The design is complemented with manually operated heaters on the LBS, payload substitution heaters to provide flexibility for on-station operation, and ground-commandable thermostatically controlled heaters for the battery and the antenna actuators during transfer orbit. Protection from the different thruster plumes provided includes titanium shields and high-temperature superinsulation.

Primary heat rejection is via an 8.2-m<sup>2</sup> optical solar reflector (OSR) radiator located on the fixed cylindrical part of the spacecraft near the earth-facing platform which supports the antenna farm. During transfer orbit, the radiator is covered by the deployable solar panel in its stowed position. In that configuration, the small heat rejection requirements are satisfied and the



(a) Antenna Farm



(b) Spacecraft Body

Figure 19. INTELSAT VI Thermal Design Features

temperatures of all internal equipment are maintained near ambient. On-station, after deployment of the solar panel, the radiator is exposed and a minimum power dissipation is required to keep all equipment within temperature requirements. This is accomplished by using replacement heaters if all or part of the payload is not in use. To account for the expected degradation of the OSR mirrors covering the radiator, the design solar absorptance value ( $\alpha$ ) used at BOL is 0.08, and a value of 0.23 is estimated at the end of 10 years of design life. The large physical separation between the radiator and the C-band reflectors results in a low thermal interaction, with minimum infrared backloading.

The communications units, which are the major heat dissipators, are mounted on the despun platform. The high-power amplifiers mounted on the rim shelf view the back of the rotating radiator and dispose of approximately 80 percent of their heat by radiative interchange. Heat transfer from the equipment mounting shelves to the drum radiator and solar panel is maximized by using high-emittance coatings and installing thermal doublers under high-dissipating amplifiers. The low-dissipating RF units, as well as those requiring a stable temperature environment, are mounted on the horizontal shelf, which does not have a direct view of the radiator.

Thermal control of the LBS is achieved by proper selection of surface finishes and by conduction isolation. Lines and valves employ heaters covered with a low-emittance finish. A titanium shield around each thruster protects adjacent spacecraft structures during firings. The radial thrusters, which fire through holes in the fixed and deployable solar panels, have titanium shields to protect these panels.

The Ni/H<sub>2</sub> battery cells mounted on a shelf inside the thrust tube dispose of their heat to space through the cavity formed by the deployable solar panel. The black interior of the solar panel precludes sunlight from reaching the shelf and provides the batteries with an unobstructed view of deep space. The exterior of the battery cells is painted white to limit the potential sun load in transfer orbit operation during the winter season when the deployable solar panel is stowed. Thermostatically controlled heaters maintain the batteries within a tight temperature range during transfer orbit operation.

The temperature of the forward portion of the spacecraft is controlled by a thermal barrier of aluminized Kapton coated with an electrically conductive black paint for electrostatic discharge protection. The barrier isolates the despun equipment from the diurnal temperature variation of the antenna farm. A light baffle at the interface between the spun solar panel substrate and the barrier prevents sunlight from entering the despun compartment. Each element of the antenna farm thermal design is protected by superinsulation blankets, except for the front face of the C-band and Ku-band reflectors, which are

painted white. Antenna deployment actuators have thermostatically controlled heaters which are disabled after all deployments are completed. The C-band feed arrays, Ku-band feed horns, and global horns are all wrapped with blankets having germanium vapor-deposited aluminum-gridded Kapton aperture covers.

The aft thermal barrier consists of sectors with aluminized Kapton blankets (indium tin oxide [ITO] being on the space side) and two titanium sectors centered around each 490-N thruster for protection during AMFs. The heating rate on the Kapton aft barrier is low enough to maintain temperatures well below its 343°C service temperature.

### Structures

The INTEL.SAT VI structural configuration is derived from an earlier HAC spin-stabilized satellite. The spun section (Figure 20) is constructed around a composite shear tube or central cylinder. The launch vehicle interface ring forms the aft end of the shear tube and mates to the shear frustum. The battery shelf ring is located at the intersection of the top of the frustum and the bottom of the cylindrical portion of the tube. The honeycomb spun shelf attaches to the top of the tube and is supported on the outer periphery by a series of struts.

One unique feature of the INTEL.SAT VI spun section is the triangular torque box composed of the aft ring, the inner tank support ring, the outer tank support ring, and shear plates and closeouts. This arrangement provides a means of transmitting the loads from the eight spherical propellant tanks

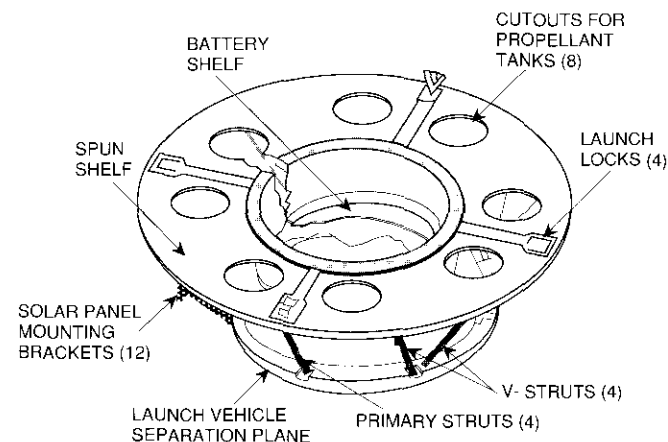


Figure 20. Structural Configuration of Spun Section

directly to the launch vehicle interface. The eight tanks also have a diaphragm support at the upper boss which transmits lateral loads directly into the spun shelf.

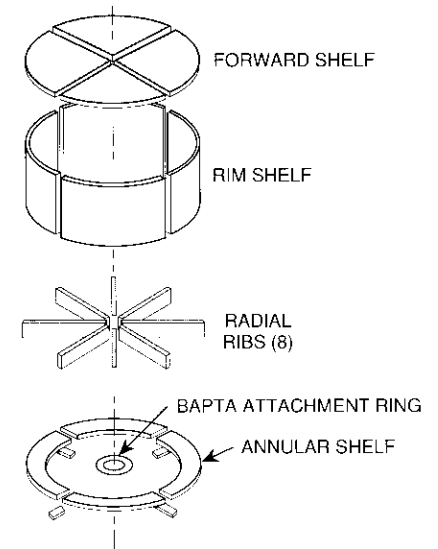
The spun and despun sections are joined by the BAPTA and have four pyrotechnically initiated launch-lock assemblies to transfer the despun section load to the spun structure during launch. The BAPTA is mounted on four beams that attach to the intersection of the shear tube and the spun shelf with a unique flexure T-clip design which limits the magnitude of the launch loads carried through the BAPTA to prevent damage to bearings.

The Ni/H<sub>2</sub> battery is packaged in four honeycomb quadrants which nest into a battery cruciform. The battery assembly bolts inside the shear tube to the battery shelf ring, which is located at the top of the frustum. This arrangement provides a view to space for battery thermal control.

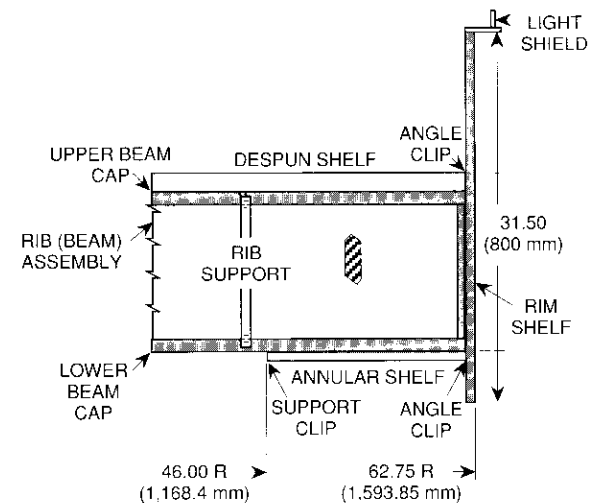
The despun section, shown in detail in Figure 21, resembles a wheel with eight spokes. The eight radial ribs attach to a hub which mates directly to the despun flange of the BAPTA. The forward shelf attaches to the upper flange of the ribs and provides the primary mounting surface for the antenna farm and the low-dissipative elements of the repeater. The annular shelf attaches to the lower flange of the ribs, near the outer edge, to provide additional mounting surface. The final element is the rim shelf, which attaches to the ribs, the forward shelf, and the annular shelf. This approach provides a very stiff, compact structure. The TWTAs are mounted to the outer surface of the rim shelf, which allows excess thermal energy to be dissipated through the mirror-covered radiator portion of the cylindrical solar panel that envelops the spun and despun sections.

The design of the antenna support structure was driven by the complex deployment requirements, coupled with the need for light weight and stiffness. The two large C-band reflectors are mounted on deployable booms and fold to fit inside the cylindrical envelope required by the launch vehicle fairing. Additional structural support is provided by a tripod which doubles as the base of the deployable omni boom; a bipod which pyrotechnically releases the transmit boom and one edge of the receive reflector; a monopod that supports both the transmit and receive reflectors with a double-nested, spherical-seat pyro release; and an auxiliary monopod which reacts the moment loads on the end of the transmit boom. The bipod lock, shown in detail in Figure 22, is a unique design which allows a moment-free joint between the receive reflector, the transmit boom, and the bipod support structure.

The struts are built with graphite epoxy tubes and bonded aluminum end-fittings. Assembly is performed on the alignment tooling and is custom-fitted



(a) Primary Despun Platform Elements



(b) Cutaway View of Despun Shelf Assembly

Figure 21. Structural Configuration of Despun Section

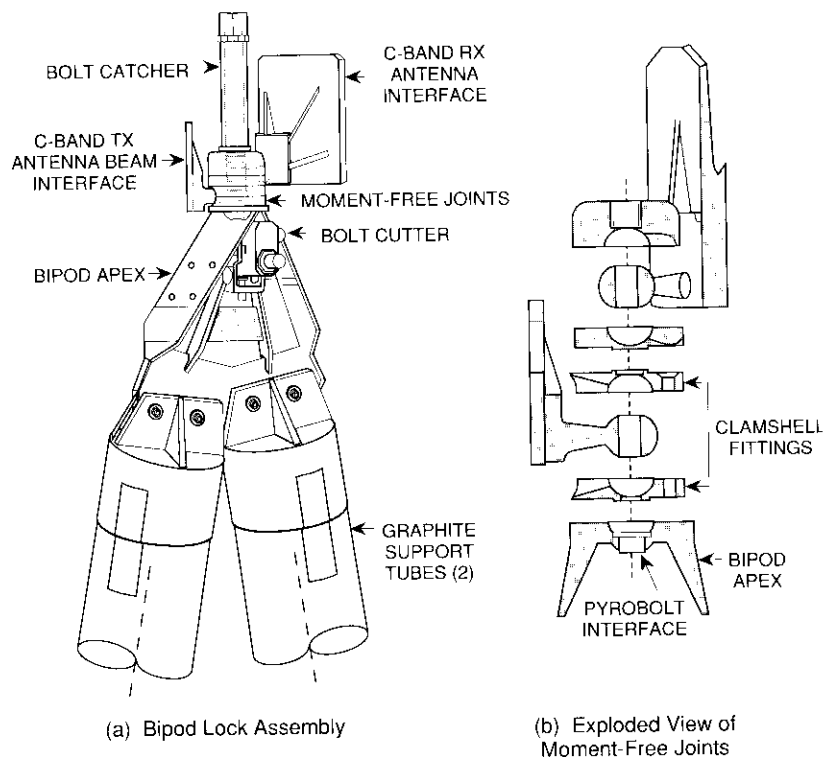


Figure 22. Antenna Support Bipod Lock

to provide correct deployed alignment, while still allowing the pyrotechnic release points to mate properly in the stowed configuration. All mechanical fasteners utilize close-tolerance reamed holes to maintain on-orbit pointing.

The transmit and receive feed array support structure is fitted in place following far-field pattern optimization, in which the feed arrays are repositioned relative to the fixed reflector positions. A mechanical adjustment feature is provided on one end of the graphite epoxy support struts. After the deployed alignment has been confirmed by RF testing, approximately 36 mirrors and tooling balls are surveyed to provide a baseline reference for subsequent near-field testing.

The two Ku-band spot beam antennas are configured with the feed horn and reflector on an integral graphite arm that attaches to a two-axis stepping mechanism. They are then stepped to a nested launch configuration, and each

antenna is held during launch with a single pyro bolt. The additional degrees of freedom are reacted by a retractable shear cone around the pyro bolt, and by a close-tolerance shear wedge/mating vee block.

The assembly of global coverage horns mounts to a single azimuth axis deployment mechanism and is held in its stowed position by a single pyro bolt. The deployment mechanism sits on a tripod, and the pyro bolt is located at the apex of a small bipod under the end of the global assembly.

The INTELSAT VI structure provides a very efficient, lightweight vehicle with easily accessible mounting surfaces for the payload and bus components, and incorporates one of the most complex antenna deployment schemes ever flown on a commercial spacecraft. Information on the tradeoffs leading to the antenna design is provided in Pontano *et al.* [5]. The electrical design and performance of the antennas are detailed in Persinger *et al.* [6].

### Mechanisms

The INTELSAT VI mechanisms subsystem comprises 16 independently commandable pyrotechnic releases, five damped/spring-driven actuators, two undamped actuators, and six stepper motor positioners to achieve the satellite BOL configuration. This complement of mechanisms, and the complex deployment sequence, were driven primarily by the geometry of the high-gain C-band antenna system, which required multiple hinge lines in order to fit within the launch vehicle envelopes. Once on-station, stepper motor antenna positioners allow repositioning of the spot beam, global, and C-band hemi/zone coverages. Two other stepper motor positioners can be used to reconfigure the C-band feed squareax network to produce the three unique C-band zone coverages for the different ocean regions. Additionally, three stepper motor positioners working in unison provide the capability to remove spin-axis coning (wobble) by allowing tilt adjustment of the aft deployable solar drum. The BAPTA is used throughout the anticipated stationkeeping mission to provide the gyrostad despin function and slip rings for spun-to-despun power and signal interfaces. Table 6 contains a complete listing of the mechanisms in this subsystem.

Because of the interleaved nature of the deployment sequence, the deployment events are mission-critical. For example, if the omni azimuth actuator failed to rotate the omni mast out of the deployment path of the C-band transmit reflector, none of the subsequent deployments could be accomplished. High mechanism torque margins and a thorough ground test program provide the high degree of confidence needed for each event in the complex deployment sequence, which is summarized in Table 7.

TABLE 6. MECHANISMS SUBSYSTEM

MECHANISM	TYPE
Omni Elevation Actuator	Viscous-damped/spring-driven
Omni Azimuth Actuator	Viscous-damped/spring-driven
Transmit Dish Actuator	Viscous-damped/spring-driven
Transmit Boom Actuator	Viscous-damped/spring-driven
Receive Boom Actuator	Viscous-damped/spring-driven
Monopod Actuator	Undamped/spring-driven
Auxiliary Monopod Actuator	Undamped/spring-driven
Solar Drum Positioners (3)	Stepper motor
C-Band Antenna Positioners (2)	Two-axis stepper motor
Spot Beam Antenna Positioners (2)	Two-axis stepper motor
Global Horn Antenna Positioner	Stepper motor
Squareax Switch Positioners (2)	Planetary/stepper motors
BAPTA	Synchronous DC motor
Separation/Ejection Mechanism	Pyro-release clampband
Spun-to-Despun Launch Locks (4)	Undamped/spring-driven

As shown in Table 7, the pyrotechnic release devices include bolt cutters, pin pullers, and explosive bolts. Bolt cutters and pin pullers employ redundant NASA-standard initiators. The 229-cm separation system is a unique design developed at British Aerospace for the INTELSAT VI program. The vec-clamp system ties the satellite to the launch vehicle adapter for Ariane launches, or to the perigee stage adapter for commercial Titan launches. Three pyrobolts are located at 120° intervals around the clampband, which is tensioned to 56 kN for flight. The explosive bolts in the separation clamp use single initiators; however, this system was qualified for the case where only two of the three bolts release. Shear loads during launch are carried by 60 shear cones, which are located between the satellite aft ring and the adapter.

Viscous-damped, spring-driven actuators are employed at several locations in order to achieve high torque margins without excessive latch-up velocities. Minimum torque margin requirements were set at 3:1 (200-percent margin); however several of these mechanisms ultimately provided significantly higher margins. Figure 23 illustrates the basic design for the damped actuators. Spring lamination stacks provide the motor torque, which is counteracted by viscous damper fluid (Dow Corning 200). The damper fluid is forced through an orifice that is sized to provide the desired damping characteristic. Since

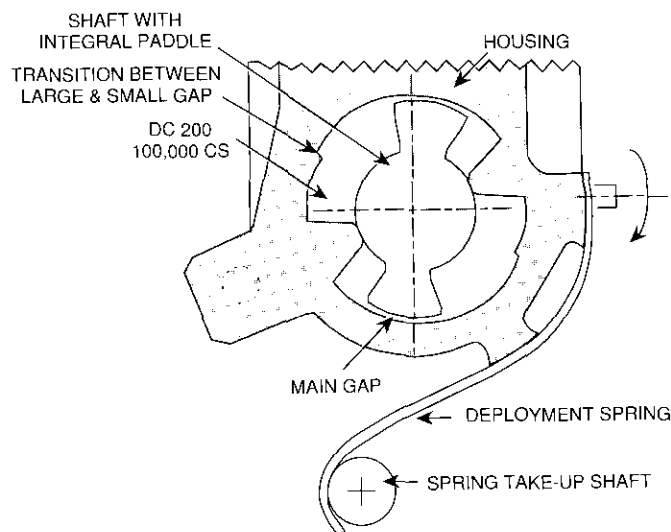
TABLE 7. INTELSAT VI DEPLOYMENT SEQUENCE

LAUNCH LOCK	PYRO DEVICE	EVENT
Omni Elevation	Bolt cutter	Omni elevation actuator deploys omni antenna 47°.
Separation Clamp	Explosive bolts (3)	Clamp retracts and 8 push-off springs separate satellite from upper stage.
Spun/Despun	Bolt cutters (4)	Belleville spring stacks retract shear cones.
Omni Azimuth	Pin puller	Omni azimuth deploys omni antenna 164.5°.
Solar Panel	Bolt cutters (3)	Solar drum positioners deploy aft panel.
Auxiliary Monopod	Bolt cutter	Auxiliary monopod actuator deploys auxiliary monopod 87°.
Global Horn and Ku-Band Antennas	Bolt cutters (3)	Stepper motor mechanisms deploy east/west Ku-band global and spot beam antennas to subsatellite point.
Monopod	Bolt cutter	Transmit and receive reflectors released at monopod lock.
Tripod	Bolt cutter	Transmit dish actuator deploys reflector 224°.
Bipod	Bolt cutter	Receive boom actuator deploys boom/reflector 84.7°.
Transmit Second Stage	Pin puller	Transmit boom actuator deploys boom/reflector 119.5°.

fluid viscosity is affected by temperature, the temperature of each mechanism is verified to be within a specified range on-orbit prior to initiating the deployment.

The monopod and auxiliary monopod actuators do not require viscous damping because these deployable appendages have relatively low inertia and can withstand the impact loads at the end of the deployment range. Both of these deployables use a Velcro retention system to preclude rebound after the deployment motion. All of the damped and undamped spring-driven actuators (except the spun/despun launch locks) include redundant microswitches to allow verification of successful deployment on-orbit.

Spun-to-despun (platform) launch locks are a direct derivation from the HAC HS-376 line. Four locks are located at 90° intervals around the periphery of the rim shelf, as shown in Figure 24. Upon initiation of its pyrobolt cutter, each lock independently rotates outboard approximately 45°, releasing the platform from the rotor. The swift deployment motion is initiated by Belleville spring stacks which impart about 890 N of kickoff force. Crushable aluminum honeycomb is used to absorb some of the impact energy at the end of launch lock travel.



- Shaft is pinned to support structure.
- Deployment spring imparts constant torque to housing.
- Housing rotates relative to shaft, compressing fluid & forcing it through main gap at controlled rate.
- Main gap decreases, lowering terminal velocity.

Figure 23. *Viscous-Damped Spring-Driven Actuator*

The satellite employs a wide variety of stepper motor mechanisms in applications ranging from antenna positioning to RF switching. The C-band antenna positioners are two-axis jackscrew drives which steer the 3-m transmit and 2-m receive reflectors. These actuators are part of a closed-loop pointing control system (beacon tracker) which allows active repositioning to correct for diurnal and seasonal thermal distortion variations in the reflector support structures. Hemi/zone beam pointing is adjusted as required in  $0.0023^\circ/\text{step}$  increments until the beacon error signal is nulled.

Stepper motor mechanisms are also used to deploy and reposition the Ku-band spot beam antennas and the global horn array. The spot beam positioners are gimbal mechanisms with  $0.089^\circ/\text{step}$  resolution in each axis. Ground controllers can command the spot beam coverages to any position on the earth's disk by sending stepper motor pulse trains and monitoring position potentiometer telemetry. At a nominal step rate of 25 steps/s, these antennas can be slewed at approximately  $13^\circ/\text{min}$ . The global horn positioner provides azimuth axis rotation exclusively.

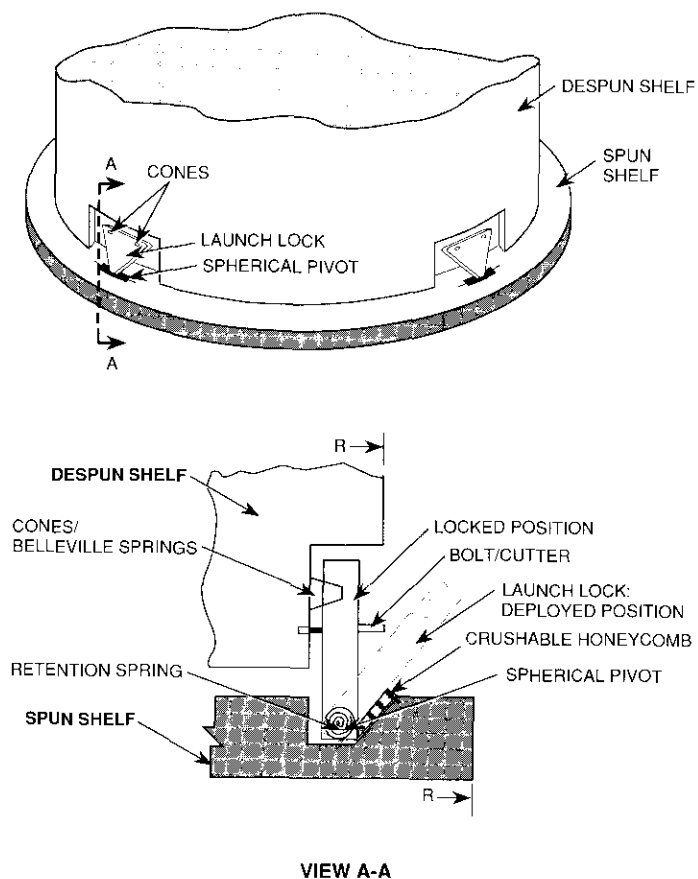


Figure 24. *Platform Launch Locks*

Squareax switch positioners are a unique feature on INTELSAT VI which make the satellite suitable for use in any of the three ocean regions. Ninety-two individual RF switches are driven in unison using a common drive plate with a planetary stepper motor drive system. These switches are used to redirect RF signals to different horns in the C-band feed arrays to form the zone beam patterns for each of the three specified ocean regions. Two-for-one redundant stepper motors can be commanded to reconfigure the satellite for a new coverage within 7 minutes.

Three differential drive stepper motors are used to deploy and adjust the telescoping solar drum at BOL. The solar drum positioners (SDPs) are similar in

design to devices which have flown on over 30 HAC HS-376 satellites. The INTELSAT VI version of the SDP is slightly larger than its predecessor, providing more torque and greater stepping life. Three of these redundant motor drives are located at the aft end of the satellite, at 120° intervals. Each drive involves a rack/pinion gear interface, with the rack attached to the inside surface of the solar drum. To deploy the panel on-orbit requires over 225,000 steps and takes approximately 3 hours of commanding. After the drum is fully extended, wobble measurements are taken using the beacon error signal, and the SDPs are differentially stepped to correct for any rotor mass imbalances. Wobble measurements are repeated periodically over the life of the satellite, and the SDPs are commanded as required to alleviate the imbalance that is induced as fuel is expended.

The INTELSAT VI BAPTA design is based on previous designs which have performed reliably in space on dozens of HAC dual-spin satellites. The INTELSAT VI version was scaled up significantly in terms of load-carrying and power/signal throughput capabilities. Redundant despun torque motors are controlled by motor drivers in the ACE. Sixteen integral index pulse generators provide feedback to establish spun/despun relative rate estimates for the controller. The 24-pole motors can develop up to 4.8 N-m each. If required, both motors can be driven simultaneously to produce twice this amount of torque. The electrical contract ring assembly contains 44 signal and four power slip rings. Total power transfer capability is about 2,000 W.

#### **Beacon tracker subsystem**

The beacon tracker subsystem nominally performs initial alignment of the C-band hemi/zone antennas with respect to the despun compartment, as well as precision closed-loop pointing of their beams. In addition, this subsystem provides backup capability for despun and nutation control.

Azimuth and elevation pointing information is generated by receiving and processing a beacon signal transmitted from a ground station. This signal is captured by small antenna elements (Yagis) located between the communications horns of the transmit and receive hemi/zone feed arrays.

Sum and difference signals are generated from the signals captured at the tracking feeds. The detection process is essentially a comparison of the beacon signal power and phase differences between specific horns. This information is used for antenna reflector pointing, despun platform pointing, and nutation control.

Azimuth and elevation pointing of the transmit and receive reflectors is accomplished using electrically redundant stepper motors (dual windings). The motors are controlled by the track receiver through the despun stepper

motor drive unit. Azimuth pointing of the receive reflector can alternatively be performed by varying the despun pointing of the platform.

Transmit and receive reflectors operate independently and can lock in on selected beacon sites in any one of the three ocean regions. An offset capability is employed to optimize C-band coverage patterns for any particular orbit situation.

Additional details on the beacon tracker subsystem are provided by Persinger *et al.* [6].

#### **Perigee stage**

For commercial Titan launch, a perigee stage is required for injection into a geostationary transfer orbit. The perigee stage consists of a solid rocket perigee motor (United Technologies-Chemical Systems Division ORBUS 21S), a structural adapter, and various units that control the mission up to placement in transfer orbit once the spacecraft and attached perigee stage are separated from the Titan launcher.

The primary structure of the perigee stage is a cylindrical aluminum honeycomb adapter which attaches to the satellite with a titanium Marmon-type V-clamp. The units mounted on the adapter are the PESS, the perigee-stage driver units, and the perigee motor safe and arm units. The PES is an on-board controller that sends sequenced commands to the satellite to deploy the omni antenna and initiate spacecraft spinning, and to the perigee stage driver unit to fire the perigee motor. In addition, acceleration switches (G-switches) are mounted on the spun section to detect and terminate the spin maneuver at 30 rpm.

To provide nutation control during the spinning perigee motor firing, a PANC is added for Titan launches. The PANC consists of gyro packages and interface electronics which utilize the satellite ACE TANC functions to produce thruster pulses when gyro excitation exceeds a threshold. The 490-N apogee thrusters perform this function and continue to provide nutation stabilization until after initial spacecraft acquisition.

#### **Launch vehicle compatibility**

The INTELSAT VI spacecraft was originally designed to be compatible with the Ariane 4 launch vehicle and the NASA STS [1]. Subsequent to the Shuttle disaster in 1986, the design was verified to be compatible with the commercial Titan III launch vehicle.

For both Ariane 4 and commercial Titan launchers, the maximum diameter of the spacecraft (3.64 m) is within the static envelopes of the fairings. The

dynamic envelope is determined from the coupled loads analysis and is also compatible with both launch vehicles.

As INTELSAT VI was designed and initially tested to meet the Ariane 4 and STS environment, and as forcing functions were modified and environments refined, the spacecraft was continually reassessed against changing requirements. With the addition of the commercial Titan, supplemental qualification tests were necessary to recertify the spacecraft. Due to the large design and testing margins established early in the program, it was possible for the basic design to remain unchanged and yet be compatible with substantially wider launch environments.

For Ariane 4 launch, an adapter is provided which attaches to the Ariane vehicle equipment bay (VEB) by 180 bolts. The adapter is an aluminum honeycomb truncated conical section, 2.35 m at the base and 1.471 m in length. The separation system consists of a titanium V-band clamp, eight pushoff springs, and four microswitches. The springs provide approximately 1,000 N of force, which generates 0.5-m/s separation velocity.

Electrical interfaces between the satellite and the Ariane 4 adapter are via two 61-pin umbilical connectors. The adapter and spacecraft are instrumented with accelerometers and strain gauges which provide measurements to the launch loads instrumentation processor (LLIP). Acceleration and strain data are provided via the launcher telemetry system to evaluate the launch environment.

When the spacecraft is attached to the Ariane 4, it is powered via the umbilicals and commanded via RF-transparent windows in the payload fairing. After launch, the telemetry omnidirectional antenna is deployed through the despun squib driver unit, which is armed prior to separation. The Ariane 4 VEB command unit generates the enable and fire commands, and also provides the current to initiate the V-band separation clamp. Three pyrotechnic bolts are used, with only one firing necessary for successful separation.

For commercial Titan launches, the primary spacecraft interface is with the perigee stage, as previously discussed, and the LLIP described above. An electrical interface was defined which retained much similarity to the STS and Ariane designs. As with Ariane, prior to launch the spacecraft is powered via the umbilicals and commanded through RF-transparent windows in the fairing. The PES performs all the initial functions of the mission after separation from stage 2 of the Titan. Separation of the payload (perigee stage and spacecraft) is initiated in the Titan stage 2 avionics. A pyrotechnical separation signal ignites an expanding tube separation system, which shears a structural member that attaches the perigee stage to the Titan stage 2.

## Acknowledgments

Numerous INTELSAT and Hughes Aircraft Company publications were used to compile this paper. The authors wish to acknowledge all the authors of these publications.

## References

- [1] G. P. Cantarella and G. Porcelli, "Specifying the Spacecraft Bus," *COMSAT Technical Review*, Vol. 20, No. 2, Fall 1990, pp. 309-333.
- [2] L. B. Perillan, W. R. Schnicke, and E. A. Faine, "INTELSAT VI System Planning," *COMSAT Technical Review*, Vol. 20, No. 2, Fall 1990, pp. 247-269.
- [3] L. Dest *et al.*, "INTELSAT VI—An In-Orbit Assessment," 13th AIAA International Communication Satellite System Conference, Los Angeles, CA, March 1990. AIAA Paper No. 90-0899.
- [4] L. I. Slafer and V. L. Seidenstucker, "Attitude and Payload Control System for INTELSAT VI," *COMSAT Technical Review*, Vol. 21, No. 1, Spring 1991, pp. 57-100 (this issue).
- [5] B. A. Pontano, A. I. Zaghloul, and C. E. Mahle, "INTELSAT VI Communications Payload Performance Specifications," *COMSAT Technical Review*, Vol. 20, No. 2, Fall 1990, pp. 271-308.
- [6] R. R. Persinger *et al.*, "The INTELSAT VI Antenna System," *COMSAT Technical Review*, Vol. 21, No. 1, Spring 1991, pp. 149-189 (this issue).



*Leonard R. Dest received B.S. and M.S. degrees in mechanical engineering design and modern control theory, respectively, from Lehigh University. He has over 18 years of spacecraft design, analysis, operations, system engineering, and management experience. His career has included technical positions at Fairchild, RCA, COMSAT, and INTELSAT. At INTELSAT he was responsible for spacecraft bus subsystems (including attitude control, propulsion, power, thermal, structure, and mechanisms) and the launch vehicle interfaces for all INTELSAT spacecraft. For 9 years, he was responsible for the INTELSAT VI space-*

*craft bus design, development, and test, and has served as the Deputy Mission Director for all INTELSAT VI launches.*

*Mr. Dest joined Hughes Aircraft Company in December 1991 as Chief Scientist/Engineer, Advanced Programs Laboratory. Additionally, he is currently the Systems Engineering and Mission Manager for the INTELSAT VI (F3) Reboost Program, which will use the Space Shuttle to capture and attach the satellite to a perigee kick motor, which will permit the reboost of the F3 satellite from low earth orbit where it was stranded after a launch vehicle failure in March 1990.*

*Jean-Pierre Bouchez received his Engineering Degree from Ecole Catholique d'Arts et Métiers, Lyon, France, in 1965; and an M.S. and Ph.D. from the University of Minnesota in 1969 and 1973, respectively, both in mechanical engineering. From 1969 to 1972, he worked at Honeywell in Minneapolis, and then moved to the European Space Agency in Noordwijk, The Netherlands, where he was involved in the development of thermal subsystems for many spacecraft, including OTS and ULYSSES. In 1984, he joined COMSAT in El Segundo to oversee the thermal subsystem of the INTELSAT VI spacecraft. He has been with INTELSAT since 1985, participating in the manufacture, testing, launch, and in-orbit operation of this series of spacecraft. In 1989 he moved to Palo Alto at the beginning of the INTELSAT VII program and has recently been appointed Bus Manager for INTELSAT VII-A.*

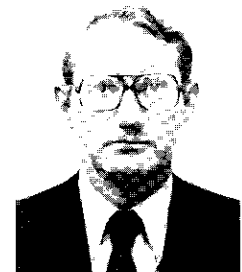


*Victor R. Serafini received a B.S. in aeronautical engineering from the University of Illinois and has taken graduate courses at both the University of Illinois and UCLA. He joined COMSAT in 1978 and is currently Director of Engineering in COMSAT System Division's Space Systems Engineering Group. Prior to joining COMSAT, he was a Project Manager at TRW Systems Group, and earlier had been a Project Engineer/Department Manager for the Rocketdyne Division of Rockwell International.*



*Michael Schavietello obtained a B.S. in general engineering, with emphasis in applied mechanics, from the University of Illinois in 1981. He has been employed by Hughes Aircraft Company since 1982, where he was involved with the design, development, test, and launch phases of the INTELSAT VI program. As a member of the INTELSAT VI systems engineering staff, his responsibilities included spacecraft mechanical integration, structures, mechanisms, alignments, propulsion, and mass properties. Since the conclusion of the INTELSAT VI program, Mr. Schavietello has served as Spacecraft Bus Manager for the UHF Follow-On Program, which consists of nine satellites (employing the Hughes HS601 bus concept) to provide a global communications network for the U.S. Navy.*

*Keith J. Volkert received a B.S. in aeronautical and astronautical engineering from Northrop University in 1968. He is currently Deputy Director of Space Systems Programs for COMSAT's Space Systems Engineering Group. In his 10 years with COMSAT he has supported numerous international communications satellite programs, including INTELSAT VI. Prior to this, he worked at JPL on the Viking Orbiter, Voyager, and Galileo programs.*



## **Attitude and payload control system for INTELSAT VI**

L. I. SLAFER AND V. L. SEIDENSTUCKER

(Manuscript received October 17, 1990)

### **Abstract**

The attitude stabilization and control system for the INTELSAT VI geosynchronous communications satellite is described. The dual-spin spacecraft design, the launch-to-final-orbit mission sequence, and the superspin technique developed to stabilize the spacecraft during geosynchronous transfer orbit operations are reviewed. Detailed descriptions are given of the functional design, implementation, and performance of the microprocessor-based control system. Key topics summarized include precision despun platform pointing control using either spinning sun and earth sensors or an RF beacon track receiver; active nutation stabilization using payload pointing control loops; extensive processor fault protection; and a high level of control system autonomy, including on-board spin axis attitude determination and control, on-board stationkeeping maneuver control, and the use of stored command processing.

### **Introduction**

The fundamental design of the INTELSAT VI geosynchronous communications satellite (Figure 1) is based on a spinning rotor which contains most of the utility subsystems (*i.e.*, power, propulsion, attitude and despun control, and a portion of the telemetry and command), and a large, mechanically despun, earth-oriented platform containing the communications payload, the RF beacon tracker subsystem (BTS), and the remainder of the telemetry and command subsystem. Basic attitude stabilization of the spacecraft is achieved through

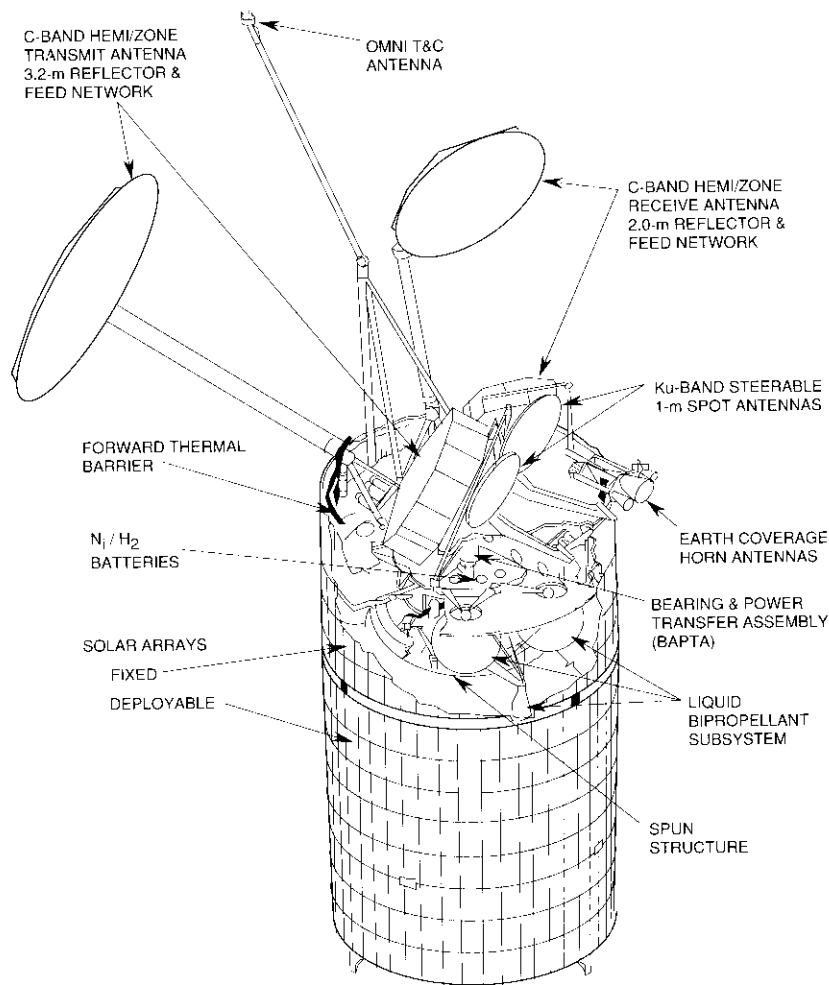


Figure 1. *INTELSAT VI Spacecraft*

gyroscopic stiffness developed by the spinning rotor, with periodic adjustments to correct for errors induced by external environmental disturbances.

The spacecraft attitude and orbit control functions for INTELSAT VI can be divided into four basic categories: spin axis attitude determination and control, platform despin (rate and pointing) control, vehicle nutation stabilization, and thruster control for stationkeeping operations. The attitude determination and control subsystem (ADCS) provides the on-board hardware and firmware

to perform all necessary attitude and orbit control functions over all phases of both Ariane- and Titan-launched missions.

The control system design concept developed for INTELSAT VI was directed toward meeting the following critical mission requirements:

- Precision pointing of the spin axis and communications antenna boresight. Absolute beam pointing to within a  $3\sigma$  error of  $0.12^\circ$  with  $0.02^\circ$  short-term stability is necessary to meet payload performance requirements.
- Extended autonomous operation to minimize the need for real-time ground control of spacecraft attitude and velocity.
- Maximum flexibility to adapt to parameter changes during the spacecraft development cycle and on-orbit operations.
- A complex transfer orbit sequence involving several modes of operation.
- High system reliability and fault tolerance.

The resulting ADCS is an integrated control system that employs a central microprocessor with all primary control functions (platform despin control, spin axis attitude determination and control, thruster control for velocity maneuvers, and attitude stabilization) implemented in firmware. Using this approach, the different control functions can be integrated for improved overall performance. For example, precision platform pointing is maintained during orbit correction maneuvers by using a feed-forward technique that internally corrects the pointing control loop for disturbance torques generated as a result of thruster mismatch and spacecraft mass center deviations from the thrust axis.

### ***Mission sequence***

The INTELSAT VI mission sequence for a Titan-launched spacecraft is shown in Figure 2. The launch vehicle places the spacecraft into a circular parking orbit, and the spacecraft is oriented into the perigee kick motor (PKM) firing attitude. Forty-five minutes prior to the selected transfer orbit injection opportunity, the spacecraft is spun up to approximately 2 rpm and separated from the Titan. Omni antenna deployment (Figure 3) is then initiated automatically by an on-board sequencer, followed by spinup to 30 rpm using spacecraft thrusters. PKM firing, automatically initiated 45 minutes after separation, places the spacecraft into an elliptical geosynchronous transfer orbit. Once the spacecraft becomes visible, the spent PKM case is ejected by ground command.

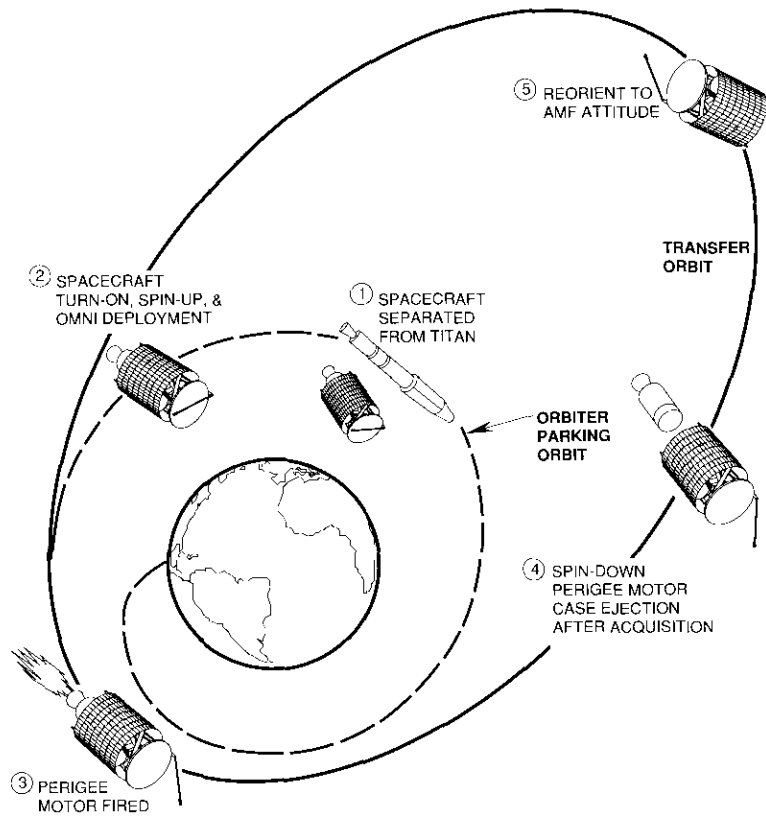


Figure 2. INTELSAT VI Mission Sequence (Titan Launch)

For an Ariane 4 launch, the spacecraft is placed directly into a synchronous transfer orbit, with the Ariane upper stage spinning up the spacecraft to about 5 rpm prior to separation.

Once transfer orbit has been achieved, the sequence is identical for both Titan- and Ariane-launched missions. At this point, the platform and rotor are mechanically locked together with a system-spin-to-transverse-inertia ratio of 1.14, representing an inherently stable configuration (*i.e.*, the spacecraft is spinning about an axis of maximum moment of inertia). The liquid bipropellant system, using two 490-N thrusters firing for approximately 30 to 50 minutes per orbit, is then used to place the spacecraft into geosynchronous orbit.

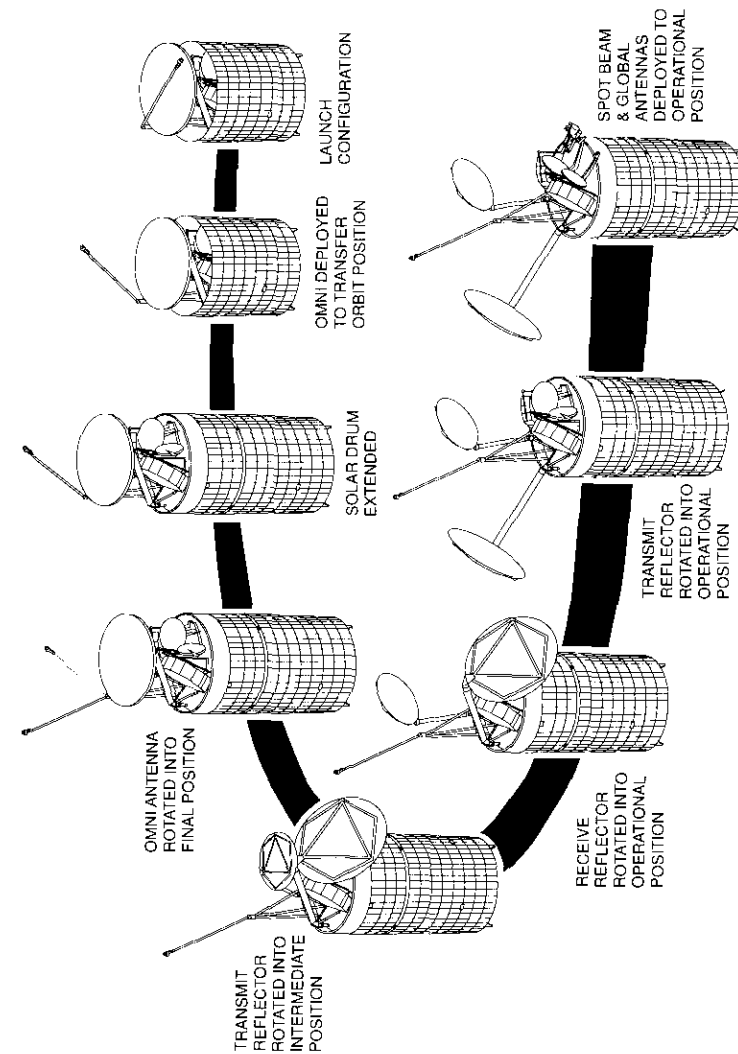


Figure 3. INTELSAT VI On-Orbit Deployment Sequence

Because consumption of liquid bipropellant during the apogee thruster firings decreases the total spacecraft spin moment of inertia faster than either the maximum or minimum transverse moments of inertia, the vehicle inertia ratio would reduce to less than 1.0 during the burns if the spacecraft were to remain locked. Dynamic instability would occur at a 45-percent propellant load level. To maintain a stable configuration throughout apogee motor firing (AMF), as propellant is reduced to the 23-percent beginning-of-life (BOL) load level, a superspin technique was developed during which the platform is unlocked from the rotor and spun forward faster than the rotor. The effective inertia ratio of the rotor is given by

$$\sigma_R = \frac{I_R + |\omega_p| I_P}{I_T + |\omega_s| I_R} \quad (1)$$

where  $\omega_p$  = inertial spin rate of platform  
 $\omega_s$  = inertial spin rate of rotor  
 $I_R$  = rotor spin moment of inertia  
 $I_P$  = platform spin moment of inertia  
 $I_T$  = spacecraft transverse moment of inertia.

With  $\omega_p = 2\omega_s$ , the resulting effective inertia ratio of the rotor for INTELSAT VI is 1.4. Thus, the superspin condition maintains a high (greater than unity) inertia ratio throughout the AMF maneuvers. This ensures that energy dissipation caused by propellant sloshing [1],[2] acts to stabilize the spacecraft spin axis attitude.

Following synchronous orbit injection, the spacecraft is reoriented to an orbit normal attitude and the platform is inertially despun ( $\omega_p \approx 0$ ), transitioning to a Hughes Aircraft Company (HAC) gyrostat configuration. In this configuration, the effective rotor-spin-to-transverse-inertia ratio is approximately 0.70, and rotor energy dissipation now serves to destabilize the spin axis attitude. Active nutation control using spacecraft thrusters is employed to stabilize the spacecraft until the operational configuration is achieved.

At this point, the telescoping solar panel is extended, the C-band antenna reflectors are deployed, and the K-band antennas are positioned using a two-axis gimbal drive. Following fine adjustment of all antenna positioners and precision dynamic balance of the spun section to a measured residual wobble amplitude of  $0.002^\circ$  using the deployed drum, the spacecraft is in its operational configuration.

### **ADCS configuration and mechanization**

The principal functions and key requirements of the INTELSAT VI ADCS are as follows:

- Provide autonomous rate and pointing control of the communications platform, including control of platform-to-rotor relative rate in both normal and superspin modes, and on-orbit pointing control of the despun platform using both sun/earth and RF beacon reference modes. On-orbit ADCS-related pointing errors of less than  $0.02^\circ 3\sigma$  short-term and  $0.08^\circ$  long-term (including during maneuvers) are required to meet overall payload pointing requirements.
- Provide sensors and processed sensor data via telemetry for satellite attitude and spin rate determination on the ground during all phases of the mission.
- Ensure spacecraft nutational stability during all gyrostat phases of the mission.
- Provide on-board logic for programmed firings of all spacecraft thrusters for control of spacecraft spin rate, attitude, and velocity.
- Autonomously determine and maintain the spin axis attitude to within  $0.04^\circ$  of orbit normal.
- Provide the mechanical and electrical interface between the spacecraft rotor and the despun platform.
- Provide the mechanisms for deploying and positioning the extendable solar panel by ground command. Provide for rotor static and dynamic balancing to ensure spin axis wobble of less than  $0.005^\circ$ .
- Provide on-board failure detection and recovery logic to detect and recover from both transient and permanent faults.

The ADCS comprises the elements shown in Figure 4. Figure 5 is a system block diagram defining the major functional elements of ADCS signal processing, along with key hardware/firmware interfaces.

The subsystem is composed of seven major hardware elements: rotor-mounted earth sensors and sun sensors, the bearing and power transfer assembly (BAPTA), a rotor-mounted nutation-sensing accelerometer, solar drum positioner (SDP) mechanisms, a platform-mounted beacon track receiver (BTR), and the attitude control electronics (ACE) units.

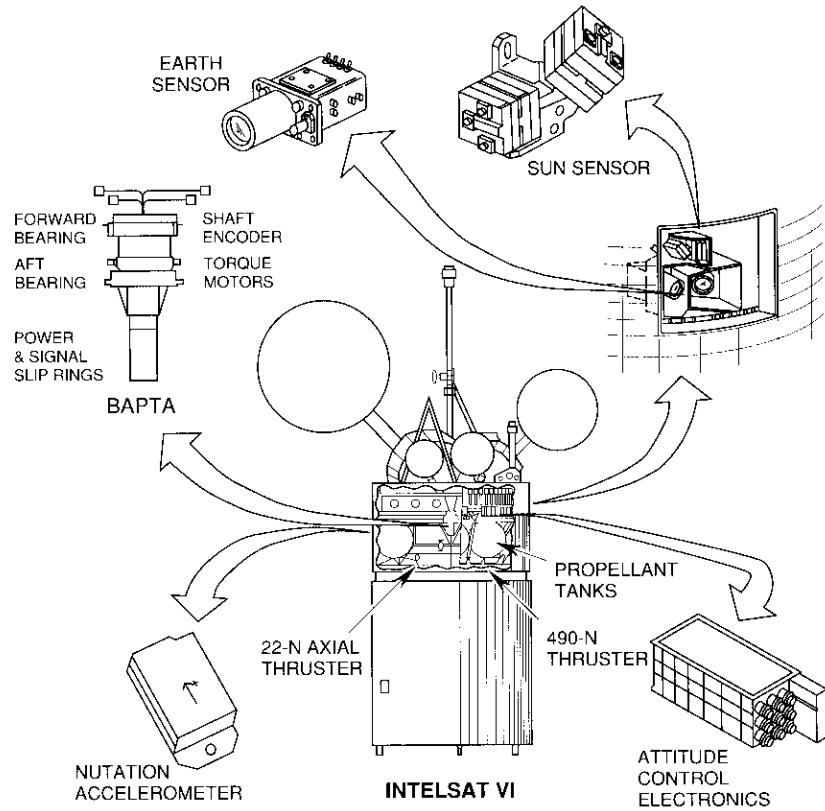


Figure 4. ADCS Elements

Earth and sun attitude sensors provide spin axis attitude data during both transfer orbit and on-station operation. The earth sensors are electro-optical devices that produce output pulses as the sensor scans the space-earth and earth-space transitions. They supply redundant inertial rotor spin phase information (relative to the earth) to the despun control system, as well as earth chordwidth data for attitude determination. Each unit has a pencil-beam field of view (FOV) and is oriented so that the FOVs are aligned in the spin plane. For the four-sensor configuration, two fields are aligned at  $+5.5^\circ$  and two at  $-5.5^\circ$  from the spin plane. Each FOV (nominally  $1.1^\circ \times 1.1^\circ$ ) is scanned in azimuth across the earth once per rotor revolution. Four sensors will accommodate a single unit failure without degrading system performance during transfer orbit. For on-station operation, only a single earth sensor is required

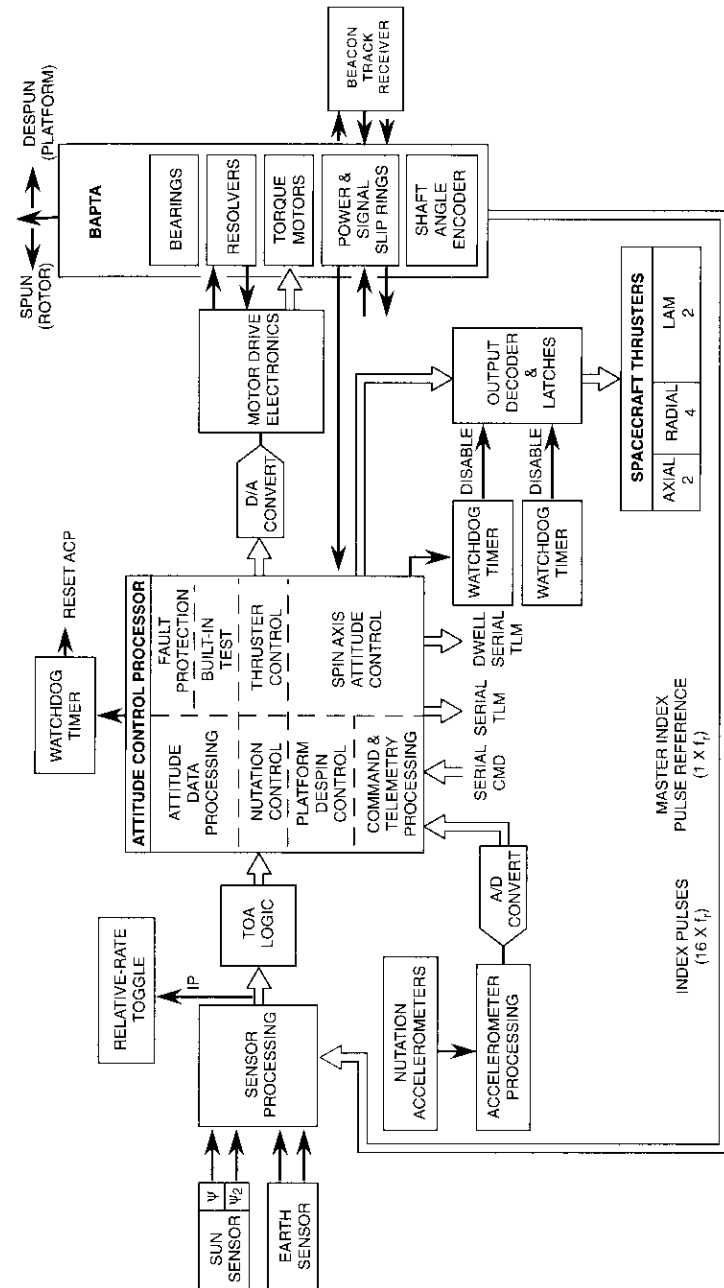


Figure 5. ADCS Block Diagram

for despun control. The use of two elevation orientations allows the sensor to be selected by ground command to avoid sun or moon interference.

The sun sensor assembly comprises four identical sensor units that provide redundant pulse pairs ( $\psi$  and  $\psi_2$ ) once per spacecraft revolution. Each sensor unit consists of n/p silicon photovoltaic cells with a fan-beam FOV ( $1.7^\circ \times 90^\circ$ ). The angular (time) relationship between the  $\psi$  and  $\psi_2$  sensor planes is used to measure the polar sun angle between the sun line of sight and the spacecraft spin axis. The  $\psi$  sensor output serves as the primary inertial despun reference.

The BAPTA provides all electrical and mechanical interfaces between the spinning and despun sections of the satellite. The assembly consists of the following major components:

- The bearings and BAPTA structure, which support the despun platform and antenna during orbital operations.
- A brushless DC torque motor, which despins and controls pointing of the platform in response to torque commands from the ACE.
- The index pulse generator (IPG) and master index pulse reference generator (MIPRG), which provide 16 pulses per revolution (IPG) of relative angle information for antenna pointing, and a pulse output once per spin cycle (MIPRG) for determination of the absolute platform pointing direction.
- The slip ring assembly, which provides electrical power and signal transfer across the rotating joint.

The nutation accelerometer provides direct sensing of spacecraft nutation to aid in active nutation control. The unit is a force-balanced linear accelerometer mounted outboard on the rotor, with its sensitive axis parallel to the spacecraft spin axis. The accelerometer produces an analog voltage in which amplitude is proportional to the nutation cone angle and frequency is the nutation frequency as observed in a rotor fixed (spinning) coordinate frame.

Three SDPs provide for extension of the deployable solar panel and on-orbit rotor dynamic balancing. Once the drum is fully deployed, precision rotor balance is accomplished by differentially driving the three independent mechanisms to tilt the solar panel, while compensating for residual rotor static and dynamic imbalance. Residual spin axis coning (wobble) of less than  $0.002^\circ$  is achieved using the SDPs.

The BTR, mounted on the communications platform in conjunction with four RF monopulse tracking signals, provides an option for closed-loop, independent azimuth and elevation pointing control of the C-band transmit and

receive reflectors. In addition, the BTR provides an azimuth control signal to the ADCS for platform boresight control, using one RF beacon error signal.

All sensor processing, ADCS telemetry and command processing, nutation control, primary thruster control, spin axis attitude control, and platform despun pointing control functions are mechanized within redundant ACE units. The ACE circuitry consists of stages of analog and discrete digital signal processing which perform sensor processing, BAPTA torque motor control, backup pointing control, and thruster monitoring functions. Also included are the attitude control processor (ACP) and an 8-bit HAC-designed microprocessor in which all ADCS control functions (telemetry and command processing, nutation control, primary thruster firing, autonomous spin axis, and platform pointing) are implemented in the firmware. Using the ACP, all control system parameters may be modified by ground command to optimize on-orbit performance. Filter pin connectors in the ACE provide an RF-tight environment to eliminate disturbances to the ADCS caused by electrostatic discharge phenomena.

Primary on-board failure detection and recovery functions are mechanized by independently powered and commanded relative-rate toggle (RRT) circuits within each ACE. Operating in either normal or superspin mode, the RRT independently monitors the platform-to-rotor relative rate—using the BAPTA index pulses as a reference—and transfers control of the platform to the redundant ACE and motor drive electronics (MDE) when the sensed rate exceeds fixed high or low thresholds. Automatic initialization logic places the ADCS in a safhold control mode following a failure-generated switchover.

Additional fault protection is incorporated into the ACP hardware and firmware to eliminate disturbances to platform pointing caused by internal single-event upset (SEU)-induced errors.

### **Attitude control processor**

The attitude control, command, and telemetry program (ACCTP) directs and regulates operation of all primary ADCS functions. The ACCTP resides in the ACP program read-only memory and controls serial command and telemetry processing, attitude data processing, BAPTA motor torque, and spacecraft thruster firing. Figure 6 shows the structure of the ACP, which consists of the program memory (with a capacity of 8,192 instructions); a 1,024-byte (8-bit) data random-access memory (RAM) which is SEU-protected with single-error correction, double-error detection Hamming code; a 2K read-only data memory for storage of critical constants; and an initialization database.

The hierarchical structure of the ACP firmware is shown in Figure 7. The firmware uses a three-level, top-down architecture. The executive top level

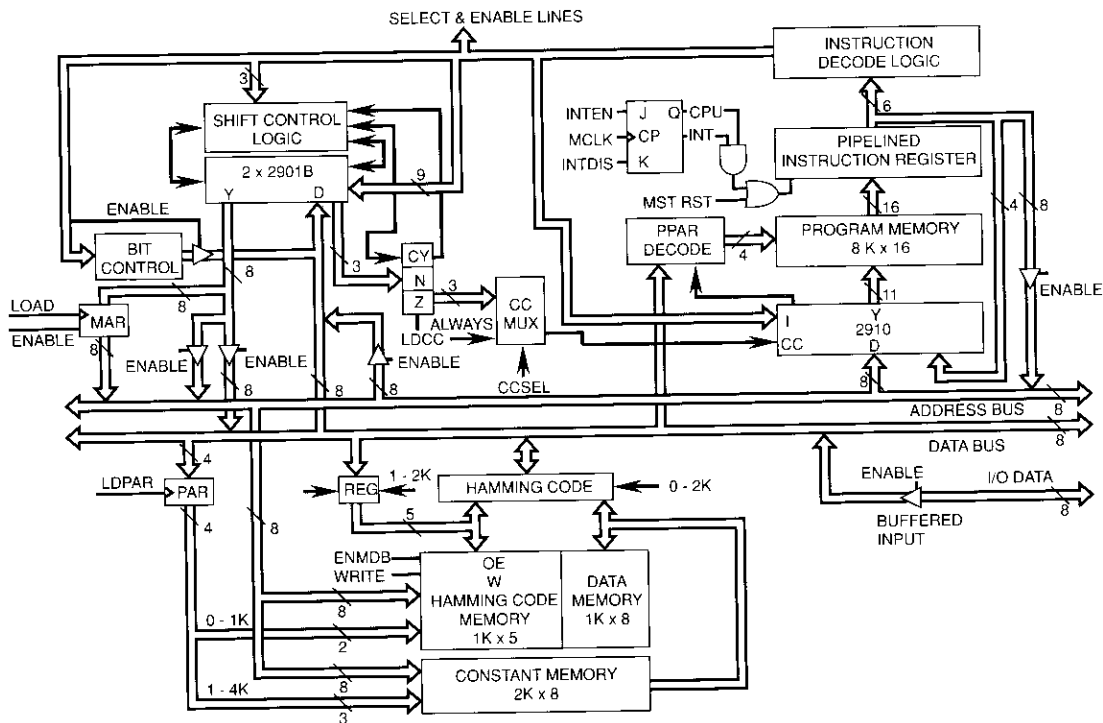


Figure 6. Attitude Control Processor Structure

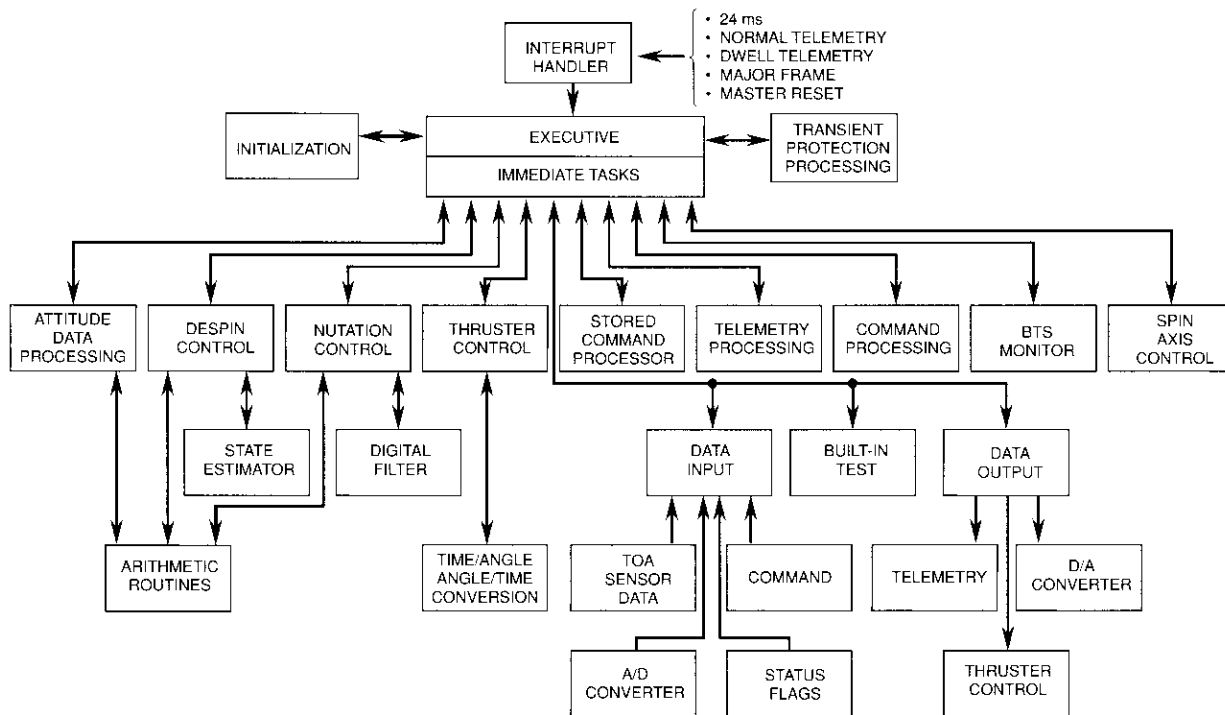


Figure 7. Attitude Control Processor Firmware Architecture

controls and coordinates the firmware program execution. The function modules form the second level, with each module responsible for a specific major firmware task. Subroutines form the bottom level. A subroutine may be dedicated to a particular module, or common to all modules; in addition, subroutines may call other subroutines.

Firmware execution is slaved to a hardware 24-ms real-time interrupt (RTI). Upon receipt of each RTI, the executive performs key time-critical functions and then calls the functions in a linear time sequence. The major functions are processed at the module level, with most control functions coded as single modules. Large, complex functions such as torque and thruster control are broken down into multiple modules. The firmware automatically starts at ACE power turn-on, with the executive gaining control at the first RTI.

The firmware is structured so that, upon completion of tasks (one pass through the program), the ACP is placed in a wait loop until receipt of the next RTI. Measured execution times range from 4 ms (with the minimum set of functions operating and no telemetry requests) to 8 ms (with all control functions operating and the maximum number of dwell telemetry requests per minor frame). This range gives a minimum execution margin of 16 ms, which is 67 percent of the time available.

The ACCTP includes a module that provides for off-line (*i.e.*, ACE not in control) testing of the ACP and its associated input/output circuitry. This built-in test (BIT) function is executed in response to ground serial commands and bypasses all normal ACP functions to execute a series of internal tests. Following BIT execution ( $\sim 7$  s), normal ACP operation is automatically resumed.

### Attitude determination over the mission

Data for ground-based determination of inertial spin axis attitude, platform and rotor spin rates, and pointing angle, as well as attitude data for use within the ADCS, are provided by digitized attitude measurements developed and preprocessed on board by the ACP. Digital sensor data consist of a sequence of time interval measurements derived from the pulse-type outputs of the sun and earth sensors and shaft angle encoders within the BAPTA.

As described earlier, each sun sensor has a narrow fan-shaped FOV that is approximately  $1.7^\circ \times 90^\circ$ . The  $\psi$  sensors are oriented so that the plane of the their FOVs is nominally parallel to the satellite spin axis. Sun sensor geometry is shown in Figure 8a. The  $\psi_2$  sensor's FOVs are canted  $35^\circ$  and rotated in azimuth  $35^\circ$  from the  $\psi$  sensor FOVs. Figure 8b shows the sensor output. The sensors produce signal pulses on each revolution of the rotor as the sun passes through their FOVs. The  $\psi$  pulses occur at nominally the same azimuth angle

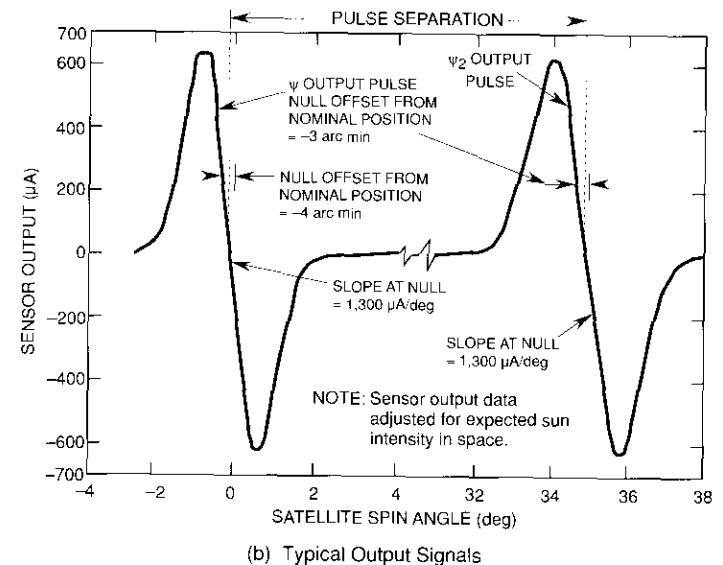
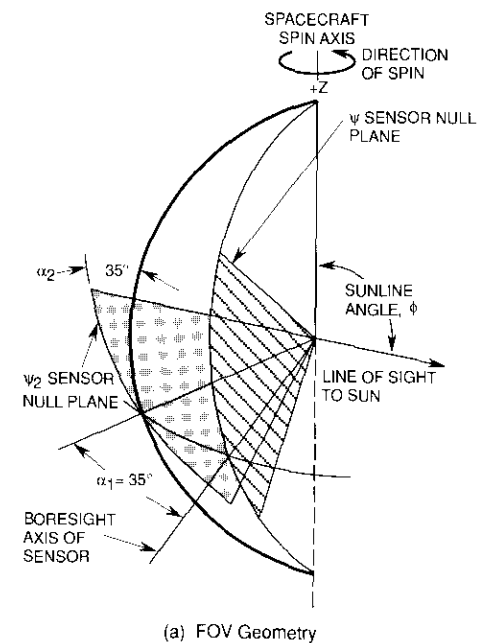


Figure 8. Sun Sensor Geometry and Output

relative to the sunlines, for a sun aspect angle position,  $\phi$ , of at least  $90^\circ \pm 45^\circ$  from the spacecraft spin axis. The  $\psi_2$  pulses are produced for sun aspect angles of at least  $90^\circ \pm 35^\circ$ , and in azimuth angle locations relative to the  $\psi$  pulses that depend on the sun angle in the following nominal relationship:

$$\cot \phi = \sin [(\psi - \psi_2) - \alpha_1] \cot \alpha_2 \quad (2)$$

where

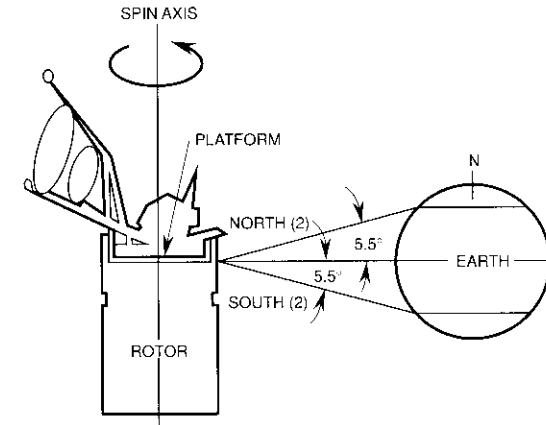
- $\phi$  = aspect angle to sun from positive spin axis
- $\psi - \psi_2$  = angle of rotation between the  $\psi$  and  $\psi_2$  pulse centers
- $\alpha_1$  = built-in angle of rotation of the  $\psi_2$  sensors from the  $\psi$  sensors (nominal  $35^\circ$ )
- $\alpha_2$  = built-in angle of cant of the  $\psi_2$  sensors relative to the  $\psi$  sensors (nominal  $35^\circ$ )

The  $\psi - \psi_2$  separation angle varies from approximately  $64^\circ$  to  $5.5^\circ$  as the sun angle goes from  $55^\circ$  to  $125^\circ$ . At equinoxes (sun at  $\phi = 90^\circ$ ), the separation is  $35^\circ$ .

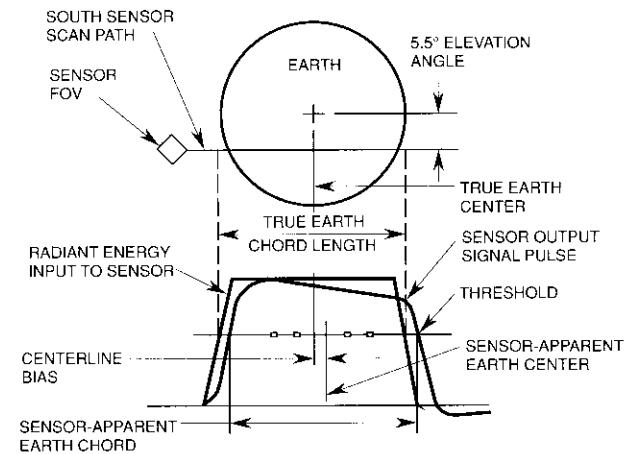
Typical earth sensor scan geometry and output signals are shown in Figures 9a and 9b, respectively. Earth leading- and trailing-edge signals are produced by sensor processing within the ACE. The leading- and trailing-edge pulses obtained from each scan of the earth permit determination of earth chordwidth at the latitude of scan. Two such chordwidth measurements from two sensors scanning at different angles determine the aspect angle between the spin axis and the spacecraft-to-earth line. This angle, combined with the sun aspect angle, establishes the spin axis attitude.

The variable-reluctance shaft encoder, shown schematically in Figure 10a, consists of dual coil assemblies mounted to the spun housing of the BAPTA, and a set of 16 exciter pole pieces spaced  $22.5^\circ$  apart on the BAPTA despun shaft. The reluctance of a generator coil is changed as each soft iron exciter pole passes over a magnet in the coil assembly. This produces the electrical signal shown in Figure 10b, in which zero-crossing provides a clocking indicator of the relative position of the spun and despun sections of the spacecraft. The shaft angle encoder also provides an absolute platform pointing reference once per spin revolution. One of the two coil assemblies is radially outboard of the other, and one of the 16 exciter poles is also extended radially.

Digitized attitude measurement data are developed by the attitude data processing function of the ACP, in the form of time interval measurements. Time-of-arrival (TOA) logic within the ACP records the occurrence of each of the key events: leading and trailing edges from two earth sensors,  $\psi$  and  $\psi_2$  pulses from the sun sensor, index pulses, and the master index pulse reference.

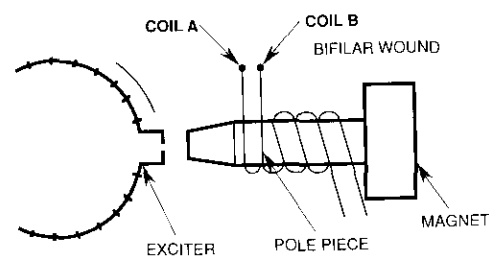


(a) Geometry

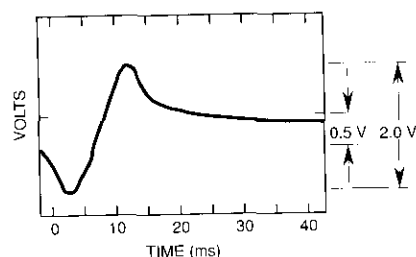


(b) Output

Figure 9. Earth Sensor Geometry and Output



(a) Coil Assembly/Exciter Schematic



PULSE GENERATOR OUTPUT SIGNAL  
AT 30 rpm INTO 10-k $\Omega$  LOAD  
0.25-mm AIR GAP (POLE PIECE TO IRON EXCITER)

(b) Output

Figure 10. Shaft Encoder Schematic and Output

All TOA measurements are made with a resolution of 5.86  $\mu$ s, which corresponds to an angular quantization of 0.0011 $^\circ$  at the nominal rotor spin rate of 30 rpm.

### Platform despun and pointing control

A major function of the ADCS is to continuously maintain control of the communications platform throughout the mission—controlling the spin rate during transfer orbit operations and maintaining precision earth pointing continuously during the expected 14-year on-orbit lifetime of the spacecraft.

### Sun/earth pointing and relative-rate control

Rate and pointing control of the communications platform is accomplished using data from a ground-selected sun or earth sensor, in conjunction with the BAPTA shaft encoder, to generate continuous feedback control commands to the BAPTA torque motor. A secondary pointing mode uses an RF BTS.

Figure 11 is a block diagram of the platform despun controller (PDC). The rotor state estimator, relative state estimator, and BAPTA torque command processing firmware functions, along with the digital-to-analog converter (DAC) and MDE, form the on-board PDC system. The PDC automatically despuns the communications platform to either a ground-commanded pointing direction or a fixed inertial (or relative) spin rate. Orienting the platform toward the earth without a despun sensor requires two references: one that establishes the phase of the rotor relative to the earth, and one that defines the phase of the platform relative to the rotor. The PDC is a dual-loop servo comprising a low-bandwidth outer loop that senses rotor phase and rate (using one of the attitude sensors) and a high-data-rate (16 times relative rate) inner loop that controls the phase (or rate) of the platform relative to the sensed rotor phase (using the IPG and MIPRG outputs for feedback data). Offset pointing of the platform boresight, platform inertial, or relative spin rate control is accomplished via ground-commandable phase and rate biases within the control loop processing.

The feedback control loop, implemented in firmware within the ACP, uses a state estimation approach based on an observer-controller technique. The PDC algorithm generates estimates of key spacecraft dynamic state variables: inertial rotor rate and phase, relative (platform-to-rotor) rate and phase, and the composite average bearing friction/motor back electromotive force torques. The inertial rate and pointing direction of the platform are computed from these data. Corrections to the state estimates are derived from the ground-selected inertial pointing reference (the sun or earth sensor) and the index pulse data existing within the ACP sensor database.

The controller is implemented using an algorithm in which the inertial platform state estimates are fed back through a set of preselected control gains to form the control command to the BAPTA torque motor. In the near-continuous algorithm developed for INTELSAT VI (see flowchart in Figure 12), state variable estimates are propagated at the ACP interrupt period (RTI) of 24 ms using a single-axis model of the platform and rotor dynamics. The estimates are corrected during the interrupt period following receipt of sensor data. The control torque is also computed for each RTI, and the value is written by the processor to the DAC for input to the MDE. Primary pointing control for INTELSAT VI uses the sun sensor as the inertial reference, with earth sensor control used for eclipse operations. When the satellite is operating in an earth-referenced mode, an earth center-finding technique is used in which the rotor phase estimate tracks the center of the detected earth chord, eliminating pointing offsets caused by seasonal chord variations or kinematic coupling of spin axis attitude errors.

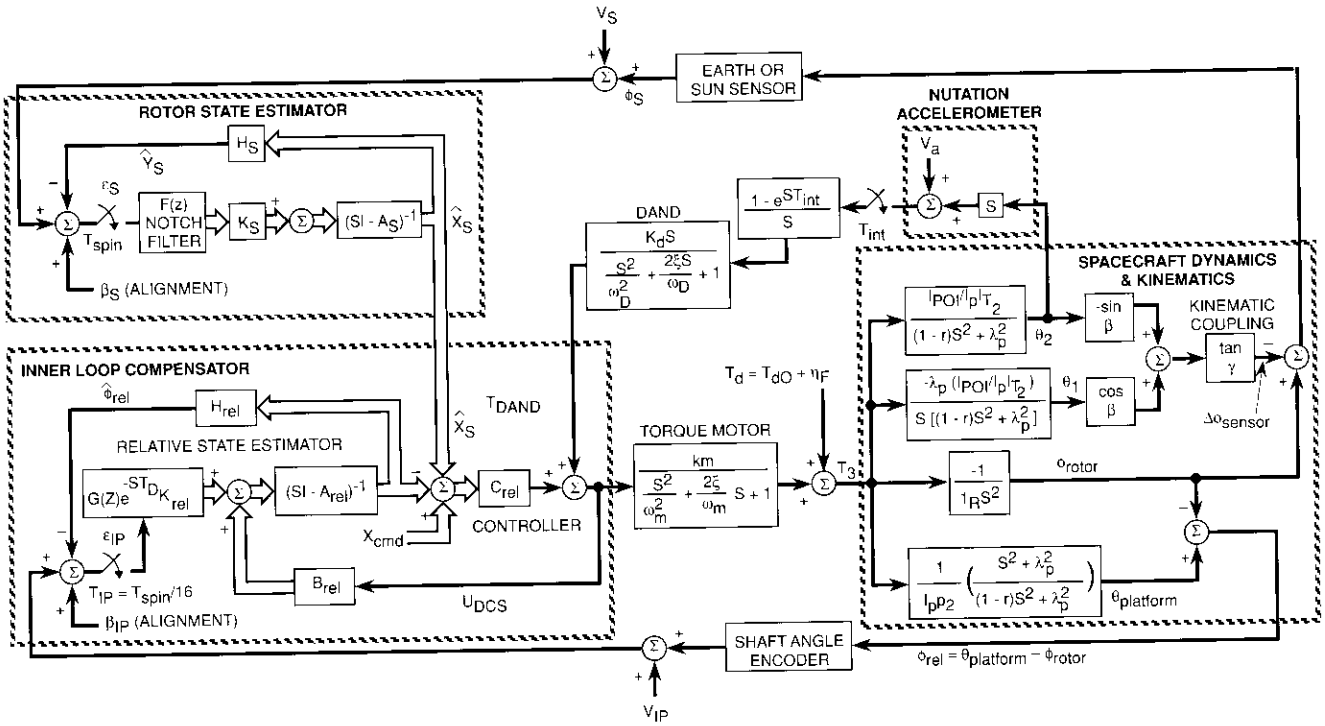


Figure 11. Platform Despin Controller Block Diagram

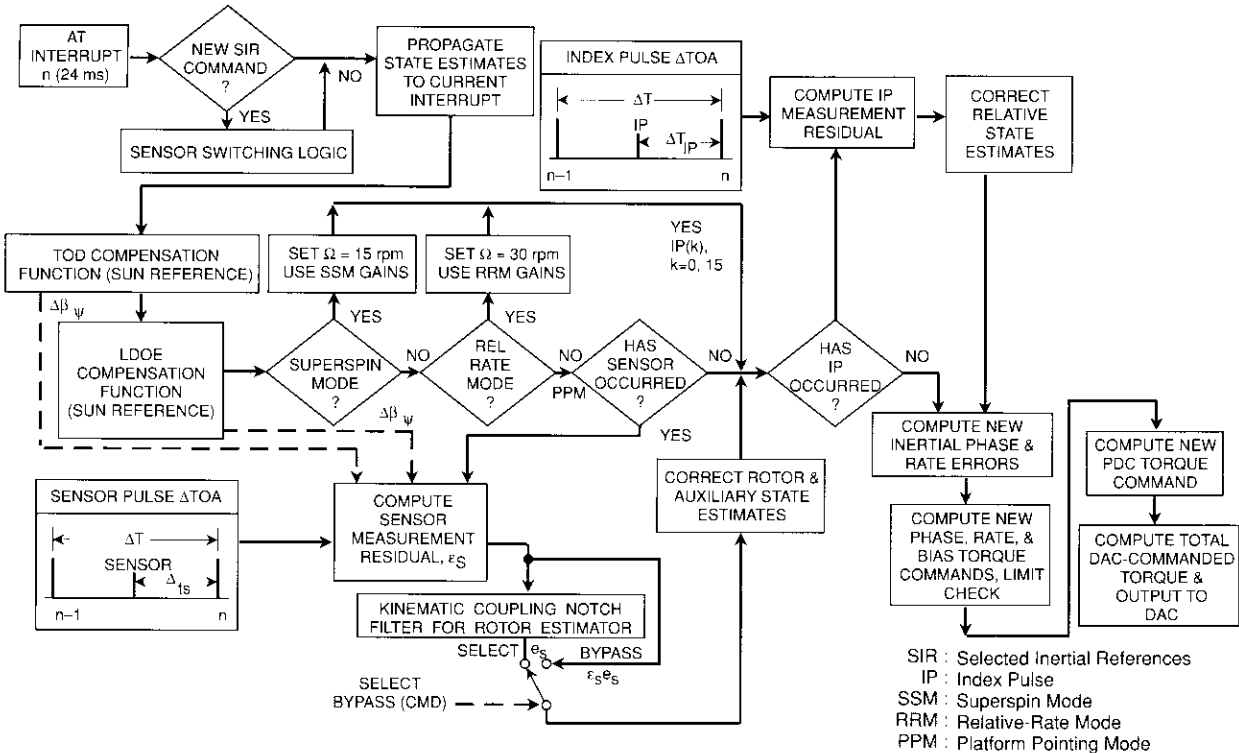


Figure 12. Platform Despin Controller Algorithm Flow Diagram

The state estimates are propagated using the torque calculated during the previous RTI and the previous states in a fifth-order spacecraft model. Terms are also included in both the rotor and relative-rate propagations to account for changes that can occur in the high-speed rotor spin rate as a result of axial or radial thruster firings. This feed-forward compensation is a ground-programmable function that is set after initial on-orbit thruster calibration and operates automatically whenever a thruster maneuver is executed.

When INTELSAT VI is operating in the sun reference mode, the rotor phase estimator tracks the sunline. The constantly changing sun-earth separation angle (nominally  $360^\circ$  per 24 hours, the mean earth rate) requires that the sun reference phase angle be updated periodically to maintain a constant earth-pointing angle. An automatic time-of-day (TOD) correction function provides this compensation. With the TOD function operating, the sun reference angle is updated by one least significant bit ( $0.00549^\circ$ ) every ground-programmed time interval (1.314 s, nominally). A separate correction factor (longitude drift orbit eccentricity [LDOE]) is used to account for the effect of boresight pointing error due to longitudinal drift and orbit eccentricity, as well as the effect of solar parallax on the sun-earth separation angle. The correction angle is a complex function of time and orbit angle, with coefficients that are all ground-programmable.

Control loop dynamics are determined by a set of seven constant gains (five estimator gains and two controller gains). Independent selection of the gains permits performance optimization with respect to the primary system disturbances: inertial sensor pulse jitter, shaft encoder pole misalignment, bearing torque noise, and processor quantization. The ability to command changes to all system gains on-orbit allows the system characteristics to be optimized after observation of the on-orbit behavior of the spacecraft. Short-term pointing stability of  $\pm 0.01^\circ$  has been demonstrated on-orbit. Pointing data from the spacecraft are shown in Figure 13.

Relative-rate control modes (normal relative-rate control and superspin rate control) for use in transfer orbit are implemented using the basic despun control algorithm by bypassing the rotor state estimators. In relative-rate control mode, the rotor rate estimate is held at a constant value (set at system initialization) and serves as a fixed reference. Control is then maintained using the relative state estimator. Control torques are computed normally. A ground-commanded rate bias is employed to maintain the desired relative rate.

Additional functions within the PDC firmware provide automatic, transient-free switching between inertial sensor references; automatic platform acquisition of the earth-pointing direction; and programmable digital filters for protection against unexpected flexible mode interactions and sun reference kinematic nutation coupling.

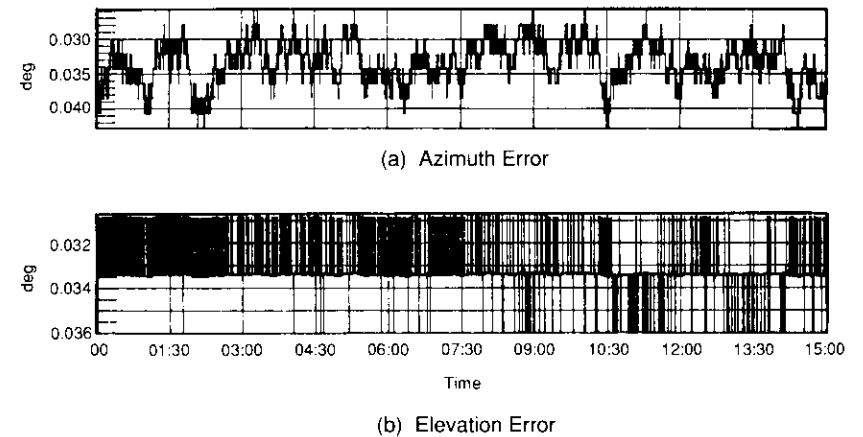


Figure 13. *On-Orbit Platform Boresight Pointing Stability*

#### RF beacon tracking

The beacon tracking function provides the capability to perform both inertial alignment and continuous closed-loop azimuth and elevation pointing control of the C-band transmit and receive reflectors by tracking RF beacons transmitted from the ground control station. Figure 14 is a functional block diagram of the BTS. Azimuth and elevation pointing information for the despun and positioning control loops is generated by receiving and processing a beacon signal transmitted from a ground station through a feed/receiver system. Respective pointing errors are shaped within the BTR and used to generate positioner stepping commands or despun motor torque commands. Transmit antenna pointing error signals (azimuth and elevation) control stepper-motor-driven actuators that position the transmit reflector. Control compensation is performed by a simple low-pass filter, followed by a deadband controller. Receive antenna pointing errors may be used to position the receive reflector in the same manner. Optionally, by ground command, the receive azimuth pointing error can command the despun motor to control east-west pointing of the entire despun platform. Furthermore, when the beacon function has control of the despun motor, receive antenna elevation pointing error is used to generate nutation-damping despun torque commands.

The BTS sensor comprises an array of RF feed horns situated in the C-band communications feed array, as well as a combining network, a ferrite modulator assembly, and antenna positioners for the BTR. The baseband-sensed error from this sensor is offset by ground-commandable biases, and then compensated to generate position control commands. Fixed- and variable-bias

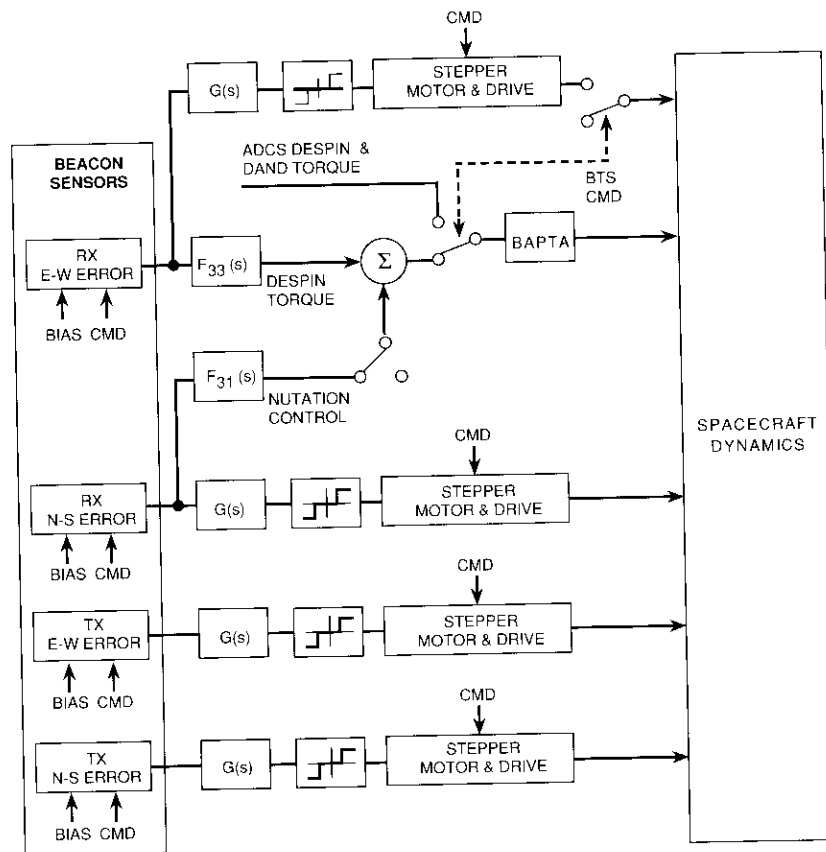


Figure 14. Beacon Tracker Subsystem Block Diagram

components are selected to fit antenna characteristics at seven tracking stations, and to minimize pointing error. All biasing and control-shaping circuits are implemented in the BTR.

Since the BTR and ACE are mounted on the despun and spun portions of the spacecraft, respectively, the torque command is routed through redundant BAPTA slip rings. The BTR superimposes a 753-Hz square wave on the base-band torque command signal as an indication that the BTR is locked on the beacon and providing a valid control signal. The 753-Hz signal is separately detected by the ACE and must be present for the satellite to enter or remain in beacon control mode. Hardware and firmware protection logic provides automatic switching from beacon to sun/earth control modes if the beacon reference signal is lost.

### Autonomous spin axis attitude control

The spin axis controller (SAC) function of the ADCS autonomously determines the spin axis attitude (roll and yaw) and automatically executes properly phased pulse firings of the 22-N axial thrusters to maintain the spin axis attitude to within  $0.04^\circ$  of orbit normal. Figure 15 shows the SAC functional block diagram. Detailed descriptions of SAC design and operation are given in Reference 3.

The SAC uses the real-time output of a spinning earth horizon sensor to derive on-board estimates of spin axis roll ( $\phi$ ) and yaw ( $\psi$ ) attitude angles, as well as the earth sensor chord bias,  $b$ . As discussed in Reference 3, the earth sensor provides a measurement of the spacecraft roll angle, and orbital kinematics are used to estimate spacecraft yaw. Earth sensor bias variations will result primarily from long-term electronic and thermal effects on the sensor, as well as the effects of non-uniform earth radiance due to atmospheric variability. Static biases result from residual sensor misalignment and electronic processing biases. Estimating sensor bias eliminates static pointing errors that would otherwise develop.

In the simplified model of the spacecraft dynamics provided in Figure 15, the nominal forcing function of the system is the angular drift rate about the sunline,  $V$ , due to solar torque. The state estimate propagation algorithm is executed every 10 minutes, corresponding to  $2.5^\circ$  of orbital motion. This calculation is based on the previous estimates, along with a command-set average drift rate to predict the present value of the states. The earth chord processor nominally uses 256 consecutive earth chord measurements to determine a heavily averaged (to reduce sensor noise) chordwidth,  $Z_{avg}$ , which is then used in conjunction with the state predictions to determine a prediction error. This prediction error is multiplied by the estimator gains ( $K_\phi$ ,  $K_\psi$ , and  $K_b$ ) and added to the respective predictions to determine the new state estimates. A coordinate transformation of these state estimates from the orbit-fixed frame ( $\phi$ ,  $\psi$ ) to a sun-fixed frame ( $U$ ,  $V$ ) is then performed before the maneuver logic is evaluated. If attitude corrections are necessary, the magnitudes of the desired corrections in the sun-fixed frame ( $U_c$ ,  $V_c$ ) are sent to the thruster command processor and the appropriate axial thruster commands are executed. Meanwhile, corresponding corrections are made to the estimates of roll and yaw ( $\phi$ ,  $\psi$ ), and the results are fed back to the state estimate propagation algorithm for use in the next cycle.

Attitude corrections for a spin-stabilized spacecraft are carried out by spin-synchronously firing an axially oriented thruster over a short portion of the spin cycle. This technique is depicted in Figure 16. By properly controlling the phase of the thruster pulse centroid, the spin axis can be precessed in any

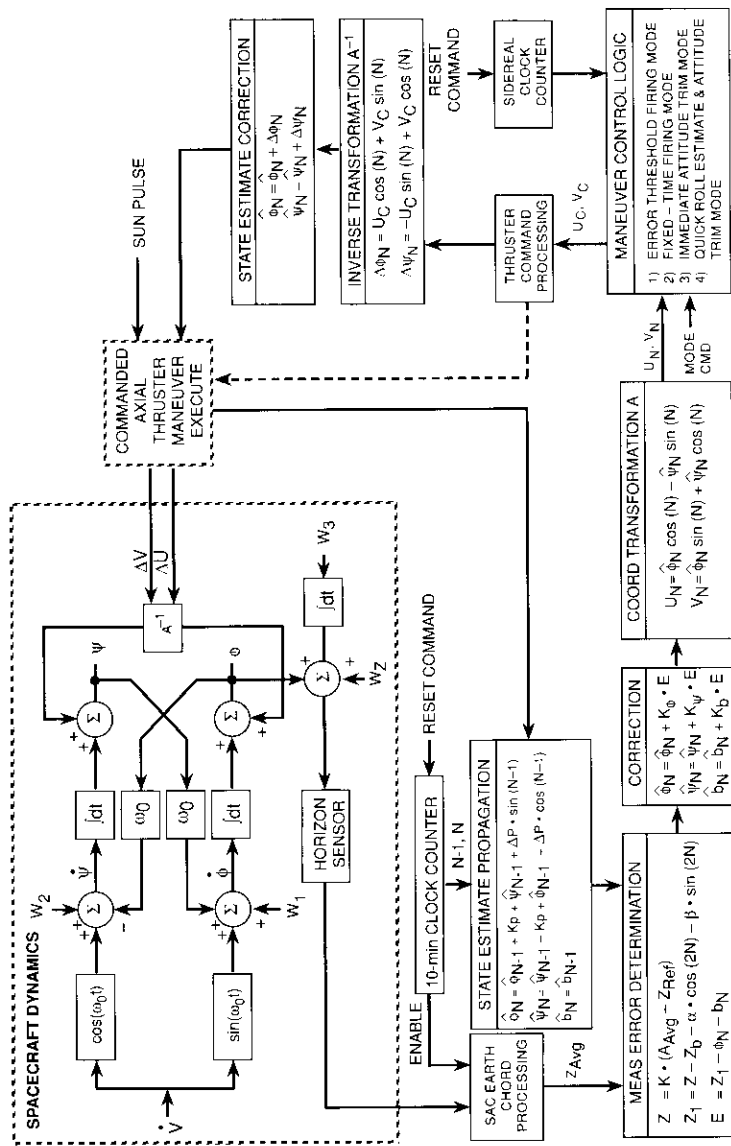


Figure 15. Spin Axis Controller Functional Block Diagram

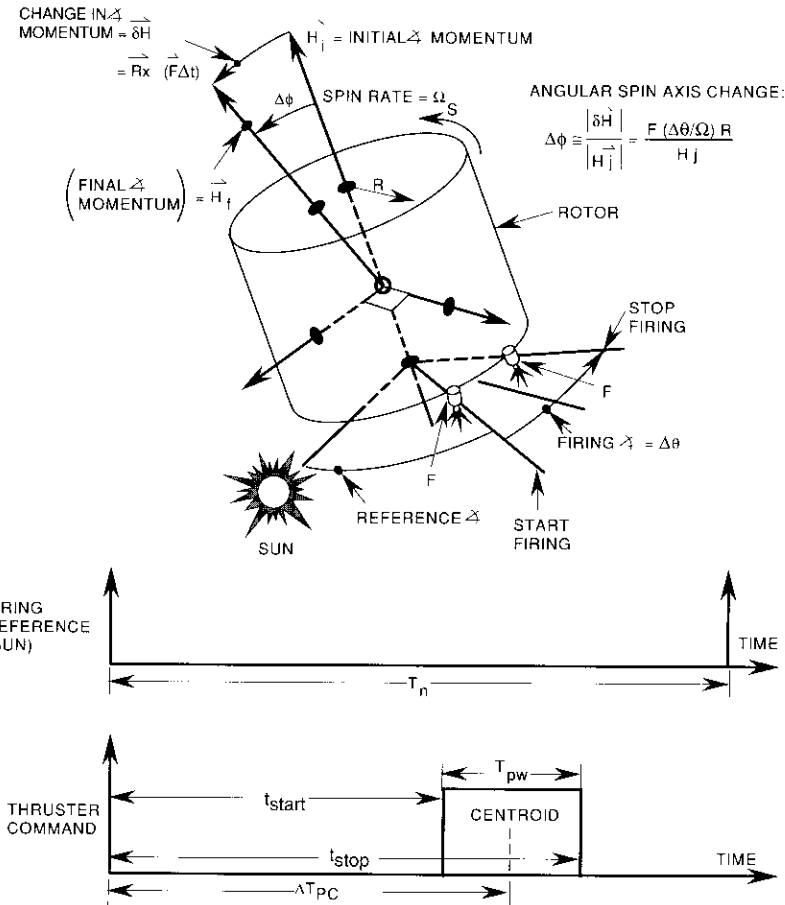


Figure 16. Attitude Control Using Spin-Synchronous Thruster Firings

desired direction. For INTELSAT VI, which has a rotor spin rate between 30 and 40 rpm, thruster (22-N force level) pulse widths of 0.096 s provide a precession control increment of less than 0.01°.

The automatic attitude maneuver control logic comprises two operational modes: a fixed-time firing (FTF) mode for normal steady-state operation, and an error threshold firing (ETF) mode for normal transient-state operation. In the FTF mode, attitude corrections are constrained to occur at specific orbit intervals (as marked by a sidereal period clock) relative to the nominal orbit node. The design goal is to have all FTF-generated attitude correction maneu-

vers take place at orbital locations as close as possible to the orbit node. This provides the maximum amount of attitude control fuel available for north-south (inclination) orbit control. The ETF mode uses an error threshold detection logic in which attitude corrections take place whenever either of the sun-referenced, coordinate-frame-estimated attitude components exceeds ground-programmable thresholds. SAC performance in the ETF mode is shown in Figure 17.

**Spin axis stabilization**

During the pre-PKM ejection phase of the Titan-launched mission, and subsequent platform despin from the superspun state (post-apogee injection), INTELSAT VI operates in a configuration in which the rotor spins about the

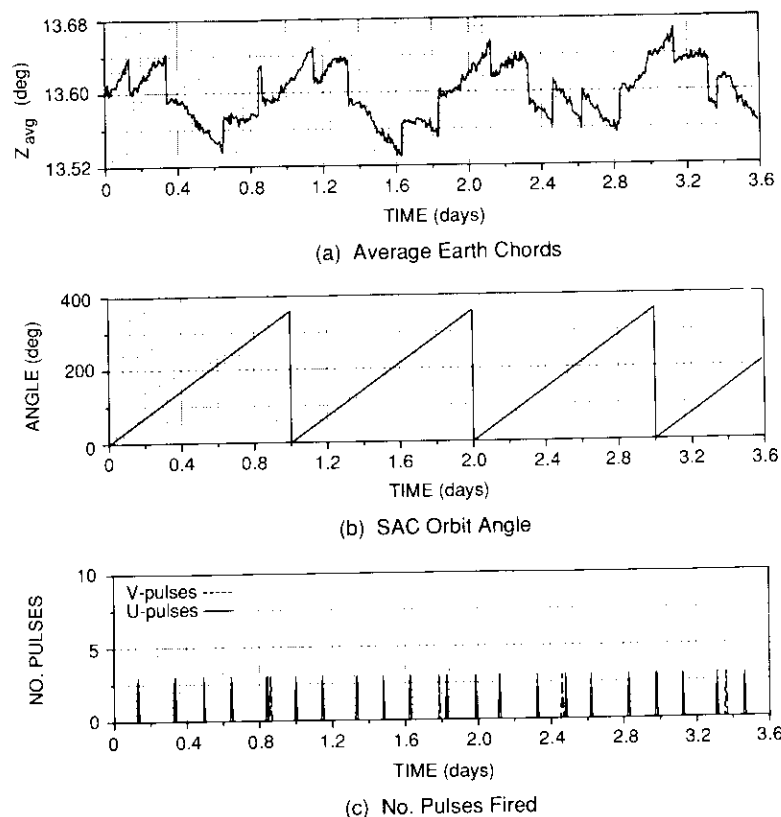


Figure 17. SAC Performance in Error Threshold Firing Mode

spacecraft axis of minimum moment of inertia—the system’s highest energy state. For this configuration, energy dissipation on the rotor (e.g., propellant slosh) acts as a destabilizing influence, attempting to force the system to its minimum energy state (spinning about an axis of maximum inertia).

The effect of propellant slosh—the dominant source of destabilizing energy dissipation—was determined by performing a series of nutation-divergence measurements on a test vehicle scaled to the INTELSAT VI spacecraft configuration. Data were taken over a wide range of tank loadings and spacecraft roll-to-pitch inertia ratios. The test results established design requirements for the nutation control functions of the ADCS. Estimated energy dissipation from other sources (i.e., the deployable solar drum and structural flexing) was analyzed and found to be much weaker than the effects of propellant slosh.

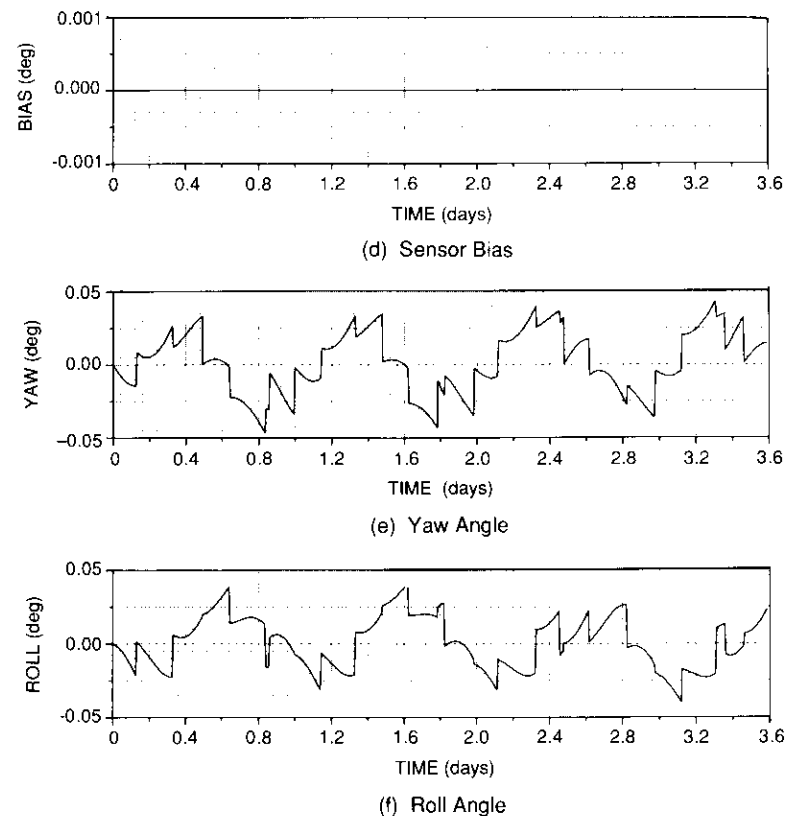


Figure 17. SAC Performance in Error Threshold Firing Mode (cont'd)

To stabilize this inherently unstable configuration, several active control functions have been incorporated into the ADCS. During transfer orbit (prior to antenna deployment) and as an on-station backup, the ADCS provides for nutation control using spacecraft thrusters. Thruster-active nutation control (TANC), functionally depicted in Figure 18, generates logically controlled thruster firings based on nutation data provided by the rotor-mounted accelerometer to remove transverse angular momentum [4]. On-station, TANC will reduce any nutation to a level ( $\sim 0.3^\circ$ ) at which the linear despin controller will dominate and asymptotically remove residual nutation.

Also on-station, with the platform fully deployed, primary stabilization is provided actively by the platform despin controller and the despin-active nutation damper (DAND). These functions are based on the inherent dynamic coupling between spacecraft nutation and the control torques applied to the platform spin axis that results from the large dynamic imbalance of the platform [5]–[7]. Similarly, the BTS combines the despin pointing command with a shaped evaluation RF error signal to provide active nutation damping in the BTS mode.

PDC nutation damping is implemented by proper design of the control loop dynamics [5]. The DAND function provides stronger control by using the output of the nutation-sensing accelerometer to form an additional feedback control loop within the ADCS [6],[7]. The performance of these linear controllers is summarized in Figure 19. For the nominal BOL conditions (30 rpm and 25-percent propellant loading), the sun/earth pointing mode alone will provide a nutation-damping time constant of 90 s. Enabling the DAND substantially improves system performance, with a nominal damping time constant of 40 s. Both modes have substantial margins over the predicted worst-case dedamping time constant of 350 s.

### Spacecraft stationkeeping operations

Orbit maintenance for a geosynchronous satellite involves periodic thruster firing maneuvers to correct the longitudinal (east-west) drift of the spacecraft, which is a function of station location and residual eccentricity, and the progressive increase in orbit inclination of approximately  $0.9^\circ$  per year. For a spin-stabilized spacecraft, east-west stationkeeping (EWS) maneuvers are conducted by firing a pair of radially aligned thrusters over a short ( $\sim 25^\circ$ ) portion of the spin cycle to impart a pure translational velocity change to the spacecraft. For INTELSAT VI, these maneuvers are executed autonomously by the ACP based on ground-commanded maneuver parameter data (pulse width, maneuver duration, and thruster phasing). Maneuvers can be executed immediately, or be delayed using the stored command processing function.

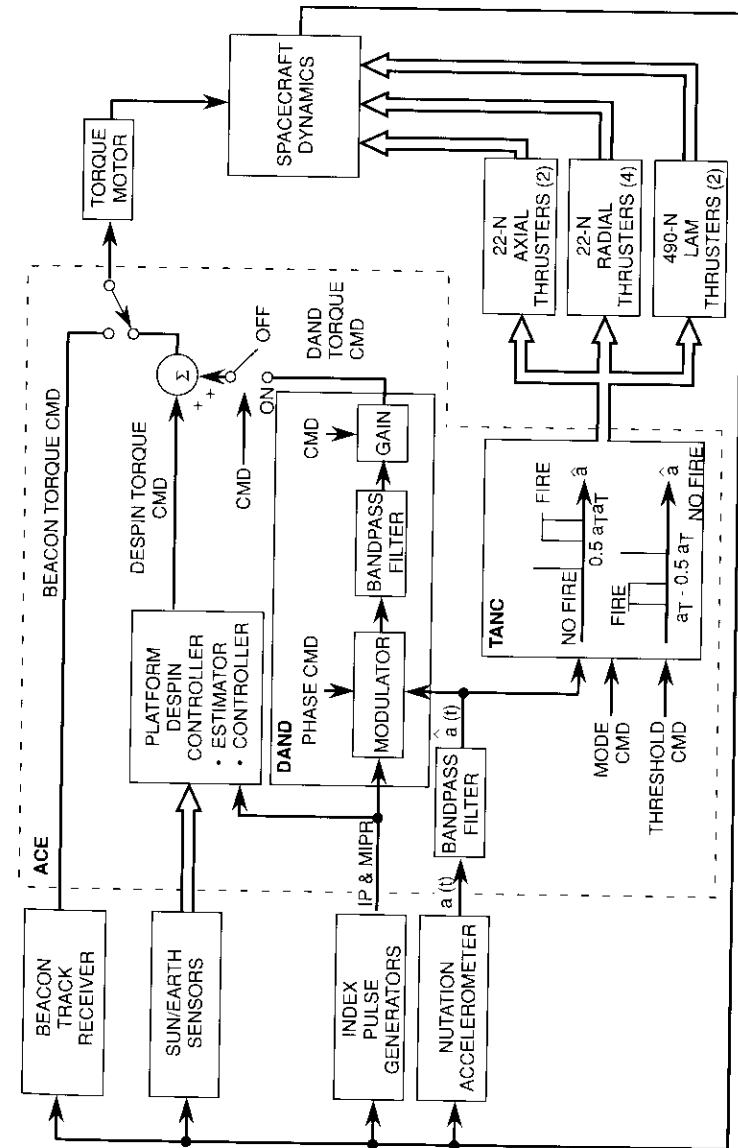


Figure 18. Spin Axis Nutation Stabilization Functions

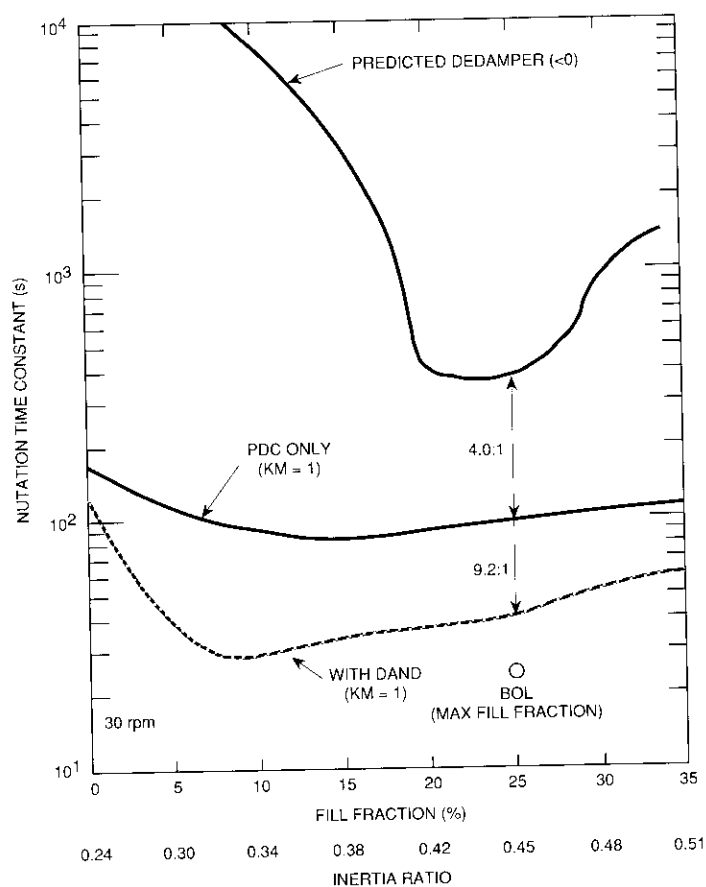


Figure 19. *Nutation Stabilization System Performance*

Because of the large static imbalance of the despun platform, radial thruster firings during EWS generate a platform disturbance torque about the spin axis. To minimize the resulting transient pointing error to below  $0.03^\circ$ , a feed-forward compensation (FFC) technique is used. FFC consists of ground-programmable acceleration terms that are automatically added to the rotor and relative-rate state estimation propagation equations whenever a thruster is firing. This forces the states to respond quickly to changes in short-term dynamics, thus permitting the estimators to track only residual errors. FFC parameters can be adjusted after on-orbit calibration of thruster performance and alignment.

North-south stationkeeping (NSS) maneuvers for orbit inclination control are performed by firing the 22-N axial thrusters. With a statically balanced despun platform, the thrusters would be fired continuously; however, because of the offset of the platform mass center from the bearing axis (the nominal thrust vector alignment), a transverse torque is produced with continuous axial thruster firing. This torque will precess the momentum vector, inducing a significant yaw pointing error. To avoid this effect, an off-pulsing scheme was developed in which each thruster is turned off for a short period of the rotor spin cycle. The off-pulse width and phasing are adjusted to produce zero average yaw torque during the maneuver, and thus negligible yaw precession. NSS maneuver dynamics are shown in Figure 20. Again, NSS maneuvers are controlled autonomously by the ACP using ground-transmitted maneuver parameters. FFC is also used for on-orbit compensation of thruster misalignment disturbances.

### **Control system autonomy and fault protection**

The ADCS incorporates several additional functions to minimize the need for real-time ground intervention and to protect the spacecraft from internally or externally generated faults.

### **Stored command processing**

The ADCS provides enhanced spacecraft autonomy by incorporating a stored command processor (SCP), which permits delayed execution of all ADCS functions. Maneuver commands to be executed (and their execution times) are set by serial command and stored in the ACP data memory. The stored command time tags have a command resolution of 98.3 s and a maximum range of 74.6 days. Ninety-two commands can be stored simultaneously. Stored commands are used for the following functions:

- Platform despun controller mode control and sensor reference switching.
- Control system parameter modification and selection.
- Ground-generated attitude maneuvers.
- NSS and EWS velocity maneuvers.
- Parameter updates for the TOD and longitude drift/orbit eccentricity compensators.
- Platform offset pointing control.
- TANC and DAND mode control and parameter modifications.
- Sensor redundant unit selection.
- Mode and parameter modifications to the spin axis controller.

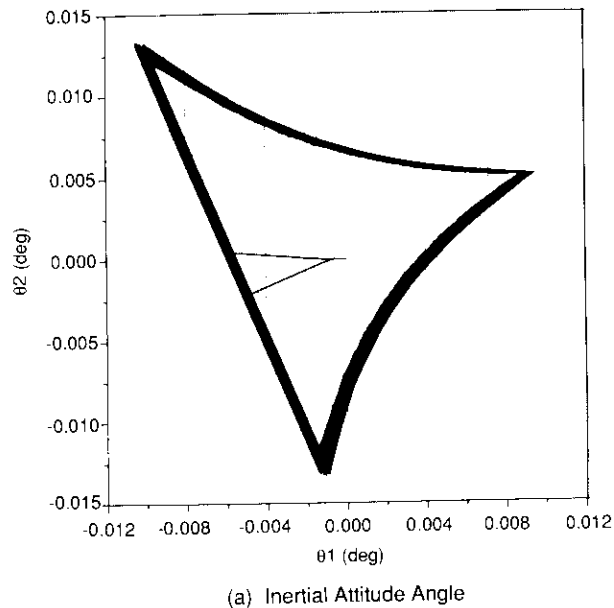


Figure 20. *Spacecraft Dynamics During North-South Stationkeeping*

Stored command data are monitored using a data memory readout telemetry function. SCP editing functions are provided to delete individual, or all, stored commands.

#### ACP fault protection

Fault protection is provided in the ACP hardware and firmware for detection, masking, or recovery from random soft errors in the microprocessor and its associated input/output circuitry, and to limit the effect of single hard component failures. Fault protection establishes a safe-hold state for the ADCS in response to a major noncorrectable disturbance. Response to a soft error is designated to prevent loss of despun pointing control, minimize transient pointing errors, and prevent erroneous or extended firing of spacecraft thrusters. All special fault protection features can be verified during both unit- and system-level testing. The evaluation of fault protection functions is incorporated into the BIT of the ACP. Key elements of ADCS fault protection are summarized below.

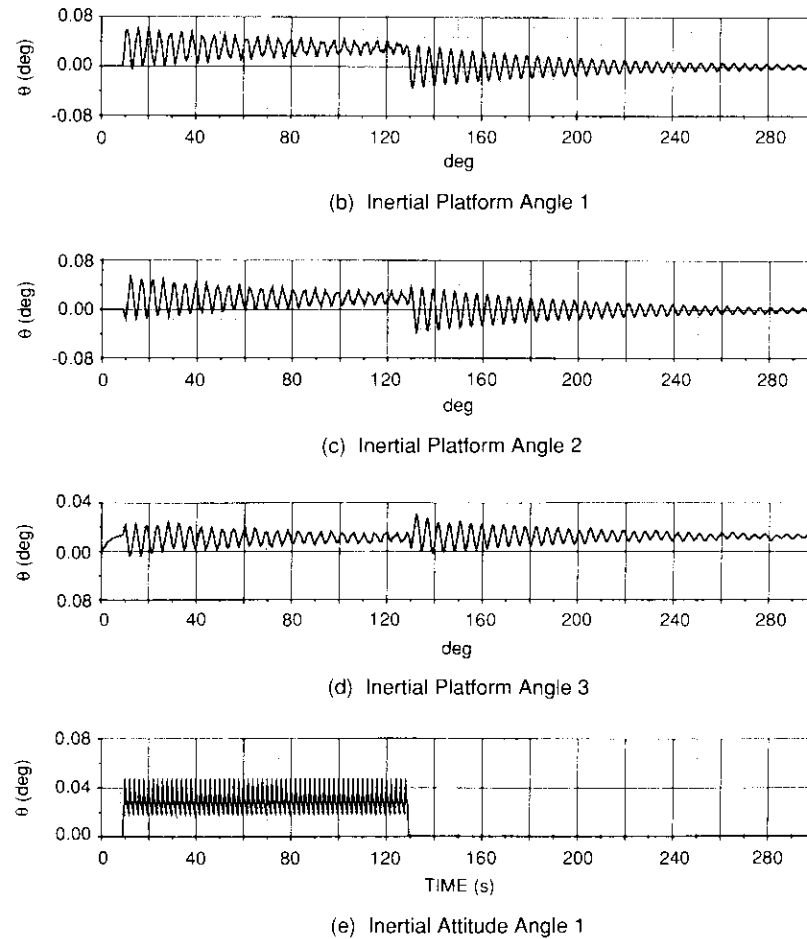


Figure 20. *Spacecraft Dynamics During North-South Stationkeeping*  
(cont'd)

#### HAMMING CODE ERROR DETECTION AND CORRECTION

Hamming code protection is provided to eliminate the effects of high-energy cosmic particles on ADCS operation. The physics of the particles, and the RAM, limit errors to single bits within memory that are defined as SEUs. Studies have shown that the RAM used in the ACP (93L425) will have an upset rate of approximately  $5 \times 10^{-5}$  SEU/bit-day. This will result in a predicted

average of one-half bit flip per day in the 1K ACP memory, or one bit flip every 2 days.

The Hamming code error-correction circuitry corrects all single-bit errors and detects all double and most multiple-bit errors. All RAM locations are updated or corrected within 6.144 s (4 bytes per RTI). This update rate is fast enough to ensure that the probability of multiple errors in one RAM word is negligible.

The RAM chips are organized  $1K \times 1$ , with eight RAMs containing the stored data and five containing the Hamming code check bits. This architecture has the advantage that the memory (with the aid of the Hamming code) will still be functional even if the entire single RAM chip should fail. Hamming code checking and RAM refreshing are performed each RTI. Data at the current refresh address in each RAM page are checked and refreshed. The detection of single- and multiple-bit errors is made available to telemetry and sets internal software flags.

#### FIRMWARE FAULT PROTECTION

Features are provided in the ACP firmware to protect microprocessor operations from soft errors created by high-energy particles or other noise sources that can cause sequence or data corruption errors. Out-of-sequence execution of instructions can develop when soft errors occur in the ACP program counter, stack pointer, or stack register, causing faulty decisions and/or jumps. The following techniques are used to minimize the impact of these errors:

- *Execution Sequence.* Critical ADCS functions are executed first in response to an RTI.
- *Protection Firmware Region.* Critical calculations are performed before interrupts are enabled.
- *Sequence Control Codes.* Sequence control code (SCC) checks have been placed within the code to detect out-of-sequence execution of instructions. Error checks are performed prior to output/storage of critical variables, including despin state and thruster output control. Detection of an SCC error causes the processor to jump to the wait loop and the register values to be output on the serial telemetry. The last SCC error is maintained on telemetry until a new error has been detected. Normal processing resumes at the next RTI.
- *Filters.* All digital filters are grouped together to minimize missing an update.

To minimize errors due to data corruption, the following additional techniques are used:

- *Triple Data Storage.* Critical parameters are triply stored and are checked at every RTI. A single mismatch is corrected; a double mismatch is flagged, and processing assumes that the value in the telemetry data page is correct.
- *Variable Limiting.* Critical variables are limited every interrupt.
- *Hardware Control.* If the BIT is not in progress, the DAC input is forced to select the accelerometer during each RTI. The input to each earth sensor processing electronics element, and the accelerometer unit selection logic, are also set to the commanded value at each RTI.
- *Wait Loop.* Critical instructions in program memory contain immediate wait loop returns. All other locations are unused and will force a return to the top of the wait loop. The watchdog is reset only if the RTI sequence is successfully executed, or at the end of a master reset. This ensures that inadvertent jumps to incorrect instructions will force a return to the wait loop.
- *Command Processing.* Critical commands require that multiple bits be set to activate their functions.

#### DESPIN ERROR CORRECTION MODE

To minimize any transients that might occur in the platform pointing control loop as a result of transient hardware or firmware errors, an error correction mode (ECM) has been included. This mode is enabled/disabled by serial command and is prohibited from operating in relative-rate or superspin mode.

The ECM logic detects errors in estimated platform pointing greater than a fixed threshold ( $\pm 0.2^\circ$ ). When activated, the ECM overrides the normal PDC processing and commands a 10-s safe-hold despin mode, using the last average despin control torque required to maintain pointing. During the hold state, special logic is enabled that allows the system to recover automatically. A 30-s wait state follows the hold state to preclude minor transients retriggering the ECM logic. Following the wait state, the system is restored to its pre-ECM condition. The maximum pointing error in response to an ECM transient is  $0.03^\circ$ .

## THRUSTER FIRE PROTECTION

Protection against internal errors that would cause erroneous firing of either the 490- or 22-N thrusters is provided through both hardware and firmware. There are six primary protective features associated with thruster firing, as follows:

- Thrusters are enabled by ground-generated pulse commands. The output circuitry consists of two series pass switches to protect against hardware failures.
- A FIRE OK signal is generated within the firmware and must strobe a fire-enable flip-flop (thruster watchdog) each 24 ms. If this strobe is not present, firing is terminated.
- Slow clock detection circuitry checks for the appropriate 24-ms RTT period; if the RTT period is not found, all thruster firing is terminated.
- If the ACP watchdog timer is triggered, all thruster firing is terminated.
- The ACE initialization sequence inhibits 490-N thruster firing.
- 22-N fire circuitry contains a hardware timer (the hardware window) to limit the accumulated fire duration. If an ACE is turned on by either an RRT or post-ejection sequencer command, the timer is set to 26.2 min. If the ACE is commanded on by a normal command, the timer is not initialized. Once the ACE is on, a command to initialize the timer will load 1.6 min. It is possible to disable the timer so that thruster maneuvers of extended length may be performed.

## ACP WATCHDOG TIMER WARM RESTART

A watchdog timer is provided in the ACP to preclude the occurrence of a failure that may cause the processor to enter a loop from which it cannot exit. Near the end of the real-time processing sequence, an output instruction that clears the watchdog flip-flop is executed. The occurrence of two 24-ms RTTs without clearing the watchdog results in a time-out and forces a warm restart of the ACP.

**PKM-active nutation control**

In response to growing industry concern over the large coning induced by spin-stabilized solid rocket motor firings, an additional PKM-active nutation control (PANC) system was added late in the INTELSAT VI program during the integration and test phase for the two spacecraft using a perigee stage. Previous firings of the PAM-D and PAM-D II motors had been analyzed and modeled,

with questionable success. However, since the INTELSAT VI PKM would be the largest solid motor to be spin-fired in space, extrapolations from already questionable models led to the incorporation of this control system.

The basic PANC system uses the radial TANC signal processing incorporated in the ACE and described previously. However, the accelerometer inputs are replaced with strategically mounted rate gyro inputs, and the two liquid apogee motor (LAM) thrusters are used to fire stabilizing pulses. Due to gyro parameter selections, the TANC threshold of 18 mg is equivalent to 1.25° of nutation pre-PKM burn and 0.81° of nutation post-PKM burn. The reconfiguration requirements were implemented using a spacecraft-mounted switch stack. Commands from the booster separation sequencer are used to automatically switch the rate gyro signals into the ACE units, while simultaneously routing thruster firing command lines from their normal 22-N radial/spin thruster connection to the 490-N LAM drivers. At the completion of PANC operation, the PANC-OFF command reestablishes the original configuration for use during the on-orbit spacecraft mission. To eliminate the possibility of unwanted bus interference from the rate gyros at any later time, the bus power to the rate gyros is looped through the PKM stage umbilical connection, thereby permanently cutting off bus power at PKM separation. Figure 21 is a block diagram of the PANC system.

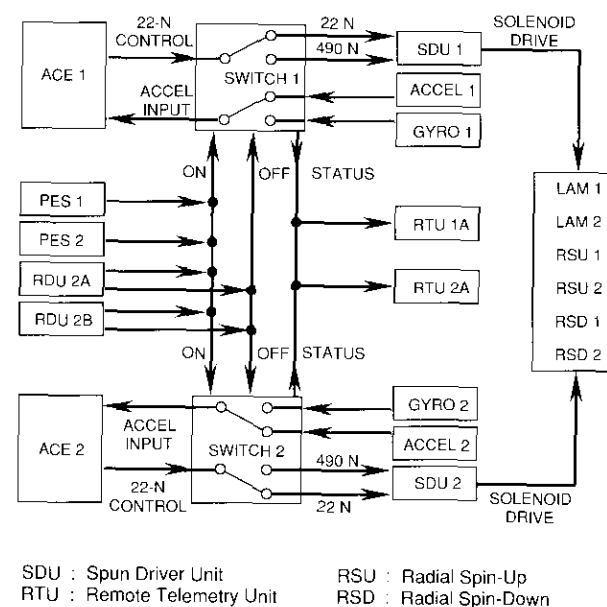


Figure 21. PKM-Active Nutation Control Block Diagram

Detailed design analyses and simulation studies were conducted to support PANC development. A key element of the design validation process was a mixed simulation test environment consisting of a high-fidelity, real-time, hardware-in-the-loop simulation in which the breadboard or flight ACE unit was integrated with a complete spacecraft simulation. For validation of the basic ADCS, the test was modified to incorporate the unique aspects of PKM firing, including time-varying moments of inertia and vehicle mass center, thruster alignment, PKM thruster vector alignment, and a model of the hypothesized "slag" dedamper.

A full parametric study was run to verify proper PANC operation over the range of parameter sensitivity, design margins, and string failures. The sensitivity tests varied parameters within the specification ranges, which determine the basic performance of the major system components. The parameters included rate gyro gain, damping and nutation frequency, ACE timing/overlap, LAM thrust, initial nutation angle, dedamper range, and spacecraft spin speed. In the margin tests, the parameters (gyro gain, damping and nutation frequency, LAM thrust, and initial nutation angle) were increased and decreased until unsatisfactory performance was observed. Adequate system margins of between 4 and 10 were noted. In the failure mode cases, a string failure would result in a LAM thruster failing either on or off; hence, there were six failure cases. All cases were stable with the exception of both LAM thrusters failed on or off. These tests provided a high confidence level for the PANC system.

System-level PANC testing primarily concentrated on verifying proper rate gyro polarity and system-level connections and operation. The switch stacks were thoroughly exercised, and telemetry was verified to ensure that the sensor inputs and thruster firing signals were properly routed and reconfigured. Phase and threshold measurements were also made and compared against PANC predictions.

### **System-level testing of the ADCS**

Testing of the ADCS at the system level was concentrated primarily during four phases of the system-level test flow: integrated system test 1 (IST 1), infrared thermal vacuum (IRTV), IST 2, and launch site testing. IST 1 was performed following initial integration of the ADCS components into the spun structure, IRTV, and IST 2. Identical ADCS tests were performed in IST 1 and IST 2 to allow complete correlation and tracking of performance as a result of exposure to the IRTV environment. The same set of tests, with somewhat reduced depth, was performed in IRTV and launch site testing. ADCS testing was conducted with the spun section both spinning and nonspinning. Nonspinning tests were open-loop, while spinning tests were generally closed-

loop. The set of ADCS tests can be further divided into the functional groups described below.

### **Nonspinning tests**

Nonspinning ADCS testing entailed the static excitation of ADCS sensors and the monitoring of processing functions and ACE outputs.

*Open-Loop Performance.* This is the initial test sequence to which the ADCS is subjected. It verifies the basic health, functionality, and interconnectivity of the ADCS components, such as ACE power-on, initialization, ACE self-test, sensor and MDE polarities, and ADP functioning (sensor time interval measurements). Additionally, earth sensor moon discrimination is verified and RRT thresholds are measured.

*Thruster-Active Nutation Control.* This sequence consists of both mechanical and electrical TANC testing. During mechanical TANC tests, the accelerometers are unbolted from the spacecraft shelf and physically rotated in a controlled manner. The thruster valves are actuated in response to positive or negative acceleration, with audible verification by the test conductor. The electrical TANC tests are performed with a function generator sine wave input to the accelerometers and the thruster driver electronics connected to simulated loads. This allows accurate measurement of phase and threshold for all thruster combinations.

*Automatic Thruster Firing.* This test sequence is divided into three sections that cover the various types of ADCS-initiated automatic thruster firing. The ground maneuvers section thoroughly exercises the hardware window for proper functioning and for one of each of the other maneuver types: primary and backup NSS, EWS, LAM, and a radial maneuver to verify feed-forward torque operation. The stored command processing section loads a series of commands into the SCP and verifies proper operation of the five maneuvers. The spin axis controller section tests the SAC feature for each ACE, including all modes and eclipse operation.

### **Spinning tests**

Spinning ADCS tests involved mounting the rotor structure on a spin machine, using a platform inertia simulator mounted on the BAPTA.

*Despin-Active Nutation Control.* This test sequence is performed with the spun section spinning, but is not a closed-loop test. The accelerometers are again driven by a constant sine wave input, and platform pointing (the despin loop is closed-loop pointing) is measured and compared to the sine wave

input. The gain and phase measurements for DAND operation are checked over a range of parametric selections.

*BAPTA Motor Torque Calibration.* This sequence is used to measure the stall, friction, and running torques for all the BAPTA/MDE configurations, over the full range of torqued values.

*Despin Performance.* This test sequence accomplishes a thorough check-out of the despin control system. Each ACE/MDE combination is first tested in superspin and relative-rate modes. Tests are then conducted in the platform pointing mode, in which despin pointing is performed and measured for all combinations of ACE, MDE, earth sensors, and sun sensors. Transient-free switching is performed between reference sensors and all redundant equipment.

*ADCS Burn-In.* This is a 250-hr test sequence in which an accelerated-activity lifetime test for the ADCS is conducted. All the ADCS functions are operated simultaneously at some point in the test sequence to rule out unexpected interactions. As in the despin performance test sequence, all pointing combinations of ACE, MDE, earth sensors, and sun sensors are evaluated. TANC, DAND, SAC, TOD, LDOE, and SCP thruster maneuvers are also performed for each pointing configuration. A 24-hr run is performed on each ACE, with TOD operational, to verify that there will be no long-term (one full revolution vs a few minutes of operation) anomalous behavior. This test is generally performed in two sections: 150 hr in 1ST 1, and 100 hr in 1ST 2. Each section conducts the test with reduced time allotments for the various configurations.

### **Concluding remarks**

The attitude control functions for the INTELSAT VI spacecraft have been described. Functional design and operation of the attitude determination, platform pointing, spin axis control, and nutation stabilization loops were presented. The unique attitude control features of the spacecraft include precision payload pointing using sun/earth inertial references, autonomous spin axis attitude determination and pointing control, active nutation damping (without passive damping mechanisms), and superspin control for transfer orbit stabilization. Extensive fault protection is in place to maintain system performance in the event of processor and unit hardware upsets. On-orbit performance is optimized with parameter reprogrammability, and enhanced using stored command processing. All attitude and velocity maneuvers can be controlled on board the satellite. Experience with development of the INTELSAT VI

ADCS has demonstrated that a design that integrates all control functions within a central microprocessor can achieve significantly improved performance at low cost, with extended spacecraft autonomy and enhanced fault protection.

### **References**

- [1] D. L. L. Mingori, "Effects of Energy Dissipation on the Attitude Stability of Dual Spin Satellites," *AIAA Journal*, Vol. 7, No. 1, January 1969, pp. 20-27.
- [2] J. T. Neer, "Intelsat VI Nutation Dynamics," AIAA 4th Communications Satellite Conference, April 1972, Washington, D.C. AIAA Paper No. 72-537.
- [3] C. L. Chen, L. I. Slafer, and W. F. Hummel, "Autonomous Spin Axis Controller for Geostationary Spinning Satellites," SAE Conference, Williamsburg, Virginia, August 1986.
- [4] L. H. Grasshoff, "An Onboard, Closed-Loop, Nutation Control System for a Spin-Stabilized Spacecraft," *Journal of Spacecraft and Rockets*, Vol. 5, No. 5, May 1968, pp. 530-535.
- [5] L. Slafer and H. Marbach, "Active Control of the Dynamics of a Dual-Spin Spacecraft," *Journal of Spacecraft and Rockets*, Vol. 12, No. 5, May 1975, pp. 287-293.
- [6] J. W. Smay and L. I. Slafer, "Dual-Spin Spacecraft Stabilization Using Nutation Feedback and Inertia Coupling," *Journal of Spacecraft and Rockets*, Vol. 13, No. 11, November 1976, pp. 630-639.
- [7] L. I. Slafer, "COMSTAR Spacecraft Product-of-Inertia Coupled Electronic Nutation Damper," *AIAA Journal of Guidance and Control*, Vol. 1, No. 4, July 1978, pp. 273-278.



*Loren Ian Stafer received the B.S., M.S., and Engineer degrees in electrical engineering in 1968, 1970, and 1973, respectively, from the University of Southern California, Los Angeles, with majors in control systems and communications theory. He joined Hughes in 1968 while working as a graduate student at USC. In 1970, he transferred to the then Hughes Space Systems Division, specializing in satellite attitude control system design and analysis. He subsequently was named head of the Control Subsystem Engineering and Test Department. He is currently Assistant Manager of the Guidance and Control Systems Laboratory of Hughes*

*Aircraft Company's Space and Communications Group, which is responsible for design, development, and testing of payload and spacecraft attitude control subsystems for all Hughes satellites. He has participated in a number of spacecraft programs, including INTELSAT IV and IV-A, Comstar I, ANIK I, Orbiting Solar Observatory 8, the Geostationary Meteorological Satellite, MARISAT, LEASAT, INTELSAT VI, and several government programs. He was technical leader of the INTELSAT VI ADCS development program and is currently Attitude Control Subsystem Task Manager for the new Hughes HS601 body-stabilized spacecraft program.*

*Mr. Stafer is a member of AIAA and a registered Professional Engineer in Control Systems Engineering in California.*

*Valle Louise Seidenstucker received a Bachelor of Science Engineering degree from the University of California at Irvine in 1979, and a Master of Science Electrical Engineering degree from the University of California at Berkeley in 1980. She began her career at Ford Aerospace and Communications Corporation as an attitude control systems engineer for the INTELSAT V and INSAT satellite programs. In 1986, she joined INTELSAT to actively participate in the INTELSAT VI attitude control system manufacture, subsystem and system-level test, and launch base test activities. In addition to verifying perfect operation of the five attitude control systems on the ground, she participated in the launch and in-orbit testing of all the INTELSAT VI satellites.*



Index: communication satellites, INTELSAT

## **INTELSAT VI communications subsystem design**

G. N. HORVAI, L. A. ARGYLE, T. L. ELLENA, R. R. PERSINGER,  
AND C. E. MAHLE

(Manuscript received October 12, 1990)

### **Abstract**

An overview and description of the complex communications payload of the new-generation INTELSAT VI series satellites are presented. Performance data are given for the key elements of the communications subsystems. The design of the antennas and repeater subsystems are discussed in detail, and testing of the payload is briefly described.

### **Introduction**

In the spring of 1982, Hughes Aircraft Company (HAC) began designing, building, and testing a complex commercial communications payload for the new generation of INTELSAT VI satellites. The successful launch in late 1989 of the first of this series of satellites was followed by initiation of commercial service via this payload to the international telecommunications user community. This paper presents an overview of the design and performance of the complex payload of this satellite, as well as a detailed description of the antenna and repeater subsystems.

### **Design overview**

While based on a traditional architecture employing space-proven principles and technology, the new payload design for INTELSAT VI incorporates a number of unique features developed or adapted for this series of satellites [1],[2]. These features include complex on-orbit reconfigurable C-band

hemi/zone antennas that can be pointed by an RF beacon tracker subsystem (BTS) using a terrestrial beacon; Ku-band antennas steerable over the earth's surface; sixfold C-band frequency reuse; and extensive interconnectivity on a channel-by-channel basis. The interconnectivity is enhanced by a dynamic microwave switch matrix (MSM) for INTELSAT satellite-switched time-division multiple access (SS-TDMA) operations at 120 Mbit/s, and a switch network which provides compatibility with the previous generation of satellites.

The communications payload of the INTELSAT VI satellites consists of 50 repeater channels at C- and Ku-band, with 48 available at one time. The payload receives signals at 5.850 to 6.425 GHz and 14 to 14.5 GHz, translates them to the 3.625- to 4.2-GHz range where channelization takes place, and retransmits them in the 3.625- to 4.2-GHz range or, after up-conversion, in the 10.95- to 11.7-GHz range. A unique feature of INTELSAT VI, the SS-TDMA system makes it possible for two channels to dynamically interconnect six antenna-defined coverage areas. The other C- and Ku-band channels are interconnected through static switches for dedicated traffic patterns. All active units are redundant for high overall payload reliability.

Figure 1 is a simplified block diagram of the communications subsystem. The C- and Ku-band up-link signals are routed into the subsystem via the respective receive antennas. In the input section of the repeater, the wideband low-noise receivers convert the up-link RF signals to a common 4-GHz IF, and the wideband spectrum is then channelized by the input multiplexer filters. Next, the interconnectivity network distributes signals from the individual channels, via static and dynamic switches, to the output section, where all the signals are amplified and some are up-converted to Ku-band. Finally, the output multiplexers recombine the individual channels into wideband spectra, which are connected to the appropriate C- or Ku-band transmit antennas.

The sections that follow provide a more detailed description of the performance and hardware realization of key elements of the communications subsystem. An Appendix lists the major participants that joined with the HAC team in the design, manufacture, and testing of the INTELSAT VI communications payload.

### Key element performance summary

The 50 individual transponders contained in the INTELSAT VI communications subsystem provide over 3,200-MHz of usable bandwidth. This bandwidth can support up to 120,000 two-way telephone circuits and three television channels, simultaneously.

In order for this number of distinct channels and associated usable bandwidth to exist, sixfold frequency reuse is required for the majority of channels

at C-band. To achieve this reuse, the INTELSAT VI payload employs six hemi/zone C-band coverages (zone and hemi being orthogonally polarized), two spot Ku-band coverages, and two orthogonally polarized global C-band coverages. Design and implementation of the transponders, distributed over 10 coverages, was an engineering challenge.

The implemented design required a 3.6-m-diameter by 11.8-m-tall, 1,900-kg spacecraft to house and support the payload. In addition, the power system provided 2-kW of electrical power to the payload and in support of the spacecraft. Maintaining the proper earth-pointing of the hemi/zone antennas was an equally difficult task. The solution was a sophisticated attitude control system, described by Slafer and Scidenstucker [3], and a monopulse-type BTS which is described later in this paper.

### Payload design parameters

Because of the complexity of the INTELSAT VI spacecraft, many factors influenced its payload design [4]. Table 1 presents the major performance requirements which defined the scope of the design.

Effective isotropically radiated power (e.i.r.p.), coupled with thermal, power, and weight requirements, led to the use of high-power amplifiers (HPAs) with eight different power levels. The e.i.r.p. values given in Table 1 are minimums for edge-of-antenna-beam coverage. Hemi/zone e.i.r.p. values were required to be 28 dBW in the 36-MHz channels and 31 dBW in all others. The steerable spot beams had considerably higher requirements of 44.7 dBW for

TABLE I. KEY PAYLOAD SPECIFICATIONS

REQUIREMENTS	HEMI	ZONE				SPOT	GLOBAL
		1	2	3	4		
e.i.r.p. (dBW)	28/31	28/31	28/31	28/31	28/31	44.7/47.7	23.5/26.5
C/I (dB)	27	27	27	27	27	-	27
C/I (dB) for Spot Bore-sight Separation Angle							
4.5°-6.1°	-	-	-	-	-	25	-
6.1°-8.5°	-	-	-	-	-	27	-
>8.5°	-	-	-	-	-	33	-
Receive G/T (dB/K)	-9.2	-2.0	-7.0	-2.0	-7.0	1.0/1.7	-14
Saturation Flux Density (dBW/m <sup>2</sup> )	-77.6	-77.6	-77.6	-77.6	-77.6	-78	-77.6



the 72- and 77-MHz channels, and 47.7 dBW for the 150-MHz channels. Global coverage e.i.r.p. values were specified to be 23.5 dBW for channel 9 and 26.5 dBW for the remaining channels.

Carrier-to-interference ratio,  $C/I$ , specifications proved to be a significant antenna design driver. For the hemi/zone antennas, both spatial and cross-polarization isolation were employed to allow sixfold frequency reuse. Beam-to-beam isolation was generally required to be greater than 27 dB. For the steerable spot beams, spatial and cross-polarization isolation were used to provide the desired beam isolations vs separation angle, as given in Table 1. Global beam isolation was provided by cross-polarization isolation only, and was required to be at least 27 dB.

Receive gain-to-noise temperature ratio,  $G/T$ , specifications strongly influenced both the antenna and repeater designs. Receive antenna gains were required to exceed a minimum (including pointing errors) over the coverage areas in the three ocean regions (Atlantic [AOR], Pacific [POR], and Indian [IOR]) and all specified orbital slots. In addition, the need to minimize antenna-to-repeater losses dictated the waveguide layout and run length. Finally, receiver noise figures had to be minimized to achieve the overall system noise temperature required. As with e.i.r.p., the  $G/T$  specifications are for edge-of-receive-antenna-beam coverage and transponder normal gain.

The saturation flux density (SFD) requirements in the transponder normal gain state are  $-77.6 \pm 2$  dBW/m<sup>2</sup> for C-band up-links and  $-78 \pm 2$  dBW/m<sup>2</sup> for Ku-band. SFD is also specified at edge-of-receive-antenna coverage. This requirement includes gain variation due to temperature and aging of the electronic hardware.

In addition to the communications performance requirements, implementation factors such as physical size, mass, and power influenced the design of both the payload and the supporting spacecraft, and resulted in the characteristics listed in Table 2.

Despite its complexity and stringent specifications, the INTELSAT VI payload met all significant design requirements due to thorough design and careful implementation, as well as an extensive test program.

#### Frequency reuse/polarization plan

As mentioned previously, the INTELSAT VI payload has 50 distinct transponders: 40 operating at C-band and 10 at Ku-band. To accommodate this number of transponders, the INTELSAT VI frequency plan features extensive reuse of the spectrum through spatial and polarization isolation between the various antenna beams. The implementation of this plan is shown in Figure 2.

TABLE 2. KEY SPACECRAFT DESIGN PARAMETERS

PARAMETER	VALUE
Spacecraft Diameter	3.64 m
Solar Panel Height	
Fixed	2.16 m
Deployable	3.97 m
Spacecraft On-Station Height	11.84 m
Spacecraft Mass	
Antenna	373.0 kg
Repeater	779.0 kg
On-Station Total, BOL	2,570.0 kg
Solar Array On-Station Power	2.2 kW
Battery Capacity	2.9 kW

Both the C- and Ku-band channels occupy approximately 500 MHz. The C-band spectrum is divided among the coverages into twelve 36-MHz, two 41-MHz, and twenty-six 72-MHz channels. Similarly, the Ku-band spectrum consists of six 72-MHz, two 77-MHz, and two 150-MHz channels. The hemi transponders are each allocated five 72-MHz and one 36-MHz C-band channel. Each of the four C-band zone coverages occupies four 72-MHz and one 36-MHz channel. The global beams each utilize three 36-MHz and one 41-MHz C-band transponder. East and west spot beams have identical Ku-band channel allocations of three 72-MHz, one 77-MHz, and one 150-MHz transponder.

Spatial isolation allows frequency reuse between the east and west hemi and zone antenna beams. In addition, polarization isolation allows frequency reuse within the same coverage between hemi and zone antenna beams. The global coverages also employ polarization isolation for frequency reuse. The C-band coverages all use circular polarization. The hemi antenna receive polarization is left-hand circular polarization (LHCP), while the zone antenna receives right-hand circular polarization (RHCP). The transmit beams are oppositely polarized from their corresponding receive beams, with hemi transmit being RHCP and zone transmit being LHCP. The global receive and transmit antennas support both polarization senses.

The Ku-band spot beam antennas use orthogonal linear polarization to achieve the required frequency reuse. The east spot receive beam and west spot transmit beam are horizontally polarized, while the west spot receive and east spot transmit beams are vertically polarized.

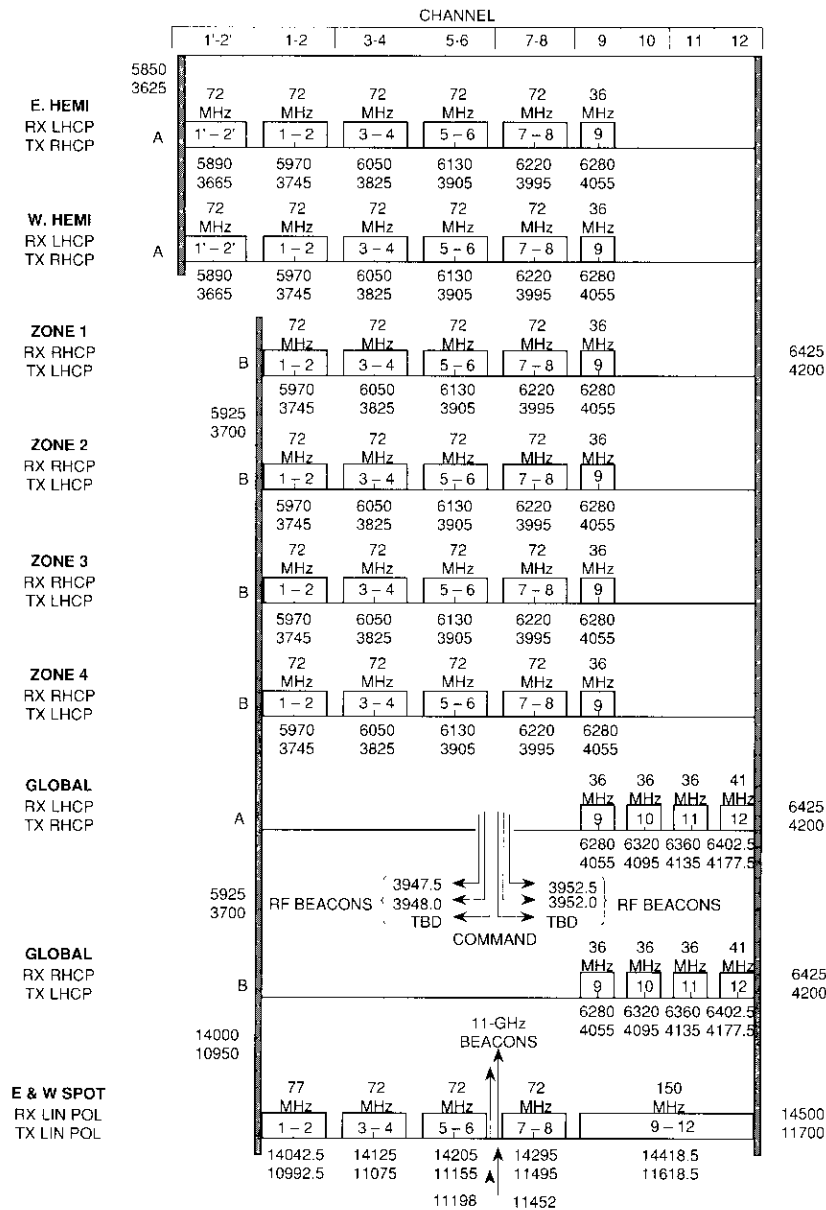


Figure 2. Transponder Frequency Plan

By implementing this complex frequency channelization plan, the INTELSAT VI payload is able to provide over 3,200-MHz of usable bandwidth within its allocated frequency spectra.

### Antenna subsystem

The INTELSAT VI antenna subsystem is described in detail by Persinger *et al.* [5]. It consists of two separate transmit and receive C-band (4/6-GHz) hemi/zone parabolic reflector systems; two separate transmit and receive C-band, dual-polarized global horn antennas; and four east and west, fully steerable, elliptical Ku-band (11/14-GHz) spot beam antennas, each of which has transmit and receive capability. The hemi/zone antennas offer sixfold frequency reuse via four spatially isolated zone beams and two spatially isolated hemispheric beams with polarization orthogonal to that of the zone beams. To provide specialized coverage for the AOR, IOR, and POR, one of three sets of zone beams can be selected by in-orbit switching. To meet the stringent spatial isolation requirements, both hemi/zone antennas include a set of RF monopulse feeds as part of a tracking system that provides closed-loop pointing. The INTELSAT VI antenna farm also has two C-band global telemetry horns, one Ku-band beacon horn, and two C-band biconical antennas which provide command, ranging, and transfer orbit telemetry. Figure 3 depicts the INTELSAT VI antenna farm in both stowed and deployed configurations.

Figure 4 illustrates communications antenna coverages for the AOR, IOR, and POR, as well as for the global and Ku-band spot beam antennas. With hemi/zone coverage, a beacon station can operate in a limited region within zone 1 (the northwest area) of each ocean region. The specialized zone coverages for the AOR, IOR, and POR are shown in Figures 4a, 4b, and 4c, respectively. A tracking beacon located at an earth station provides the RF source for pointing both the transmit and receive hemi/zone reflectors.

### Hemi/zone antennas

The transmit (4-GHz) hemi/zone antenna is a double-offset parabolic reflector with a projected aperture of 3.2 m, illuminated by a feed array of 146 Potter horns. A 3.2-m aperture and a focal-length-to-diameter ratio, *f/d*, of 1.3 were required for beams separated by only 1.6°, in order to achieve the necessary 27-dB spatial isolation. The 1.55-wavelength Potter horn and associated four-probe polarizer are designed for minimum length of the feed element, while meeting the far-field circular cross-polarization isolation specification of 27 dB. By exciting both ports of the four-probe launcher, the zone (LHCP) and hemi (RHCP) beams are obtained simultaneously. The

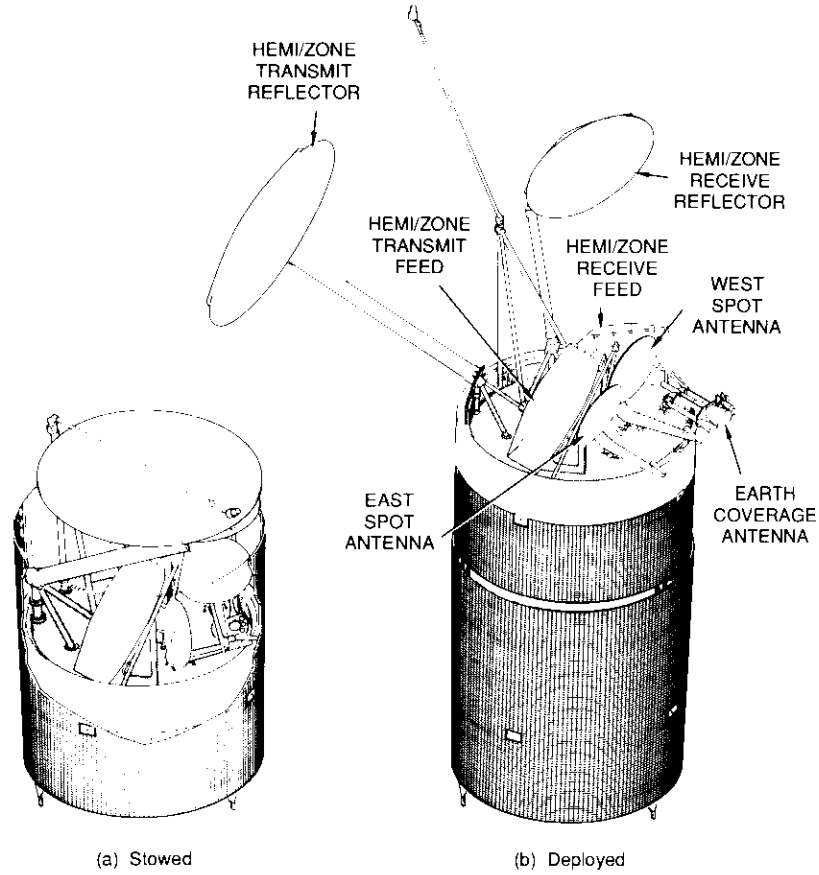


Figure 3. INTELSAT VI Antenna Configuration [5]

large-diameter feed horn is consistent with the long focal length, and beam-shaping efficiency is provided through good component beam crossover. Because existing theoretical models of the Potter horn lead to excellent agreement between computed and measured antenna performance as far down as 35 dB below beam peak, far-field range adjustment of the network coefficients is not necessary. The Potter horn and four-probe polarizers are fabricated from aluminum, while the reflector is built using carbon fiber-reinforced plastic with a Kevlar honeycomb core.

Figure 5 shows how the hemi/zone feed network is built using transverse electrical mode line squareax technology. The array of Potter horns is fed by

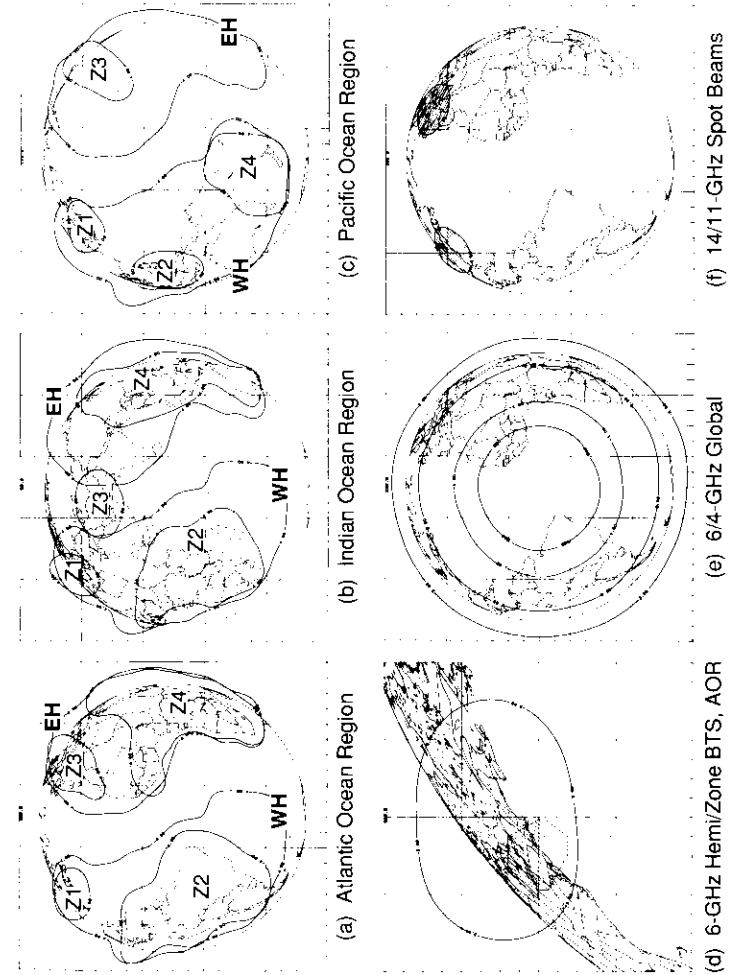


Figure 4. INTELSAT VI Beam Coverages [5]

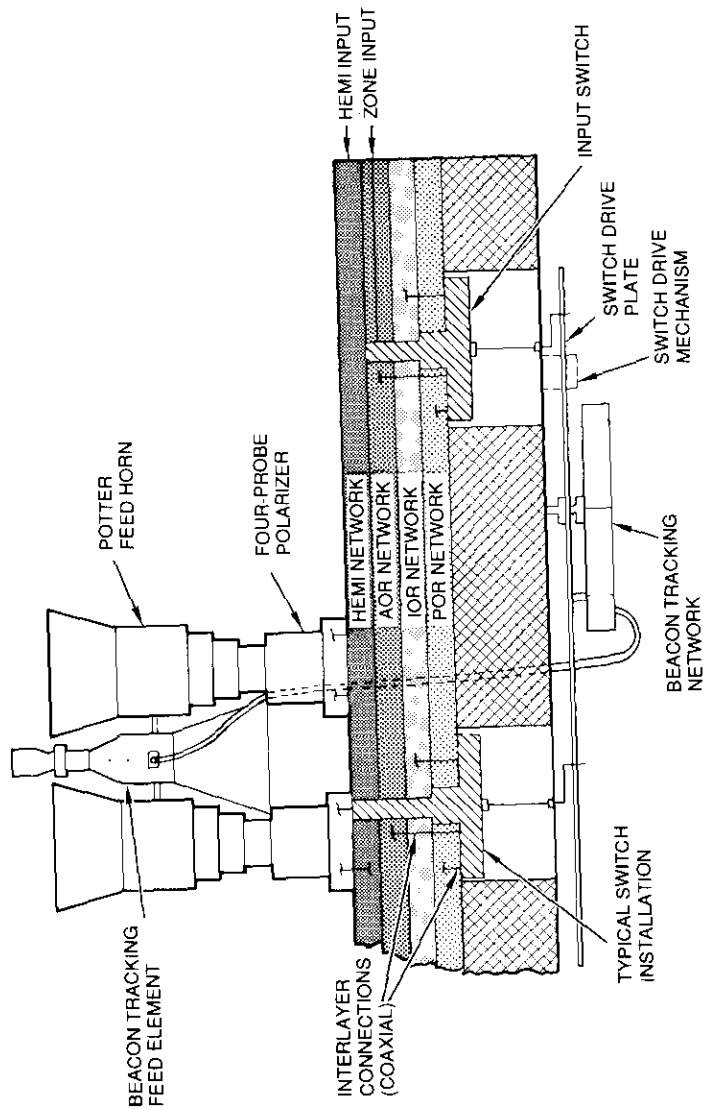


Figure 5. HemiZone Squareax Feed Network Implementation [5]

four separate networks (three zone and one hemi). A layer of switches driven by a switch drive plate interconnects the required zone network and the feed horns to select the ocean region coverage desired. A highly compact feed network is obtained by stacking the four squareax networks and the switching layer.

The receive (6-GHz) hemi/zone antenna is essentially a scale model of the transmit antenna; however, to reduce RF scattering between the two antenna subsystems, the double-offset 2.0-m receive reflector is offset to the northwest at a 45° angle (instead of to the northeast as shown in Figure 3).

### Beacon tracker subsystem

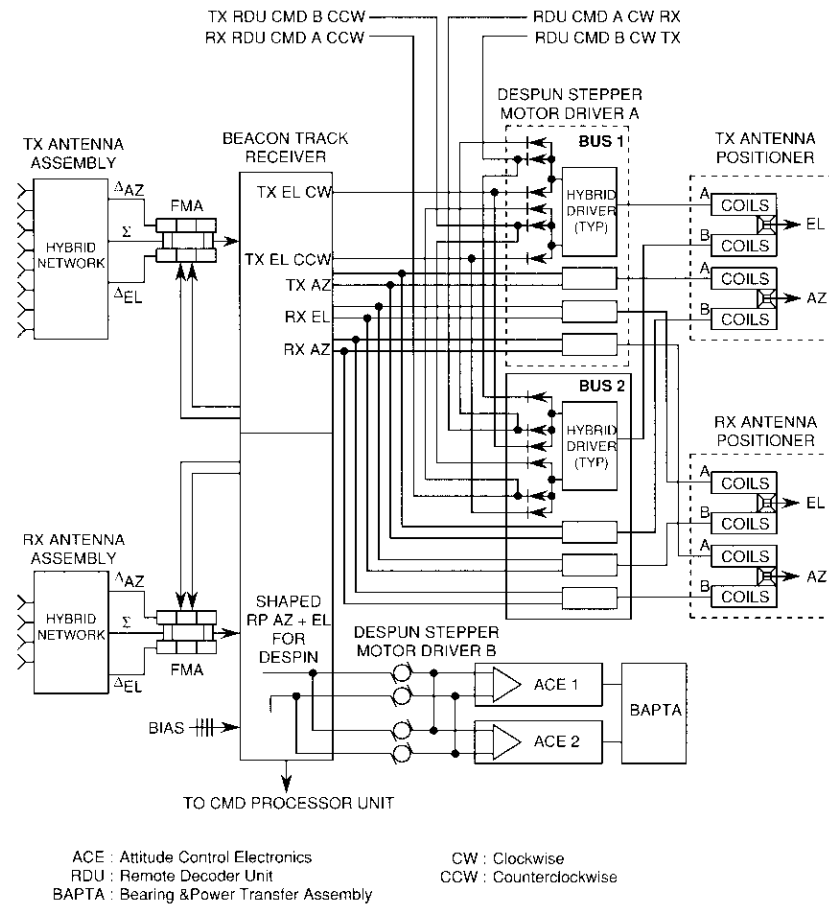
The BTS nominally performs initial alignment and precision closed-loop pointing of the hemi/zone transmit and receive antennas. It also provides backup capability for despun and nutation control. A schematic of the BTS is shown in Figure 6.

The hemi/zone pointing performance of the BTS is presented in Table 3. The subsystem maintains antenna pointing in one of two modes: platform despun provided by the attitude determination and control subsystem (ADCS), or with the BTS controlling despun. The pointing errors given are worst-case  $3\sigma$  numbers and include reflector thermal distortion.

The BTS requires only a single 6.175-GHz LHCP up-link beacon as a pointing reference. Four Yagi feed elements, located in the spaces between the zone 1 communications horns (with an associated network), form a monopulse system yielding sum, delta-azimuth, and delta-elevation beams. With proper amplitude and phase adjustment of these beams, a ferrite modulator assembly (FMA) in the network generates AM modulation which, when processed in the beacon tracking receiver, is proportional to the beam pointing errors. In the closed-loop mode, the system drives the reflectors in azimuth and elevation until zero AM modulation is achieved.

The BTS removes initial deployment errors, as well as thermally induced errors and spacecraft orbital and attitude pointing errors, via a ground-selectable bias that is added to the appropriate error voltage. This allows for some flexibility in locating the beacon station, as shown in Figure 4d.

The transmit reflector BTS is very similar to the receive system except that eight feed elements are used. The feed elements are dielectrically loaded waveguide sections which (as shown in Figure 5) are tapered to allow placement between the transmit Potter horns. Eight feed elements are required because of the larger horn-to-horn spacing that is needed when placing such a 6-GHz BTS antenna array into the 4-GHz Potter horn array.



ACE : Attitude Control Electronics  
 RDU : Remote Decoder Unit  
 BAPTA : Bearing & Power Transfer Assembly  
 CW : Clockwise  
 CCW : Counterclockwise

Figure 6. Beacon Tracker Subsystem Schematic

TABLE 3. BTS HEMI/ZONE ANTENNA WORST-CASE POINTING ERROR (deg 3σ)

MODE	TRANSMIT N-S/E-W	RECEIVE N-S/E-W
BTS Mode, ADCS Despin	0.14/0.14	0.12/0.12
BTS Mode, BTS Despin	0.14/0.14	0.12/0.12

**Dual-polarized global antennas**

Two dielectric sleeve-loaded conical horns provide transmit (4 GHz) and receive (6 GHz) dual circularly polarized global communications coverage. Each antenna is fed by a polarizer and orthomode tee combination. The axial ratio performance, measured in orbit on the INTELSAT VI (F2) satellite, was better than 0.5 dB over the earth's disk.

The two global communications antennas are mounted in a cluster with the global telemetry and beacon horns. The mounting structure allows for a ±2.0° azimuth steering capability to optimize performance based on the chosen hemi/zone platform pitch bias.

**Ku-band spot antennas**

The 14/11-GHz receive/transmit east and west steerable spot beam antennas consist of two separate offset reflectors, each fed by a single dual-polarized/dual-frequency feed horn. The polarization is linear, with orthogonally polarized east and west spot beam antennas. The transmit polarization is also orthogonal to the receive polarization. Each antenna produces a 1.64° × 3.04°, 3-dB elliptical footprint. The east spot beam is oriented 23° from horizontal, and the west spot beam is oriented 37° from horizontal, as shown in Figure 4f.

The east and west spot beam antennas have 1.0-m offset reflectors that are quasi-parabolic. The surface is shaped (and thus departs from the paraboloid) to achieve optimum performance. The focal length is 1.0 m for both antennas. The reflector and feed horn of each antenna are rigidly connected by a graphite support structure. The entire antenna assembly is connected to an antenna positioning mechanism, which is used for both beam steering and deployment from the stowed position. No scan loss occurs as the beam is steered over the full earth disk because the reflector and feed horn maintain a fixed relationship.

Figure 7 shows that good agreement was obtained between the near-field chamber measurement and the in-orbit measurements of the F2 west spot beam. The location of the beam center was determined to within ±0.03° using in-orbit measurement techniques.

**Repeater subsystem**

The repeater is the active translator between the receive and transmit antennas. The signal enters the front-end section of the repeater from the receive antenna output port. The wideband signal is then channelized by the input

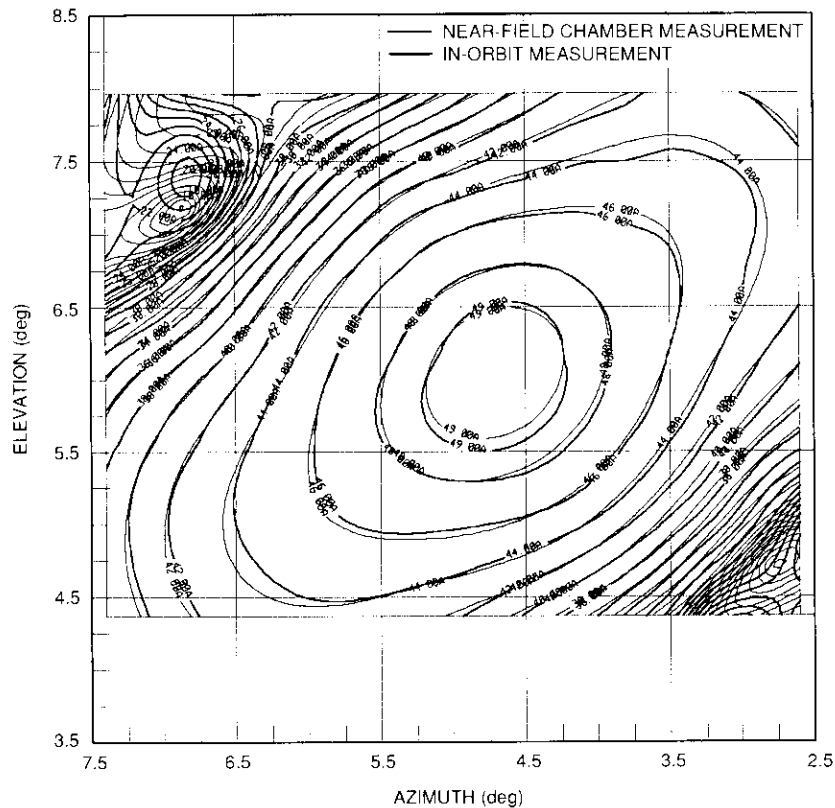


Figure 7. West Spot Beam (11 GHz)

multiplexer assembly, which is followed by the static and dynamic interconnectivity network. After being rerouted to the required beams, the channels are connected to the HPA section, which is followed by the output multiplexer assemblies. The recombined wideband high-power signal is then connected to the transmit antenna of the relevant beams. The major building blocks of the repeater are described below.

#### Input section

The repeater input section consists of input test couplers, preselect filters, receivers, a receiver redundancy switch network, an input multiplexer, commandable channel gain step attenuators, and interconnecting waveguide and

coax. The receivers are arranged into five independent four-for-two redundancy groups. The 20 receivers comprise four 14/4-GHz receivers serving the east and west spot beams, and four groups of 6/4-GHz receivers serving the northeast and northwest zone beams, the southeast and southwest zone beams, the east and west hemispherical beams, and the two global beams.

To minimize noise figure, the receivers are mounted on the low-power side of the despun shelf, as close as possible to the antenna interfaces. In addition, the eight zone receivers are delay-equalized to within 1 ns to minimize intelligible crosstalk when the repeater is operated in the INTELSAT V/V-A mode (see below).

The input multiplexers, which channelize the up-link received signals, consist of two 4-channel, six 5-channel, and two 6-channel noncontiguous multiplexers configured in a circulator-coupled channel dropping arrangement.

#### RECEIVERS

The repeater utilizes receiver designs developed by HAC and three of its partners (see Appendix). Although the individual designs differ somewhat, the receivers are functionally similar. For illustrative purposes, this subsection describes the HAC 6/4-GHz and the NEC 14/4-GHz receiver designs.

Table 4 summarizes the various 6/4-GHz receiver performance parameters by beam and frequency band, and Figure 8 is a block diagram of the receiver. The 6-GHz up-link signals enter the receiver through a waveguide bandpass filter (BPF). The filtered input signals are amplified by a 6-GHz, three-stage preamplifier using NE137 gallium arsenide (GaAs) field-effect transistor (FET) amplifiers. The amplified signals are down-converted to the 4-GHz down-link band using a microwave integrated circuit (MIC) balanced mixer. The mixer local oscillator (LO) signal is derived by multiplication of the 139.0625-MHz crystal oscillator. Frequency update circuitry allows the LO frequency to be incremented or decremented  $\pm 12$  kHz in 15 steps to allow matching at all hemi/zone receiver conversion frequencies to within 9 kHz of each other.

After down-conversion, the signals are filtered to remove oscillator harmonics and higher order mixing products, and amplified in a low-level, 4-GHz, NE244 GaAs FET amplifier. Following this post-mixer amplifier, temperature compensation modules and a selectable attenuator stabilize and set the overall receiver gain. The signals are then fed to a two-stage driver amplifier, and finally pass through a ferrite isolator to the receiver output port. To ensure the +28 dBm third-order intercept required for the communications receiver, the driver amplifier uses a Hewlett-Packard (HP) 5101 bipolar transistor amplifier.

The overall gain of the receiver is stabilized over the expected spacecraft qualification temperature range by using a PIN diode attenuator controlled by a

TABLE 4. RECEIVER

PARAMETER	NORTH ZONE	SOUTH ZONE
Input Frequency Range (MHz)	5,925-6,300	5,925-6,300
Output Frequency Range (MHz)	3,700-4,075	3,700-4,075
Translation Frequency Error		
Over Life (10 yrs) (ppm)	±5	±5
30 days (excluding eclipse), (ppm)	±50	±50
Unit-to-Unit (kHz) p-p	9	9
Short-Term Stability (Hz)	30	30
Gain (dB)	56.0 ± 0.5	62.5 ± 0.5
Extra High-Gain Step (dB)	4.5 ± 0.2	4.5 ± 0.2
Gain Stability (dB)		
Over Life and Qualification Test at $f_0$	1.0	1.0
Over Any 15°C at $f_0$	0.3	0.3
Over 36 MHz	-	-
Gain Flatness (dB) p-p		
Over 500 MHz	0.5	0.5
Over 72 MHz	0.3	0.3
Gain Slope (dB/MHz)		
Acceptance Test	0.008	0.008
Qualification Test	0.010	0.010
Change in Gain Slope Over Qualification Test (dB/MHz)	0.006	0.006
Noise Figure (dB)	3.2	3.2
3rd-Order Intermodulation (dB)		
26	-43	-50
36	-48	-55
46	-53	-60
Group Delay Variation (ns) p-p		
Entire Passband	6	6
72 MHz	3	3
36 MHz	-	-
Phase Shift (dBm)		
1.5°	-40	-47
0.2°	-49	-56
Intercept Point	32	31
DC Power Consumption (W)	6.0	6.0

PERFORMANCE

GLOBAL	HEMI	14/4-GHz SPOT
6,260-6,425	5,850-6,300	14,000-14,500
4,035-4,200	3,625-4,075	3,700-4,200
±5	±5	±1
±50	±50	±10
9	9	-
30	30	50
62.5 ± 0.5	62.5 ± 0.5	59.5 ± 0.5
4.5 ± 0.2	4.5 ± 0.2	6.0 ± 0.2
1.0	1.0	1.0
0.3	0.3	0.3
0.3	-	-
0.5	0.5	0.5
-	0.3	0.3
0.008	0.008	0.008
0.010	0.010	0.010
0.006	0.006	0.005
3.4	3.2	5.0
-56	-52	-48
-61	-57	-53
-66	-62	-59
10	6	6
-	3	3
6	-	-
-53	-49	-45
-62	-58	-54
24	29	30
6.0	6.0	8.3

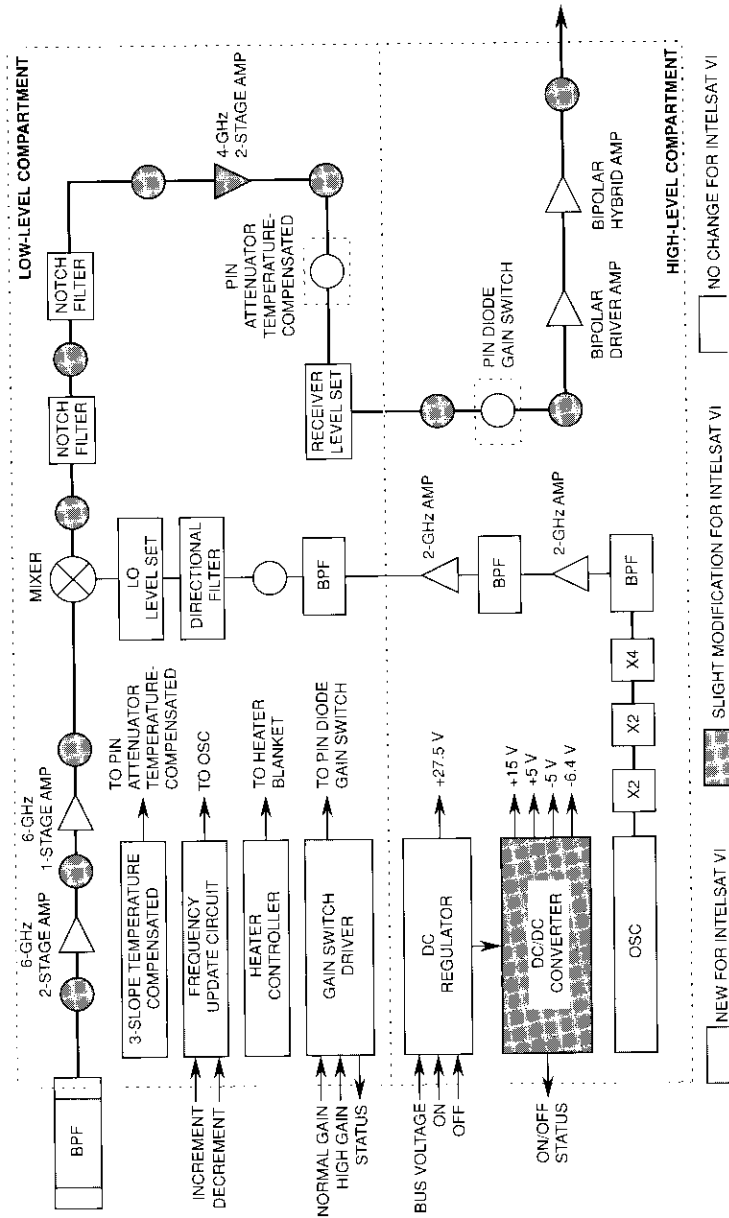


Figure 8. HAC 6/4-GHz Receiver Block Diagram

three-slope temperature compensation circuit, and by gate bias temperature compensation of the 4-GHz low-level amplifiers. The PIN diode gain-step switch, which provides a commandable +4.5-dB step in the receiver gain, is identical to the temperature compensation attenuator except for a change of bias resistor to provide the required gain step. Each receiver contains a DC-series regulator and a switching DC/DC converter operating at 20 kHz to provide the necessary voltages.

Mechanically, the receiver consists of 28 MIC modules mounted into compartmentalized boxes (half-housings). The high-level modules, consisting of the DC/DC converter, DC regulator, LO group, and 4-GHz bipolar driver amplifiers, are packaged in one half-housing. The low-level modules, which include the 6- and 4-GHz FET amplifiers and down-converter, as well as the frequency and gain compensation circuitry, are in the other half-housing. The half-housings are bolted together back to back and connected through the common walls to form an integrated unit. Each module is an MIC assembly consisting of a thin-film RF circuit on an alumina ( $Al_2O_3$ ) substrate soldered to a gold-plated Kovar carrier.

Figure 9 is a block diagram of the 14/4-GHz receiver. The 14-GHz up-link signal enters through an eight-stage Chebychev waveguide BPF, which provides the required out-of-band rejection. The signal is then amplified by a 14-GHz low-noise preamplifier consisting of two modules, each employing a two-stage NE137 GaAs FET amplifier with input/output MIC isolators. This preamplifier achieves a noise figure of 3.7 dB and a gain of 28.5 dB at room temperature.

The MIC mixer down-converts the applied 14-GHz signal to the 4-GHz down-link band using a 10.3-GHz LO signal. Post-mixer filtering reduces LO harmonics and higher order intermodulation products. The 10.3-GHz LO signal is obtained from a 64.375-MHz, oven-controlled, temperature-compensated crystal oscillator, through a chain of frequency multiplications. Frequency update command capability ensures that the long-term frequency stability requirement of  $\pm 1$  ppm/10 yr will be met.

The down-converted signal is amplified by a two-stage, low-noise linear NE137 GaAs FET amplifier and fed to a driver amplifier module consisting of a two-stage medium-power GaAs FET amplifier. A single-stage PIN diode attenuator before the 4-GHz medium-power amplifier is used for receiver temperature compensation and overall gain-setting. DC power is regulated by a switching regulator that converts the input voltage of 28 V to the required values of +11 V and -5 V for the FET amplifiers and LO, respectively.

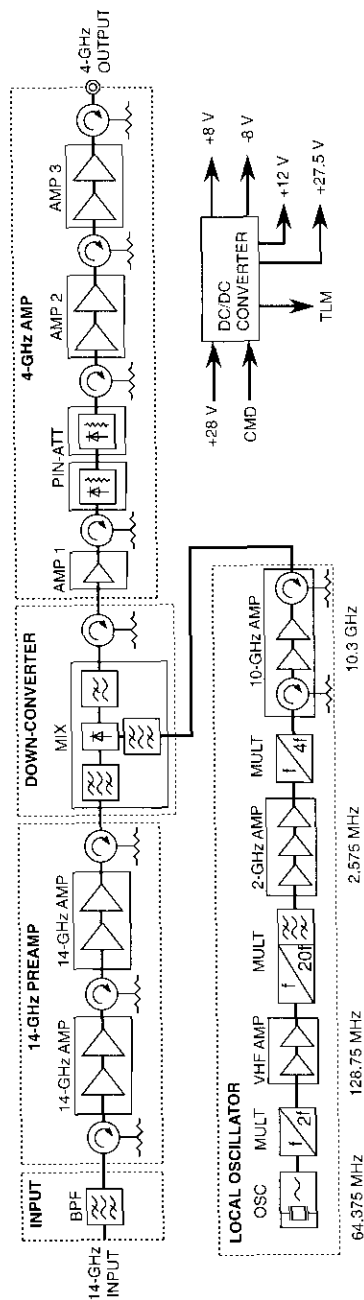


Figure 9. NEC 14/4-GHz Receiver Block and Level Diagram

The 14/4-GHz communications receiver is packaged in a three-part housing. The RF section of the receiver is assembled into the left side of the housing; the LO module and the DC/DC converter are assembled into the right side; and the BPF is assembled into the top. The crystal oscillator is attached to the narrow sidewall of the housing. The housing is covered with thin metal plates, using RF gaskets to provide RF shielding.

MIC technology is used to the maximum extent possible in the module designs. Alumina and ferrite substrates are attached to gold-plated Kovar and titanium carriers, which in turn are assembled into the housing with screws. The substrates are interconnected using gold ribbon, which is easily attached to the substrates and easily replaced. DC power is provided to the RF modules through feedthrough filters to exclude noise from the power lines.

#### INPUT MULTIPLEXERS

The 10 multiplexers (two 4-channel, six 5-channel, and two 6-channel) each consist of a hybrid power divider and two pairs of two- or three-channel, noncontiguous, circulator-coupled coaxial resonator BPFs. These are 10th- or 12th-order, quasi-elliptic, self-equalized filters having four finite frequency loss poles and four or six poles of self-equalization to provide sharp out-of-band rejection characteristics and very flat in-band, passband, and group delay performance. The filters are realized using a silver-plated aluminum housing with Invar resonators. Typical unloaded  $Q$ 's range from 4,500 to 5,000, and temperature stability is less than  $\pm 1$  ppm/ $^{\circ}\text{C}$ . Theoretical passband flatness, gain slope, group delay, and out-of-band rejection performance for 36-, 72-, and 150-MHz bandwidth filters is shown in Figures 10 through 13. The performance of the 41- and 77-MHz-wide channels is similar to that of the 36- and 72-MHz-wide channels.

For optimum TDMA and INTELSAT V/V-A-like operation, the differential delay between all 1-2 and 3-4 hemi/zone channels and co-frequency zone channels was minimized by grouping the input filters by channel number, as shown in the subsystem block diagram in Figure 1. Since the global transponders are located in one sector of the communications shelf, all the global-A and global-B filters are grouped together. The two hemi channels (1'-2') are also grouped together as shown. The resulting configuration has five groups of eight filters, two groups of four filters, and one group of two filters.

All the filters in each group are mechanically integrated to form one structural unit. Figure 14 shows the mechanical configuration of a typical group of input filters. The filters are arranged in a staggered configuration to allow easy access for connection of the input and output coax lines.

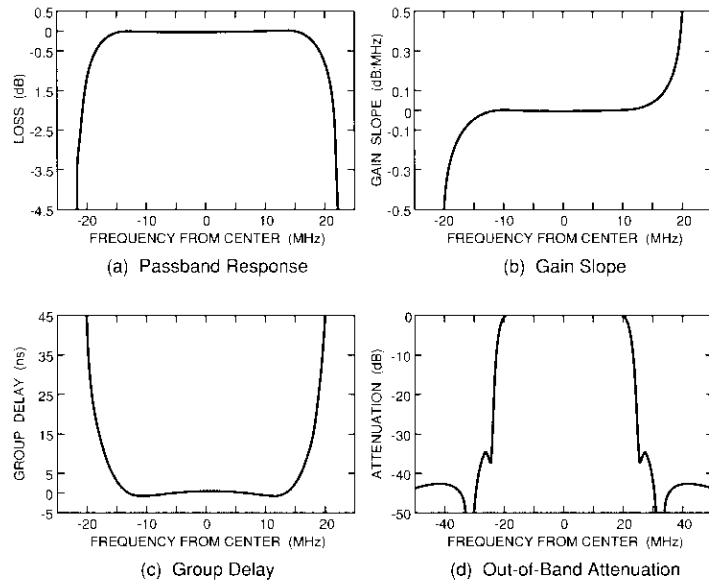


Figure 10. Performance Data for 36-MHz Channels ( $N = 10$ )

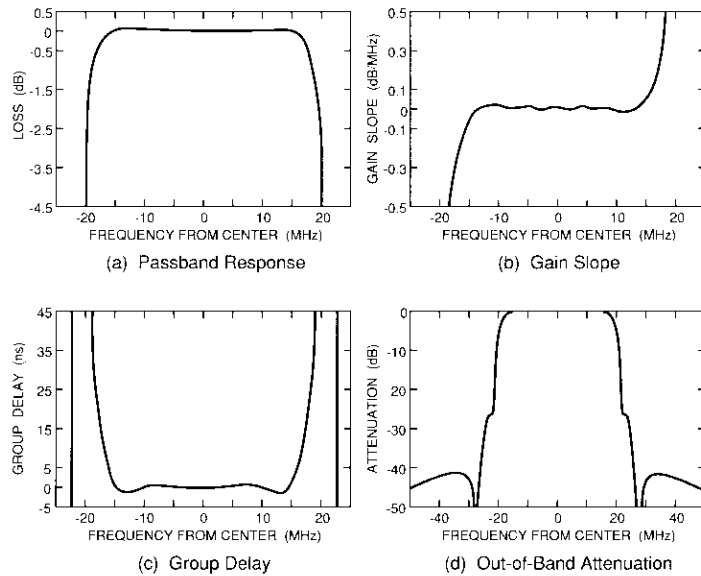


Figure 11. Performance Data for 36-MHz Channels ( $N = 12$ )

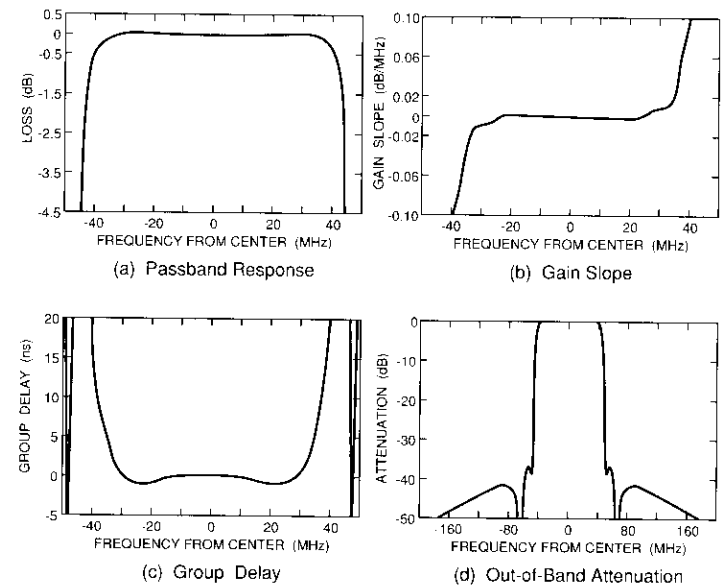


Figure 12. Performance Data for 72-MHz Channels

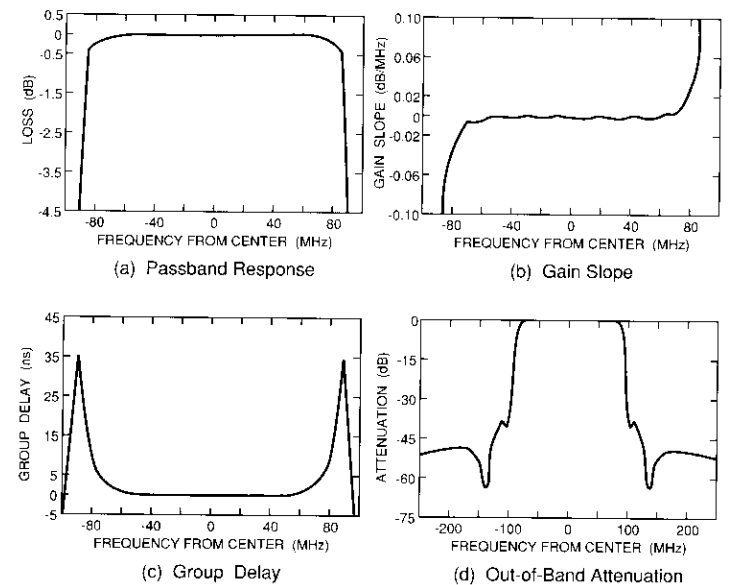


Figure 13. Performance Data for 150-MHz Channels ( $N = 10$ )

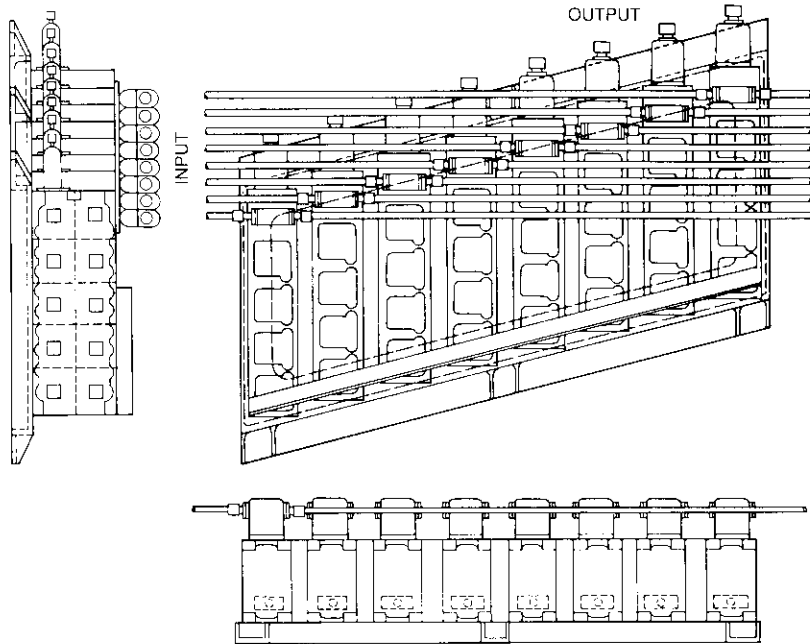


Figure 14. Input Multiplexer Group Mechanical Configuration

**Interconnectivity**

As shown in Figure 1, the INTELSAT VI payload incorporates extensive interconnection capabilities. The hemi and zone repeaters can be interconnected statically via static switch matrices (SSMs) or dynamically through the SS-TDMA subsystem's MSMS. Since all up-link signals are down-converted to C-band by the receivers, the Ku-band spot repeaters can be connected statically to the hemi and zone repeaters as well. However, the global transponders cannot be interconnected with other beams.

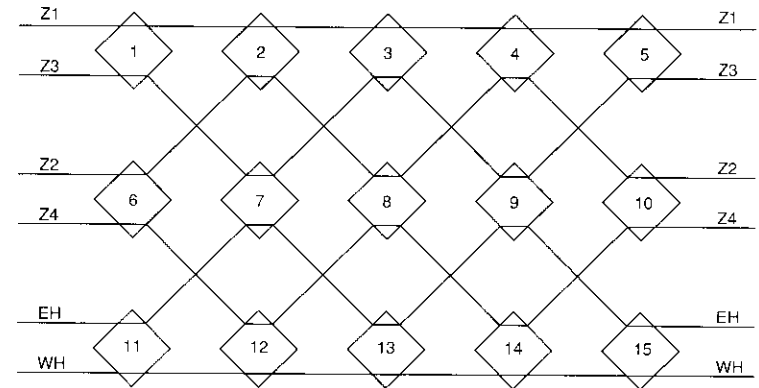
In addition to the beam connectivity provided by the SSMs and MSMS, three types of beam-combining networks are present in the payload. INTELSAT V/V-A compatibility networks allow the combining of zone up- and down-link beams to form pseudo-INTELSAT V/V-A zone coverages. A hemi interconnection and pseudo-global network provide coverage flexibility in hemi channel (1'-2'). And finally, the spot channel (9-12) transponders can be interconnected via static switches.

This combination of interconnection possibilities creates an extremely versatile payload that allows the INTELSAT VI satellite to provide users with a wide variety of telecommunications options.

STATIC SWITCH MATRICES

The SSMS allow spot, hemi, and zone beams to be interconnected. The adjective "static" implies that once a connectivity pattern is established it will remain fixed for a reasonably long time. With this in mind, the SSMS are made up of mechanical-latching coaxial RF switches (called C-switches). The static matrices are configured as 6 x 6 (six inputs by six outputs, as shown in Figure 15) or 8 x 8 blocks employing 15 or 22 coaxial switches, respectively. The 8 x 8 matrices are used in channels 1-2 through 7-8 to allow interconnection among the two spot, two hemi, and four zone beams. A 6 x 6 matrix is used in channel 9 because only hemi and zone interconnections are required. Switches in each matrix can be commanded individually or as a group on a channel-by-channel basis.

The large number of switches in each type of SSM provides considerable redundancy. The SSMS are tolerant of several switch failures (a switch that



RF INTERCONNECT:  
 Z1 - Z1  
 Z3 - Z3  
 Z2 - Z2  
 Z4 - Z4  
 EH - EH  
 WH - WH

Each switch in the 6 x 6 network can be uniquely commanded parallel or crossed to provide 2<sup>15</sup> different configurations. This network exists for Ch 9.

STATE	POSITION	
DIRECT	1 TO 3	2 TO 4
CROSSED	1 TO 4	2 TO 3

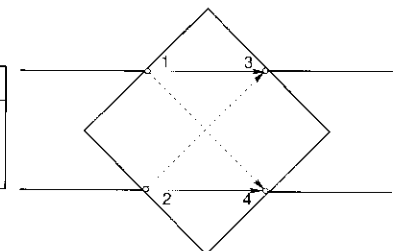


Figure 15. 6 x 6 SSM Configuration

cannot change input to output port connectivity) without loss of beam inter-connection flexibility. Because of the number of switches and the large number of paths through the switch matrix, considerable attention was paid to optimizing the layout to ensure good match and minimal path-to-path loss variation.

#### MICROWAVE SWITCH MATRIX

The INTELSAT VI spacecraft has been designed for the first large-scale commercial application of on-board dynamic switching, with the on-board SS-TDMA subsystem forming the heart of the communications payload (see Figure 1). The introduction of this technology provides cyclic and dynamic interconnections among six isolated beams for two independent 72-MHz frequency-multiplexed channels at C-band. The resulting dynamic frequency reuses within the existing spectra significantly increase satellite utilization efficiency and flexibility.

Figure 16 is a block diagram of the INTELSAT VI on-board SS-TDMA subsystem. In each of the two SS-TDMA channels, the on-board subsystem comprises three main elements. The MSM provides the RF switching capability

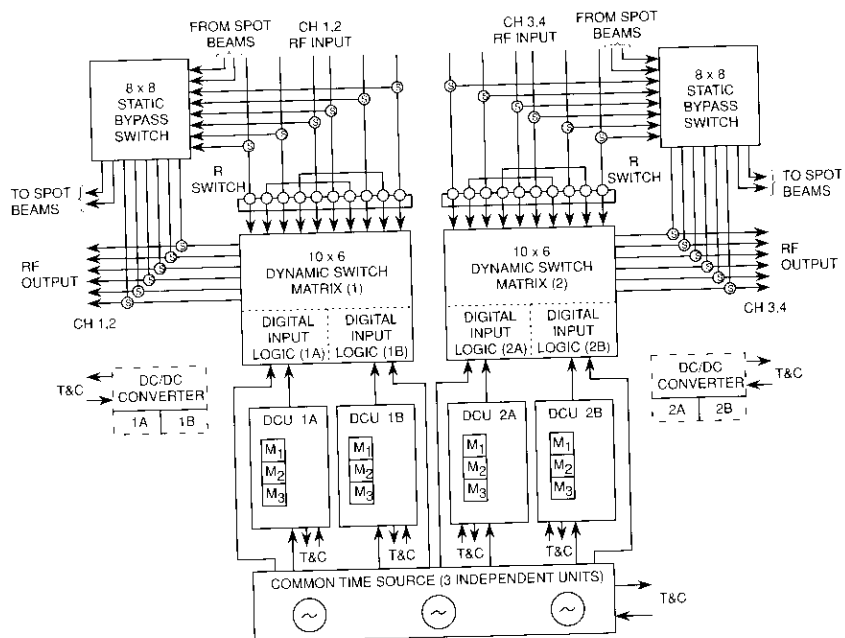


Figure 16. SS-TDMA Block Diagram

and cyclically connects the input and output ports that correspond to up- and down-link beams. The distribution control unit (DCU) is a digital device that controls the ON/OFF switch states of the MSM according to preassigned ground-command programmable switch configurations stored in the DCU memory. The timing source is the time-base generator which provides stable reference timing for plesiochronous operation with the terrestrial networks. To achieve the desired long-term stability of  $1 \times 10^{-11}$ , the timing source is placed in a temperature-controlled oven and has a frequency correction capability commandable via telemetry and command (T&C) interfaces.

A more detailed description of the on-board SS-TDMA subsystem is presented in a companion paper by Gupta *et al.* [6].

#### INTELSAT V/V-A COMPATIBILITY AND PSEUDO-GLOBAL NETWORKS

Complementing the payload flexibility provided by the SSMS, INTELSAT VI is equipped with two beam-combining networks and a pseudo-global network.

Since INTELSAT is still using the INTELSAT V/V-A series of satellites, some compatibility was required between antenna coverages provided by INTELSAT VI and those of this earlier satellite series. The difference lies in the number and shape of the zone beams—INTELSAT VI satellites have four independent zone beams, whereas INTELSAT V/V-A satellites have only two. The INTELSAT V/V-A compatibility networks implement the required zone beam combinations to form pseudo-INTELSAT V/V-A zone beam coverages. Each zone channel has an up-link compatibility network consisting of five coaxial C-switches and two 3-dB hybrids. Channel 5-6 is equipped with an additional down-link network. The internal path loss and propagation delays between beams into and out of the network are equalized to minimize intelligible crosstalk caused by multipath propagation through the two combined up-links.

The hemi channel (1'-2') pseudo-global network consists of six coaxial C-switches and a 3-dB hybrid and serves two functions. First, it is a  $2 \times 2$  matrix providing cross-connection capabilities for the channel. Second, the network allows the channel to approximate a global coverage transponder by combining the two hemispheric beams into a hybrid. Either hemi up-link can be broadcast to both hemi down-links simultaneously, thereby completing the global coverage transponder. As in the case of the INTELSAT V/V-A networks, beam-to-beam loss and delay equalization are required.

#### Output section

The output section of the repeater contains the power amplifiers (with their redundancy switch network), the output multiplexer assemblies, harmonic

filters, and isolators. In case of the Ku-band transponders, up-converters generate the Ku-band down-link signal from the common C-band (4-GHz) frequency. The signal enters the output section from the interconnectivity network, passes through the power amplifier redundancy switches, and enters the selected amplifier, from which it is connected to the output multiplexer. The recombined wideband spectrum exits the repeater toward the transmit antennas from the common output of the multiplexers, through the high-power isolators. In the case of high-power C- and Ku-band channels, harmonic filters are individually placed in front of the output multiplexers, whereas the lower power transponders have one harmonic filter at the common output of the multiplexer.

UP-CONVERTERS AND MASTER LOCAL OSCILLATORS

The up-converter and master local oscillator (MLO) translate the repeater 4-GHz IF band to the 11-GHz down-link frequency band. Since the up-link frequency bands are contiguous 500-MHz bands, but the 11-GHz down-link bands consist of two 250-MHz bands separated by 250 MHz, two frequency-option up-converters are used: 3.7- to 3.95-GHz input converted to 10.95- to 11.2-GHz, and 3.95- to 4.2-GHz input converted to 11.45- to 11.7-GHz. The up-converters are three-for-two redundant and obtain their LO signal of 7.25 or 7.5 GHz from two independent groups of three-for-one redundant MLOs.

Figure 17 is a block diagram of the up-converter. The performance specifications, including command and telemetry requirements, are given in Table 5. The up-converter consists of a 4-GHz amplifier, a 4-GHz filter, a 4/11-GHz mixer, an 11-GHz BPF, a 7-GHz limiter, a 7-GHz low-pass filter (LPF), a voltage converter, and various isolators and bias circuits.

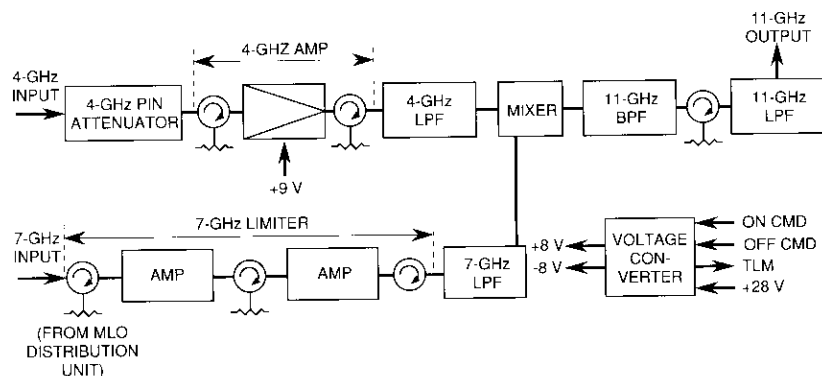


Figure 17. 4/11-GHz Up-Converter

TABLE 5. 4/11-GHz UP-CONVERTER PERFORMANCE

PARAMETER	VALUE
Input Frequency Range	
Type 1	3,704.0–3,941.0 MHz
Type 2	3,959.0–4,193.5 MHz
Output Frequency Range	
Type 1	10,954.0–11,191.0 MHz
Type 2	11,459.0–11,693.5 MHz
Translation Frequency and MLO Frequency	
Type 1	7,250.0 MHz
Type 2	7,500.0 MHz
Input Power From MLO Combiner/Divider	+4 dBm ± 4 dB
Up-Conversion Gain, $P_{in} = 15$ dBm and Below	
Type 1	1.7–2.24 dB
Type 2	1.65–2.25 dB
Gain Flatness	
Over Any 72-MHz Bandwidth	0.25 dB p-p max
Over Any 150-MHz Bandwidth	0.40 dB p-p max
Gain Slope	0.005 dB/MHz max
Gain Stability Over Any 15°C Range	0.2 dB p-p
Change in Gain Slope Over Acceptance Temperature Range	0.001 dB/MHz max
Noise Figure	14.4 dB max
Amplitude Linearity (3rd-order intermod)	
Input Power of Each of Two Equal Carriers	
-18 dBm	-50.5 dB max
-25 dBm	-64.5 dB max
-32 dBm	-78.5 dB max
Spurious Output	
In-Band of Each Channel	-94 dB max
9 to 18 GHz, Except Below	-94 dB max
$3 F_{in}$	-82.5 dB max
$2 LO - F_{in}$	-45 dB max
2 LO	-83 dB max
$3 LO - 3 F_{in}$	-93 dB max
DC Power Consumption	1.89 W

The 4-GHz input signal level is adjusted and amplified, and the bandwidth is limited by a PIN attenuator, an amplifier, and a BPF. The signal is then up-converted to 11 GHz by an image-enhanced double-balanced mixer, using a frequency of 7.25 or 7.5 GHz. The converted signal is routed to the output terminal through a BPF. Isolators are used at the input and output ports and between the devices (*i.e.*, amplifier and filter, or mixer and filters) to provide good frequency response.

The up-converter is packaged in a two-compartment aluminum housing. The DC/DC converter is contained in one compartment, and the RF circuit assemblies in the other. The up-converter uses MIC contraction techniques with each MIC module that consists of thin-film circuits on alumina or ferrite substrates. The substrates are soldered to a gold-plated Kovar or titanium carrier, and the carriers are then fastened to the housing and interconnected using gold-plated molybdenum ribbons.

The MLOs contain oven-controlled crystal oscillators, followed by a multi-stage frequency multiplier similar to the LO chains in the receivers. To minimize MLO warm-up time in the event of a failure, standby MLOs are operated with the oscillator on and multiplier off.

DRIVER AMPLIFIERS

Three types of driver amplifiers are used in the repeater. One operates at Ku-band and two are C-band units—one with a single stage of amplification (11-dB total gain) and the other with two stages of amplification (22-dB total gain). The Ku-band amplifiers drive the 40-W traveling wave tube amplifiers (TWTAs) and have a single amplification stage (14-dB gain). The higher-gain C-band driver amplifiers are used in channels 1-2 and 3-4 to compensate for the loss through the TDMA microwave switch. The lower-gain type is used to drive the TDMAs.

Figure 18 is a block diagram of the two-stage, 4-GHz driver amplifier which uses an MIC design. The one-stage design is similar. Each stage is terminated at both input and output with MIC isolators to minimize reflective interactions between the stages and to provide a good match at the driver input and output ports. Each driver amplifier is packaged in an individual housing with appropriate filtered feedthrough connectors and an RF-sealed cover. The MIC amplifier design was the result of a combination of initial computer-aided design and final individual circuit tuning, in which gold ribbon was gap-welded over extra gold circuit tuning pads provided in the design.

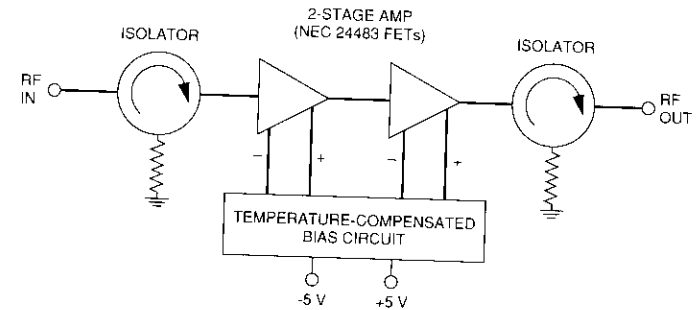


Figure 18. Two-Stage Driver Amplifier Block Diagram (HAC design)

SOLID-STATE POWER AMPLIFIERS

The C-band repeater uses 1.8- and 3.2-W solid-state power amplifiers (SSPAs) as the final HPA for the high-gain northeast and northwest zone antenna beams. The SSPAs are three-for-two redundant and are divided into five types, depending on operating frequency band and output power level, as shown in Table 6.

To minimize the maximum SSPA temperature, the amplifiers are mounted on the rim shelf opposite the optical surface radiators, which are mounted on the spinning solar panels. The units are painted black and mounted to the rim shelf using screws and a thermally conductive room-temperature vulcanizer to ensure maximum radiated and conductive cooling.

TABLE 6. SSPA TYPES

TYPE	FREQUENCY RANGE		OUTPUT POWER (W)	GAIN (dB)
	MAXIMUM (MHz)	MINIMUM (MHz)		
1	3,704	3,861	3.2	63-67
2	3,869	4,031	3.2	63-67
3	3,704	3,861	1.8	62-66
4	3,869	4,031	1.8	62-66
5	4,037	4,073	1.8	62-66

Figure 19 is a block diagram of a typical SSPA. The SSPAs consist of a driver amplifier, a post-amplifier, two power amplifier stages, a PIN-diode attenuator, six isolators, a DC/DC converter, and bias circuitry. The primary difference between the two power levels of SSPAs lies in the post-amplifier and power amplifier sections.

The one- or two-stage driver amplifiers provide 11 dB of gain per stage, while the two-stage post-amplifiers achieve a gain of 19 dB. Following the post-amplifiers are two final power amplifier stages, which are tuned for optimum linearity. The 3.2-W power amplifier stages achieve approximately 16 dB of gain, typical two-carrier linearity of 10 dBc, and 3.55-W output power at approximately 3-dB gain compression. The 1.8-W power amplifier provides 2.0 W of output power and similar two-carrier linearity at the 3-dB compression point. Individual amplifier stages are separated by isolators to ensure that SSPA input and output match, and to minimize interstage mismatch problems. The output isolator is constructed in coax for low loss, while the other isolators employ an MIC structure on a ferrite substrate.

To provide overall SSPA temperature compensation, gain-setting, and a 2.5-dB ground-commandable gain step, each SSPA uses a PIN attenuator following the first driver amplifier module. The pulse-width-modulation power supply provides sequenced gate and drain bias to the FETs, and a gain control voltage to the PIN attenuator. It has a switching circuit for an external heater to accommodate overall spacecraft thermal control. The overall DC-to-RF efficiency is approximately 21 percent at the nominal output power of 1.8 and 3.2 W.

#### TRAVELING WAVE TUBE AMPLIFIERS

The repeater requires TWTAs at 4 and 11 GHz with significantly different power output. Figure 20 shows the application of the different TWTA power levels by channel assignment. Table 7 summarizes the TWTA complement for the spacecraft and indicates major design features of each type.

All four multicollector 4-GHz tube versions use a triply depressed collector to improve efficiency, with the attendant benefit of nearly constant thermal dissipation at all operating drive levels. Oxide-coated cathodes are used in all 4-GHz tubes and operate at temperatures of approximately 685°C and current densities of about 130 mA/cm<sup>2</sup>. The 13.5- and 16.0-W traveling wave tubes (TWTs) use a sealed 246-H electron gun—a stack gun construction used on many spaceborne TWTs. This gun allows high-power TWTs with higher current requirements to maintain a relatively low cathode loading consistent with long life requirements.

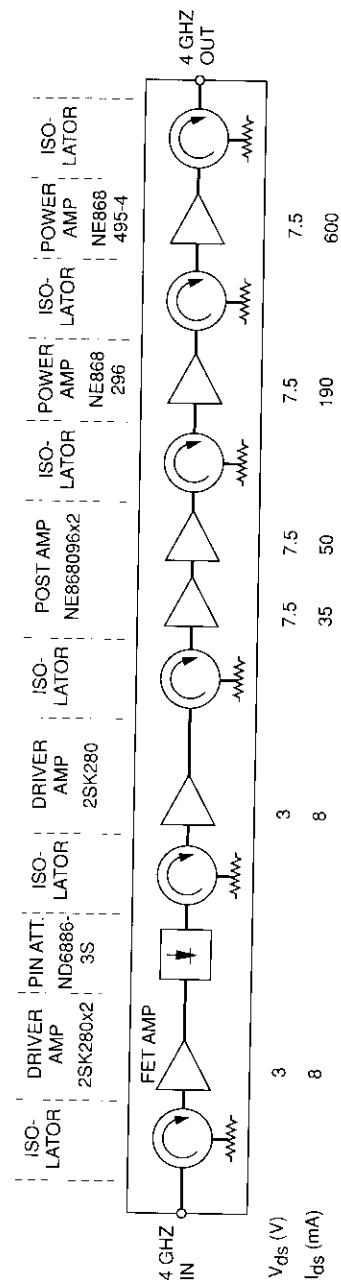
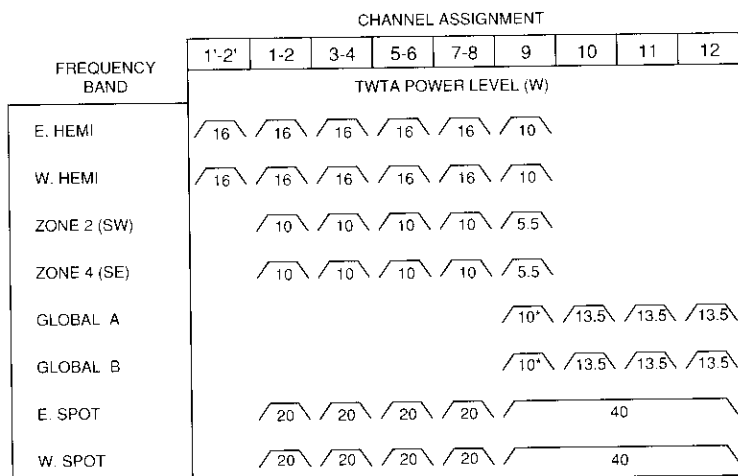


Figure 19. 1.8-W SSPA Block and Level Diagram



\*Shared with hemisphere.

Figure 20. TWTA Power Level Assignment

TABLE 7. TWTA TYPES

MODEL NO.	FREQUENCY BAND (GHz)	NOMINAL POWER		QTY. PER SPACECRAFT	DEPRESSED COLLECTOR	CATHODE TYPE
		LEVEL (W)				
8513H	4	5.5		3	Single	Oxide
8524H	4	10		15	Multiple (3)	Oxide
8525H	4	13.5		9	Multiple (3)	Oxide
8526H	4	16		15	Multiple (3)	Oxide
TH 3593	11	20		16	Multiple (2)	Dispenser
8534HA	11	20		16	Multiple (3)	Oxide
8805HA	11	40		4	Multiple (3)	Dispenser

The slow wave structure provides a nominal 13.5 W of RF power at 6percent over-voltage. The TWT circuit utilizes a 0.03-cm-diameter helix wire with a coil radius between 0.13 and 0.14 cm for all 11.5- to 16.0-W designs. The helix is coated with vapor-deposited copper for efficiency.

The triply depressed multistage collector provides greater optimum efficiency than the singly depressed type. Because the beam distribution to the collectors changes with the drive, thermal dissipation is relatively constant.

Oxygen-free copper electrodes are brazed within a high-alumina cylinder, which in turn is brazed within a grounded vacuum envelope. Ceramic feedthroughs are used for voltage connection to the collectors. The TWTs employ a samarium cobalt magnet stack.

In the gun design, electrical insulation is provided by three ceramic rods between the cathode-focusing electrode and ground base, three between the cathode-focusing electrode and anode 0, and three between anode 1 and ground base.

The delay line obtains high interaction efficiency by using a double tapered helix supported by three isotropic boron nitride rods. The interaction circuit is divided into three sections by means of two pyrolytic graphite attenuators. The taper configuration optimizes beam efficiency, phase shift, and gain flatness. The helix and supporting rods are interference-fitted in the vacuum envelope.

The power supply designs are of three basic types: one for single-collector, 5.5-W, 4-GHz TWTs; a group for the 10-W, 13.5-W, and 16.0-W, 4-GHz TWTs; and a third type for the 11-GHz TWTs. Each power supply operates from the unregulated bus, which may vary from 28.0 to 42.5 V. All power supplies also contain an under-voltage turnoff circuit to protect the TWT and the spacecraft bus.

The TWT power supplies (with the exception of the 5.5-W, 4-GHz supply) are similar to others developed previously for multiple-collector TWTs. The primary differences within this family of power supplies developed for TDMA operation are the scaling of voltage and power (as required by the TWT) and minor differences in telemetry. Each power supply contains a heater control circuit that provides power to a resistive heater on the shelf. To maintain the thermal balance of the spacecraft, the circuit can be turned on when the TWTA is turned off. The heater control circuit is packaged inside the power supply to simplify the wiring harness, since the heater commands are cross-strapped to the power supply commands.

The TWT power supplies use a series-dissipative regulator, followed by a filament inverter and a high-voltage (HV) converter. The series regulator is used for simplicity of design, superior ripple rejection, and maximum efficiency at end-of-life when the unregulated bus voltage is at a minimum. For improved efficiency, the base drive for the pass stage of the series regulator is supplied from a 4-V output of the internal bias oscillator. The power supplies receive separate pulse commands to turn the filament on and to turn the HV converter on and off. The filament warm-up time is determined by ground command. The auxiliary heater control needed to maintain thermal balance can be turned on by a TWTA OFF command, and turned off by an HV ON command. The filament inverter supplies a current-limited, square-wave

voltage to the TWT filament. The HV converter contains a custom HV transformer to provide the individual voltages required by a TWT. Each HV transformer contains a standard tapped anode winding to provide the expected range of voltage. Experience has shown that TWTs often have the same collector and cathode voltages, but seldom have the same anode voltage. The tapped anode winding thus allows some standardization of HV transformers.

#### OUTPUT MULTIPLEXERS

The repeater contains two 5-channel Ku-band spot multiplexers, as well as two 6-channel hemi, four 5-channel zone, and two 4-channel global C-band multiplexers.

Contiguous-band multiplexers [7] use a single manifold to achieve direct serial multiplexing of contiguous channels on a waveguide manifold. Although this design approach leads to a more difficult electrical synthesis of the multiplexers and to more extensive tuning efforts than are required in the conventional approach, the desirable features of lower mass, smaller size, and lower expected insertion losses make it the preferred choice.

The filters for both the zone and global multiplexers are all six-pole, pseudo-elliptic designs constructed using three slot-coupled  $TE_{111}$  dual-mode cylindrical resonators that achieve an unloaded  $Q$  of 10,000.

For both the global multiplexer configuration and the zone multiplexer configuration, the input port of each channel is coaxial, with an isolator at the input of each filter. The output cavity of each filter is slot-coupled to the common manifold, which is constructed in half-height WR-229 silver-plated aluminum waveguide. A waveguide isolator and a single-ridge, dielectrically loaded LPF (used to reject harmonics) are connected to the output of the multiplexers. The channel filters are constructed of thin-wall (15-mil) silver-plated Invar with brazed flanges for low loss, good temperature stability (typically 2 ppm/°C), and reduced weight. Typical performance characteristics of the zone and global multiplexers are summarized in Tables 8 and 9, respectively.

The hemi multiplexer combines five 72-MHz-wide channels and one 36-MHz-wide channel. The channel filters use three physical cylindrical waveguide resonators operating in the dual  $TE_{111}$  mode (*i.e.*, each resonator is used twice) and achieving an unloaded  $Q$  of 10,000. The coupling irises are clamped between flanges, and a coaxial probe coupling is employed at the input. The use of clamped irises and resonator tubes allows for ease of plating and simple interchange of irises if required.

The filters are mounted on a manifold constructed in half-height silver-plated aluminum WR-229 waveguide. Individual harmonic filters are placed

TABLE 8. ZONE OUTPUT MULTIPLEXER PERFORMANCE

PARAMETER	CH 1-2	CH 3-4	CH 5-6	CH 7-8	CH 9
Channel Center Frequency, $f_0$ (MHz)	3,745	3,825	3,905	3,995	4,055
Usable Bandwidth (MHz)	72	72	72	72	36
Passband Insertion Loss at $f_0$ (MHz)	0.9	0.9	0.9	0.9	0.95
Out-of-Band Attenuation (dB)					
Narrowband					
$f_0 \pm 25$ MHz	-	-	-	-	25
$f_0 \pm 30$ MHz	-	-	-	-	30
$f_0 \pm 55$ MHz	25	25	25	25	-
$f_0 \pm 60$ MHz	30	30	30	30	-
Wideband					
5.85-6.425 GHz	60	60	60	60	60
7.4-8.4 GHz	58	58	58	58	58
11.1-12.6 GHz	55	55	55	55	55
14.0-14.5 GHz	55	55	55	55	50
Gain Slope (dB/MHz)					
80% Usable BW	0.035	0.035	0.035	0.035	0.600
90% Usable BW	0.050	0.050	0.050	0.050	0.200
100% Usable BW	0.300	0.300	0.300	0.300	0.800
Group Delay (ns)					
$f_0$	-	-	-	-	-1.5
$f_0 \pm 8$ MHz	-	-	-	-	-1.5/9.7
$f_0 \pm 12$ MHz	-	-	-	-	-1.5/23
$f_0 \pm 16$ MHz	-	-	-	-	1.5/34.8
$f_0 \pm 18$ MHz	-	-	-	-	-1.5/60
$f_0$	-1.5	-1.5	-1.5	-1.5	-
$f_0 \pm 16$ MHz	-1.5/4.7	-1.5/4.7	-1.5/4.7	-1.5/4.7	-
$f_0 \pm 24$ MHz	-1.5/11	-1.5/11	-1.5/11	-1.5/11	-
$f_0 \pm 32$ MHz	1.5/16.8	1.5/16.8	1.5/16.8	1.5/16.8	-
$f_0 \pm 36$ MHz	-1.5/29	-1.5/29	-1.5/29	-1.5/29	-
Group Delay Slope (ns/MHz)					
100% BW	6.1	6.1	6.1	6.1	25.2
VSWR Input and Output of Multiplexer	1.15	1.15	1.15	1.15	1.15

TABLE 9. GLOBAL OUTPUT MULTIPLEXER PERFORMANCE

PARAMETER	CH 9	CH 10	CH 11	CH 12
Channel Center Frequency, $f_0$ (MHz)	4,055	4,055	4,135	4,177.5
Usable Bandwidth (MHz)	36	36	36	41
Passband Insertion Loss at $f_0$ (MHz)	1.0	1.0	1.0	0.95
Out-of-Band Attenuation (dB)				
Narrowband				
$f_0 \pm 25$ MHz	$\geq 25$	$\geq 25$	$\geq 25$	-
$f_0 \pm 30$ MHz	$\geq 30$	$\geq 30$	$\geq 30$	-
$f_0 \pm 22$ MHz	$\geq 13$	-	$\geq 10$	-
$f_0 \pm 28.5$ MHz	-	-	-	$\geq 25$
$f_0 \pm 34$ MHz	-	-	-	$\geq 30$
Wideband				
5.85-6.425 GHz	60	60	60	60
7.4-8.4 GHz	50	50	50	50
11.1-12.6 GHz	55	55	55	55
14.0-14.5 GHz	40	40	40	40
Gain Slope (dB/MHz)				
80% Usable BW	0.055	0.055	0.055	0.055
90% Usable BW	0.200	0.200	0.200	0.200
100% Usable BW	0.800	0.800	0.800	0.800
Group Delay Variation (ns) (min/max)				
$f_0$	-1.5	-1.5	-1.5	-
$f_0 \pm 8$ MHz	-1.5/9	-1.5/9	-1.5/9	-
$f_0 \pm 16$ MHz	-1.5/39	-1.5/39	-1.5/39	-
$f_0 \pm 18$ MHz	-1.5/85	-1.5/85	-	-
$f_0 + 18$ MHz	-1.5/85	-	-	-
$f_0 - 18$ MHz	-1.5/60	-	-	-
$f_0$	-	-	-	-1.5
$f_0 \pm 10$ MHz	-	-	-	-1.5/9
$f_0 \pm 16$ MHz	-	-	-	-1.5/19
$f_0 \pm 18$ MHz	-	-	-	-1.5/35
$f_0 + 20.5$ MHz	-	-	-	-1.5/55
$f_0 - 20.5$ MHz	-	-	-	-1.5/80
Group Delay Slope (ns/MHz)				
$f_0 \pm 8$	<2.5	<2.5	<2.5	-
$f_0 \pm 12$	<6.5	<6.5	<6.5	-
$f_0 \pm 16$	<8.5	<8.5	<8.5	-
$f_0 \pm 18$	<30	<30	<30	-
$f_0 \pm 10$	-	-	-	<1.8
$f_0 \pm 16$	-	-	-	<4.2
$f_0 \pm 18$	-	-	-	<10.8
$f_0 \pm 20.5$	-	-	-	<23
VSWR Input and Output of Multiplexer	1.15	1.15	1.15	1.15

on the inputs of each of six cylindrical waveguide resonators. This difference from the global and zone multiplexer design is necessitated by the higher total peak output power, which makes the output circuit components more susceptible to multipaction. All output components, including the isolator, are realized in half-height WR-229 waveguide. The filter resonators, irises, and other components are constructed of silver-plated thin-wall Invar for thermal stability.

Table 10 summarizes the worst-case computed performance of the hemi multiplexer filters at specific frequency points, taking into account manufacturing tolerances and frequency shift with temperature. For the latter, a qualification-level differential temperature range of  $\pm 27.5^\circ\text{C}$  and an effective thermal coefficient of expansion of a silver-plated Invar resonator of  $2.34/^\circ\text{C}$

TABLE 10. HEMI MULTIPLEXER PERFORMANCE

PARAMETER	72-MHz CHANNELS	36-MHz CHANNELS
Insertion Loss (dB)	0.9	1.0
Loss Variation (dB)		
Across $f_0 \pm 16.2$ MHz	-	0.5
Across $f_0 \pm 18$ MHz	-	1.0
Across $f_0 \pm 32.4$ MHz	0.3	-
Across $f_0 \pm 36.0$ MHz	0.5	-
Gain Slope (dB/MHz)		
Across 80% BW	0.035	0.060
Across 90% BW	0.050	0.200
Across 100% BW	0.300	0.800
Group Delay Variation (ns) (min/max)		
At $f_0 \pm 0$ MHz	-	-1.5/0
At $f_0 \pm 8$ MHz	-	-1.5/10.0
At $f_0 \pm 12$ MHz	-	-1.5/23.0
At $f_0 \pm 16$ MHz	-	-1.5/38.0
At $f_0 \pm 18$ MHz	-	-1.5/68.0
At $f_0 \pm 0$ MHz	-1.5/0	-
At $f_0 \pm 16$ MHz	-1.5/4.7	-
At $f_0 \pm 24$ MHz	-1.5/11	-
At $f_0 \pm 32$ MHz	-1.5/16.8	-
At $f_0 \pm 36$ MHz	-1.5/29	-
Out-of-Band Attenuation (dB)		
At $f_0 \pm 22$ MHz	-	>21
At $f_0 \pm 25$ MHz	-	>25
At $f_0 \pm 30$ MHz	-	>30
At $f_0 \pm 50$ MHz	>25	-
At $f_0 \pm 60$ MHz	>30	-

are assumed. These assumptions yield a maximum frequency shift of 0.26 MHz. The values in the table assume a total worst-case shift of 0.5 MHz.

Typical performance of the spot multiplexer filters is presented in Table 11. A wide guard band separates channels 5-6 and 7-8, thereby allowing a diplexer and a triplexer to form a five-channel contiguous multiplexer. The center frequencies of these two channels are separated by 340 MHz, with 258 MHz between band edges. With such a wide frequency separation, there is negligible interaction when the two channels are combined and share the same short-circuited manifold. Therefore, the diplexer and triplexer can be independently designed and each can be independently tuned prior to being combined on the manifold.

The Ku-band channel filters are pseudo-elliptic, six-section (6, 2) designs with approximately 0.05-dB ripple level, similar to the C-band design. The ratio of bandwidth to channel spacing for the triplexer is the same as for the three lower channels on the global multiplexer; their selectivity is also the same. The guard band between the two channels of the diplexer is wider than that of any of the C-band multiplexers.

Contiguous channel multiplexers require nulling networks in order to achieve a symmetrical response for the lowest and highest frequency channels. These networks are provided internally to the appropriate channel filters, using a symmetrical bridge coupling.

The filters are constructed in cylindrical waveguide using dual  $TE_{113}$  modes. With these modes, only three physical resonators are required, and an unloaded  $Q$  of over 10,000 is achievable. The filters are mounted on a straight manifold constructed of silver-plated WR-75 Invar waveguide. The filter inputs are also WR-75 waveguide. In addition, thermal strips are connected to each input isolator load to ensure that the loader can handle the full reflected TWTA output power (*i.e.*, 20 or 40 W) in the case of an out-of-band carrier.

### Repeater test program

When a piece of spaceflight hardware is complex, so too are the tasks of defining and performing an adequate test program. For the INTELSAT VI payload, the tasks were doubly difficult because the antenna and repeater subsystems were equally complex.

Repeater subsystem testing can be divided into three major areas: shelf integration, end-to-end hardline, and despun compartment thermal vacuum (DCTV) testing. Similar tests are performed at each level to establish a baseline for further testing. The product of nearly 1 year of testing is a completed repeater subsystem whose performance has been verified over in-orbit thermal extremes.

TABLE 11. KU-BAND OUTPUT MULTIPLEXER PERFORMANCE

PARAMETER	CH. 3-4*	CH. 9-12
	ASSUMED $Q = 13,000$	ASSUMED $Q = 13,000$
Insertion Loss at $f_o$ (dB)	0.92	0.72
Loss Variation (dB)		
$f_o + 90\%$ Usable BW	0.45	0.33
$f_o + 100\%$ Usable BW	1.2	0.68
Out-of-Band Attenuation (dB)		
$f_o \pm 50$ MHz	34.5	35.7
$f_o \pm 60$ MHz	42.0	34.3
Gain Slope (dB/MHz)		
$f_o \pm 80\%$ BW	0.05	0.017
$f_o \pm 90\%$ BW	0.09	0.05
$f_o \pm 100\%$ BW	0.55	0.11
Group Delay (ns)		
$f_o \pm 16$ MHz	-1.5/6.0	-
$f_o \pm 24$ MHz	-1.5/12.0	-
$f_o \pm 32$ MHz	-1.5/21.0	-
$f_o \pm 36$ MHz	-1.5/42.0	-
$f_o \pm 32$ MHz	-	-1.5/3.5
$f_o \pm 50$ MHz	-	-1.5/6.0
$f_o \pm 66$ MHz	-	-1.5/10.5
$f_o \pm 75$ MHz	-	-1.5/20
Group Delay Slope (ns/MHz)	<2 $\times$ slope of group delay mask	<2 $\times$ slope of group delay mask
Group Delay Stability (ns)	< $\pm 15\%$ of group delay mask	< $\pm 15\%$ of group delay mask
Group Delay Ripple (ns)	<1.0	<1.0
VSWR: Input and Output, 10.9-11.8 GHz	<1.15	<1.15
Power Rating (W)	<20	<40

\*Channels 5-6 and 7-8 exhibit the same performance.

Shelf integration testing can be divided into two major parts: input section tests and output section tests. The repeater input section includes all hardware from the receive antenna interface to the TWTA or SSPA RF input. Output section testing verifies the remaining repeater hardware from the TWTA or SSPA input to the transmit antenna interface. The main goal of this level of testing is to verify unit installation integrity. The major tests common to both sections include in-band frequency response, out-of-band frequency response,

and group delay. Additional input section tests include receiver frequency responses over the entire 500-MHz operating band. Output section testing includes HPA input power vs output power transfer characteristics. All of these tests primarily verify unit installation integrity. The tests also allow the various transponders to be gain-set end-to-end. Finally, some transponder requirements can only be verified on a section-by-section basis.

At the conclusion of section testing, the input and output sections are connected for end-to-end hardline tests. At this level, the key repeater performance parameters are verified. These include noise figure, power-in to saturation, power output at saturation, total in-band frequency response, total out-of-band frequency response, and total channel group delay. For the INTELSAT VI repeater, hundreds of signal paths are possible (not including the MSMs). With the inclusion of redundant hardware and the MSMs, the paths are in the many thousands. In order to maintain test adequacy while reducing the overall test time to a reasonable length, it was decided to measure a subset of paths and calculate the remainder. Even after significantly reducing the number of possible tests, completion of a flawless set of hardline repeater tests required more than 2 weeks.

Completion of hardline testing was followed by repeater subsystem preparation for DCTV testing, which typically lasted several months, culminating in a nominal 5-week environmental test program. DCTV testing has two main goals. First, to show compliance with specified performance over the expected orbital environment (plus margin), and second, to verify the integrity of the repeater subsystem. DCTV testing consisted of performing nearly all of the tests performed during hardline testing, but in each of four test phases: first ambient, hot thermal vacuum, cold thermal vacuum, and final ambient. The ambient test phases were conducted at ambient temperature and pressure and served as pre- and post-environmental checks. The two thermal vacuum phases were performed at temperatures above and below those predicted for on-station exposure and at simulated vacuum ( $1 \times 10^{-5}$  Torr).

At that point, all 50 transponders (including redundant units) had been thoroughly tested and were deemed ready for antenna integration and full payload testing.

### Conclusions

A detailed description of the INTELSAT VI communications payload has been provided. The performance of key system parameters and of the major units was presented, along with a description of the hardware. The heritage, specifics of the design, and realization of the most important building blocks (receivers, filters, switch networks, and power amplifiers) were also discussed.

The on-board SS-TDMA unit was touched upon only briefly, since it is discussed in more detail in a separate paper. The antenna and repeater test program was also covered, with emphasis on the uniqueness of the procedures and facilities.

The INTELSAT VI communications subsystem represents the state of the art in commercial communications satellite payloads. Four of these payloads are currently in geosynchronous orbit, serving the AOR and IOR with excellent performance.

### Acknowledgments

*The authors would like to thank the INTELSAT and HAC teams for their efforts in compiling the materials contained in this paper. Special thanks are due to M. Burr for her devotion to the almost impossible task of typing and editing the paper based on our handwritten notes from various continents of the world. Thanks are also due to many unnamed colleagues at COMSAT Laboratories, INTELSAT, and HAC who contributed much to the research, development, and design of the new features of the INTELSAT VI payload. Without the help of these people, we could not have provided the detailed information necessary to present the INTELSAT VI communications subsystem performance and design.*

### References

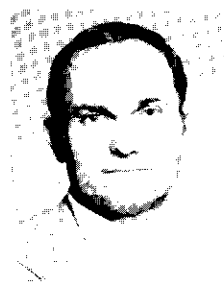
- [1] A. Ghais *et al.*, "Summary of INTELSAT VI Communications Performance Specifications," *COMSAT Technical Review*, Vol. 12, No. 2, Fall 1982, pp. 413-429.
- [2] L. Dest *et al.*, "INTELSAT VI—An In-Orbit Assessment," AIAA 13th International Communication Satellite Systems Conference, Los Angeles, CA, March 1990. AIAA Paper No. 90-0899.
- [3] L. I. Slafer and V. L. Seidenstucker, "Attitude and Payload Control System for INTELSAT VI," *COMSAT Technical Review*, Vol. 21, No. 1, Spring 1991, pp. 57-100 (this issue).
- [4] B. A. Pontano, A. I. Zaghoul, and C. E. Mahle, "INTELSAT VI Communications Payload Performance Specifications," *COMSAT Technical Review*, Vol. 20, No. 2, Fall 1990, pp. 271-308.
- [5] R. R. Persinger *et al.*, "The INTELSAT VI Antenna System," *COMSAT Technical Review*, Vol. 21, No. 1, Spring 1991, pp. 149-189 (this issue).
- [6] R. K. Gupta *et al.*, "INTELSAT VI On-Board SS-TDMA Subsystem Design and Performance," *COMSAT Technical Review*, Vol. 21, No. 1, Spring 1991, pp. 191-225 (this issue).
- [7] M. H. Chen, F. Assal, and C. Mahle, "A Contiguous Band Multiplexer," *COMSAT Technical Review*, Vol. 6, No. 2, Fall 1976, pp. 285-307.

## Appendix

A large and experienced team of international partners was assembled to join the HAC team in designing and manufacturing the INTELSAT VI communications payload. Table A-1 lists the major participants in the payload program.

TABLE A-1. INTERNATIONAL PARTICIPATION IN THE INTELSAT VI PAYLOAD PROGRAM

COMPONENT	COMPANY	COUNTRY
<b>Antennas</b>		
Ku-Band Spot Antenna	Selenia	Italy
C-Band Global Antenna	Selenia	Italy
C-Band Hemi/Zone Reflectors	BAe	U. K.
Ku-Band Reflectors	BAe	U. K.
<b>Repeater</b>		
C-Band Receivers	T-CSF/ALCATEL	France
	SPAR	Canada
Ku-Band Receivers	T-CSF/ALCATEL	France
	NEC	Japan
Up-Converters and MLOs	NEC	Japan
C-Band Driver Amplifiers	SPAR	Canada
Ku-Band Driver Amplifiers	NEC	Japan
SSPAs	NEC	Japan
Ku-Band TWTs	T-CSF	France
EPC and TWTA Integration	SPAR	Canada
C-Band Output Multiplexers	T-CSF/ALCATEL	France
Ku-Band Output Multiplexers	COMDEV	Canada

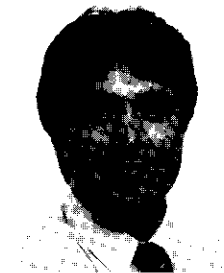


George N. Horvai received his Electrical Engineering Diploma in communications, and his Specialist Diploma in control theory, from the Technical University of Budapest. He is currently serving at INTELSAT in the Spacecraft Engineering Department, managing the communications payloads for the INTELSAT VI and VII-A satellites. He is also involved in defining the payload concepts for INTELSAT's future generation of satellites. Previously, he has held positions at TELESAT CANADA, at the Communications Research Center in Canada, and at the Telecommunications Research Institute in Hungary. He is a Senior Member of IEEE.

Lou A. Argyle received a BSEE in 1976 and an MSEE in 1977, both from the University of Illinois. He is currently with INTELSAT as Supervisor of the INTELSAT VII Payload Engineering Group, and was previously Manager of the INTELSAT VI Repeater Engineering Group. His responsibilities include on-site technical evaluation and test monitoring of the communications hardware and subsystem during unit design, development, and test, and during spacecraft integration and test. Prior to joining INTELSAT, he had a similar role at COMSAT as Manager of the INTELSAT VI Communications Subsystem Group.



From 1977 to 1983, Mr. Argyle was a Member of the Technical Staff at Bell Telephone Laboratories' Satellite Transmission Laboratory, where he was responsible for TELSTAR 3 and Iranian satellite system definition and specification, and for on-site technical monitoring during TELSTAR 3 procurement.



Tim L. Ellena received a BSEE from California State University, Fresno, in 1981, and an MSEE from the California Institute of Technology in 1982. He has worked as a Communications Systems Engineer for Hughes Aircraft Company, Space and Communications Group, since 1982, and is currently working on advanced programs. Prior to his present assignment, he worked on the Galileo deep space mission, the INTELSAT VI spacecraft program, and development of the Hughes direct broadcast satellite system. As Payload Systems Engineering Manager for INTELSAT VI, he was responsible for testing the complex payloads at Hughes and the launch site, as well as providing in-orbit test support.



Randy Persinger received the B.S.E.E and M.S.E.E. degrees from Virginia Polytechnic Institute and State University, in 1976 and 1978, respectively. He is currently Manager of COMSAT's RF Systems Group, Space Systems Engineering, at COMSAT General in El Segundo, California. While his area of expertise is satellite antenna subsystems, his current responsibilities include the communications payload implementation monitoring of several different types of satellites. Mr. Persinger has worked on the INTELSAT VI program from 1979—when initial feasibility concepts were initiated—to the present, and continues

to support in-orbit testing. Prior to joining COMSAT Laboratories in 1979, he worked for the Antenna Department at Hughes Aircraft Company.

Christoph E. Mahle received the Dipl. Ing. and Dr. sc. techn. degrees from the Swiss Federal Institute of Technology in 1961 and 1966, respectively. He joined COMSAT Laboratories in 1968 as a Member of the Technical Staff in the Transponder Department. In 1983, he was appointed Executive Director of the Microwave Technology Division, where he directed R&D in areas such as high-technology microwave circuits for satellites and earth stations, MMICs, satellite transponder performance, antennas, microwave systems, optical communications, and wave propagation. He also served as Acting Director of the newly formed Micro Electronics Division, which was set up to combine COMSAT's efforts in analog and digital GaAs integrated circuits.

Dr. Mahle is currently Executive Director of the Satellite Technologies Division at COMSAT Laboratories, directing R&D in such areas as spacecraft bus technologies, microwave circuits for satellites and earth stations, analysis and verification of satellite transponder performance, microwave systems, and radio wave propagation. He designed and evaluated communications transponders for the INTELSAT IV, IV-A, and COMSTAR programs, and was responsible for the design, development, and testing of the transponder orbited on ATS-6 as part of the COMSAT Propagation Experiment. In addition, he has advanced the state of the art of automated satellite in-orbit measurements. He is a Fellow of IEEE, has published numerous papers, and has been awarded several U.S. patents.



Index: antennas, beacon tracking, communication satellites, frequency reuse, INTELSAT

## The INTELSAT VI antenna system

R. R. PERSINGER, S. O. LANE, M. F. CAULFIELD, AND A. I. ZAGHLOUL

(Manuscript received January 20, 1991)

### Abstract

This paper describes the antenna system design, implementation, and measurement program for the INTELSAT VI spacecraft, which is the largest commercial communications satellite currently in orbit. Following a description of the complete antenna farm, detailed design tradeoffs and construction techniques for the hemi/zone antennas are presented. The discussion focuses on the interaction of the stringent spatial isolation, cross-polarization isolation, and pointing requirements. The extensive INTELSAT VI antenna measurement program is also described, including alignment, feed array measurement in a near-field chamber over temperature, reflector distortion over temperature, far-field range testing, system-level and spacecraft measurement in a planar near-field chamber, and in-orbit measurements.

### Introduction

The INTELSAT VI satellites designed and built for INTELSAT by the Hughes Aircraft Company (HAC), Space and Communications Group, are the largest and most complex commercial satellites launched to date. The stringent spatial and cross-polarization performance requirements of the hemi/zone antennas [1], which provide sixfold frequency reuse over three different ocean regions, were key design drivers for the antenna farm and the spacecraft. With the additional requirement for two fully steerable Ku-band spot beam antennas, global communications, and telemetry and command coverage, the INTELSAT VI antenna farm and associated structure accounted for 50 percent of the payload mass.

Because of a conflict between the limited launch vehicle envelopes and the large hemi/zone reflector sizes (and associated focal lengths) required to achieve the required spatial isolation, 10 separate antenna deployments are necessary for the satellite to become fully operational in orbit. This paper provides insight into some of the key design tradeoffs, as well as the implementation and measurement challenges, of the INTELSAT VI antenna system. Special attention is given to the complex hemi/zone transmit (4-GHz) and receive (6-GHz) antennas. The remaining antennas are briefly described for completeness.

Prior to a discussion of specific design tradeoffs, each of the INTELSAT VI antennas is described to familiarize the reader with key design parameters. Geometric parameter selection for the hemi/zone antenna is presented, followed by a more in-depth discussion of such key antenna components as the feed horn/polarizer assembly, the zone switch, and the squareax networks [2]. The development plan, implementation, assembly process, and alignment sequence for the hemi/zone antennas are then discussed. Finally, the various aspects of the extensive INTELSAT VI antenna test program are explored, including far-field, near-field, and in-orbit antenna measurement.

### Antenna farm description

The INTELSAT VI antenna farm consists of 11 separate antennas. The two largest are the transmit and receive C-Band (4/6-GHz) hemi/zone parabolic reflector systems. East and west fully steerable spot beam antennas, each having transmit and receive capability, provide Ku-band (11/14-GHz) service. A cluster of global antennas consisting of transmit and receive C-band dual circularly polarized global horn antennas, two C-band telemetry horns, and a Ku-band beacon horn is mounted adjacent to the west spot antenna. An omni-directional biconical telemetry antenna and an omni-directional command antenna provide coverage for on-station and transfer orbit operations. The hemi/zone antennas offer sixfold frequency reuse by providing four spatially isolated zone beams, in conjunction with two spatially isolated hemispheric beams that utilize the orthogonal circular polarization of the zone beams. One of three sets of zone beams can be selected by in-orbit switching to provide specialized coverage for the Atlantic (AOR), Indian (IOR), and Pacific (POR) ocean regions. Because of stringent spatial isolation requirements, both hemi/zone antennas incorporate an RF beacon tracker subsystem (BTS) that provides closed-loop pointing.

Figure 1 illustrates the INTELSAT VI antenna farm in the stowed and deployed configurations. Figure 2 shows the communications antenna coverages for the three ocean regions, as well as for the global and Ku-band spot beam

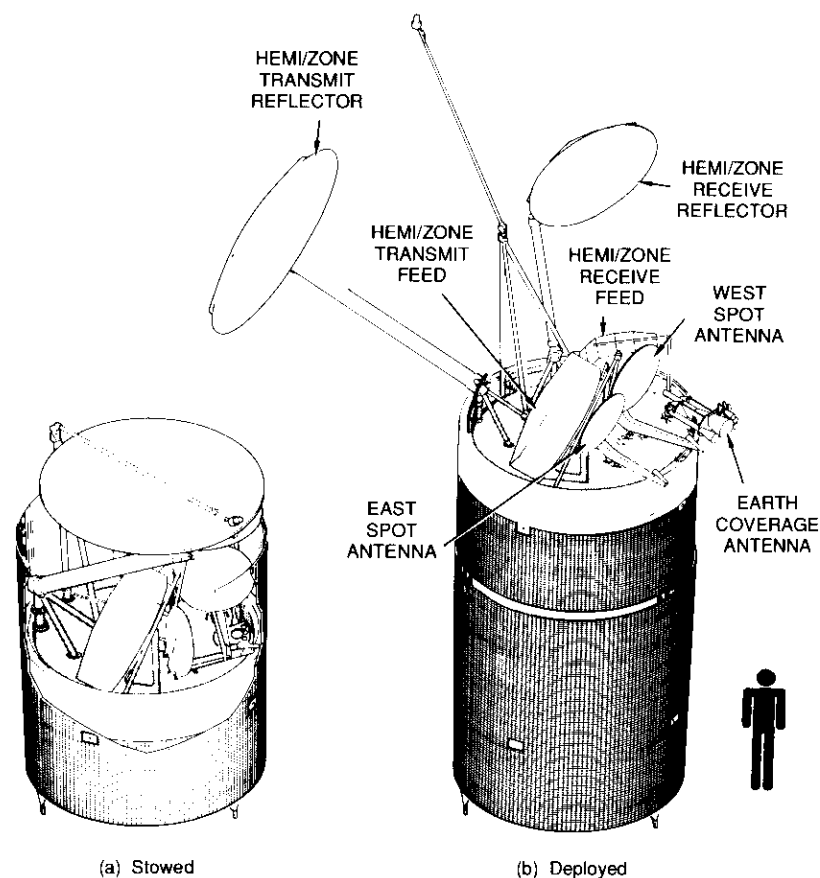


Figure 1. INTELSAT VI Antenna Farm Configuration

antennas. The hemi/zone BTS coverage allows a beacon station to operate in a limited region within the zone 1 (or northwest) area of each ocean region. One 6.175-GHz up-link beacon provides the RF source for both the transmit and receive hemi/zone reflectors. The edge-of-coverage data shown are for the INTELSAT VI (F2) spacecraft and were measured in the HAC planar near-field chamber. The F2 satellite is currently in service at 335.5°E longitude in the AOR.

Tables 1 and 2 summarize the dimensions of the INTELSAT VI reflector and horn antennas. Table 3 lists the measured peak gain of each of the INTELSAT VI (F5) transmit and receive communications antennas.

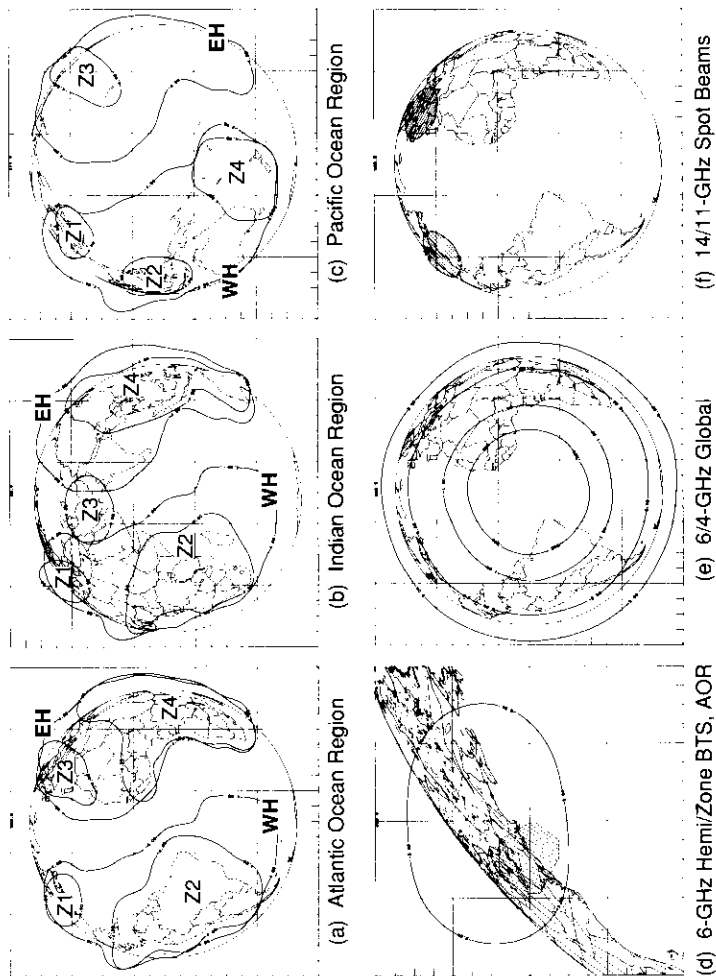


Figure 2. INTELSAT VI Beam Coverages

TABLE 1. ANTENNA DIMENSIONS: REFLECTOR

ANTENNA	DIAMETER (m)	OFFSET FOCAL LENGTH (m)	OFFSET HEIGHT (m)	SYMMETRY AXIS (deg)
4-GHz Hemi/Zone Transmit	3.2	4.19	1.68	45.0
6-GHz Hemi/Zone Receive	2.0	2.62	1.05	-45.0
14/11-GHz E. Spot	1.0	1.00	0.04	22.9
14/11-GHz W. Spot	1.0	1.00	0.04	-37.0

TABLE 2. ANTENNA DIMENSIONS: HORN

ANTENNA	APERTURE DIAMETER (m)	LENGTH (m)
4-GHz Communications, Global	0.267	1.259
6-GHz Communications, Global	0.178	0.772
4-GHz Global Telemetry	0.126	0.375
11-GHz Beacon	0.107	0.343

### Hemi/zone antennas

The transmit (4-GHz) hemi/zone antenna is a double-offset parabolic reflector with a projected aperture of 3.2 m, which is illuminated by a feed array of 146 Potter horns. To achieve the 27-dB spatial isolation requirement for beams that are only 1.8° apart, a 3.2-m aperture and a focal-length-to-diameter ratio,  $f/d$ , of 1.3 were required. The 1.55-wavelength-diameter Potter horn and associated four-probe polarizer were designed to minimize the length of the feed element while ensuring a far-field, circular cross-polarized isolation of 27 dB. Both the zone (left-hand circularly polarized [LHCP]) and hemi (right-hand circularly polarized [RHCP]) beams are obtained simultaneously by exciting both ports of the four-probe polarizer. The relatively large-diameter feed horn is consistent with the long focal length and provides good component beam crossover for beam-shaping efficiency. Another benefit of the larger horn size is that existing theoretical models of the Potter horn were very accurate and led to excellent agreement between computed and measured antenna performance 35 dB below the beam peak. Thus, no far-field range

TABLE 3. INTELSAT VI (F5) ANTENNA PEAK GAIN MEASUREMENTS

COVERAGE REGIONS	TRANSMIT GAIN (dBi)	RECEIVE GAIN (dBi)
<b>AOR</b>		
Zone 1	34.1	32.9
Zone 2	26.3	26.1
Zone 3	32.1	31.1
Zone 4	26.2	25.4
<b>IOR</b>		
Zone 1	33.6	33.1
Zone 2	27.0	26.2
Zone 3	32.1	30.9
Zone 4	27.4	26.3
<b>POR</b>		
Zone 1	34.0	32.5
Zone 2	26.8	25.6
Zone 3	31.9	29.8
Zone 4	26.9	26.6
<b>E. Hemi</b>	24.6	24.7
<b>W. Hemi</b>	24.0	24.1
<b>E. and W. Spot</b>	37.3	37.2
<b>Communications, Global</b>	19.3	19.3

adjustment of the network coefficients was required, resulting in significant cost savings.

The hemi/zone feed networks utilized HAC-developed squareax technology for power distribution. Figure 3 illustrates the network implementation. Four separate networks (three zones and a hemi) feed the array of Potter horns. Depending on the ocean region desired, a layer of switches driven by a switch drive plate connects the required zone network to the feed horns. The four squareax networks and the switching layer are stacked to obtain a highly compact feed network.

The receive (6-GHz) hemi/zone antenna is nearly a scale model of the transmit antenna, except that the double-offset, 2.0-m receive reflector is offset to the northwest at a 45° angle instead of to the northeast, as shown in Figure 1. This greatly reduces RF scattering between the two antenna subsystems.

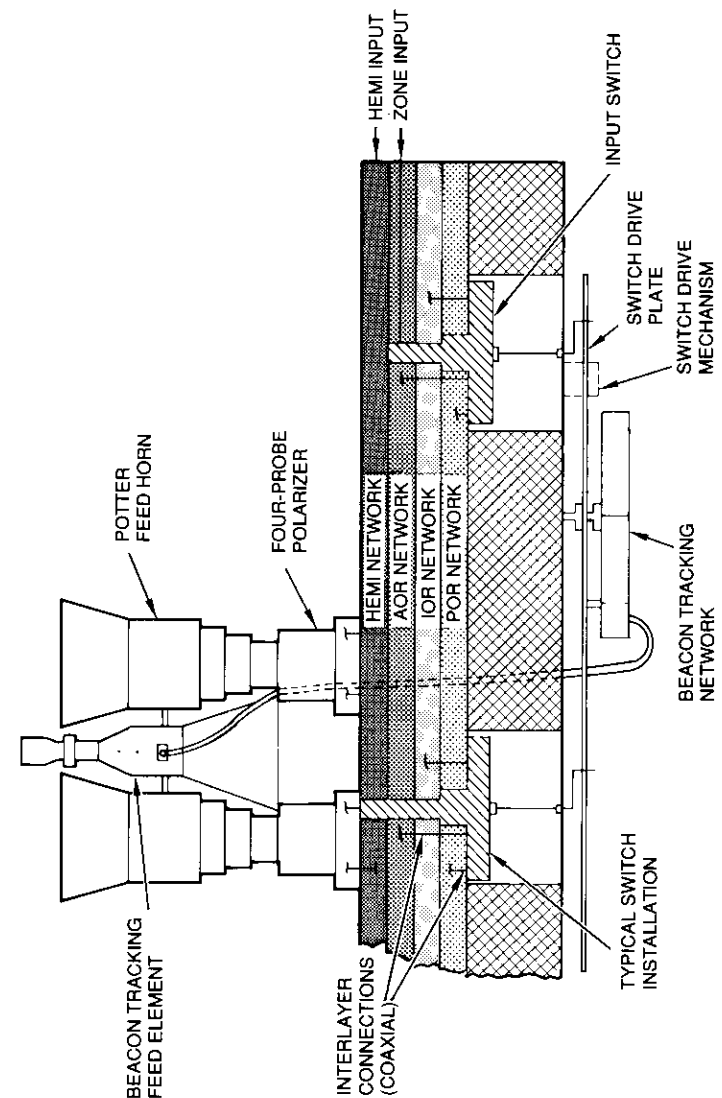


Figure 3. Hemi/Zone Feed Network Implementation

### **Beacon tracker subsystem**

The INTELSAT VI BTS provides closed-loop pointing adjustment for both the transmit and receive hemi/zone reflectors. Only a single 6.175-GHz LHCP up-link beacon is required. The receive BTS is a simple, four-element, linearly polarized monopulse system with the BTS feed elements located in the spaces between the zone 1 communications horns. The associated BTS beam-forming network produces the sum, delta-azimuth, and delta-elevation beams. Proper amplitude shimming and phasing of the beams, combined with a ferrite modulator assembly (FMA), results in AM modulation that is proportional to the beam-pointing error. The AM modulation is detected by a beacon tracking receiver (BTR) whose output is a DC voltage proportional to the amount of AM modulation. The BTS in closed-loop mode drives the transmit and receive reflectors independently in azimuth and elevation until zero BTR output voltage is achieved.

The BTS removes initial deployment errors, as well as thermally induced errors and spacecraft orbital and attitude pointing errors. The BTS is also designed to allow for an arbitrary beacon station location within an operating region, as shown in Figure 2d. During calibration, the bias voltages required to drive the BTR output to zero are determined for each point of interest in the operational region. During operation, the BTR then sums the detected error voltage (representing the current pointing) and the desired bias voltage (representing the desired pointing) and moves the reflectors until a zero voltage condition is obtained.

The transmit reflector BTS is very similar to the receive system except that eight feed elements are used. The elements are tapered for placement between the transmit Potter horns, as shown in Figure 3. Eight elements were required because of the larger element-to-element spacing necessary when a 6-GHz BTS antenna array is placed into a 4-GHz Potter horn array.

### **Ku-band spot beam antennas**

The 14/11-GHz receive/transmit east and west steerable spot beam antennas comprise two separate offset reflectors, each fed by a single dual-polarized/dual-frequency corrugated feed horn. The polarization is linear, with the east and west spot beam antennas having orthogonal polarization. The transmit polarization is also orthogonal to the receive polarization. Each antenna produces a  $1.64^\circ \times 3.04^\circ$  3-dB elliptical footprint. The east spot beam is oriented  $23^\circ$  from horizontal and the west spot beam is oriented  $37^\circ$  from horizontal, as shown in Figure 2f.

The east and west spot beam antennas each have a 1.0-m offset reflector whose surface is shaped to achieve optimum performance. The focal length is 1.0 m for both antennas. The graphite reflector and feed horn of each antenna are rigidly connected by a graphite support structure. The entire antenna assembly is connected to an antenna positioning mechanism, which is used for both beam steering and deployment from the stowed position. Because the reflector and feed horn maintain a fixed relationship, no scan loss occurs as the beam is steered over the full earth disk.

### **Global coverage antennas**

Two dielectric sleeve-loaded conical horns provide transmit (4-GHz) and receive (6-GHz) dual circularly polarized global communications coverage. Each antenna is fed by a polarizer and orthomode-tee combination to generate both senses of circular polarization. To avoid interference, the global communications band is separated by frequency from the hemi/zone communications band. One channel (channel 9) can be used for either global or hemi/zone coverage.

The transmit and receive global communications antennas are mounted in a cluster with the global telemetry and beacon horns. The mounting structure allows for a  $\pm 2.0^\circ$  azimuth steering capability to optimize performance based on the chosen hemi/zone platform pitch bias.

### **Telemetry and command omni antennas**

Transfer orbit telemetry (4-GHz) and command (6-GHz) coverage is provided by two biconical antennas collocated at the end of a deployable boom, as shown in Figure 1. The boom is deployed in two steps. Initial deployment occurs during transfer orbit and orients the antennas parallel to the spin axis of the spacecraft. Another deployment occurs on-station to move the antennas to their final position. Each biconical antenna provides dual linear polarization and is connected to two different command receivers or telemetry transmitters for redundancy.

### **Hemi/zone antenna geometric parameter selection**

The INTELSAT VI hemi/zone communications antennas offered the greatest antenna design challenges on the spacecraft. The key design driver for the hemi/zone antennas was the 27-dB spatial isolation requirement for beams that were spaced only  $1.8^\circ$  apart, as viewed from the spacecraft. In particular, the zone 1 and zone 3 beams of the IOR, and the zone 3 and zone 4 beams of

the AOR (shown in Figure 2) were difficult to realize. These beams also required a high degree of beam shaping to optimize the available antenna gain over the desired regions. Previously, on the INTELSAT IV-A and V series of satellites, spatial isolation was dictated only by the relatively large spacing of the hemispheric beams. For such a complex multibeam antenna design, an orderly and efficient design procedure [3] was used to determine reflector size, offset height, focal length, feed element size, feed array size, and the amplitude and phase of the feed elements.

The first design problem involved the conflict of limited space on-board the spacecraft vs the desire to have large reflectors (with their associated focal lengths and feed arrays) to meet the spatial isolation requirements. To achieve 27-dB spatial isolation, the reflector diameter,  $D$ , should ideally be chosen to realize a 3-dB component beamwidth smaller than the minimum beam edge-to-edge spacing,  $\sigma$ . The diameter of the reflector is inversely proportional to the 3-dB component beamwidth, and smaller beam-to-beam separations require larger-diameter reflectors. The following expression ensures that the minimum angular beam-to-beam spacing is larger than the 3-dB component beamwidth realized by a beam at the focus of a reflector with diameter  $D$ :

$$D > 62 \lambda / \sigma \quad (1)$$

Ideally, the reflector diameter should be 10 to 20 percent larger. For a frequency of 3.7 GHz and a beam-to-beam separation of  $1.8^\circ$ , the suggested value for  $D$  is 2.8 m. A transmit reflector projected aperture of 3.2 m (a 14-percent increase) was the largest solid circular aperture that would fit within the launch vehicle envelope. Initial feasibility studies had considered aperture sizes of 4.0 to 6.0 m for the transmit hemi/zone antenna. Fortunately, this size class offered no significant RF performance advantage when compared to the 3.2-m reflector, and mesh unfurlable or foldable solid reflectors were not required, thus decreasing complexity and cost.

The next and more complicated design tradeoff was the selection of the focal-length-to-aperture-diameter ratio,  $f/d$ . Longer focal lengths minimize component beam distortion and scan loss when the component beam is scanned away from the reflector focus. This was very important in the INTELSAT VI hemi/zone antenna because the 3.2-m reflector produced a 3-dB beamwidth of about  $1.6^\circ$ , requiring up to seven beamwidths of scan for a beam on the edge of the earth. Beam-shaping analysis indicated that the optimum transmit  $f/d$  was 1.3, which corresponded to a focal length of 4.16 m; however, the conflict between focal length and available space had to be resolved. The final solution was to locate the feed arrays for the transmit and receive antennas near

the center of the despun shelf and use a two-stage deployment for the transmit reflector, as shown in Figure 1. Initially, the reflector is folded upside down on top of the receive reflector. The first stage of deployment deploys the transmit reflector  $120^\circ$  in front of the satellite. The second stage deploys the reflector and the reflector support boom to their final location. The smaller receive reflector requires only a simple single-stage deployment. Antenna positioning mechanisms in the azimuth and elevation directions remove initial deployment error, as well as any beam squint caused by in-orbit thermal distortion.

The feed array size, number of horns required, and reflector offset height are also significantly affected by the choice of reflector focal length. The offset parabolic reflector 3.2-m projected aperture is taken from the "parent" paraboloid such that no portion of the feed array blocks the RF energy leaving the reflector. The longer the focal length, the bigger the feed array becomes, and the larger the offset height and parent paraboloid diameter ( $D_p$ ) required. The parameter  $f/D_p$  is an indirect measure of the scan performance of a reflector—with better scan performance achieved for increasing  $f/D_p$ . Figure 4 shows the relationship of  $f/D_p$  (offset height) and feed array size (normalized to reflector diameter) as a function of  $f/d$  for a projected aperture of 3.2 m. Note that the feed array becomes quite large for long focal lengths, but scan

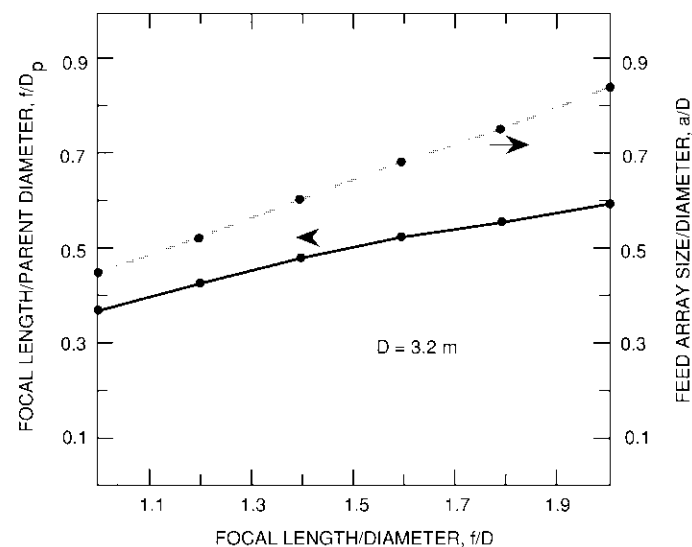


Figure 4. Parent Paraboloid Diameter and Feed Array Size vs Focal Length

performance does not significantly improve. The INTELSAT VI transmit hemi/zone feed array is roughly  $1.9 \times 1.4$  m, or about 50 percent of the reflector diameter. The area of the feed array is about 30 percent of the reflector. The receive feed array is a size-scaled version of the transmit array, but with opposite polarization. Also, the feed networks are not identical and were optimized independently.

The final geometric parameter to be selected was the feed horn aperture diameter. A circular aperture was chosen to optimize cross-polarization performance. The diameter of the feed horn is related to the focal length and the desired component beam crossover level, which affects beam-shaping and sidelobe suppression efficiencies. It was desired to have a feed horn diameter greater than 1.4 wavelengths so that a multimode, or Potter, horn could be used. The Potter horn has the properties of low cross-polarization and negligible mutual coupling between horns, both of which are crucial in achieving the 27-dB cross-polarization isolation. In addition, the lack of mutual coupling allows very accurate prediction of the antenna patterns using physical optics. Agreement between predicted and measured patterns was excellent, even at levels -35 dB from the peaks of the beams. Using a reflector  $f/d$  of 1.3 and an optimum component beam crossover level of 3.5 to 4.0 dB resulted in a feed horn aperture of 1.55 wavelengths—satisfying the Potter horn constraint. Although a somewhat more complex antenna deployment system was required for the transmit hemi/zone reflector, the selection of a longer focal length and a larger feed horn aperture resulted in excellent cross-polarization isolation, nondistorted component beams, excellent beam shaping, excellent sidelobe suppression efficiency, and spatial isolation superior to that achievable using smaller feed horns.

After the geometric parameters of the hemi/zone antenna subsystem had been defined, extensive computer analysis was performed to optimize the gain and spatial isolation of each hemispheric and zone beam. First, the 146 component beams were generated using physical optics programs. Optimization algorithms were then used to yield the correct set of feed element amplitude and phase excitations. Realistic amplitude and phase tolerances were included during beam sensitivity analysis, and a spatial isolation implementation margin of 5 dB was required before a given set of coefficients was selected.

During layout of the complete INTELSAT VI antenna farm, further geometric constraints were enforced to ensure the absence of RF blockage and to minimize RF scattering. The transmit and receive hemi/zone reflectors were doubly offset, with the axis of symmetry being in the plane  $45^\circ$  from vertical so that the hemi/zone feed arrays were decoupled from each other. The Ku-band spot antennas and global antennas all had a minimum clearance cone of  $38^\circ$  and

were mounted on the forward edge of the despun shelf to minimize interaction with the hemi/zone antennas. Finally, the telemetry and command bicone antennas were deployed using a two-stage sequence. Their in-orbit location above and behind the hemi/zone reflectors was chosen to eliminate RF scattering. The first stage omni deployment provided transfer orbit operation only.

### ***Hemi/zone antenna development hardware***

The greatest challenge in developing the hemi/zone antenna was to accomplish the actual hardware implementation and measurement of the paper design described above, in a manner that was cost effective. The physical size, tremendous number of parts, and multiple subcontractors posed significant new challenges with respect to previous satellite antenna hardware projects. The basic soundness of the development plan, from paper design to flight hardware, was crucial in achieving the desired performance.

The developmental hardware consisted of a partial receive breadboard antenna and a complete protoflight antenna, which was built to flight standards but was never intended to be used as flight hardware. The breadboard antenna was constructed very early in the program to demonstrate that the required spatial isolation between the zone 1 and zone 3 IOR beams could be met. The breadboard did not have flight-like polarizers or beam-forming networks.

The protoflight antenna then became the focus of detailed tradeoffs to realize the desired performance with flight hardware. Attention was divided into two basic areas: the mechanical performance of the large reflectors and associated deployment booms, and the construction of the rather large and complicated feed arrays. All protoflight testing was performed over the qualification temperature ranges and vibration levels.

### ***Key hemi/zone antenna components***

Once the basic geometric parameters of the hemi/zone antennas were chosen, the detailed design of the key antenna components was begun. This section discusses the design and manufacture of the Potter feed horn, polarizers, squareax feed networks, zone reconfigurability switches, BTS horns, and parabolic reflectors.

#### **Feed horns**

The feed horn used in the hemi/zone antenna is a dual-mode circular Potter horn which employs the fundamental  $TE_{11}$  mode and a higher order  $TM_{11}$

mode. Combining the two modes with the proper amplitude and phase equalizes the E- and H-plane far-field patterns, resulting in excellent polarization purity when circular polarization is used. The aperture diameter of 1.55 wavelengths results in less mutual coupling between adjacent horns, providing less degradation of the axial ratio and better agreement between the theoretically predicted and measured far-field antenna patterns.

The cross sections shown in Figure 5 illustrate the overall dimensions of the transmit and receive dual-mode feed horns. The initial step discontinuities are simply a four-step waveguide quarter-wave transformer from the polarizer waveguide to the horn input waveguide. The final step discontinuity excites the  $TM_{11}$  mode. The length of the horn from the final step discontinuity to the aperture is designed to provide the correct phase between the two modes over the required 11.5-percent transmit and 7.5-percent receive bandwidths.

Each horn was machined from a solid block of aluminum using a numerically controlled lathe. Nominal wall thicknesses varied from 0.254 mm at the aperture, to 0.508 mm in the stepped areas, to 2.54-mm-thick flanges. The transmit horn weighed 0.1 kg.

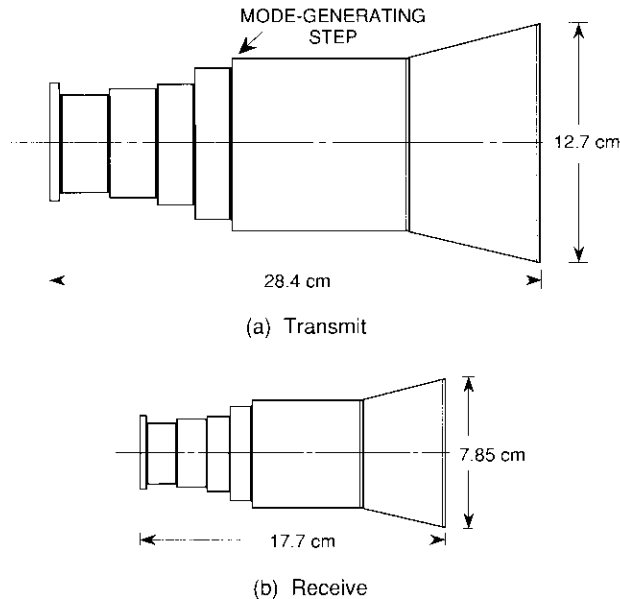


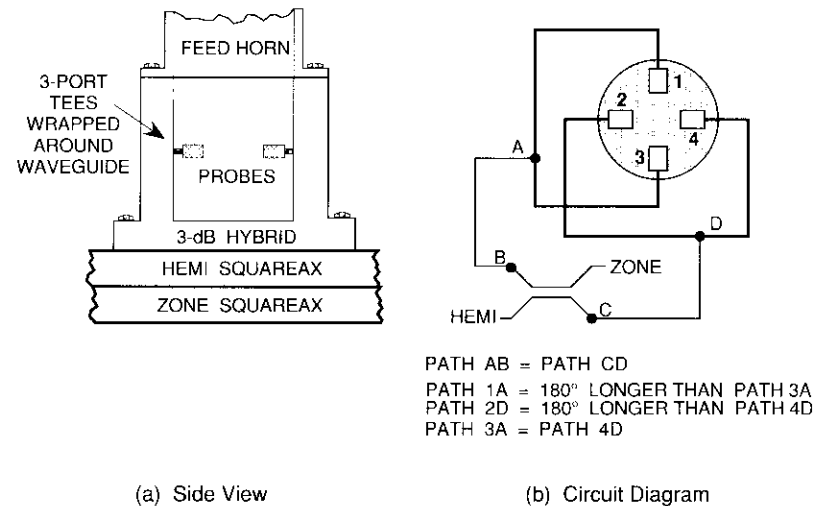
Figure 5. Hemi/Zone Dual-Mode Feed Horns

**Polarizers**

Low axial ratio dual circular polarization was generated by a compact four-probe aluminum polarizer located at the throat of each feed horn. Each polarizer had two inputs, one for each sense of circular polarization. Figure 6 shows a side view and electrical circuit diagram of the four-probe polarizer.

Circular polarization is generated by exciting the four probes equally in amplitude, and with the phase progression appropriate for the sense of circular polarization desired. This is accomplished by a small squareax network built into the polarizer which has two inputs and four outputs, as shown in Figure 6. The two inputs of the polarizer are connected to the hemi and zone squareax feed networks, and the four outputs are attached to the four spatially orthogonal launching probes. The 3-dB quadrature hybrid and 3-dB tees generate the four equal-amplitude probe excitations. The 90° phase shift of the hybrid provides the required phase progression. Opposite phase progressions are obtained for the two input ports, resulting in opposite senses of polarization for the hemispheric and zone beams.

The four-probe polarizer is capable of generating very pure circular polarization over 15-percent bandwidths. A typical transmit polarizer achieved an



(a) Side View

(b) Circuit Diagram

PATH AB = PATH CD  
 PATH 1A = 180° LONGER THAN PATH 3A  
 PATH 2D = 180° LONGER THAN PATH 4D  
 PATH 3A = PATH 4D

Figure 6. Four-Probe Polarizer

axial ratio of less than 0.2 dB (-38 dB cross polarization) over the 11.5-percent transmit band. The achievable cross-polarization level of the polarizer is the sum of the port-to-port isolation (including aperture mismatch) and the return loss at the input ports. The flight feed network output port return losses were tuned to better than 18 dB, for a total on-axis axial ratio performance of better than 0.4 dB (-32 dB cross-polarization). A completed transmit polarizer, with feed horn attached, is shown in Figure 7. Extensive weight removal and thin-wall construction techniques were employed to minimize the mass of the polarizer.

#### Feed networks

The hemi and zone feed networks employed 50- $\Omega$ /square coaxial (squareax) transmission line technology, first developed by HAC for use on INTELSAT IV-A, to distribute power at the proper amplitude and phase to the feed horns.

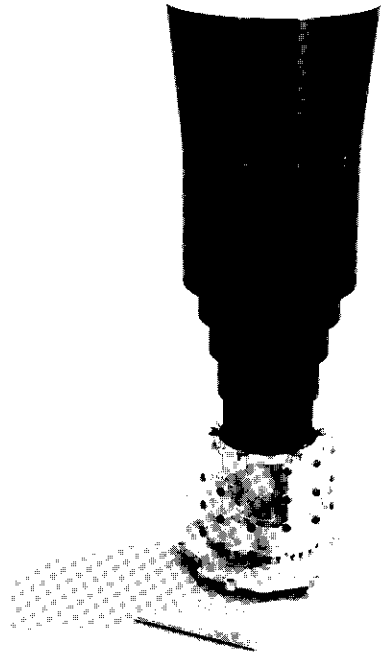


Figure 7. *Transmit Horn and Polarizer*

This transmission line combines the geometry and design features of stripline with the performance features of waveguide. The basic circuit element for power division is the hybrid directional coupler. Phasing between outputs is determined by the lengths of the squareax lines.

Each of the 12 zone beams (four beams in each of three ocean regions) and two hemispheric beams has its own feed network. One or more of these feed networks are grouped into nine modules of a size convenient for machining. Computer-aided design/computer-aided manufacturing (CAD/CAM) facilities were used extensively in both the electrical and mechanical design layouts of the squareax networks. Electrically, hybrid coupling values and line lengths were optimized for best response over the frequency band. Mechanically, interferences were eliminated, extensive weight reduction was performed, and a "paperless" transfer of information between design and manufacturing was implemented. The end result was a repeatable, accurate, and minimum-cost design. A typical CAD/CAM layout is shown in Figure 8.

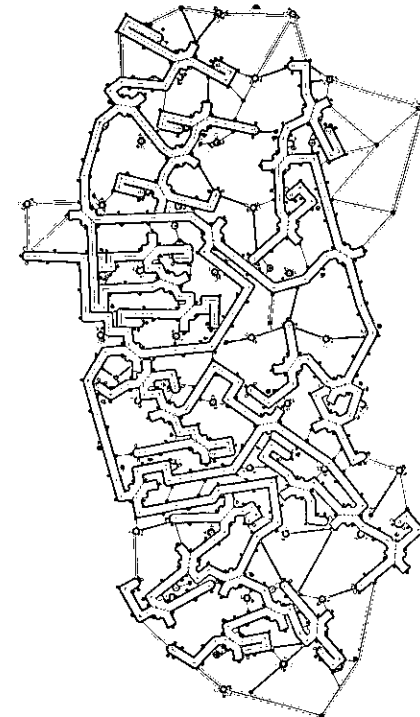


Figure 8. *CAD/CAM Layout of Transmit IOR Zone 4 Squareax*

The squareax modules were placed in a precision test fixture, and the output powers and phases were measured. Typical performance achieved for an cast hemi transmit feed network with one input and 64 outputs was 0.45-dB insertion loss, with output power and phase values within 0.2 dB and  $3^\circ$  rms, respectively, of the desired excitations. The output port return loss was better than 18 dB. The test methodology used will be discussed in detail later in this paper.

### Zone reconfigurability switches

Switches were needed to enable the reconfiguration of the zone beams when the spacecraft moves from one ocean region to another. As shown in Figure 3, switches connect most horns to the proper feed network, and the proper feed network to the repeater. Horns used in only one ocean region were connected directly to the feed network. Overall, 92 transmit and 91 receive switches were required. Some were single-pole triple-throw, and others were single-pole double-throw with a load on the third port.

Figure 9 illustrates the INTELSAT VI switch design. Three squareax lines spaced  $120^\circ$  apart form the input lines. A rotating squareax conductor at the center of the device connects capacitively to one of the three input lines. The rotating conductor is connected in turn to a section of conventional (cylindrical) coaxial line that extends through the stack of network layers to connect to the zone port of the polarizer. The squareax center conductor is moved by a crankshaft (connected to the conductor by a dielectric pin) which extends out of the bottom of the switch housing. The switch crankshafts are connected to a common orbiting plate, which is driven in a circular motion by a step motor to turn all crankshafts simultaneously. Full redundancy is incorporated into the switch motor design.

The individual zone beam switches were designed as independent, preassembled and pretested modules. Typical measured performance data were excellent, with insertion loss of less than 0.1 dB, return loss of better than 25 dB, and port-to-port isolation of better than 33 dB being achieved at 4 GHz.

### BTS feed array

The operation of the BTS has been described previously. The beacon tracking antenna was implemented by placing the beacon tracking feed elements in the spaces between the zone I feed horns. The receive BTS used four 2-element Yagi antennas as the feed elements. For transmit, eight dielectrically loaded, open-ended waveguide elements, tapered to fit between the Potter horns, were required because of the wider spacing between component

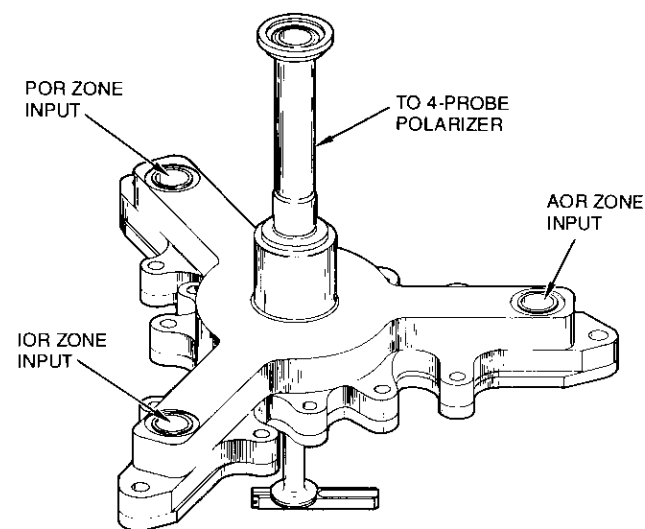


Figure 9. Squareax Switch

beams encountered when using 6-GHz beacon tracking off the 4-GHz transmit reflector. Each feed element was connected by a phase-stable flexible cable to a small squareax feed network mounted on the rear of the hemi/zone feed network support structure.

The BTS feed network combines the elements to generate the sum, delta-azimuth, and delta-elevation beams. These three outputs are connected via amplitude and phase shims to the FMA, which generates a single output that is amplitude-modulated in proportion to both the azimuth and elevation pointing error. The FMA consists of an input and an output launcher separated by a modulation section containing a ferrite core wound by a bifilar coil. The FMA output is routed to the BTR, which synchronously detects the AM modulation. The BTR also adds the bias voltage corresponding to the operational beacon up-link station and generates DC output signals proportional to the azimuth and elevation pointing errors. These signals are routed to the control logic, which drives the reflector pointing mechanisms until a receiver output of 0 V is achieved.

### Reflectors

The transmit and receive offset parabolic reflectors, designed and manufactured by British Aerospace Dynamics Group, Stevenage, England, were fabricated from two primary components: the reflector shell and stiffening ribs. The reflector shell is a co-cured composite sandwich using a segmented

Kevlar core 6.35-mm thick with two-layer facing skins. Each skin consists of one Kevlar and one carbon fiber-reinforced plastic (CFRP) layer. The Kevlar core was chosen because of its high degree of thermal stability, while the Kevlar-CFRP skin combination was selected to minimize thermal distortion. The shell was laid up on a precision temperature-compensated aluminum mandrel and cured in an oven at 175°C. The composite sandwich was balanced for minimum thermal distortion by reversing the layup order between the front and rear skins.

The stiffening ribs, laminated for minimum thermal expansion, provided the required stiffness and strength, as well as the interfaces with the spacecraft deployment and launch support structures. The ribs consisted of two end caps separated by a composite sandwich panel constructed of a co-cured Kevlar honeycomb core with CFRP and Kevlar cloth skins. The end caps were made of unidirectional CFRP and boron fiber prepreg tape. The rib caps were first laid up and cured in an autoclave at 175°C. They were then bonded to the rib panel, and in turn to the reflector shell, using Lefkowied room-temperature cure adhesive. Figure 10 shows a finished transmit reflector with the front surface painted white to enhance its thermal radiation properties. The rear of

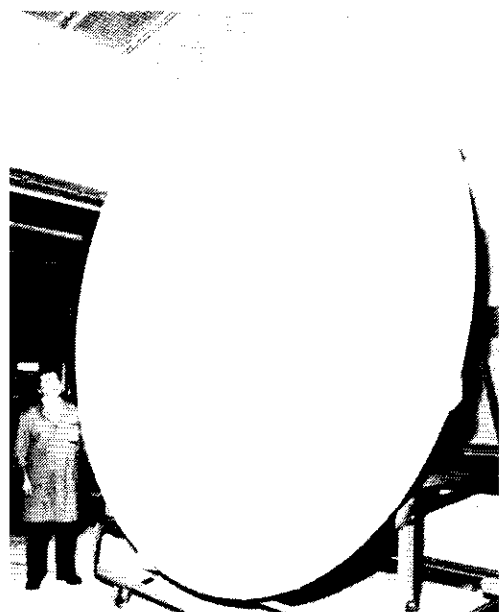


Figure 10. Completed Transmit Reflector

the reflector is protected by thermal blankets to minimize temperature gradients. The rms surface tolerances of 0.381 mm for transmit and 0.254 mm for receive were specified in order to keep the total pointing error of the reflector to  $\pm 0.02^\circ$  or less in both azimuth and elevation. These tolerances included all manufacturing, short-term thermal, and long-term thermal errors. The performance achieved was excellent, as will be discussed later.

### **Hemi/zone antenna assembly and alignment**

The major goals of the INTELSAT VI hemi/zone antenna assembly and alignment plan were that all hardware tuning and adjustment be performed at the sub-unit level prior to unit assembly, and that exhaustive testing occur at each level of assembly to ensure that workmanship was verified and high quality maintained. Thus, after assembly and testing of the feed arrays (at the unit level) and alignment of the feed arrays to the reflector, only far-field range performance measurements would be required to verify final performance. Figure 11 shows the intertwining of integration and test during the hemi/zone antenna assembly sequence, both at the sub-unit and unit levels. This section presents a detailed description of the assembly and alignment sequence, including sub-unit testing, while a later section discusses the complete INTELSAT VI antenna test program.

### **Feed array assembly**

Transmit and receive feed array assembly began with the fabrication and sub-unit testing of the polarizer, zone switches, and squareax feed network subassemblies. Each component type was built and measured in parallel, with each having separate laboratory space and test equipment.

The polarizers were adjusted and measured on special spring-loaded test fixtures that simulated the mechanical interface to the feed array. Because over 1,700 polarizers were needed for the six-spacecraft program, significant design effort was expended so that the test fixtures provided repeatable measurements and were easy to use during multiple connects and disconnects of a given polarizer. Multiple test stations were constructed to ensure that polarizer production was timely. The test fixtures consisted of a rotating loaded circular waveguide section, attached to the polarizer, with a small linear probe placed in the rotating section. As the section was rotated, the response of the linear probe to the circular polarization was measured and displayed. The difference between the maximum and minimum response was the axial ratio. The polarizer squareax network and probes were adjusted to achieve the proper axial ratio, port-to-port isolation, and return loss. Each polarizer was numbered, and

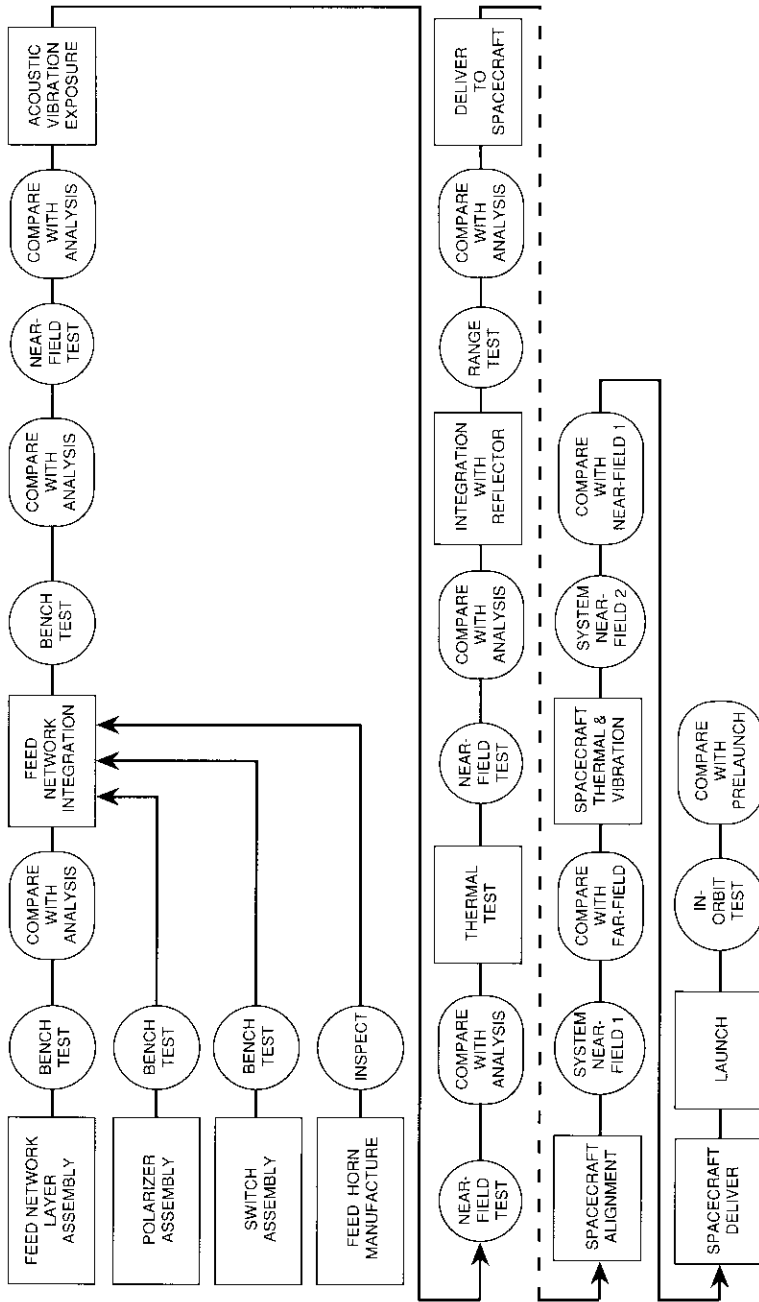


Figure 11. Hemi/Zone Antenna Assembly and Measurement Sequence

all measurements were recorded to aid in assembly of the feed arrays. Prior to the production phase, a set of 10 polarizer assemblies was successfully subjected to temperature cycling and vibration qualification tests to verify that the tuning was not sensitive to environmental exposure.

The zone reconfigurability switches were tested on a similar spring-loaded test fixture. Because the switches were nonadjustable, only measurements of the insertion loss, input and output return loss, and port-to-port isolation were required in order to characterize the switch. All testing was conducted after each switch had been thermal-cycled over 10 cycles at acceptance-level temperatures. Like the polarizers, a set of 10 switches was successfully subjected to thermal cycling and vibration qualification tests, including performance measurements at temperature extremes.

After assembly, the squareax feed network modules were placed into precision test fixtures known as "clamshells." These fixtures held spring-loaded connectors that attached to each output port of the network and were designed to allow the squareax cover to be removed quickly and easily. Twenty-two clamshells were built, some capable of testing more than one feed network module, to allow for flexibility and parallel testing of many feed networks simultaneously. The return loss and insertion loss between output and input ports were measured. Specialized test software was written to aid in conducting the test. The software also analyzed the data and compared them to a set of requirements to determine if the network needed to be adjusted, and to suggest possible adjustments. Measured data could also be up-loaded to a minicomputer and input to physical optics analysis programs to determine the effect of small errors in power and phase on the total antenna performance. The measured data analysis program also verified the insertion losses.

After the zone and hemi feed array networks had been assembled and tested to verify the amplitude and phase coefficients, unit-level integration was begun by installing the networks onto the feed network honeycomb support structure. After stacking the three zone and one hemi network layers, the polarizers and zone switches were mounted onto the feed array. At this stage, a circular waveguide probe was used to perform swept frequency axial ratio measurements to ensure that each polarizer and switch was integrated properly. Each polarizer was measured for both polarizations and for all beams by exciting the appropriate hemi or zone network input. The axial ratio was, in most cases, between 0.3 and 0.4 dB. The increase from the measured isolated polarizer performance was caused by the feed network mismatch. The amplitude and phase coefficients were verified by replacing the linearly polarized probe with a circularly polarized probe and repeating the measurements. Again, special test software was used to compare measured data with requirements and with the data measured for the individual feed network modules.

The probe measurements were especially important to verify that all polarizers and switches were properly installed, ensuring that no workmanship errors could propagate. Finally, the waveguide loads used during the measurements were removed and the Potter feed horns were installed, completing the feed array assembly.

### **Feed array/reflector alignment**

After thorough feed array testing (described in the next section), the feed networks were ready for integration with the reflectors for final testing. Integration and alignment of the transmit and receive hemi/zone antennas were performed in an assembly area adjacent to the far-field test range. For far-field range testing, the two antennas were mounted on an aluminum range dolly designed to zero-g off-load the reflectors and feeds in their flight configuration. The range dolly had mounting holes that were drilled to exactly match those on the satellite despun shelf. A coordinate system was defined on the range dolly by using optical tooling balls. The far-field range boresight telescope, reflectors, booms, and support structure were then aligned to the dolly coordinate system. The reflector flight support structure was attached via its match-drilled mounting holes. Each reflector was held by a three-point attachment ring and supported by a tower, mounted on the dolly, which provided full translational and rotational adjustment. Once the reflectors were aligned in the deployed configuration and the reflector support structure was properly positioned, the reflector booms were off-loaded and cut to fit. Final bonding of the boom end fittings fixed the reflectors to the support structure.

The feed arrays were nominally aligned to the dolly coordinate system, and thus to their associated reflectors. A temporary adjustable support structure was used for each feed array so that the array could be adjusted on the far-field range to optimize beam coverages. Throughout the alignment process, the range dolly was maintained in a zero-g off-loaded state, with the same support attachment points required by the far-field range pedestal.

For all of the alignments, tooling balls and a two-theodolite Zeiss coordinate measuring system were used. Alignment support software was written to aid in performing coordinate transformations and determining the various adjustments. Mirrors and auto-collimating theodolites were also used for convenience during the adjustment phase and as a second reference system.

Prior to movement to the far-field range, the stowed configuration of the transmit and receive hemi/zone antennas was also verified. The reflectors were removed from the alignment towers and supported temporarily by flight

structure. After it was demonstrated that the proper launch configuration could be achieved (as depicted in Figure 1a) with the proper critical clearances, the reflectors were repositioned on the alignment towers in the deployed condition, as shown in Figure 1b. The deployed alignment was re-verified, and these data served as a baseline for alignment measurements made on the far-field range.

Because of the large size of the dolly, the reflector towers and dolly "wings" were removed for transport. These interfaces used pinned joints to preserve the alignment. However, after reinstallation on the range pedestal, data were taken to reconfirm that the alignment was the same as the baseline alignment. Preliminary RF contours were measured, and the feed arrays were adjusted slightly to achieve optimum beam alignment. The flight feed array support structure was then installed, and the temporary support tooling was removed. Alignment data were again taken and recorded. Extensive range measurements (described below) were made, using the boresight scope as an optical reference.

After completion of far-field range testing, final alignment data were taken prior to movement back to the alignment and assembly building. Final flight-quality processes and cleanup were performed. The antennas were inspected and accepted by the quality assurance staff. The feed arrays, support structure, booms, and reflectors were then shipped separately to the spacecraft assembly and integration area to be mounted on the despun shelf, which at this point had completed transponder thermal vacuum testing.

As each part of the hemi/zone antennas was attached to the flight despun shelf, alignment was measured and compared to the range alignment data to verify that the stowed hardware positions had not changed. The deployed configuration alignment was also verified during the initial and post-spacecraft environmental near-field measurements.

### **INTELSAT VI antenna test program**

The INTELSAT VI antenna system was extensively tested during development and performance verification. In fact, each antenna was measured for absolute performance three times during the integration and testing of the INTELSAT VI satellites. This section discusses and compares the measurements performed on the INTELSAT VI antennas during four different measurement phases: unit-level, subassembly-level (including far-field range testing), system-level near-field, and in-orbit. A flow diagram of the complete assembly and test sequence was presented in Figure 11.

### Unit-level measurements

As previously discussed, extensive measurements were performed at the sub-unit level (on the hemi/zone polarizers, switches, and squareax networks) to ensure proper spatial and cross-polarization isolation performance prior to integration at the unit level. An extensive test program was also conducted at the unit level on the hemi/zone feed arrays and on the hemi/zone reflectors to verify that in-orbit thermal distortion would be below acceptable levels. Testing of the Ku-band spot beam and global antennas was also completed by the responsible subcontractors.

To ensure that the feed arrays were acceptable for far-field alignment and integration, near-field measurements were made on each complete feed array before, during, and after exposure to flight-level thermal and vibration environments. Testing was done using a  $4 \times 4.6$ -m planar near-field scanner, as shown in Figure 12. The feed array to be tested was placed in a thermal enclosure in front of the planar scanner. The enclosure had an RF-transparent

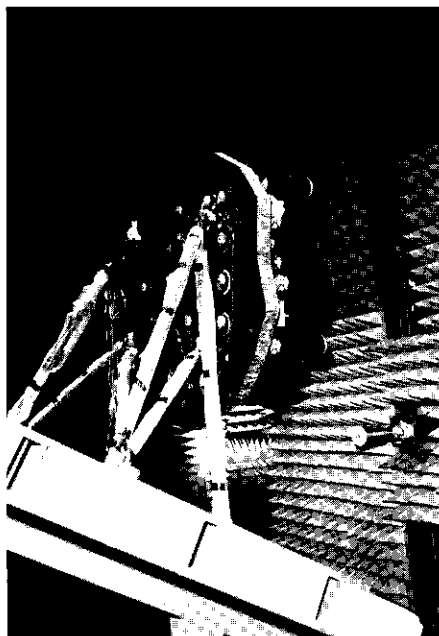


Figure 12. Testing the Transmit Hemi/Zone Feed Network Using the  $4 \times 4.6$ -m Planar Near-Field Scanner

insulated window to allow the feed array to radiate in the direction of the scanner. Measurements were made at ambient temperature, at ambient again after five thermal cycles, then at the hot extreme, the cold extreme, and then ambient again. For the acoustic vibration test, measurements were made before and after vibration. A sine vibration program was also conducted on the first protoflight feed array.

The near-field data scans were transformed via fast Fourier transform (FFT) to obtain the far-field patterns of the feed array. A spherical wave expansion was then performed to obtain the near fields of the feed array. These were applied to an "analytic" main reflector, using physical optics to determine the resulting far-field performance of the feed array/main reflector combination. Results were compared for all cases, and comparisons were made with predictions and with previously measured sub-unit data.

Another significant test at the unit level was the thermal test of the hemi/zone transmit and receive reflectors. This testing was performed by Industrieanlagen-Betriebsgesellschaft mbH, Ottoburn, West Germany, under subcontract to British Aerospace Dynamics Group. The purpose of this test was to measure the thermal distortion of the transmit and receive reflectors under simulated on-orbit conditions and to compare these measurements with predictions based on thermal and structural models. The reflector to be measured was mounted in a thermal vacuum chamber, in a vertical orientation to minimize the effects of gravity. In-orbit thermal conditions of cold bulk, front sun, back sun, and several gradient cases were then applied while the shape of the reflector surface was monitored using laser holography. Good correlation was obtained between the measured data and the analytic predictions. The measurements indicated that the receive reflector, the smaller of the two, would experience more thermal distortion in-orbit. This has been verified in-orbit by observing the BTS open-loop error voltages. As indicated in Figure 13, the thermal distortion of the F4 transmit hemi/zone reflector is less than  $\pm 0.02^\circ$  in azimuth and elevation. However, the receive reflector has movement in the azimuthal direction of about  $\pm 0.04^\circ$ . The maximum and minimum movement corresponds to the front-sun and back-sun thermal conditions, respectively. The receive elevation movement is within  $\pm 0.02^\circ$ . These curves also show the response of the reflectors during eclipse. Measured in-orbit data from the F2 spacecraft show similar behavior.

All other INTELSAT VI antennas were tested at the unit level. Prior to shipment of the Ku-band spot beam antennas and global antennas to HAC, Selenia Spazio measured these antennas on their far-field range in Rome, Italy. Performance was verified and accepted. To reduce the scope of the far-field measurements at the HAC range, these antennas were tested as part of

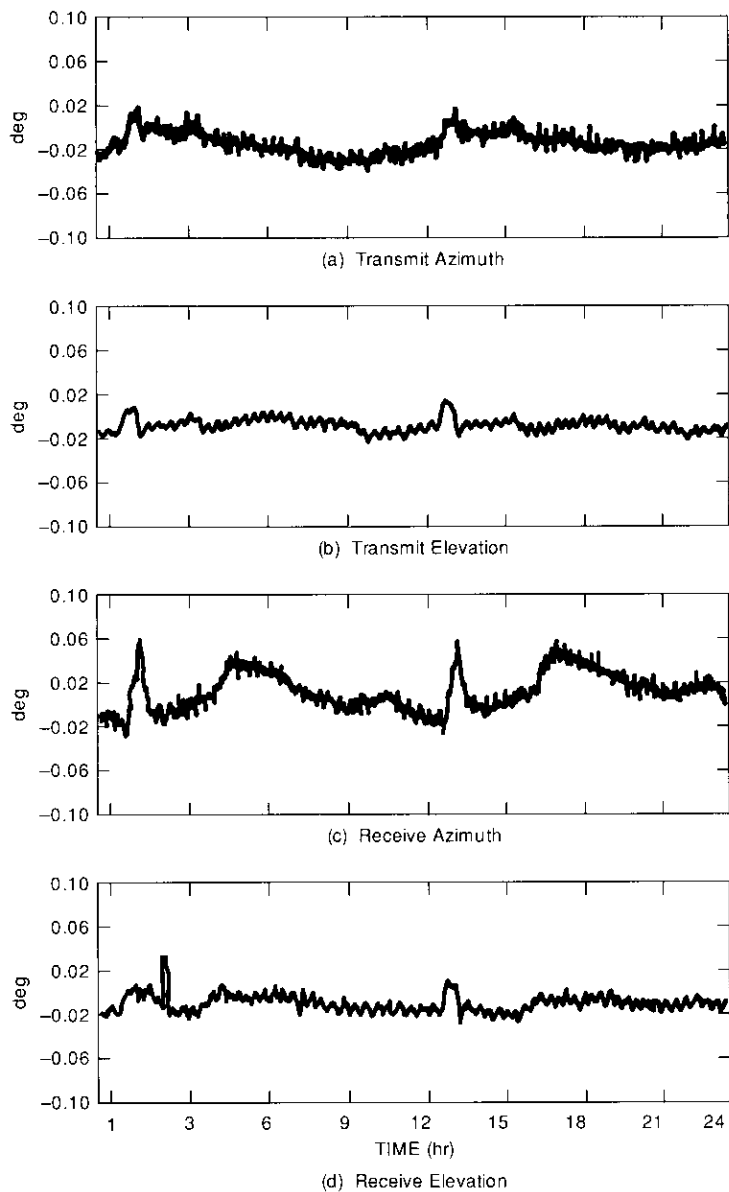


Figure 13. *F4 Reflector Thermal Distortion Pointing Error*

the complete flight antenna farm during system-level near-field measurements. Before this decision was made, a complete Y1 (development) antenna farm was measured on the HAC far-field range.

#### Far-field hemi/zone measurements

One of the most challenging measurement tasks in terms of sheer volume of data was the far-field range testing of the transmit and receive hemi/zone antennas. The testing was conducted on HAC's 200.5-m range located at Malibu, California. The receive building, shown in Figure 14, had a  $12 \times 12$ -m opening covered by an RF-transparent curtain facing the source building, with a metal roll-up door that could be lowered when testing was not in progress. The quiet zone was large enough to allow testing of the entire INTELSAT VI antenna farm in its fully deployed configuration.

The subsystem test plan called for an extraordinary number of measurements compared to the requirements of previous programs. Therefore, a fast range receiver system was designed and built to speed the collection of range data. This system, diagrammed in Figure 15, consisted of a fast amplitude-only IF receiver; frequency-hopping synthesizers to serve as both the RF source and the local oscillator (LO); fast 8-to-1 PIN-diode switches to switch between

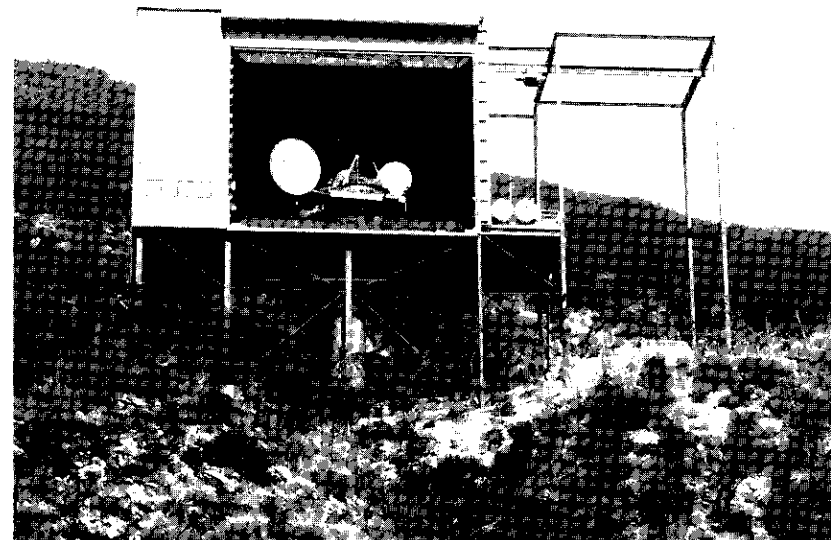


Figure 14. *INTELSAT VI Far-Field Range, Malibu, California*

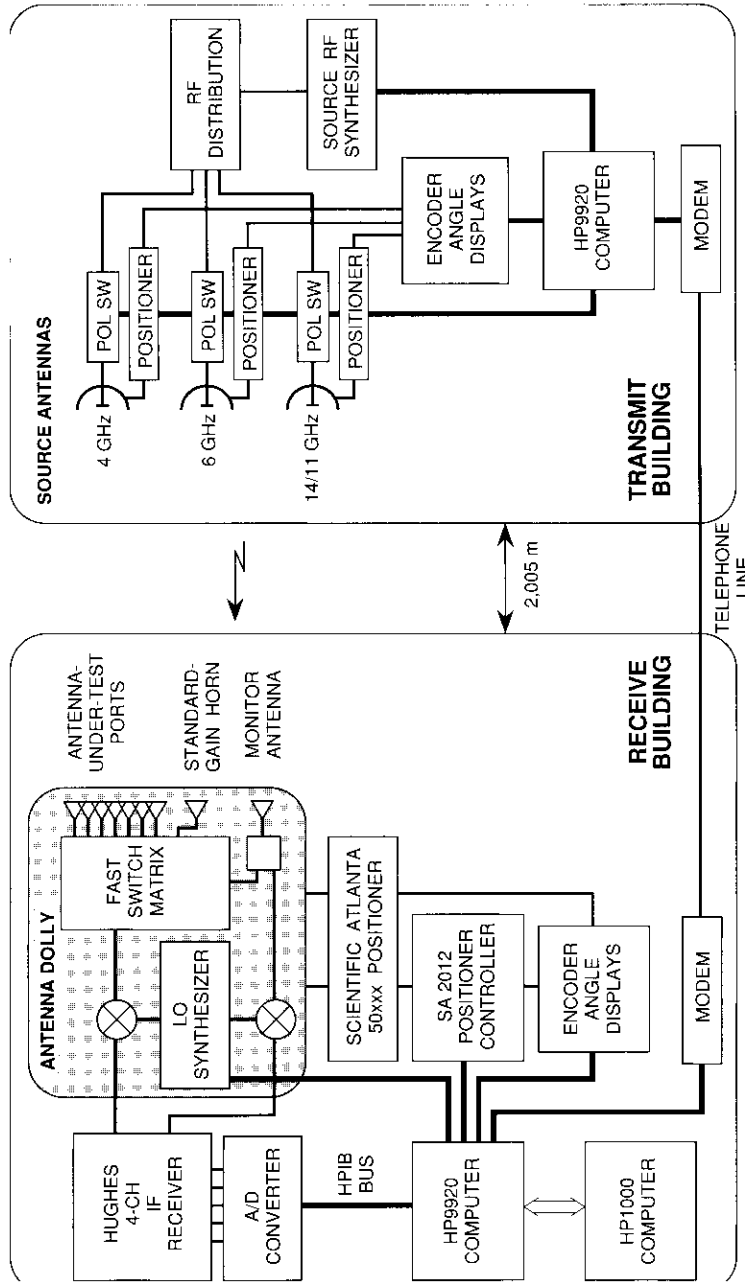


Figure 15. HAC Fast Range Receiver System

antenna ports; and three computers to control the receiver, RF source, LO source, PIN switches, and antenna positioner. Two small Hewlett-Packard (HP) 9920 computers were also used—one dedicated to controlling the sources, and the other to controlling everything in the receive building and actually executing the test. An HP1000 minicomputer was used to configure the tests and to store and analyze the measured data.

Measured data were collected in the form of raster scans consisting of azimuthal cuts along constant-elevation steps. Raster data were taken "on the fly" for six antenna ports and 24 frequencies. Because the data as measured were unequally spaced, software was written to interpolate the data as evenly spaced (or "regularized") raster scans. As the antenna positioner was rotated about its azimuthal axis, the receiver and the angle encoder were read simultaneously. The PIN switch was then hopped to the next port and another receiver and angle reading was made. After all antenna ports had been read, the RF source and LO synthesizers were hopped to the next frequency and the port-hopping was repeated. This process was repeated for each point in an azimuthal cut, and each cut was repeated for each elevation step to form a raster. Rasters of  $61 \times 61$  points were used, and over 700,000 receiver readings were required to complete one measurement, which took 2 to 3 hours. Because each receiver reading was at a slightly different angle, a routine employing cubic splines was used to interpolate the raw data into uniformly spaced rasters. Cross-polarized data were collected in the same manner by switching the source polarization. Two source orientations  $90^\circ$  apart were used, and the cross-polarized rasters were averaged to remove most of the error caused by having an imperfectly (less than 0.4 dB) polarized source. Data were collected for all three ocean regions by moving the reconfigurability switch and repeating the tests.

Data processing software was used to interpolate from data in the raster files to the desired grid point; analyze the data; calculate the carrier-to-interference ratio,  $C/I$ , and compare it with specification at each INTELSAT earth station; plot antenna patterns and histograms of gain and  $C/I$  performance; and print summary reports of performance. Figure 16 shows a spatial  $C/I$  histogram for IOR zone 3 interfering into IOR zone 1. The total number of earth stations shown on the vertical axis, or the number of "points in a bin," were sampled over four different orbital slots and included a  $\pm 0.15^\circ$  pointing error. All of the earth stations meet the 27-dB specification, with an average  $C/I$  value of 35.7 dB. The raster files were also translated to an INTELSAT-specified test data handling system (TDHS) [4] format for delivery via tape to INTELSAT for further analysis. The analysis was highly automated to speed processing and prevent operator error. The deliverable data volume for one

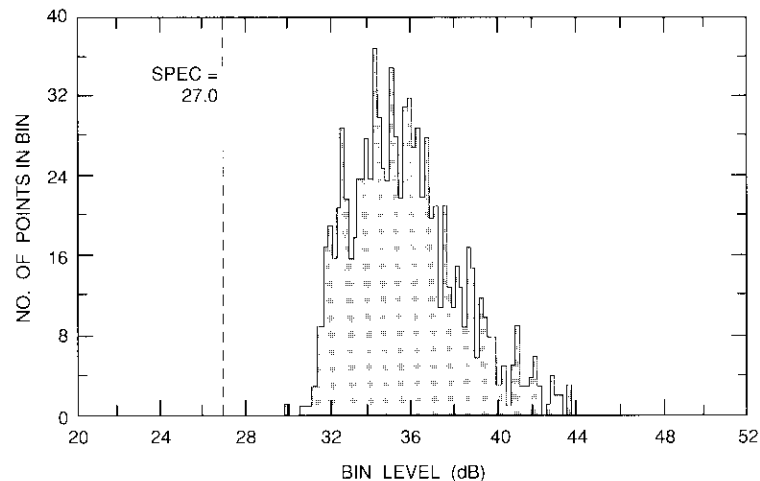


Figure 16. *Spatial C/I Histogram for Transmit IOR Zone 1 Being Interfered by IOR Zone 3*

hemi/zone antenna was 65 Mbyte of integer data, and the total data processed during analysis was about 360 Mbyte.

#### System-level near-field measurements

The INTELSAT VI system-level measurement plan required that antenna pattern measurements be made for the complete antenna farm before and after spacecraft environmental exposure. Originally, it was thought that these measurements would be performed in a relatively short slant range which existed at the beginning of the INTELSAT VI contract in April 1982. Because of the large size of the antenna farm and despun compartment, it was quickly recognized that the slant range would present significant zero-g off-load requirements when trying to measure antenna patterns over a  $20^\circ$  square measurement window. This problem was resolved by implementing a planar near-field anechoic chamber.

An anechoic chamber approximately  $12 \times 12 \times 12$  m was constructed to house a  $6.4 \times 6.4$ -m planar scanner. The planar near-field chamber provides absolute co-polarized and cross-polarized far-field measurements without the need to move the spacecraft under test. Compact and spherical near-field ranges were considered, but rejected because movement of the antenna farm was required. Over the course of the INTELSAT VI program, the HAC near-field facility has yielded programmatic advantages and proven to be cost effective.

Absolute saturated effective isotropically radiated power (e.i.r.p.), flux density to saturate, and gain-to-noise temperature ratio ( $G/T$ ) measurements were conducted in the near-field chamber for each antenna subsystem. These tests verified the combined performance of the antenna and transponder subsystems. It is interesting to note that this did not require the combination of separate antenna gain and output power measurements, but consisted of a single measurement at the peak of the near-field beam [5]. The near-field power measurement was then transformed to a far-field peak e.i.r.p. using the pattern data.

The most ambitious use of the near-field chamber on the INTELSAT VI program involved the near-field calibration of some of the BTSs [6]. Normally, the BTS was calibrated on a far-field range, where a plane wave illuminated the reflector and the resulting modulation index contours were measured. The advantage of far-field calibration is that the BTS antenna, FMA, and BTR can be calibrated as a system. However, a late redesign of the receive BTS feed horns required that the F1 spacecraft BTS be calibrated in the near-field chamber for programmatic reasons. Near-field calibration of the BTS requires that accurate mathematical models of the FMA and BTR be combined with the measured amplitude and phase antenna data to predict the modulation index response of the BTR. Amplitude and phase calibration between the sum and difference channels is required to be accurate to  $\pm 0.25$  dB and  $\pm 3.0^\circ$ . Figure 17 illustrates the near-field to far-field antenna pattern agreement for the F4 transmit BTS azimuth channel, as well as the in-orbit to near-field agreement of the F2 receive azimuth channel modulation index contours.

#### In-orbit measurements

After launch of the spacecraft and deployment of the INTELSAT VI antennas, in-orbit measurements were performed on the payload and BTS from the INTELSAT ground station at Fucino, Italy [7]. The BTS checkout was performed first to ensure proper pointing of the hemi/zone reflectors for the payload in-orbit test. The modulation index contours are mapped, as shown in Figure 17b, to verify that the BTS antenna performance is the same as indicated by prelaunch data. The BTS error voltage response is then observed for 48 hours to determine the effect of reflector thermal distortion (as shown in Figure 13) and to minimize pointing error. The BTS error voltage originally is contaminated by spacecraft attitude and orbital errors. The curves presented in Figure 13 have had these errors removed and represent only the reflector distortion.

Closed-loop performance of the BTS was also verified. Figure 18 indicates that, over a 24-day period, the pointing variation of the F2 satellite is less than

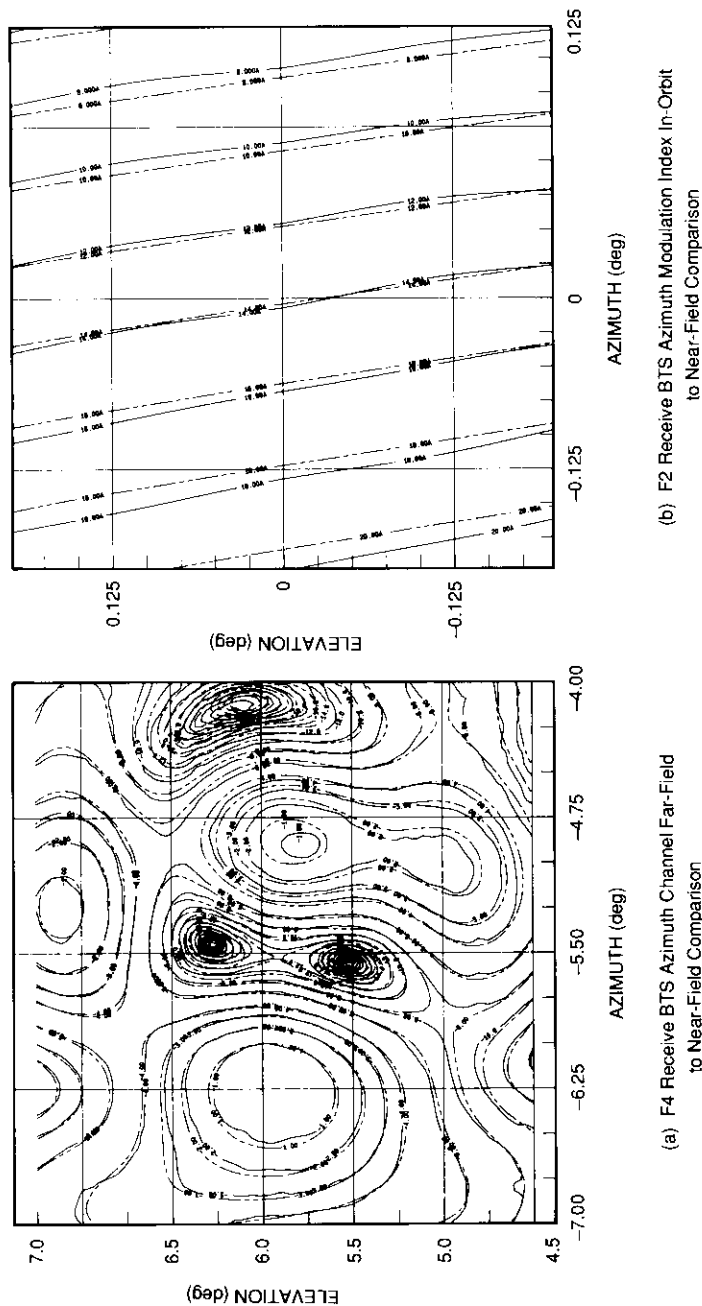


Figure 17. Near-Field BTS Calibration

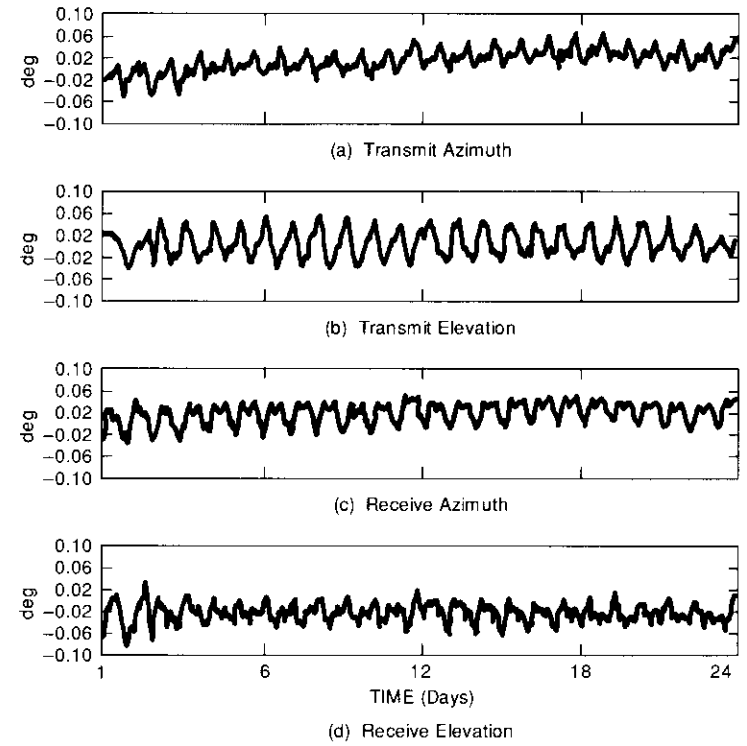


Figure 18. F2 Hemi/Zone Antenna Pointing Error (24 days)

$\pm 0.06^\circ$  for all four channels. This figure includes all pointing error effects, such as open-loop operation of the BTS, changing spacecraft attitude as a result of spacecraft solar torque, and north-south and east-west stationkeeping maneuvers, as well as attitude control operation in sun and earth mode. Adding a BTS-to-communications-beam calibration uncertainty of  $\pm 0.04^\circ$  to the  $\pm 0.06^\circ$  value yields a total INTELSAT VI hemi/zone pointing error of less than  $\pm 0.10^\circ$ . The pointing error can be reduced to  $\pm 0.05$  by closed-loop operation of the BTS.

The in-orbit antenna pattern measurement simply measures e.i.r.p. and the flux-density-to-saturate for various positions of the despun shelf. By constantly referencing the data to a single point of the high-power amplifier gain transfer curve, transmit and receive co-polarized patterns can be separated. Other cross-strapping techniques are employed to measure transmit and receive sidelobes [7]. Cross-polarized isolation is measured by earth station

switching, where the earth station axial ratio performance is better than 0.15 dB. To obtain different elevation angles than those achieved at orbit normal (approximately  $6.15^\circ$  in spacecraft coordinates), the spacecraft is moved away from orbit normal by firing thrusters. The maximum movement from orbit normal of the spin axis is about  $11^\circ$ .

Because the imposed roll transforms into spacecraft yaw 6 hours later, these patterns must be measured at specific times, and the IOT data comparison software must be able to handle changing azimuth and elevation. The correct attitude of the spacecraft is determined by the INTELSAT Attitude Determination Group, and this database is sampled during antenna measurement.

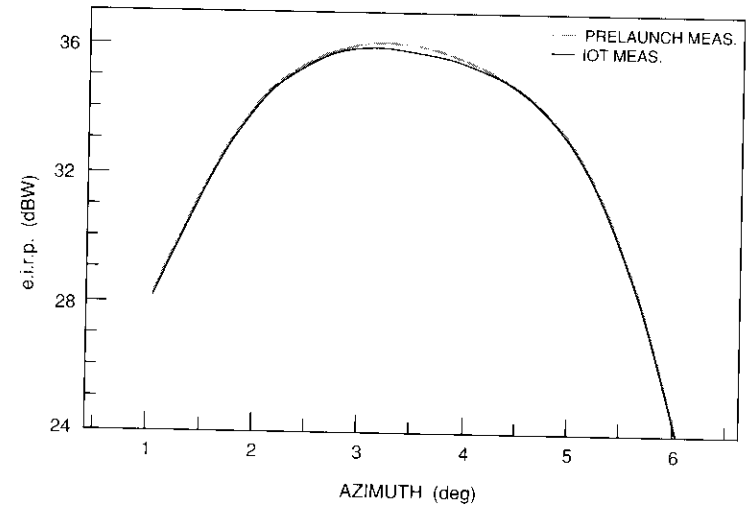
Figure 19 shows typical comparisons of measured in-orbit data with far-field and near-field prelaunch data. Co-polarized, cross-polarized, and side-lobe data comparisons are presented for the F2 spacecraft. Both inclined and orbit normal cuts are provided.

### Conclusions

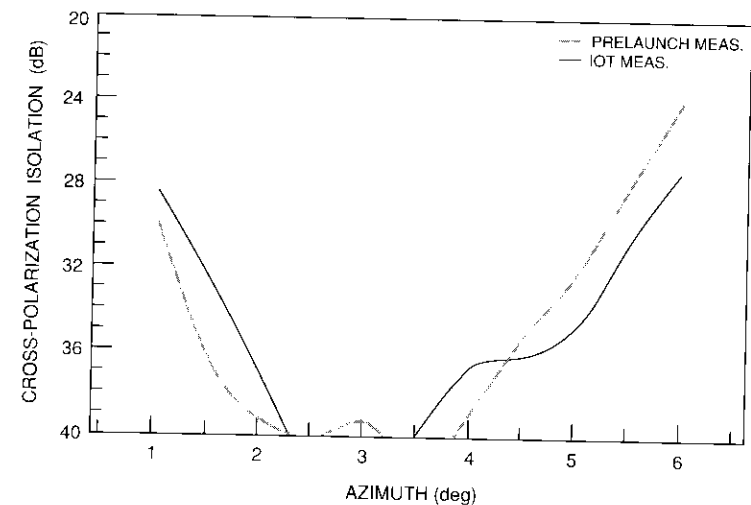
Development of the INTELSAT VI antenna system was a challenging experience for the many people who contributed to the successful design and implementation of five flight spacecraft over a 9-year period. The feed array and associated squareax and switch networks are the largest and most complex successfully designed, tested, and deployed to date. All of the spacecraft have finished ground testing, and two satellites are in operation in the AOR. In-orbit measurements have shown that all design parameters have been met and excellent pointing performance has been achieved. The INTELSAT VI satellites are expected to achieve 13 to 15 years of spacecraft life and to provide INTELSAT with the service flexibility to support ever-changing traffic demands.

### References

- [1] B. A. Pontano, A. I. Zaghoul, and C. E. Mahle, "INTELSAT VI Communications Payload Performance Specifications," *COMSAT Technical Review*, Vol. 20, No. 2, Fall 1990, pp. 271-308.
- [2] S. O. Lanc, M. F. Caulfield, and F. A. Taormina, "INTELSAT VI Antenna System Overview," AIAA 10th Communication Satellite Systems Conference, Orlando, Florida, March 1984. AIAA Paper No. 84-0060-CP.

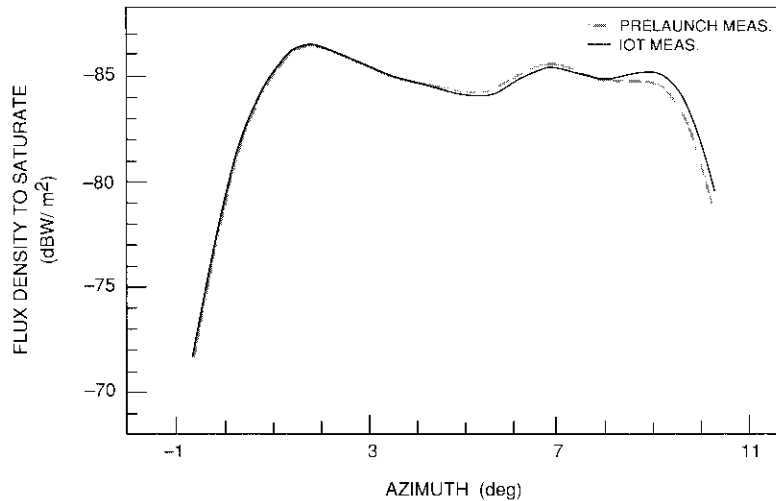


(a) Transmit Zone 3 e. i. r. p.

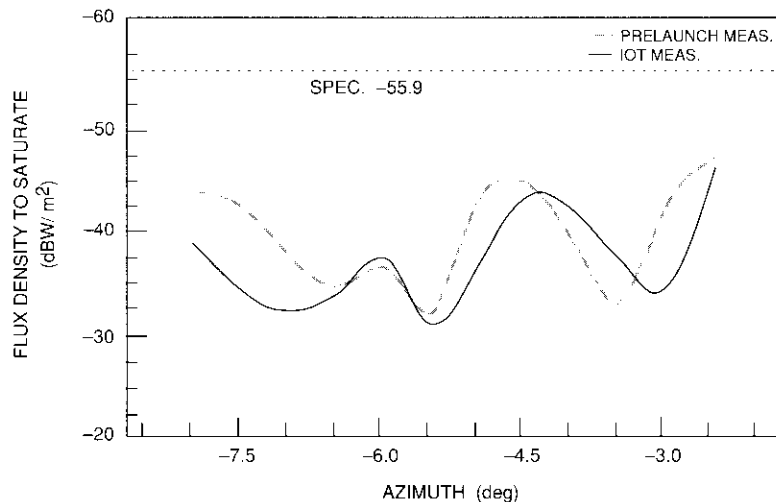


(b) Transmit Zone 3 Cross-Polarization Isolation

Figure 19. F2 In-Orbit Test Data



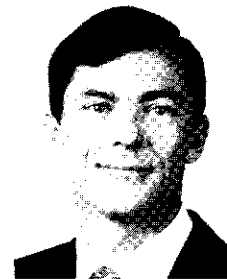
(c) Receive E. Hemi Flux Density to Saturate Inclined Cut



(d) Receive E. Hemi Sidelobe

Figure 19. F2 In-Orbit Test Data (cont'd)

- [3] A. I. Zaghloul, R. R. Persinger, and D. F. DiFonzo, "Design Optimization Procedures for Multi-Feed Satellite Shaped-Beam Antennas," 11th European Microwave Conference, Amsterdam, The Netherlands, September 1981, *Proc.*, pp. 540-545.
- [4] C. Johnson *et al.*, "Ensuring a Reliable Satellite," scheduled for publication in *COMSAT Technical Review*, Vol. 21, No. 2, Fall 1991.
- [5] A. C. Newell, R. D. Ward, and E. J. McFarlane, "Gain and Power Parameter Measurements Using Planar Nearfield Techniques," *IEEE Transactions on Antennas and Propagation*, Vol. AP-36, No. 6, June 1988, pp. 792-803.
- [6] Private communication.
- [7] G. Rosell *et al.*, "In-Orbit RF Test of an INTELSAT VI Spacecraft," scheduled for publication in *COMSAT Technical Review*, Vol. 21, No. 2, Fall 1991.



Randy Persinger received the B.S.E.E and M.S.E.E. degrees from Virginia Polytechnic Institute and State University, in 1976 and 1978, respectively. He is currently Manager of COMSAT's RF Systems Group, Space Systems Engineering, at COMSAT General in El Segundo, California. While his area of expertise is satellite antenna subsystems, his current responsibilities include the communications payload implementation monitoring and procurement of several different types of satellites. Mr. Persinger has worked on the INTELSAT VI program from 1979—when initial feasibility concepts were initiated—to the present, and continues to support in-orbit testing. He made significant contributions to the successful INTELSAT VI antenna alignment program, system near-field measurement, and near-field calibration of the beacon tracking system. He also helped to develop several software packages to aid in the analysis of antenna data, from performance evaluation at the Malibu far-field range, to real-time inclined-orbit measurement analysis during in-orbit testing. Prior to joining COMSAT Laboratories in 1979, he worked for the Antenna Department at Hughes Aircraft Company.



Steven O. Lane received the B.S.E.E. and M.S.E.E. degrees from Virginia Polytechnic Institute and State University in 1978 and 1980, respectively. In 1980, he joined Hughes Aircraft Company, Space and Communications Group, where he was involved in the design, unit integration, and testing of the hemi/zone antennas for the INTELSAT VI program. His major responsibilities included design of the hemi/zone antenna beams, design of the hemi/zone squareax feed networks, development of automated testing techniques for the feed networks and integrated feed package, and development and implementation of the fast receiver and data analysis systems used in the far-field range testing of the hemi/zone antennas. In addition, he was responsible for range testing of the first four INTELSAT VI hemi/zone antennas.

From 1988 through 1989, Mr. Lane was responsible for all antenna electrical engineering activities on the UHF F/O program for the U.S. Navy. He was subsequently involved with the Phase B study for the NASA ATDRSS spacecraft, with responsibility for design and analysis of the S-band multiple-access phased-array antenna. He is currently a Senior Scientist in the Antenna Systems Product Line at Hughes Space and Communications Group, with responsibility for R&D in the areas of planar phased-array antennas and active antennas. Mr. Lane is a member of IEEE and Eta Kappa Nu.

Michael F. Caulfield received a B.S. in electrical engineering from Northeastern University, in 1976; an S.M. in electrical engineering and computer science from the Massachusetts Institute of Technology in 1978; and an M.B.A. from Pepperdine University in 1987. He joined Hughes Aircraft Company, Space and Communications Group, in 1978 as a Member of the Technical Staff and became immediately involved in the early INTELSAT VI conceptual studies and design tradeoffs for the antenna system. He followed the INTELSAT VI program from the proposal through the final flight antenna systems implementation in 1987. During this time, he was involved in all aspects of the INTELSAT VI antenna farm design, integration, and test, and was directly responsible for the electrical aspects of the design. This included development of innovative techniques to measure the near-field performance of the hemi/zone feed arrays over environmental extremes; and the development of fast, multifrequency, multipoint data acquisition/processing techniques for far-field range evaluation of the antenna farm.

Following the INTELSAT VI program, Mr. Caulfield served as Task Manager on several Government programs, including the U.S. Navy's UHF F/O program, and as



the Payload Manager on the NASA ATDRSS Phase B Study. He is currently Assistant Manager of the Antenna Systems Product Line in the Space and Communications Group at Hughes, where his duties include the design, production, and advanced technology development of space antenna systems for both government and commercial customers. Mr. Caulfield is a member of IEEE, Eta Kappa Nu, Tau Beta Pi, and Sigma X.

Amir I. Zaghloul received a B.Sc. from Cairo University, Egypt, in 1965, and an M.A.Sc. and Ph.D. from the University of Waterloo, Canada, in 1970 and 1973, respectively, all in electrical engineering. He also received an M.B.A. from the George Washington University in 1989. Prior to joining COMSAT Laboratories in 1978, he held faculty positions at the University of Waterloo and Toronto, Canada, and at Aalborg University in Denmark. At COMSAT Laboratories, he has been a member of the Microwave Technology and Systems Division, where he is presently Manager of the Satellite Systems Department. His responsibilities have included the study, design, and development of microwave integrated circuits, microwave switch matrices for SS-TDMA systems, multibeam antennas, phased-array systems, microstrip antennas, reflector antenna systems, and future satellite systems. He has also been involved in study and support efforts for several satellite programs.

Dr. Zaghloul is a Fellow of IEEE; a Senior Member of AIAA; a Member of the Electromagnetics Academy; past Chairman of the Washington, D.C., Chapter of the IEEE Antennas and Propagation Society; and recipient of the 1986 H. A. Wheeler Applications Prize Award for best applications paper in IEEE Transactions on Antennas and Propagation. He is also a co-recipient of the 1986 COMSAT Laboratories Research Award, and of COMSAT's Exceptional Invention Award in 1990.



## ***INTELSAT VI on-board SS-TDMA subsystem design and performance***

R. K. GUPTA, J. N. NARAYANAN, A. M. NAKAMURA, F. T. ASSAL,  
AND B. GIBSON

(Manuscript received January 17, 1991)

### ***Abstract***

The design and performance of the satellite-switched time-division multiple access (SS-TDMA) subsystem on board the INTELSAT VI spacecraft is described. A brief overview of the subsystem hardware and capabilities is presented, followed by a discussion of the key design features of the microwave switch matrix (MSM), distribution control unit (DCU), and timing source for the subsystem, including their hardware implementations. The design of redundancy configurations for enhanced reliability, and for recovery from failures after fault identification, are then addressed. A 10-year probability of survival in excess of 0.99 has been designed by providing an input path redundancy of 10-for-6 for the MSM, 2-for-1 redundancy for the DCU, and 3-for-1 redundancy for the timing source. The philosophy guiding the extensive test program adopted for the SS-TDMA subsystem, from design conception through full-scale spacecraft integration, is also described.

### ***Introduction***

The INTELSAT VI spacecraft features the first large-scale commercial application of satellite-switched time-division multiple access (SS-TDMA) technology to enhance the efficient utilization of the allocated frequency spectrum [1]-[3]. A number of evolutionary technology trends contributed to the successful introduction of the SS-TDMA hardware on board the INTELSAT VI spacecraft. These included the use of TDMA transmission techniques, which make

the satellite more bandwidth- and power-efficient through single-carrier operation; reuse of the available frequency spectrum by multibeam antenna patterns with sufficient beam pattern isolation; successful development and performance demonstration of the SS-TDMA hardware [4]–[7]; and environmental testing and flight qualification of the subsystem units [8].

Figure 1 is a simplified block diagram of the INTELSAT VI on-board communications system. A total of 50 transponders are accommodated within 10 beams at C- and Ku-bands, which provide two global, two hemispheric, and four zone coverages at C-band, and two steerable spot beam coverages at Ku-band. The multibeam antennas require the use of on-board microwave switch matrix (MSM) arrays to allow interconnectivity among beams. In the INTELSAT V spacecraft, these interconnections were established in a “static” mode by using mechanical switches that could be changed by ground command to accommodate changes in traffic patterns. The SS-TDMA subsystem on board INTELSAT VI further increases satellite utilization efficiency by providing cyclical and dynamic interconnections among six isolated beams for two independent 72-MHz channels [(1-2) and (3-4)] at C-band. These dynamic interconnections allow earth stations in one beam to access earth stations in all six beams cyclically within each TDMA frame. In addition, five static MSMs provide up-link-to-down-link interconnectivity within each of five frequency-multiplexed channels. As a result of these and other enhancements, the INTELSAT VI communications payload has a traffic-carrying capacity of up to approximately 120,000 two-way telephone channels and three television channels [9].

On the INTELSAT VI spacecraft, each channelized SS-TDMA subsystem consists of an MSM, a distribution control unit (DCU), and a timing source. The MSM cyclically connects the input and output ports corresponding to up- and down-link beams, respectively. The DCU controls the on/off switch states of the MSM according to preassigned ground-command-programmable switch configurations stored in the DCU memory. The timing source [10] provides stable reference timing for plesiochronous operation with the terrestrial networks. To achieve the desired long-term stability of  $1 \times 10^{-11}$ , the timing source is placed in a temperature-controlled oven and has commandable frequency-correction capability via telemetry and command (T&C) interfaces. A detailed discussion of synchronization and overall SS-TDMA network management is provided by Campanella *et al.* [11].

This paper presents the design issues and technology associated with the on-board SS-TDMA subsystem and summarizes the test data taken at the unit and subsystem levels.

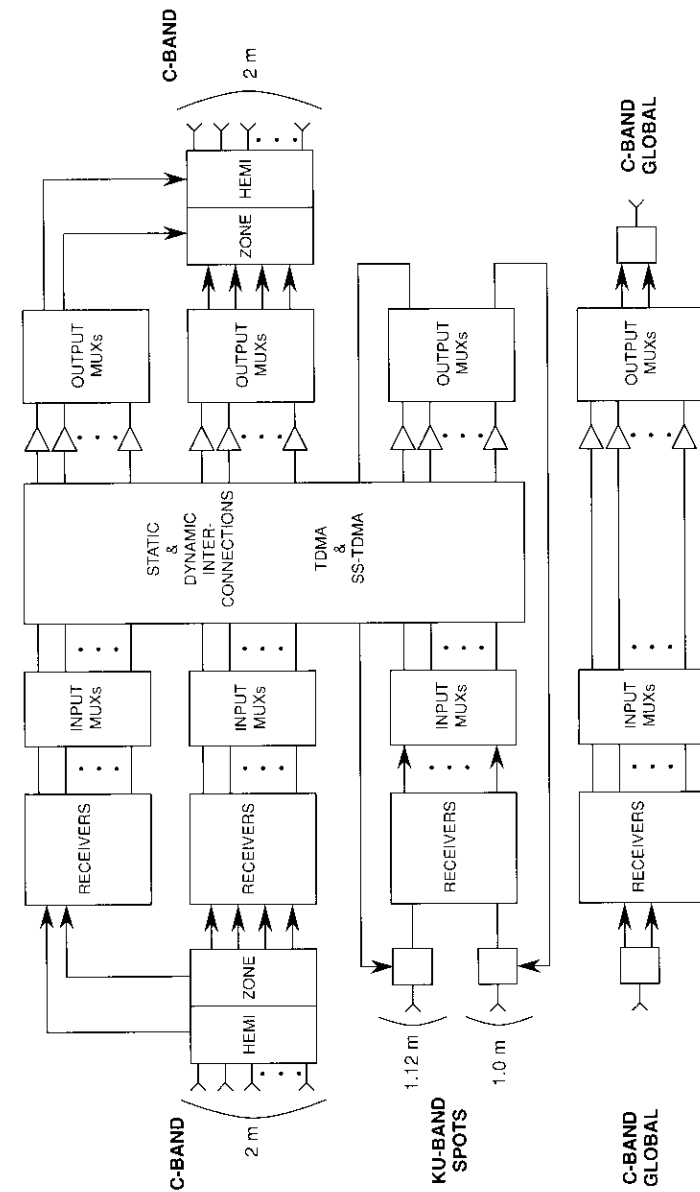


Figure 1. Simplified Block Diagram of the INTELSAT VI Communications Payload

### SS-TDMA subsystem design

The SS-TDMA subsystem provides dynamic connectivity between two of the C-band transmission channels [(1-2) and (3-4)] for two hemispheric and four zone (a total of six) beams. Thus, it is critical that the on-board SS-TDMA subsystem provide reliable interconnections between the beams over the 10-year design life of the satellite. More specifically, the SS-TDMA subsystem had to be designed with an estimated probability of survival of 0.99 or greater, since its loss could cause the loss of one or more of the RF channels in any coverage area. This required the use of a functional path redundancy configuration [12] to enhance the end-of-life probability of survival of the SS-TDMA subsystem, and the selection of radiation-hardened parts and materials. Other considerations included the adaptability of the designs to fabrication, the ability to identify and recover from failures, and the desire to reduce mass and DC power consumption.

The reliability characteristics computed for this MSM for a number of redundancy configurations are shown in Figure 2. The configurations analyzed included a  $12 \times 6$  MSM (with 2-for-1 and 4-for-2 redundancy), a  $9 \times 6$  MSM (with 3-for-2 redundancy), and  $8 \times 6$  and  $10 \times 6$  MSMs with ring redundancy. A  $9 \times 9$  MSM configuration with loop-around redundancy was also analyzed. In these computations, constant failure rates (failures in  $10^9$  hours [FITs]) due to random failures were assumed. A switch junction was assumed to be failed whenever a partial or full open or short existed due to RF device or driver circuit failure. The switch junction failure rate was taken as a variable because of the uncertainty of this failure rate. The results showed that ring redundancy provided superior MSM reliability, and that the reliability of the  $10 \times 6$  MSM using a 10-for-6 ring redundancy configuration was superior to all other configurations. In addition, by using 2-for-1 redundancy for the DCU and 3-for-1 for the timing source, an overall SS-TDMA subsystem reliability greater than 0.99 was achieved. Figure 3 is a functional block diagram of the INTELSAT VI spacecraft SS-TDMA subsystem for both channels [(1-2) and (3-4)], with the redundancy configurations discussed above. Bypass RF switch matrices are provided to reroute traffic to static MSMs for static TDMA operation.

Table 1 lists the SS-TDMA subsystem performance parameters that formed the basis for the selected design. As indicated, the frame period over which the INTELSAT VI DCU cycles through different switch states is 2 ms. This frame duration is identical to that of INTELSAT V TDMA network [13],[14], making introduction of the SS-TDMA network essentially transparent to the INTELSAT traffic terminals. The 2-ms frame duration is further divided into 1,888 frame units (FUs), where each FU defines the minimum increment for

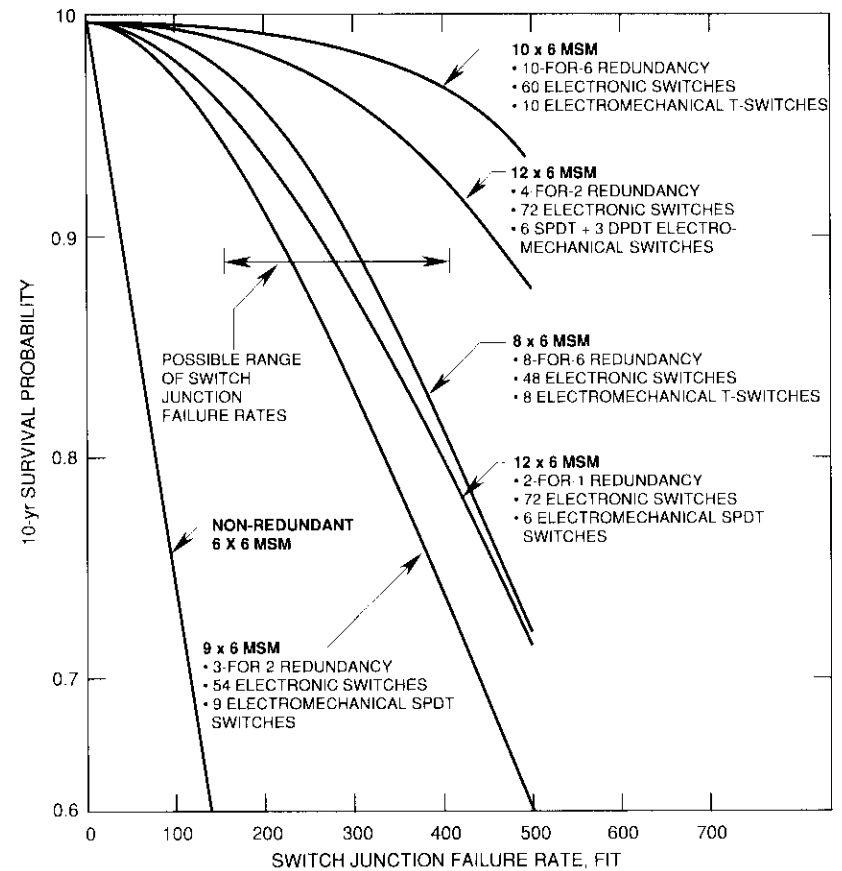


Figure 2. Computed 10-yr Probability of Survival for Redundant  $6 \times 6$  MSM

programming the switch state duration. For INTELSAT VI, the minimum FU duration is  $1.064 \mu\text{s}$ . However, the minimum duration for which an independent switch state may be defined is 4 FU ( $4.256 \mu\text{s}$ ) due to digital control data processing time requirements.

The number of switch states required for MSM control is selected to ensure full and flexible interconnectivity among the operating earth stations and to optimize traffic flow through the system. Ito *et al.* [15] and Inukai [16] have shown that  $(N^2 - 2N + 2)$  represents an upper bound on the total number of switch states required to accommodate any traffic pattern, where  $N$  is the number of beams. Thus, for sixfold frequency reuse in INTELSAT VI, the

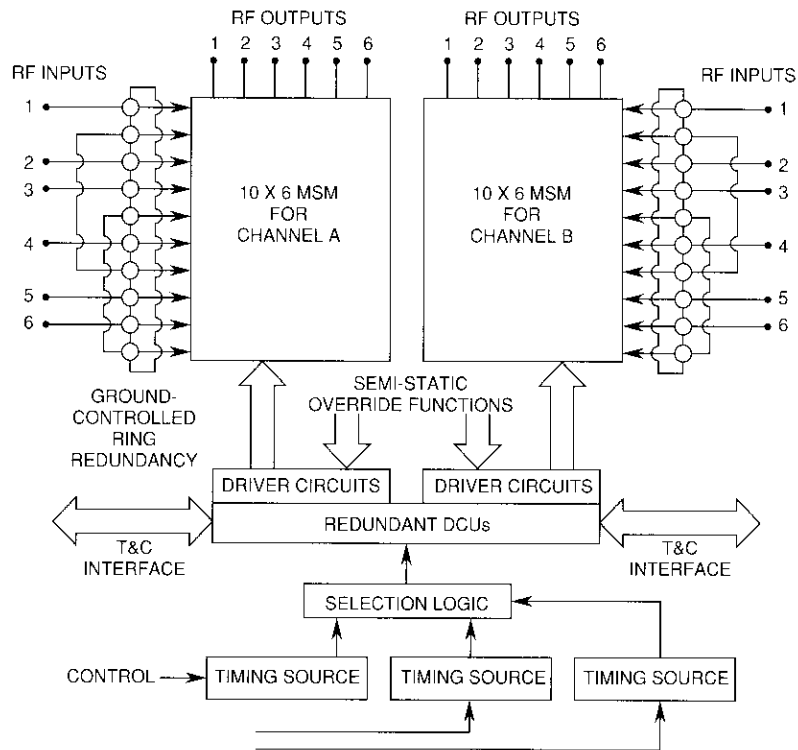


Figure 3. SS-TDMA Switching System for Two Channels and Six Beams

number of switch states required for traffic flow is 26. The INTELSAT VI hardware can program 64 switch states for the six beams within a 2-ms TDMA frame, which provides sufficient flexibility and additional switch states.

Another key feature of the on-board hardware is the provision for a special substitution state once every superframe. This allows a special state (in terms of switch interconnection pattern and/or time duration) to be substituted in one frame of each superframe in lieu of the normally executed traffic pattern. The special switch state may be used to either extend or shorten a switch state assigned to the acquisition and synchronization unit (ASU) of the reference terminal equipment (RTE), thus enabling the RTE to effect coordinated burst time plan changes by synchronizing traffic station and satellite switch times [13],[14]. The RTE and its ASU are discussed in greater detail in companion papers by Lunsford *et al.* [17] and Bedford *et al.* [18].

TABLE 1. ON-BOARD SS-TDMA SUBSYSTEM PERFORMANCE PARAMETERS

PARAMETER	VALUE
Array Size	10 × 6 for 6 × 6 operation
Connectivity	Any $N$ to any $M$
Bandwidth	3.7–3.9 GHz
Insertion Loss of Any Path	<11 dB
Path-to-Path Insertion Loss Variation	≤0.3 dB
On-to-Off Isolation	≥50 dB
Max Noise Figure	≤12.3 dB
Amplitude Linearity ( $C/I$ ) for Two Equal Amplitude Tones ( $P_o \leq -15$ dBm)	>45 dB
Rise and Fall Times	≤50 ns
Timing Jitter	≤10 ns
Frame Period	2 ms
Superframe Period	16.384 s
Frame Units per Frame	1,888
Length of Frame Unit	1.064 μs
Number of Switch States	64
Minimum Switch State Duration	4.256 μs

The overall redundancy configuration for the SS-TDMA hardware in a single channel is shown in Figure 4. The MSM has four additional rows to accommodate switch element failures, resulting in 10 input rows to service six beams. Two redundant power supplies deliver DC power to associated interface logic circuits, DCUs, and each MSM; and two interface logic circuits provide redundancy in case of MSM logic circuit failure. Two DCUs provide serial input to the MSM, resulting in 2-for-1 redundancy. Three timing sources are available, one of which provides common reference timing for both SS-TDMA units, while the other two provide standby redundancy. The timing sources have individual power supplies so that failure of any one power supply does not affect the other units.

In addition to hardware failures, which may be accommodated by signal rerouting through redundant hardware, soft failures in logic circuits may be

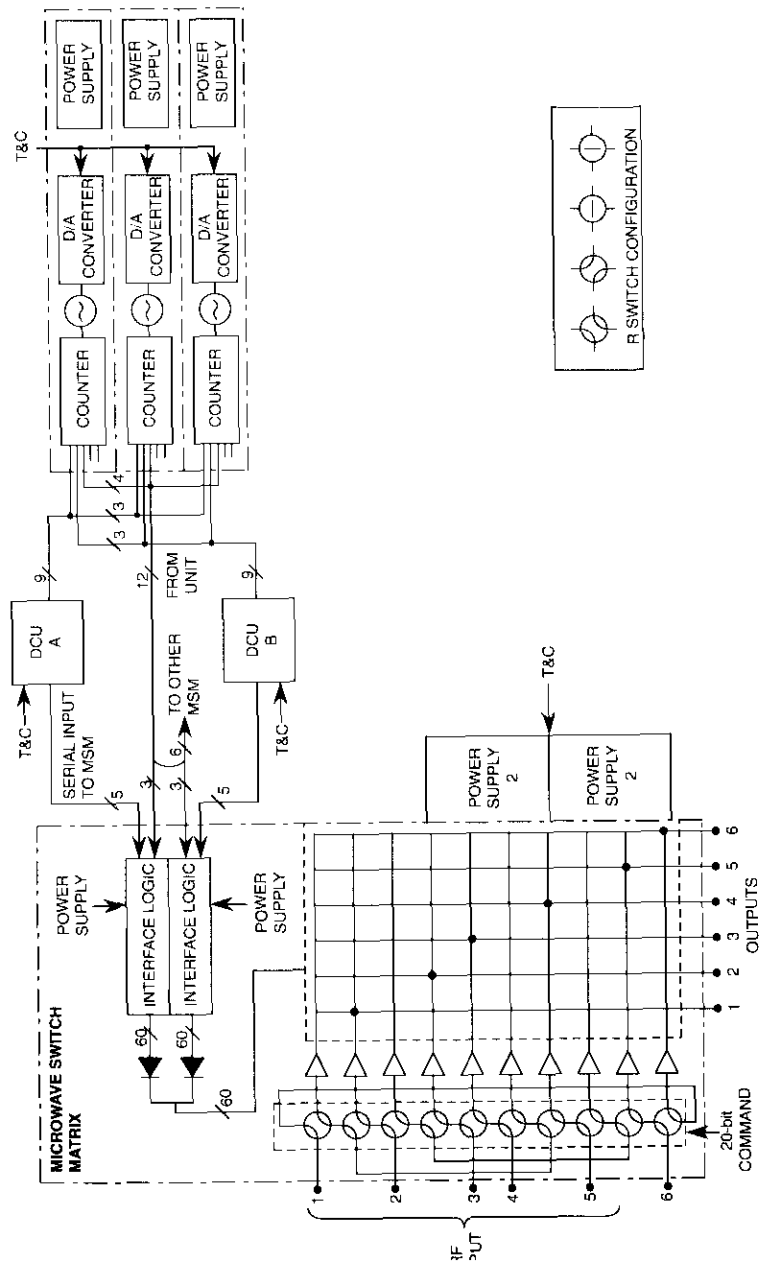


Figure 4. Single-Channel SS-TDMA Configuration

caused by single event upsets (SEUs), also known as bit-flips [19]. These soft errors are caused by a change of state in logic circuits due to direct hits by the high-energy particles of cosmic radiation. To recover from these failures, the DCU applies forward error correction (FEC) to correct for SEUs as the switch state control bits are read out from the on-line memory and then returned to that memory.

### Microwave switch matrix

The MSM in each of the two SS-TDMA channels was designed using coupler crossbar architecture. This architecture offers the advantages of simpler control implementation and interconnection programming, as well as relatively easy failure identification compared to rearrangeable and cellular configurations [7]. Furthermore, it provides broadcast-mode capability to connect any up-link beam to all down-link beams. Crossbar MSM configurations have been implemented in the past by using three-dimensional divider/combiner [4]–[7] and planar coupler configurations [20],[21]. The coupler crossbar configuration was adopted for the  $10 \times 6$  MSM design because of its ease of fabrication, with identical couplers in the input and output planes. The INTELSAT VI MSM, which interconnects six RF inputs with six outputs, consists of the following five major segments:

- RF switch matrix in which signal routing takes place.
- Preamplifiers to partially compensate for MSM insertion loss.
- Input logic to translate the serial switch states into parallel on/off commands for each of the 60 switches in the matrix.
- A ring redundancy network of mechanical coaxial "R" switches to reroute signals in the event of failure in either the matrix or the preamplifiers.
- Two power supplies and a power supply switching unit, which provide regulated power to the other units in the MSM and DCU.

### MSM hardware design

A key building block of the MSM is the PIN diode switch, which is matched in both the on and off states. PIN diodes were selected over single- or dual-gate FETs because of the simplicity of matching the circuits and their ready availability at the beginning of the INTELSAT VI program. A beam-lead device was used because it demonstrated low capacitance, repeatable performance, and reliability for space applications. The switch (shown schematically in Figure 5)

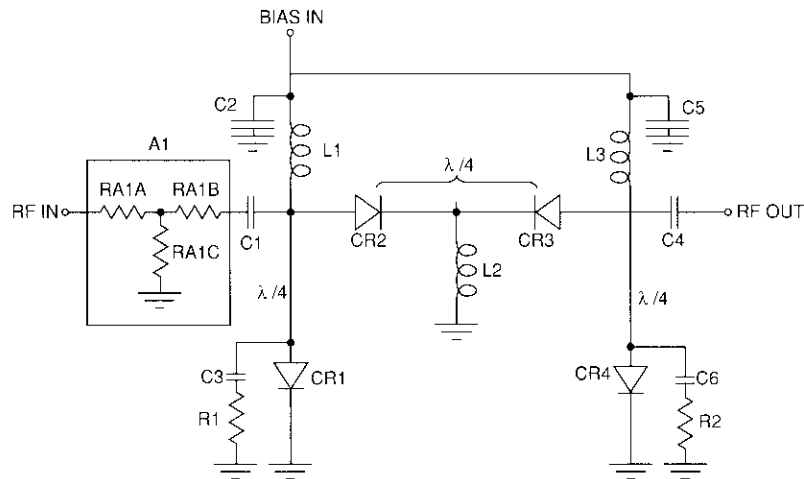


Figure 5. Schematic Diagram of the PIN Diode Switch Element

uses two PIN diodes in series to provide a high on/off ratio ( $\geq 50$  dB), and two shunt diodes to provide matching. In the ON state, the series diodes have low resistance and the shunt diodes are reflected as open circuits by transformation through the quarter wavelength. In the OFF state, all the diodes present high impedance, and matching is provided by  $50\text{-}\Omega$  resistances R1 and R2. Each switch element (Figure 6) includes a microwave integrated circuit (MIC) fixed attenuator chip to match path losses through the MSM. Each switch also has an associated driver that provides the current to turn on the PIN diodes. This driver is controlled by the output of the redundant input logic circuits and has been implemented using discrete devices, chip resistors, and chip capacitors (Figure 7).

A planar crossbar architecture was realized for the MSM by integrating input couplers and switch elements on one side of the MSM housing, and switch driver circuits and output couplers on the other side. RF feedthroughs were used for the RF path from the top side of the MSM to the bottom. The ground plane in between provides RF isolation between the input rows and output columns of the MSM. The  $10 \times 6$  MSM was divided into two submatrices ( $4 \times 6$  and  $6 \times 6$ ) to reduce the size of each MSM and facilitate assembly. Coaxial lines interconnect the two submatrices to produce a  $10 \times 6$  MSM.

Figure 8 shows a top view of the  $4 \times 6$  MSM. The RF input signal travels along each input "row" of the MSM, which consists of cascaded directional couplers. A portion of the input power is coupled to the switch element at the output of each coupler. The signal is either absorbed or passed through the

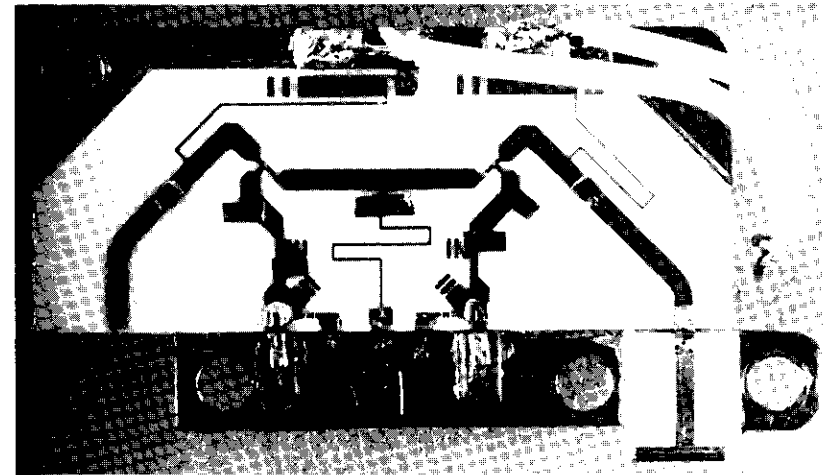


Figure 6. INTELSAT VI MSM Switch

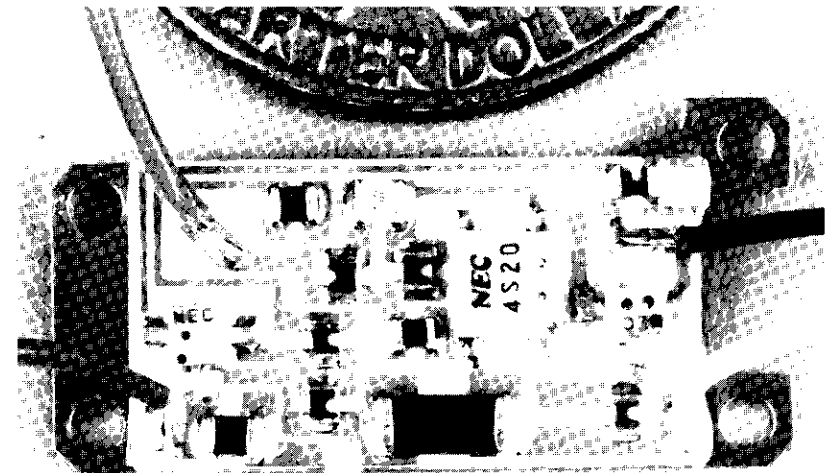


Figure 7. MSM PIN Switch Driver 7 (Engineering model)

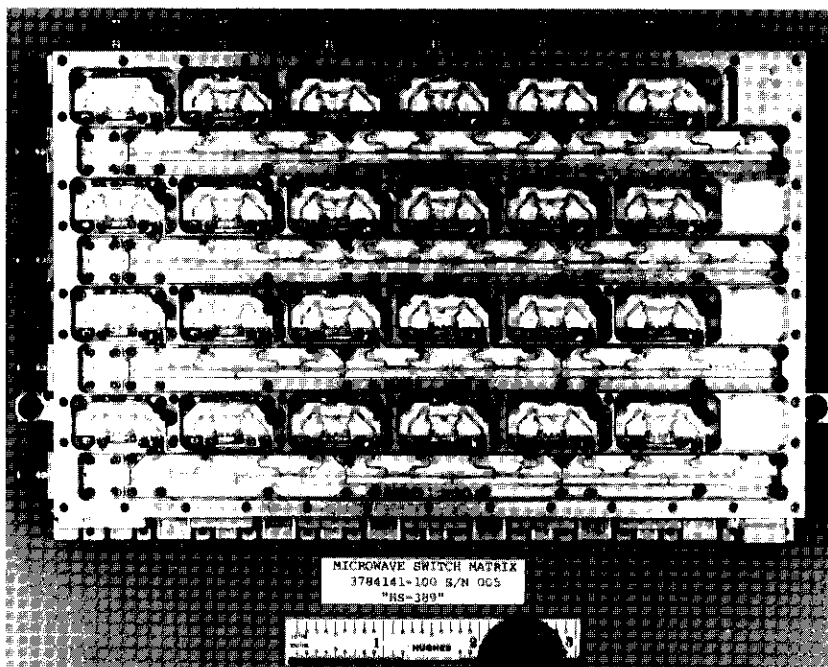


Figure 8. Top View of the  $4 \times 6$  MSM

switch element, depending on the switch state. The output of each switch element propagates to the output plane of the MSM via an RF feedthrough, and the transmitted signal is coupled to the output column in the bottom plane.

Figure 9 shows a bottom view of the  $6 \times 6$  MSM. Identical couplers were used in the input rows and output columns, rather than using different coupling ratios to equalize path-to-path insertion loss. This resulted in a single coupler design that is useful for all locations, thus minimizing the development cycle and providing design modularity.

Chip attenuators (in 0.25-dB increments) were used to minimize path-to-path insertion loss variation. The attenuator values were chosen based on the measured performance of the unequalized MSM. The losses in the MSM were partially compensated for by adding a preamplifier with approximately 22-dB gain in each row of the MSM. The preamplifier was a two-stage FET amplifier with isolators, employing a temperature-compensated bias network.

The primary function of the MSM input logic is to process and store MSM configuration data received from the DCU. Under normal operating conditions, one DCU is active and sends control signals to the MSM input logic. These

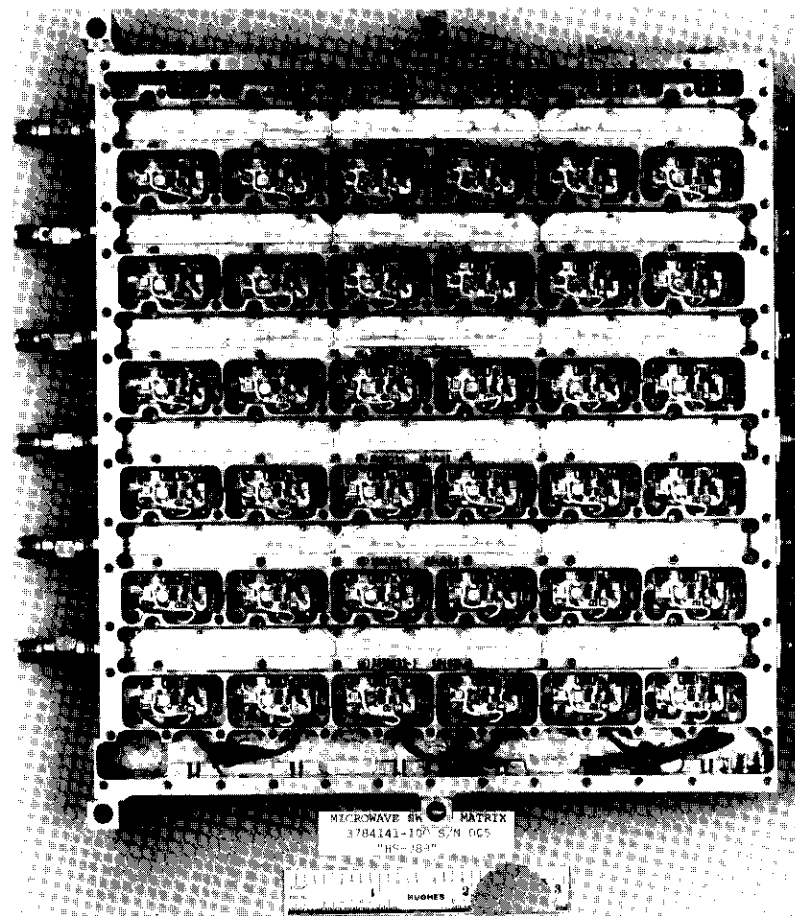


Figure 9. Bottom View of the  $6 \times 6$  MSM

signals consist of serial control words, serial transfer clocks, switchover, and timing source selection signals. The serial control words are transferred to the input logic by clock signals to minimize timing skew. To further control timing skew, the serial control words and serial transfer clocks are processed by co-packaged line receivers and multiplexers. A serial control word consists of three 4-bit groups, each containing the binary coded decimal representation of the switch to be activated in a particular output column. This arrangement takes advantage of the fact that only one switch has to be ON in an MSM column at any time. The on-board memory requirements for the DCU are thus

significantly reduced. Bias and control lines connect the switch drivers to the PIN diode switches, from one MSM plane to the other.

The redundancy switches at the input also provide protection against the possibility of a preamplifier failure. The input logic circuits are completely redundant. In particular, the input logic has two separately powered functional logic circuits diode OR-ed at the connection to the switch drivers to accommodate failures. The line receivers are powered in parallel with their corresponding DCUs to provide complete redundancy. The connections between the DCUs are cross-strapped to the two input logic circuits through the use of separate multiplexers in each circuit. A similar arrangement cross-straps the three timing sources to the input logic circuits. The power distribution scheme preserves redundancy, with the two power supplies cross-strapped independently to the MSM and preamplifiers, the input logic, and the DCUs.

The MSM power supply conditions the spacecraft bus supply to produce the required voltages for the MSM and DCU. High-efficiency operation of the power supply is achieved by using low on-state resistance power FETs as synchronous rectifiers. Switching in the MSM power supplies is accomplished by four electromechanical double-pole, double-throw (DPDT) switches. The relays in the power supply switching unit are activated by commandable solid-state drivers.

### MSM test results

An automated test setup was used to measure the critical performance parameters of the MSM, including insertion loss, on-to-off attenuation, path-to-path gain variations, RF coupling, isolation, and switch transient (rise and fall) times. This setup facilitated efficient testing of the MSM with redundant units within the MSM, and provided a computerized database. Tracking and reproduction of unit performance through subsystem, system, and spacecraft-level testing thus became relatively simple. The measurement system stepped across the frequency bands of interest in 5-MHz steps to measure frequency response. The transient responses (*i.e.*, RF waveforms during path changes) were measured through a crystal detector connected to a high-speed digital oscilloscope. The oscilloscope was also connected to the computer, and the digitized waveforms were stored for later analysis and reference as required. A custom-built T&C box simulated the spacecraft DC bus, T&C units, and the DC loads presented by the DCUs. The box was manually controlled to select the input logic, DCU, MSM power supplies, and cross-strap arrangement for test.

The on/off attenuation ratio for all MSM paths was measured to be better than 50 dB over the acceptance temperature range. The maximum path-to-

path variation of all MSM switches was less than 1 dB over the acceptance temperature range and frequency band of interest. Figure 10 shows typical MSM path-to-path gain variation data for six switches in one row.

Tests were also performed to measure the isolation between various paths in the MSM. The RF coupling was measured by turning five switches in each MSM row on and off, while maintaining one switch in the static mode. Tests verified that the dynamic performance of the SS-TDMA paths did not degrade the RF performance of any static path by more than 0.2 dB.

During MSM unit tests, all 120 rise and fall times were measured and photographed to demonstrate that there was no degradation of switch transition performance. Figure 11 shows a typical switch transition.

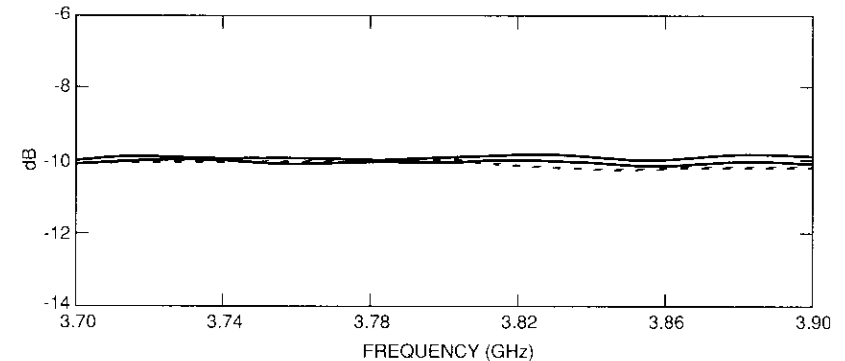
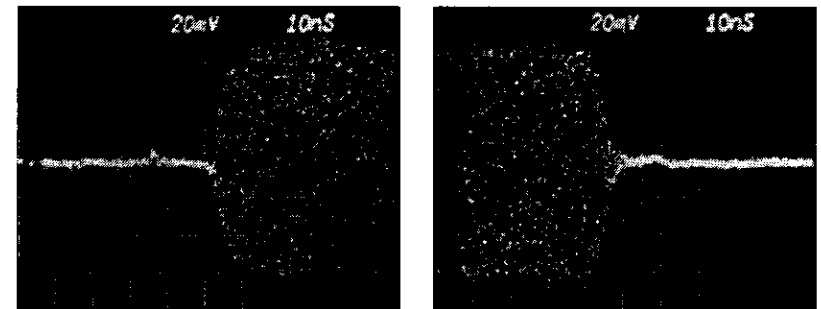


Figure 10. MSM Gain Variation in One Row



(a) Unit-Level Rise Time

(b) Unit-Level Fall Time

Figure 11. Transient Times of the MSM Switch Elements

**Distribution control unit**

The DCU [22] on board the INTELSAT VI spacecraft was designed to control, coordinate, and synchronize all the switching patterns for the on-board SS-TDMA subsystem. Each TDMA channel is provided with a set of two DCUs which act as primary and backup control units. Provision is made in the design for keeping both DCUs powered during such unusual circumstances as failure recovery and traffic switchovers, and to allow the isolation and detection of problems occurring on the spacecraft.

Each DCU is designed to operate independently using its own internal clock. A phase-locked loop is provided to synchronize the operation of the internal clock with the on-board clock for the TDMA subsystem. Each DCU receives its power from a separate power source, which also shares the MSM load. Independent command, telemetry, and status information is incorporated into the DCU design. Figure 12 is a functional block diagram of the DCU, and Figure 13 depicts the INTELSAT VI DCU hardware.

**DCU design concept**

The DCU design employs a modular concept in which the timing module, MSM interface logic, memory and error correction circuit, and T&C interface are independently designed and tested.

The timing module generates all the required timing signals used in DCU operations. The phase-locked loop locks onto the external unit clock (944 kHz), and a multiplier/divider chain in the timing module generates 8, 4, 2, 1, one-half, and one-quarter times the unit clocks signals that are used to control various operations in the DCU, such as transferring switch pattern data to the MSM, memory addressing, error correction, and T&C interfaces.

The MSM interface logic transfers the error-corrected data read from the DCU memory into a shift register in the input logic in two 12-bit words, using a 7.662-MHz transfer clock generated by the timing module. The 24-bit data stream is stored in a register in the MSM input logic before the interface logic issues a switchover signal to the MSM to implement the newest switching pattern. The MSM, in turn, gates this switchover signal with the next available unit clock and executes the switching pattern, accomplishing a synchronized switchover to the next traffic switching pattern.

The memory module covers all aspects of storage, retrieval, and processing for the traffic pattern stored in the DCU. Each DCU is provided with nine memory chips (93 L422 RAM) configured as three independently addressable and accessible 256 × 12 memories. One of these memories is kept on-line to carry the MSM traffic pattern. The contents of the on-line memory are sent

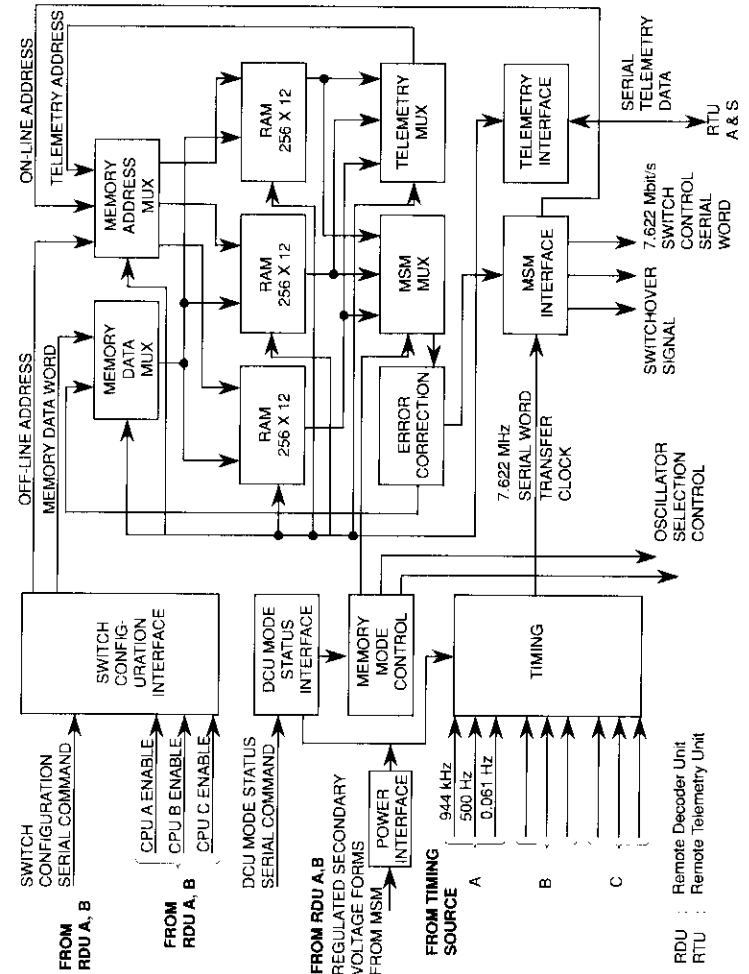


Figure 12. Functional Block Diagram of the DCU

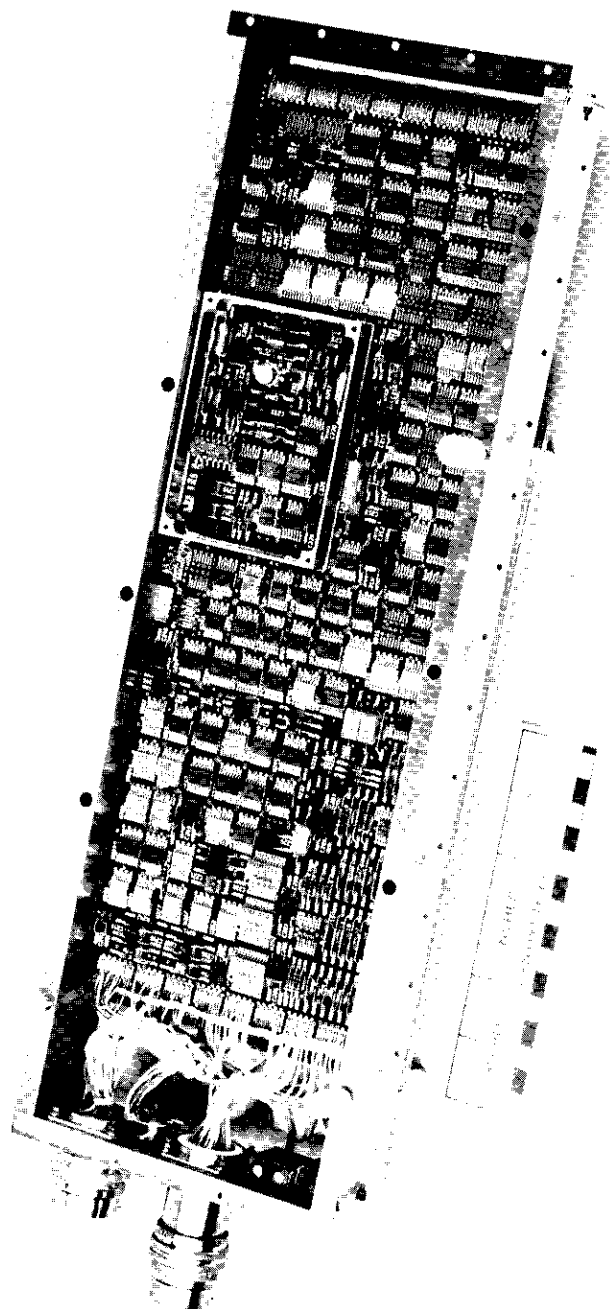


Figure 13. The INTELSAT VI DCU

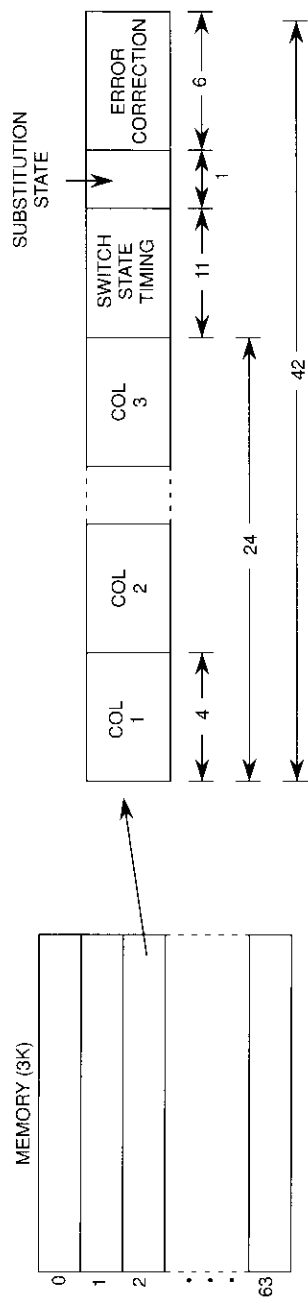
through an error correction algorithm to detect and correct all single-bit errors. The other two memories (referred to as the off-line and standby memories) provide backup functions. In actual operation, the off-line memory is programmed to have data identical to that of the on-line memory for fast recovery from memory-related failures. The standby memory may carry entirely new data or a special acquisition pattern to acquire the satellite during the TDMA system startup mode. All three memories are interchangeable by ground command, and the contents of any one of the three memories, together with overall DCU status, are telemetered at one time. The on-line memory operations and the telemetry operations are independent to allow telemetry read-out of memory contents without conflict. A similar situation exists while the off-line memory and its telemetry readout are loaded.

The error-correction scheme implemented in the DCU is a variation of the Hamming code. In this high-speed hardware implementation, the DCU reads 12 bits of data from the on-line memory four times and generates a 6-bit error syndrome. The syndrome is then compared with the 6 bits stored in the DCU memory for error detection. Once an error is detected, the hardware corrects that particular bit and updates the 12-bit word in the DCU memory. Hence, a single-bit error will be corrected in 2 ms, which is the INTELSAT VI spacecraft TDMA frame rate. The off-line and standby memories accumulate all errors that can be independently read out through telemetry and corrected from the ground.

Finally, the T&C module of the DCU interfaces with the T&C subsystem, and thus can be accessed through ground command. The off-line memory may be programmed by ground command, read through telemetry, and corrected for errors without disturbing DCU operation. This T&C interface hardware also transmits DCU configuration information every telemetry major frame. This information includes memory status, on-board clock status, the last state address (LSA) of the on-line memory carrying the active traffic pattern, and error flags indicating single-bit errors.

#### **DCU operation**

The DCU uses a 42-bit word to define each switch state of the SS-TDMA subsystem. As shown in Figure 14, 24 bits are used to control all 60 switch elements of the MSM (4 bits per column), 11 bits provide switch state timing, 6 bits are used for FEC, and 1 bit is used for the special substitution state. The DCU monitors and implements the special substitution state during the first TDMA frame of the superframe. A flag in each switch state control word indicates whether the next switch control word is part of the normally executed traffic pattern or part of the special substitution state. At the beginning



- 4 bits per column allow 16 possible connections. Only 10 are needed for a 10 x 6 MSM.
- 11 bits of switch state timing define start of switch state in terms of FUs. Total FUs per 2-ms frame = 1,888.
- Substitution state used for beginning of superframe (8,192 frames).
- 6-bit code used to correct SEU errors.

Figure 14. DCU Memory Format for Switch States

of the superframe, the DCU receives a superframe clock signal. If it is the first TDMA frame of the superframe, the DCU processes and implements the substitution state and skips the next normally executed pattern. If it is not the first TDMA frame of the superframe, the DCU processes and implements the normally executed traffic pattern and skips the substitution state. The substitution state can also be enabled and disabled by ground command so that, after ground-to-spacecraft synchronization is established, the normally executed pattern is always executed regardless of the TDMA frame count.

The DCU also provides an LSA option that allows the operator to specify the number of DCU addresses being used. During switch state data processing, the DCU checks an address counter against the value stored in the LSA command register. When the LSA is reached, the DCU does not process any more data until the TDMA frame clock clears all the registers and starts a new TDMA frame.

The INTELSAT VI DCU was designed using low-power Schottky transistor-transistor logic (TTL) because of its high speed, low power consumption, and resistance to total dose radiation. Cosmic radiation is known to transfer sufficient energy in these devices to upset the logic state, causing SEUs. Cyclotron tests on sample logic devices were conducted at Jet Propulsion Laboratories (JPL) to help quantify the upset rate of these devices and their sensitivity to cosmic radiation. The DCU on-line memory contains about 3,072 bits of information and is protected from single-bit errors by error-correction hardware. While the off-line and standby memories will accumulate the errors, they can be read out and corrected through ground command. The DCU provides error flags in the telemetry suggesting bit upsets.

**Test program**

Because of operational complexity of the INTELSAT VI DCUs, an extensive test program was implemented to evaluate the DCU hardware. The test set simulated the T&C subsystem and generated the three independent on-board clock sources to which the DCU is phase-locked. Instead of simulating the MSM, the tester read the serial data stream and switchover signal going to the MSM and flagged all errors related to bit stream and timing parameters. All performance verifications were made during module-level and unit-level tests in a thermal chamber at ambient, hot, and cold test phases. The following representative tests were successfully performed at each unit-level test phase:

- Memory verification
- Phase-locked loop locking range
- Slowest and fastest switching rates

- Timing measurements
- Error correction
- T&C verification
- Substitution state control
- Timing.

**Timing source and on-board clock generator**

The INTELSAT VI timing source [10] generates reference timing for the SS-TDMA subsystem. The daily drift of the on-board clock is controlled to limit the required terrestrial buffer capacity [23],[24]. Therefore, the on-board clock is designed to be a highly stable common clock source for all four DCUs and two MSMs, so that system synchronization can be achieved. The on-board clock consists of two units: the dual oven-stabilized crystal timing source oscillator (TSO); and the timing source digital electronics (TSDE), which generates and distributes all required timing signals to the DCU and MSM. Figure 15 is a functional block diagram of the TSO/TSDE.

Three independent TSO/TSDE chains are provided on each spacecraft. Each DCU/MSM pair can operate independently on any one of these three on-board sources. Cable lengths are equalized to minimize the propagation delay between the various drivers and input ports. The TSO/TSDE clock source provides the 944-kHz unit clock, the 500-Hz frame clock, and the 0.061-Hz superframe clocks to the DCU and MSM. TSO/TSDE unit selection is accomplished through the DCU, which commands the MSM to select the identical source for both SS-TDMA channels to facilitate synchronous switch pattern execution.

The TSO provides a 5.664-MHz source to the TSDE. Its high-Q output circuit provides a stable 5-dBm signal to the TSDE to generate the 50-percent duty cycle clock pulses for distribution to the DCU and MSM. The TSO is an oven-stabilized (72°C) voltage-controlled crystal oscillator (VCXO) designed and manufactured to provide an average maximum daily frequency drift of  $5 \times 10^{-11}$ . For plesiochronous operation, it is necessary to maintain an absolute frequency drift of less than  $1 \times 10^{-11}$  over 72 days. The TSO provides a frequency update capability to adjust its absolute frequency using a 12-bit commandable VCXO in the oscillator circuitry. The oscillator has negligible sensitivity to radiation ( $1 \times 10^{-12}$ /rad) and is well shielded to provide no more than 10,000 rad of accumulated radiation for a 10-year mission. Crystal oscillators generally age in either the positive or negative direction. Because slowly drifting, negatively aging oscillators may stabilize over time and reverse aging direction, it was necessary to screen and monitor every TSO for its long-term aging characteristics. All of the TSOs used in the INTELSAT VI

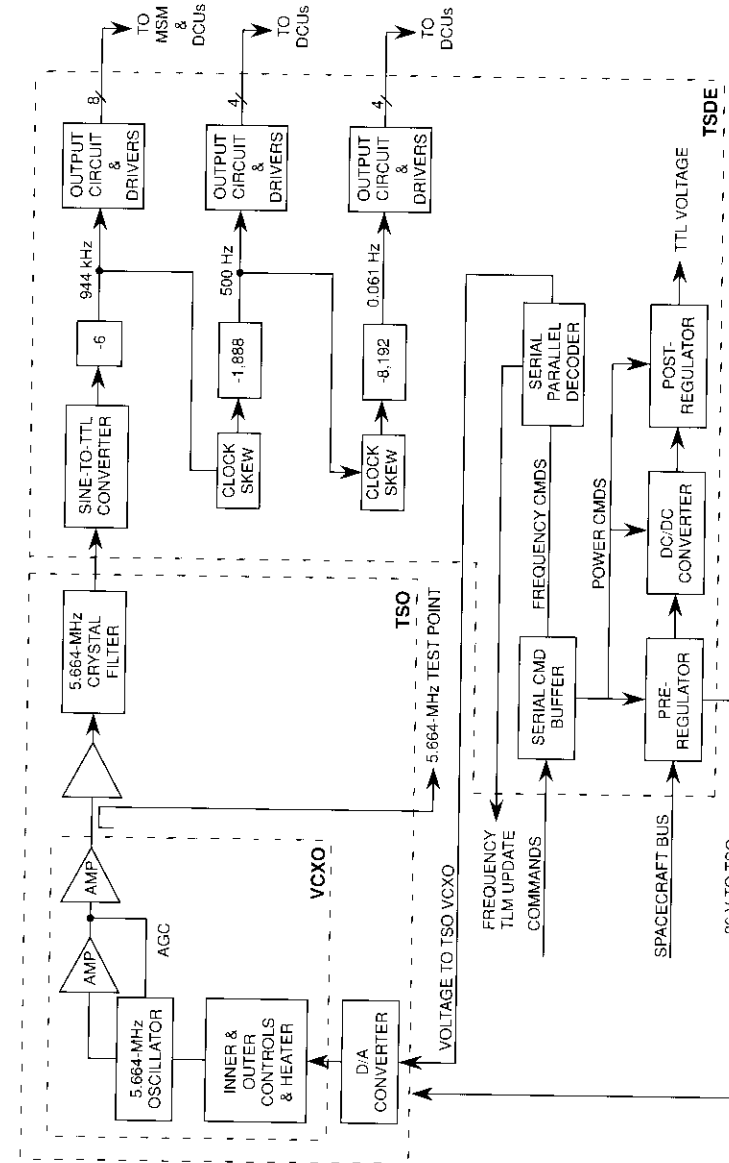


Figure 15. TSO/TSDE Functional Block Diagram

program have better than  $3 \times 10^{-8}$  per 500-ms short-term stability or equivalent phase noise performance.

The long-term drift of the TSO was specified not to exceed  $5 \times 10^{-11}$  per day, together with an average frequency step of  $\pm 8 \times 10^{-11}$  (update capability) to meet mission requirements. A burn-in program was implemented at Hughes Aircraft Company (HAC) in which every TSO was placed on a burn-in rack and its frequency drift measured over a period ranging from 6 months to 3 years. A measurement algorithm was developed in which 240 frequency measurement samples were taken every 8 hours and averaged to achieve a measurement accuracy of better than  $1 \times 10^{-11}$ . Figure 16 shows a typical burn-in curve. The TSO is tunable over a +0.6 to -1.4 Hz range centered about 5.664 MHz. Only half of this range may be used over a 10-year mission. Figure 17 shows typical TSO-commandable frequency data.

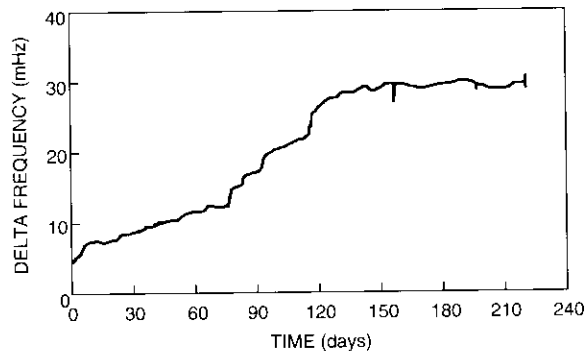


Figure 16. TSO Burn-In Curve

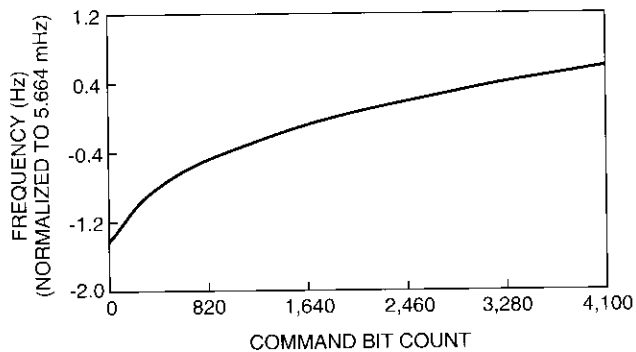


Figure 17. TSO Frequency vs Command

The INTELSAT VI TSDE (Figure 18) employs TTL counter chips to generate clocks for distribution. These chips have higher immunity to cosmic radiation than their low-power Schottky TTL counterparts. The INTELSAT VI TDMA network is vitally dependent on the stability of the clock phase. During system-level tests, a major effort was undertaken to monitor the stability of the 500-Hz frame clock phase during thermal vacuum tests.

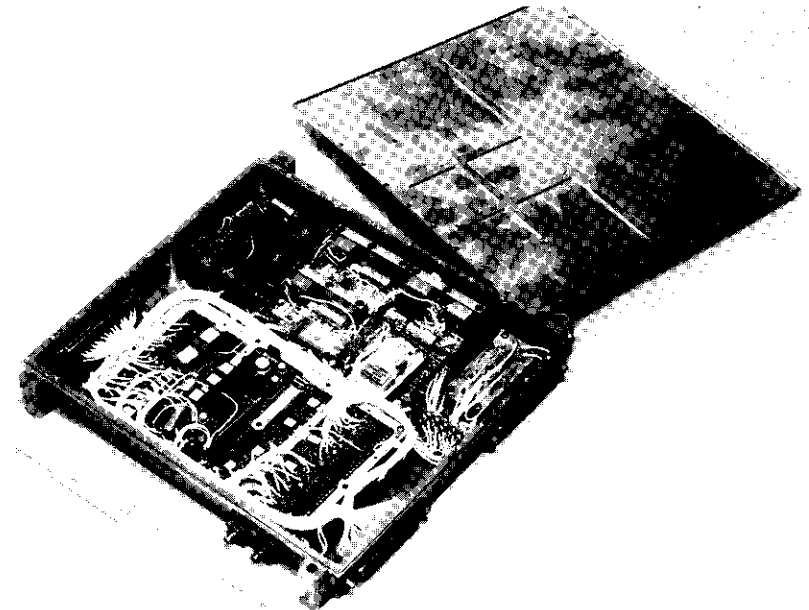
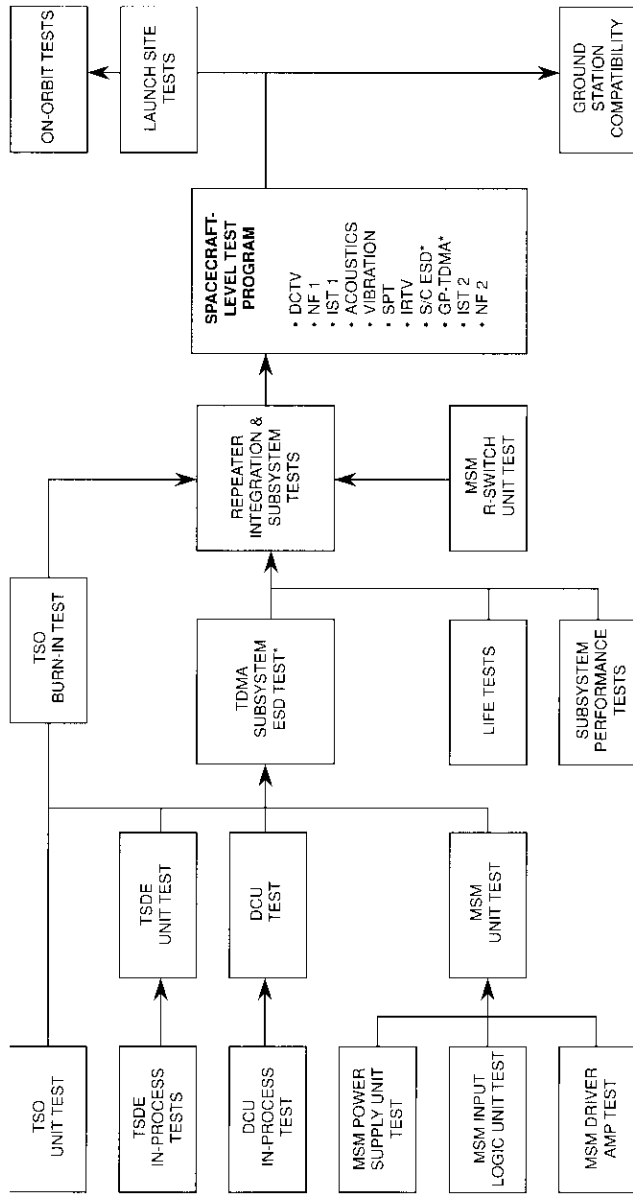


Figure 18. The INTELSAT VI TSDE

### SS-TDMA system test program

The SS-TDMA test program (Figure 19) provided extensive testing of the on-board hardware, including unit-level testing, subsystem-level testing, and testing after integration with the payload [25]. Unit-level tests of the MSM, DCU, and TSDE during the hardware development phase verified functional operation, input/output performance characteristics, and interfaces to the power and T&C subsystems. During these tests, the interface signals to each unit (*i.e.*, power supply, DCU, T&C, and TSO/TSDE) were adjusted to predicted end-of-life values to demonstrate performance margins. The fully assembled MSM, DCU, and TSDE units were exposed to environmental



\*Dual units (prototype spacecraft only).  
 SPT : Spacecraft Performance Tests  
 IRTV : Infrared (full-spacecraft) Thermal Vacuum Tests  
 NF : Near-Field  
 DCTV : Despun Compartment (payload) Thermal Vacuum Test  
 GP-TDMA : Ground-Pulsed TDMA (EM bus pulsing) Tests  
 IST : Integrated System Test

Figure 19. INTELSAT VI SS-TDMA Test Program

extremes such as temperature, vibration [22], and electrostatic discharge (ESD). Accelerated life tests were also performed under ambient conditions.

At the subsystem level, a T&C processor was designed to provide the T&C interfaces to the SS-TDMA subsystem and to generate, display, and load data pattern files to and from the DCU. These tests included operation of the SS-TDMA hardware in both semi-static and dynamic modes. In the semi-static mode, the DCU was commanded to repeatedly make one MSM interconnection for the complete 2-ms TDMA frame, and thus freeze the switch state for the duration of the test.

The RF performance of the subsystem was checked for continuous operation. In the dynamic mode of operation, control words for several switch states within the TDMA frame (maximum 64) were loaded into the DCU memory, and the interconnections and switch state durations were verified. Subsystem performance tests were conducted at HAC during ESD testing and were verified again during engineering model evaluation at COMSAT Laboratories (Figure 20).

**SS-TDMA functional and subsystem tests**

Functional tests verified that the SS-TDMA subsystem responded correctly to switch states in various modes of operation. During dynamic functional testing, the full memory capabilities of the SS-TDMA subsystem were exercised

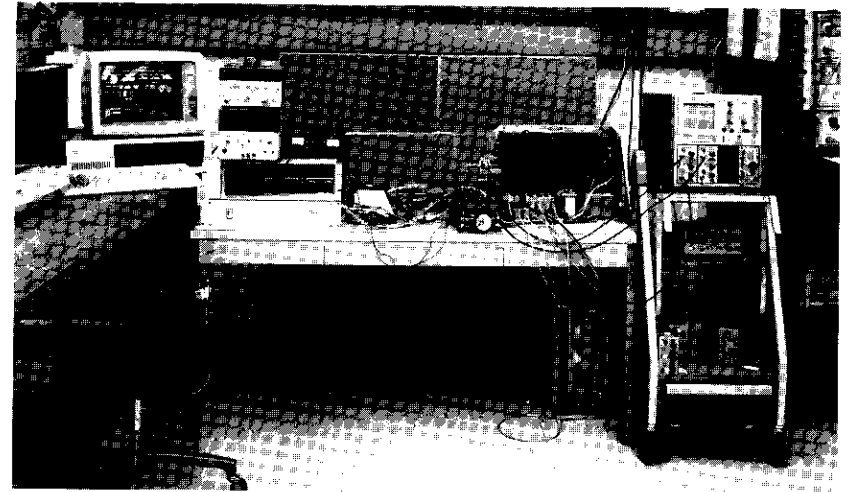


Figure 20. Test Setup for INTELSAT VI SS-TDMA Subsystem Evaluation

at the highest switching rates. A switch-state data pattern was loaded into the DCU memory at the fastest switching rate (4  $\mu$ s) to exercise each switch in each MSM row. All six outputs were detected and monitored on a logic analyzer. In the typical logic analyzer trace shown in Figure 21, each output was turned on for different time durations over a 2-ms TDMA frame. These tests were performed on all combinations of unit redundancy configurations utilizing all three DCU memories. During the test, switch uniqueness is also verified to ensure that the column decoder logic performs properly, so that the correct switch turns on and all other switches in the MSM column are off. Rows 7 and 10, which provided binary control complements (0110 and 1001), were used to test subsystem switch uniqueness. The subsystem was programmed to turn the switches in these two rows on, while applying RF to the other rows, thus verifying that the output showed no RF on the logic analyzer. RF outages during redundancy handover were characterized by configuring the SS-TDMA to the semi-static mode and performing handovers while monitoring the duration of the RF outage on the logic analyzer.

The high-resolution telemetry used during the command functional tests provided unique signatures of individual unit power consumption which, together with switching configurations and associated duty cycles, provided another means of verifying proper SS-TDMA switching operation. The command functional tests also verified DCU error-correction capability. Single-bit errors were introduced into DCU memory control words, and the memory

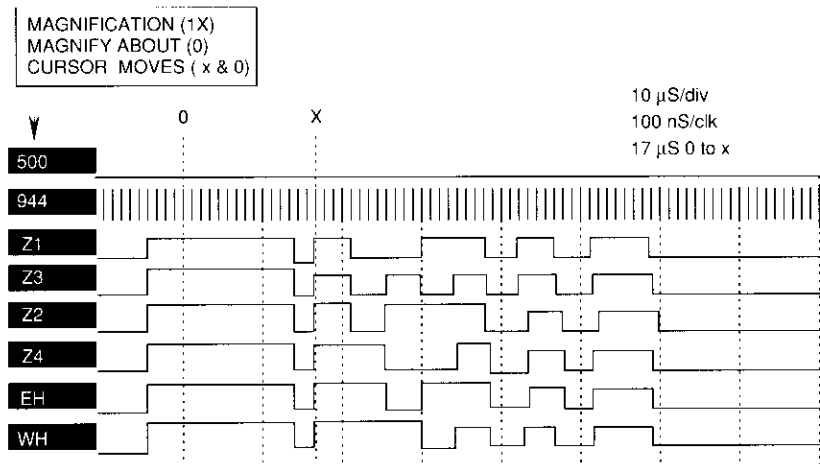


Figure 21. Logic Analyzer Trace for MSM Output

contents were then read via telemetry to verify that the error was properly corrected. Telemetry signatures of multiple errors in the DCU memory were also checked.

The timing performance of the SS-TDMA subsystem is critical to INTELSAT VI SS-TDMA network operation. Therefore, switch transient times, timing jitter, and phase offset between channels were carefully characterized to establish the SS-TDMA guard time (the time between switch states in which data transmission should not take place). These measurements were made by turning each MSM switch on and off repeatedly and measuring the detected RF signal with a time-interval counter. For each switch rise and fall time, the  $3\sigma$  value corresponding to the jitter of each switch, and the mean value of the transition time, were measured. The electrical path length variations were subtracted from the measured value, and these data were used to determine the worst-case jitter, worst-case path-to-path variation within each channel, and the phase offset between the two SS-TDMA channels. The 10- to 90-percent rise and fall times of the earliest and latest transitions were measured and recorded using a programmable oscilloscope. From this information, the guard time between switch states was calculated to be less than 128 ns (8 symbols) over the acceptance temperature range.

Because the timing aspects of the system are critical to TDMA operation, special tests were performed on the protoflight spacecraft to verify that phase jumps did not occur in the subsystem over long periods of operation. The SS-TDMA was programmed to a constant duty cycle switching rate, and the RF output was monitored for several days over the qualification thermal range to verify that no phase jumps occurred.

At the system level, the isolation performance of the entire repeater was characterized by measuring the isolation between different coverages utilizing several worst-case SS-TDMA interconnection paths (*i.e.*, longest R-switch paths, row-to-row, and column-to-column paths). Measured data demonstrated that the isolation for the entire repeater across all MSM paths is better than 47 dB over the acceptance temperature range. In addition, arc and direct-injection ESD tests were performed at the subsystem level by subjecting the operating subsystem to 25 mJ/10 kV at several ground and harness chassis points within the subsystem. The RF output and timing signals were monitored for upsets and phase jumps, as manifested by unexpected changes in the RF and/or clock signal outputs. Similarly, subsystem electromagnetic interference tests consisted of injecting a 1-V peak-to-peak signal into the bus power lines to detect anomalies in the subsystem. The switching response of the SS-TDMA subsystem was monitored during both tests.

### In-orbit tests

After launch of the INTELSAT VI spacecraft, an extensive set of in-orbit tests was performed. The tests were grouped into three categories:

- *Command Functional Tests.* These tests were carried out from the INTELSAT Satellite Operations Center in Washington, D.C. All units were functionally checked using telemetry. Power consumption, redundancy, and various operational configurations were verified in orbit. The DCU memory loading, TSO frequency update capability, and unit stabilization profile were successfully verified.
- *RF Performance Tests.* The saturation flux density, gain-to-noise temperature ratio ( $G/T$ ), and frequency response performance were measured through all 120 switches, keeping the MSM in a static mode. These tests were performed at the Fucino, Italy, test site by reorienting the spacecraft to gain access to all 12 transponders through six different antenna beams. The measured results correlated very well with predictions.
- *Digital TDMA Tests.* In-orbit, real-time, full dynamic tests were performed using four earth stations covering the Atlantic Ocean Region. Transmitting stations from Etam, West Virginia; Tanum, Sweden; Tangua, Brazil; and Zamingoc, Cameroon, were used to successfully test the TDMA payload in digital operating configuration. The DCU was programmed in broadcast mode, and each earth station was requested to transmit RF switched in a unique pattern. These patterns were verified through all four earth stations simultaneously. In addition to the dynamic tests, all unit interfaces, redundancy switches, and configurations were successfully verified.

### Conclusions

The INTELSAT VI SS-TDMA payload is currently carrying TDMA traffic on the INTELSAT VI spacecraft over the Atlantic Ocean Region. All SS-TDMA hardware is operating normally and within predicted performance values. The successful introduction of on-board SS-TDMA hardware on INTELSAT VI has been largely due to critical selection of designs for the MSM, DCU, and TSO/TSDE, in combination with a carefully planned and extensive test program. The coupler crossbar architecture for the MSM provided a simpler control implementation, broadcast capability, and a modular design for ease of fabrication. FEC was used in the DCU to correct for SEUs and to achieve proper SS-TDMA subsystem operation. Long-term stability of the TSO was achieved by placing a highly stable crystal oscillator in a temperature-controlled oven and

by providing commandable frequency correction capability. A 10-year probability of survival in excess of 0.99 has been designed by providing 10-for-6 ring redundancy for the MSM, 2-for-1 redundancy for the DCU, and 3-for-1 redundancy for the timing source. Unit tests, subsystem tests, and spacecraft-level tests verified the performance and integrity of the on-board SS-TDMA subsystem.

### Acknowledgments

*The authors wish to thank their many colleagues at COMSAT Laboratories, Hughes Aircraft Company (HAC), and INTELSAT. The hardware design and implementation documented herein were performed at HAC, El Segundo, California. The authors gratefully acknowledge the contributions of all those who participated in the concept and specification development, design, integration, and testing of the SS-TDMA subsystem for the INTELSAT VI spacecraft.*

*This paper is based on work performed, in part, under the sponsorship and technical direction of the International Telecommunications Satellite Organization (INTELSAT). Any views expressed are not necessarily those of INTELSAT.*

### References

- [1] S. B. Bennett and D. Braverman, "INTELSAT VI—A Continuing Evolution," *Proc. IEEE*, Vol. 72, No. 11, November 1984, pp. 1457–1468.
- [2] N. Wong, "INTELSAT VI—A 50 Channel Communication Satellite With SS-TDMA," Satellite Communications Conference, Ottawa, Canada, June 1983, *Proc.*, pp. 20.1.1–20.1.9.
- [3] M. F. Caulfield *et al.*, "INTELSAT VI Antenna Systems Design and Development," *Large Space Antenna System Technology*, Vol. 2, November 1982, NASA Conference Publication No. 2269, pp. 743–765.
- [4] X. Rozec and F. Assal, "Microwave Switch Matrix for Communications Satellites," IEEE International Conference on Communications, Philadelphia, Pennsylvania, June 1976, *Conf. Rec.*, Vol. 3, pp. 35.13–35.17.
- [5] F. Assal and X. Rozec, "Fast Fully Redundant, 4 GHz,  $8 \times 8$  Microwave Switch Matrix for Communications Satellites," 9th European Microwave Conference, Brighton, England, September 1979, *Proc.*, pp. 218–222.
- [6] F. Assal *et al.*, "A Wideband Satellite Microwave Switch Matrix for SS/TDMA Communications," *IEEE Journal on Selected Areas in Communications*, Vol. SAC-1, No. 1, January 1983, pp. 223–231.
- [7] F. Assal *et al.*, "Satellite Switching Center for SS-TDMA Communications," *COMSAT Technical Review*, Vol. 12, No. 1, Spring 1982, pp. 29–68.
- [8] R. K. Gupta and F. T. Assal, "Integration, Environmental, and Radiation Testing of a Microwave Switch Matrix System," IEEE International Conference on Communications, Denver, Colorado, June 1981, *Conf. Rec.*, pp. 5.4.1–5.4.6.
- [9] B. A. Pontano, A. I. Zaghoul, and C. E. Mahle, "INTELSAT VI Communications Payload Performance Specifications," *COMSAT Technical Review*, Vol. 20, No. 2, Fall 1990, pp. 271–308.

- [10] C. L. Maranon *et al.*, "Timing Source Oscillator Control," scheduled for publication in *COMSAT Technical Review*, Vol. 22, No. 2, Fall 1992.
- [11] S. J. Campanella *et al.*, "SS-TDMA System Considerations," *COMSAT Technical Review*, Vol. 20, No. 2, Fall 1990, pp. 335-371.
- [12] F. Assal, C. Mahle, and A. Berman, "Network Topologies to Enhance the Reliability of Communications Satellites," *COMSAT Technical Review*, Vol. 6, No. 2, Fall 1976, pp. 309-322.
- [13] G. Forcina and B. A. Pontano, "Network Timing and Control in the INTELSAT VI SS-TDMA System," 6th International Conference on Digital Satellite Communications, Phoenix, Arizona, September 1983, *Proc.*, pp. X-9-X-15.
- [14] S. J. Campanella and J. V. Harrington, "Satellite Communications Networks," *Proc. IEEE*, Vol. 72, No. 11, November 1984, pp. 1506-1519.
- [15] Y. Ito *et al.*, "Analysis of a Switch Matrix for an SS/TDMA System," *Proc. IEEE*, Vol. 65, No. 3, March 1977, pp. 411-419.
- [16] T. Inukai, "An Efficient SS/TDMA Time Slot Assignment Algorithm," *IEEE Transactions on Communications*, Vol. COM-27, No. 10, October 1979, pp. 1449-1455.
- [17] J. A. Lunsford *et al.*, "SS-TDMA System Design," scheduled for publication in *COMSAT Technical Review*, Vol. 22, No. 2, Fall 1992.
- [18] R. Bedford *et al.*, "SS-TDMA Reference Terminal," scheduled for publication in *COMSAT Technical Review*, Vol. 22, No. 2, Fall 1992.
- [19] R. Gupta, J. Potukuchi, and F. Assal, "Ground-Based Failure Diagnostic/Monitoring Schemes for SS-TDMA Satellites," 7th International Conference on Digital Satellite Communications, Munich, West Germany, May 1986, *Proc.*, pp. 393-400.
- [20] P. T. Ho *et al.*, "Dynamic Switch Matrix for the TDMA Satellite Switching System," AIAA 9th International Communication Satellite Systems Conference, March 1982, *A Collection of Technical Papers*, pp. 135-141.
- [21] B. J. Cory and M. Berkowitz, "A High Capacity Satellite Switched TDMA Microwave Switch Matrix," National Telecommunications Conference, December 1981, *Conf. Rec.*, pp. F.7.6.1-F.7.6.5.
- [22] K. Jarett, "Operational Aspects of Intelsat VI Satellite-Switched TDMA Communications System," AIAA 10th Communication Satellite Systems Conference, Orlando, FL, March 1984, *A Collection of Technical Papers*, pp. 107-111.
- [23] S. J. Campanella and T. Inukai, "Satellite Switch State Time Plan Control," 6th International Conference on Digital Satellite Communications, Phoenix, Arizona, September 1983, *Proc.*, pp. X-16-X-26.
- [24] T. Inukai and S. J. Campanella, "Optimal On-Board Clock Control," *IEEE Journal on Selected Areas in Communications*, Vol. SAC-1, No. 1, January 1983, pp. 208-213.
- [25] A. M. Nakamura *et al.*, "Integration and Testing of the Satellite Switched TDMA (SS-TDMA) Subsystem for the INTELSAT-VI Spacecraft," 8th International Conference on Digital Satellite Communications (ICDSC8), Guadeloupe, FWI, April 1989, *Proc.*, pp. 49-57.



Ramesh K. Gupta received a B.Sc. (Honors) in electronics and communications engineering from Punjab University, Chandigarh, India, in 1974, and an M.Sc. and Ph.D. in electrical engineering from the University of Alberta, Edmonton, Canada, in 1976 and 1980, respectively. He also received an M.B.A. from the Wharton School of Business, University of Pennsylvania, in 1989. He was Punjab University Merit Scholar (1970-74) and was awarded the Alberta Government Telephones Centennial Fellowship (1976-79) for graduate research in telecommunications.

In 1980, he joined COMSAT Laboratories, where he is a Department Manager in the Microwave Technology and Systems Division. He has contributed to the application of hybrid MIC and GaAs MMIC technology in advanced satellite subsystems, and has been responsible for development of wideband microwave switch matrix (MSM) arrays, components for a 120-Mbit/s CQPSK on-board modem, and active beam-forming networks for single- and multibeam Ku-band phased-array antennas using MIC and MMIC technologies. He also contributed to the spacecraft and ground network study and support effort for the INTELSAT VI satellite program.

Dr. Gupta has served as Vice-Chairman (1987-88) and Chairman (1988-89) of the Washington, D.C./Northern Virginia Chapter of the IEEE Microwave Theory and Techniques (MIT) Society. He has authored/coauthored more than 40 papers on solid-state devices and circuits, GaAs MMICs, advanced microwave subsystems, and satellite systems. He holds two patents and was a co-recipient of the Best Paper Award for the 8th International Conference on Digital Satellite Communications (ICDSC-8). He is a Senior Member of IEEE.

Jagan N. Narayanan received a B.Sc. (engineering) degree from the University of Kerala, India, in 1972; an M.S. in electrical engineering from the University of California, Irvine, in 1978; the degree of Engineer from the University of Southern California, Los Angeles, in 1982; and an M.B.A. from Pepperdine University in 1985.

From 1973 to 1976, he worked with the Indian Space Research Organization (ISRO) in Trivandrum, India, and subsequently was employed by TRW in Redondo Beach, California. From 1982-90, he worked with COMSAT Technical Services, where he was responsible for the SS-TDMA subsystem for the INTELSAT VI spacecraft. He is currently with Space Systems/Loral in Palo Alto, California. Mr. Narayanan was co-recipient of Best Paper Award for the 8th International Conference on Digital Satellite Communications (ICDSC-8).

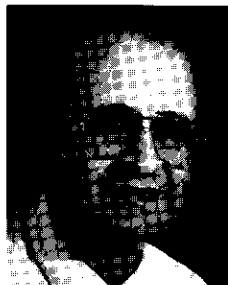




*Apryll M. Nakamura received a B.S.E.E. from the University of California at Los Angeles in 1979 and did graduate work in management at Pepperdine University, Los Angeles. She is currently Systems Engineering Manager for the SOLIDARIDAD Program, a constellation of two satellites being built by Hughes Aircraft Company to provide TV, voice, and mobile communications services to Mexico. Prior to this, she was involved in the design and development of other satellite systems for HAC, including the HS601 tri-axis developmental program, Aussat B, UHF Follow-On, MSAT, INTELSAT VI, the Ku-band radar and communications system for the Space Shuttle, and the GMS/GOES programs. Also at HAC, she has been involved in various subsystems across both the payload and bus systems. While with the INTELSAT VI program office, she was responsible for system engineering activities associated with the design, development, and testing of the INTELSAT VI satellite-switched TDMA system.*

*Ms. Nakamura is a member of IEEE, AIAA, and the Dean's Council at UCLA. She was a co-recipient of the ICDCS-8 award for her contributions to a paper documenting the development of the SS-TDMA subsystem for INTELSAT.*

*François T. Assal received a B.E.E. and an M.E.E. from the City University of New York. He is currently Executive Director of the Microwave Technology and Systems Division at COMSAT Laboratories, where he directs research, development, and production of state-of-the-art antennas, microwave circuits, microwave systems, and GaAs MMIC technology for earth stations and satellite payloads. His management functions include the development and upgrading of technical tools for the design, analysis, performance verification, and monitoring of commercial satellite systems. Over the years, he has participated in the system optimization, design, specification, monitoring, evaluation, troubleshooting, and/or in-orbit performance testing of the INTELSAT IV to VI satellites, other COMSAT-related domestic and mobile satellites, and the Italian Space Agency/ALENIA Spazio's ITALSAT, a 30/20-GHz on-board regenerative multibeam satellite.*



*Mr. Assal has written technical papers on many subjects, including on-board regeneration of QPSK signals; highly flexible payload configurations for fixed and mobile commercial communications satellite services; network topologies to enhance the reliability of satellite payloads; optimum group-delay and amplitude-equalized elliptic function filters for both analog and digital transmission; low-loss contiguous-band multiplexers; active multibeam steering antennas; in-orbit testing; TDMA communications system monitoring of commercial satellites; MIC, MMAC, and MMIC circuit modules and subsystems such as digital multibit attenuators and phase shifters,*

*microwave switch matrices for SS-TDMA applications, and 120-Mbit/s CQPSK on-board demodulators operating directly at microwave frequencies; and highly-efficient solid-state power amplifiers.*

*Mr. Assal holds patents in communications satellite configurations and hardware. In 1982, he received the COMSAT Laboratories Research Award and was co-recipient of the ICDCS-8 Best Paper Award. He is a member of Tau Beta Pi, Eta Kappa Nu, and IEEE.*

*Brian Gibson received a B.S. in physics from the California Institute of Technology in 1973; an M.S. in physics from the University of Illinois in 1974; and a Ph.D. in physics from the University of Illinois in 1978, where he conducted experiments on the heat capacity of superconductors with magnetic impurities. From 1978 to the present, he has worked in the Space and Communications Group at Hughes Aircraft Company. He was initially involved in research and development of solid-state power amplifiers (SSPAs) using GaAs power FETs for spacecraft transmitters, and headed the section that produced the first such SSPAs flown by HAC on the Telstar 3 series of satellites. He then worked on the INTELSAT VI MSM, and subsequently was responsible for the development and production of a variety of microwave products, including a similar switch matrix for Milstar, low-noise and low-power millimeter-wave amplifiers, and high-speed MSK and QPSK modulators. He is currently a Department Manager at HAC, involved in the development and production of direct digital synthesizers and millimeter-wave systems.*



*Dr. Gibson is a member of IEEE, the Microwave Theory and Techniques Society, and the Magnetics Society.*

## **High-efficiency single ridged 16-way radial power combiner**

M. OZ, B. D. GELLER, P. K. CLINE, AND I. YOGEV

(Manuscript received February 11, 1991)

### **Abstract**

A new single ridged, 16-way, high-efficiency radial power combiner for C-band has been developed. The design employs ridged waveguide theory to calculate bandwidth and impedance, as well as a new end-launch waveguide-to-coaxial transition. The power combiner has an average insertion loss across the 3.7- to 4.2-GHz band of 0.1 dB (a combining efficiency of 98 percent), less than 1.35:1 standing wave ratio,  $\pm 0.2$  dB amplitude tracking, and  $\pm 2.5^\circ$  phase tracking. The amplitude flatness is  $\pm 0.1$  dB, and the port-to-port isolation is better than 8 dB across the band.

### **Introduction**

The demand for higher power solid-state amplifiers, and the output power limitation of individual solid-state devices, have increased the need for multiport combiners that can handle relatively high powers with low loss, and over a wide bandwidth. The radial combining structure has the advantage of low insertion loss and good amplitude and phase balance, compared to tree-type power combiners having the same transmission media [1]. The radial-cavity power combiner has more power-handling capability and lower insertion loss than the microstrip radial power combiner, but suffers from narrower bandwidth. To overcome the bandwidth limitation of the cavity combiner and the high insertion loss of the nonresonant combiner, and to obtain the advantages of both waveguide and microstrip transmission media, a radial multiport ridged waveguide has been developed [2].

This paper describes the high-efficiency, single ridged, 16-way radial power combiner shown in Figure 1. This design is based on a double-ridged, wide-bandwidth combiner covering the 4- to 10-GHz band [2], and on other versions designed for a wide range of frequencies up to Ku-band. The transmission medium is waveguide, and the combining is a nonresonance type. The combiner has the advantage of very low insertion loss and good amplitude and phase balance over the 3.7- to 4.2-GHz frequency range. It has 16 coaxial input ports and one coaxial output port, and the input ports can be replaced by pins for compact integration. This combiner has the advantage of wide bandwidth, and thus can be used as a component for wider bandwidth amplifier applications.

The power combiner design is based on ridged waveguide theory and parallel-plate characteristic impedance for the dividing structure [3],[4]; on waveguide transformer theory [5]; and on a new end-launch waveguide-to-coaxial-line transition [6]. The center probe was developed experimentally.

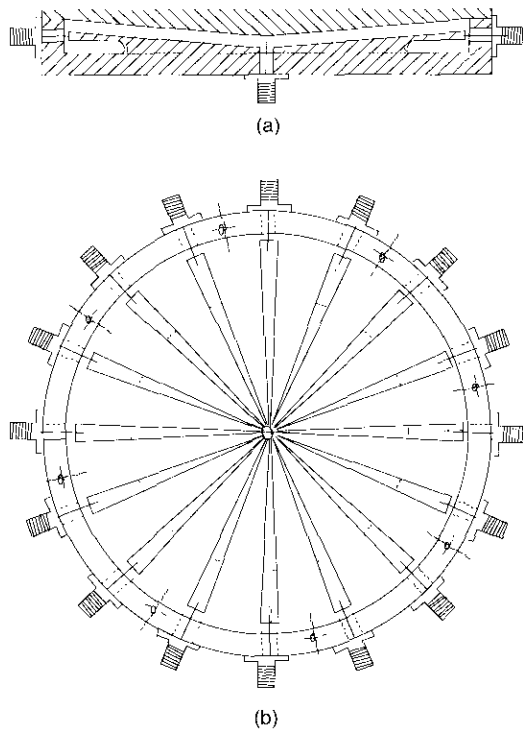


Figure 1. Single Ridged 16-Way Power Combiner

**General properties of N-way power dividers/combiners**

This section addresses some of the general properties of N-way power dividers/combiners. In particular, the effect of gain and phase imbalance on combining efficiency will be examined. Power combining losses may be due to resistive transmission line losses, mismatch losses, or imperfect phase and amplitude tracking. This discussion is based on the work of Schellenberg [7].

**Power combining losses**

The combining loss which occurs even with perfect, lossless materials is considered circuit loss and is independent of material losses. Circuit losses exist if the load and source impedances are not matched to the combiner; if the phase and amplitude tracking are not perfect; and if the combiner does not have perfect isolation between adjacent ports. An equation considering the completely general case is so complicated as to prevent insight into the characteristics and sensitivities of combiner parameters. Useful properties of power combiners become apparent when some of the variables are removed by simplifying assumptions.

Figure 2 is a general block diagram of a divider/combiner system consisting of an ideal input power divider and an output power combiner. For this analysis, the divider network is considered to be an ideal dividing network with one input and N output ports with equal amplitude and phase. The power combiner has N input ports and one output port, with an amplitude and phase

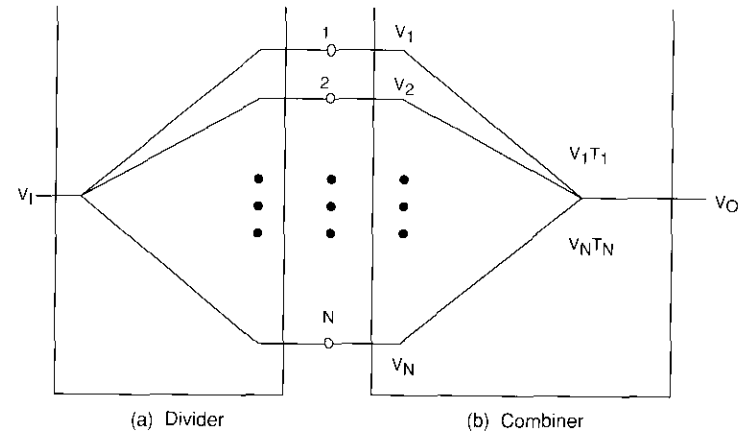


Figure 2. N-Way Power Divider/Combiner System

difference between the input ports. Assuming perfect isolation between the combiner input ports, it can be shown that the transmission coefficients and port voltages are independent of each other. With this assumption, the generalized  $N$ -way combining equation can be expressed as

$$V_o = T_1 V_1 + T_2 V_2 + \dots + T_N V_N \quad (1)$$

where, in general, all parameters are complex quantities. The variable  $T_j$  is the voltage transmission coefficient from the combiner port  $j$  to the combiner output, with a magnitude given by

$$|T_j| = (\text{power coupling, port } j \text{ to output})^{1/2}$$

Due to the assumed ideal divider and combiner and perfect combiner and divider isolation, the  $V$ 's are equal at the divider output ports, but unequal at the combiner's output common port because of the phase and amplitude imbalance at the combiner ports. The ideal coupling for an  $N$ -way combiner is  $1/N^{1/2}$ , such that in equation (1) all the  $T$ 's will be replaced by  $1/N^{1/2}$  and the phase and amplitude imbalance will be at the center port voltages. Therefore, equation (1) will become

$$V_o = 1/N^{1/2} (V_1 + V_2 + \dots + V_N) \quad (2)$$

This equation may be transformed to a more useful form by using the normalized relationship

$$P_j = |V_j|^2$$

and therefore,

$$P_o = \frac{1}{N} \left| P_1^{1/2} \theta_1 + P_2^{1/2} \theta_2 + \dots + P_N^{1/2} \theta_N \right|^2 \quad (3)$$

A vector sum of terms is used to account for the different relative phases of the combiner input signals. A combining efficiency,  $\eta_c$ , can be defined as the ratio of the combiner output power to the total combiner input power. Employing this definition, the combining efficiency is given by

$$\eta_c = \frac{1}{NP_T} \left| P_1^{1/2} \theta_1 + P_2^{1/2} \theta_2 + \dots + P_N^{1/2} \theta_N \right|^2 \quad (4)$$

where  $NP_T$  is simply the algebraic sum of the input powers. The parameter  $\eta_c$  gives a measure of the amount of available power from the input ports that reaches the combiner output port.

Equations (3) and (4) are the basic equations used to analyze the effect of the combiner amplitude and phase imbalances on the overall combining system. By setting  $\theta_j = 0$ , the equations can be employed to analyze amplitude imbalances. Alternately, with  $P_1 = P_2 = \dots = P_N$ , they can be used to study the effects of phase imbalance.

For the special case of unequal amplitude but equal phase ( $\theta_1 = \theta_2 = \dots = \theta_N = 0$ ), the equations for combiner output power and efficiency reduce to

$$P_{oA} = \frac{1}{N} \left( P_1^{1/2} + P_2^{1/2} + \dots + P_N^{1/2} \right)^2 \quad (5)$$

and

$$\eta_{cA} = \frac{1}{NP_T} \left( P_1^{1/2} + P_2^{1/2} + \dots + P_N^{1/2} \right)^2 \quad (6)$$

In general, combining efficiency is a slowly changing function of the ratio of input powers. For a two-way combiner, equation (6) becomes

$$\eta_{cA} = \frac{1}{2} \cdot \frac{\left[ 1 + \sqrt{(P_2/P_1)} \right]^2}{1 + (P_2/P_1)} \quad (7)$$

This is illustrated in Figure 3, which plots combining efficiency as a function of the ratio of the input powers. As indicated in the figure, a 3-dB difference ( $P_1/P_2 = 0.5$ ) in input power levels produces a combining efficiency of 97.14 percent, or equivalently, a combining loss of only 0.126 dB.

To further illustrate equal-phase power combining, consider a 16-way power combiner with 16 in-phase inputs of unequal amplitude. The assumed amplitude variation is equally spaced from -1 to +1 dB. For this case, the resultant combining efficiency [using equation (6)] is 99.6 percent, which implies a combiner loss of only 0.017 dB.

Compared to amplitude imbalances, phase imbalances are more detrimental to the performance of the combiner. The effect of these phasing errors can be analyzed using the general combining equation [equation (3)] with  $P_1 = P_2 = \dots = P_N$  and  $\theta_j \neq 0$ . For an  $N$ -way power combiner driven by  $N$  equal amplitudes,  $M$  of which are out of phase, equation (3) becomes

$$P_{oP} = \frac{P_{in}}{N^2} \left\{ [(N - M) + M \cos \theta]^2 + M^2 \sin^2 \theta \right\} \quad (8)$$

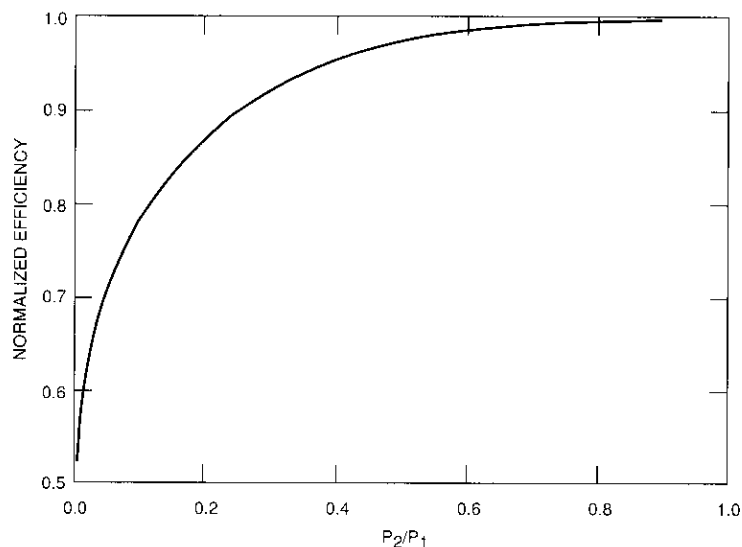


Figure 3. Combining Efficiency of a Two-Way Combiner

where  $P_m$  equals the power of each individual port and  $\theta$  equals the phase error of the out-of-phase peripheral port. For this case, the combining efficiency,  $\eta_c$ , which is defined as the ratio of the total output power of the combiner to the total input power, can be expressed as

$$\eta_{cP} = \frac{1}{N^2} \left\{ [(N - M) + M \cos \theta]^2 + M^2 \sin^2 \theta \right\} \quad (9)$$

After some algebraic manipulation, the above reduces to

$$\eta_{cP} = 1 - 2 \frac{M}{N} \left( 1 - \frac{M}{N} \right) (1 - \cos \theta) \quad (10)$$

Equation (10) is plotted in Figure 4 for  $N = 16$  and  $M = 1$  and 8. For the case where  $M/N = 1/2$  (half of the peripheral ports are out of phase), the combining efficiency is reduced to 99.8 percent, for a phase error of  $5^\circ$  (less than 0.01-dB loss).

The above discussion has considered the effect of amplitude and phase imbalance at the combiner peripheral port. While the effects of both amplitude and phase errors were treated separately for the sake of clarity, they can also be considered directly with the aid of the general combining equation [equa-

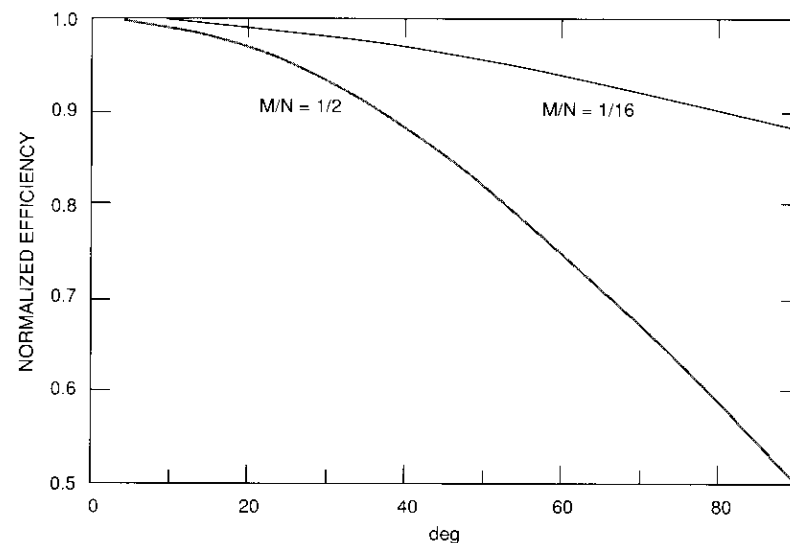


Figure 4. Effects of Phase Imbalance on Combining Efficiency

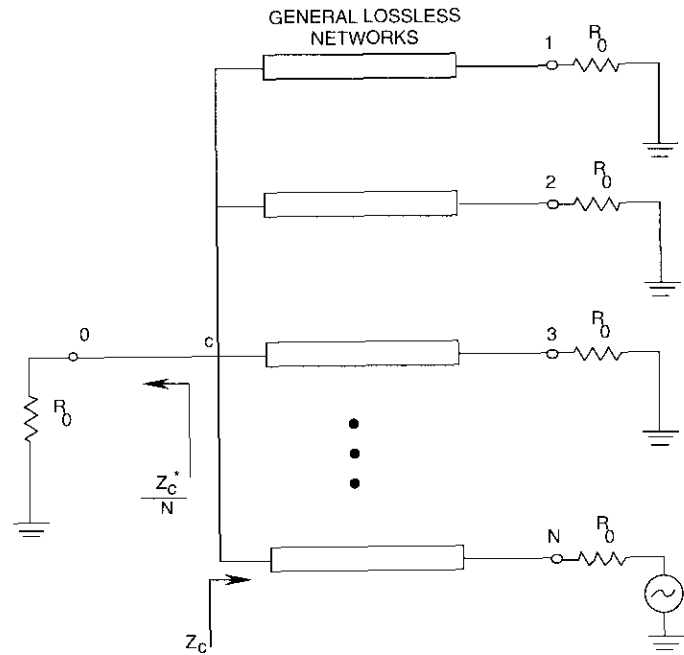
tion (3)]. The results indicate that the amplitude imbalance needs to be kept below about 1 dB to achieve 99-percent efficiency, while the phase imbalance must be kept below  $10^\circ$  for the same efficiency.

**Isolation properties**

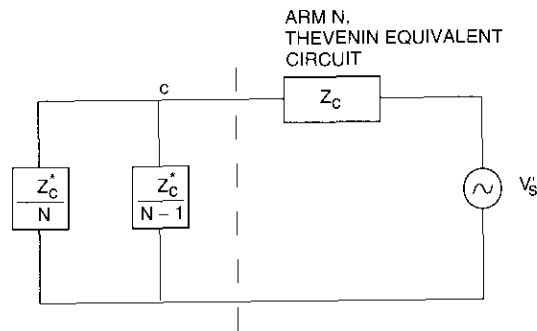
In a power combining system, a critical property required of the divider/combiner circuit is isolation between its distributed ports. Isolation is required in order to prevent interaction or oscillation between devices and to permit a graceful degradation in the event of failure.

The isolation properties of a simply connected  $N + 1$  port reactive power divider/combiner are addressed here. The basic geometry considered (shown in Figure 5a) consists of  $N$  lossless networks connected in parallel at node  $C$ . While this is not a practical configuration as presented, it can provide insight into the source and limitations of isolation. It is also assumed that the central port is conjugately matched.

Given the general network configuration described above, it is necessary to determine the isolation between the peripheral ports, and how it varies with  $N$ . This is accomplished by considering the system equivalent circuit relative to node  $C$  (Figure 5b). Each arm is represented at node  $C$  by  $Z_C$ . Arm  $N$  is transformed to the central node and is represented by its Thevenin equivalent



(a) Reactive Power Divider/Combiner



(b) Equivalent Circuit at Node C

Figure 5. *N*-Way Reactive Power Divider/Combiner

circuit. The remaining  $N - 1$  arms are combined in parallel and are represented by  $Z_c/(N - 1)$ . The impedances are generally assumed to be complex. Since the central port is conjugately matched to the parallel combination, it is represented by  $Z_c^*/N$ . Based on this simple equivalent circuit, the power delivered to the termination in the  $i$ th arm is

$$P_i = \frac{|V_s|^2}{4 N^2 \text{Re}(Z_c)} \quad (11)$$

The isolation, which is defined as the ratio of the power delivered to the  $i$ th port to the power available from the source in arm  $N$ , is given by

$$\frac{P_i}{P_o} = \frac{1}{N^2} \quad (12)$$

or, in dB,

$$I = 10 \log (P_o/P_i) = 20 \log N \quad (\text{dB}) \quad (13)$$

This is the expression for the isolation between any two distributed ports. It is valid for the above matched parallel-connected network or its series-connected dual. It is interesting to note that while the power division loss is  $1/N$ , its isolation is  $1/N^2$ . This  $1/N^2$  isolation dependence means that there is an inherent isolation advantage in combining a large number of devices. However, for a ridged radial combiner, the measured isolation is significantly lower than that calculated by the isolation equation. The measured isolation is 8 dB (minimum) between adjacent peripheral ports, as shown in Figure 6, due to a coupling between each pair of adjacent ridges. The coupling is very high near the center, where the ridges are very close. Therefore, the ideal model for the coupling is not accurate for a ridged radial combiner and serves only as a guide. For an eight-way ridged radial combiner, a minimum isolation of 6 dB has been reported [2]. This is in agreement with the general concept that increasing  $N$  will increase the isolation. These coupling calculations are for the transverse electromagnetic (TEM) mode only.

**Transmission media characteristics**

The design of the combiner takes into account the frequency band, insertion loss, characteristic impedance, and power handling capability, as discussed below.

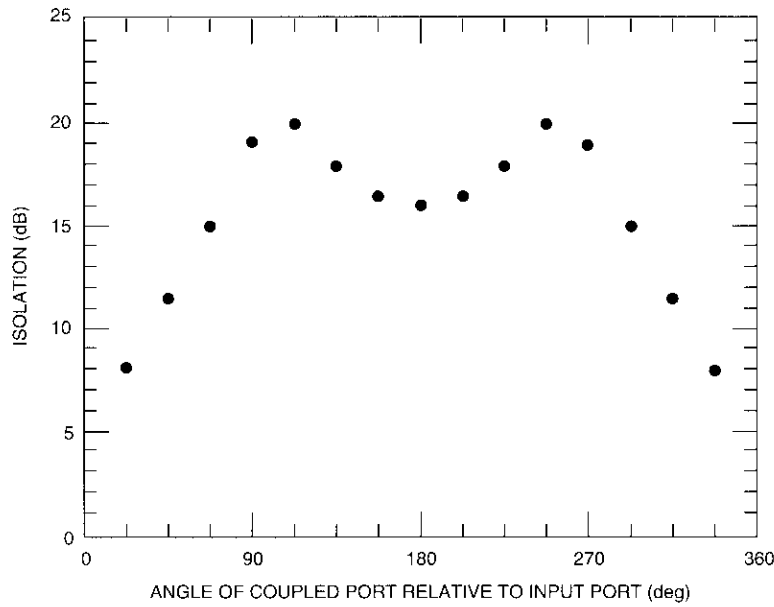


Figure 6. Isolation Between the Combiner's Peripheral Ports at 4 GHz

**Characteristic impedance**

The key element in the combiner design is the transformation from the 50-Ω characteristic impedance at the peripheral ports, to 800-Ω at the center port. Since the combiner has radial symmetry, the calculation of one sector gives the needed characteristic impedance. However, the coupling that occurs between adjacent sectors will change the characteristic impedance near the center port.

The characteristic impedance can be calculated based on the parallel-plate characteristic impedance, when the ridge-fringing capacitance and field tapering across the cross section are taken into account. Another approach uses ridged waveguide theory to calculate the infinite characteristic impedance. Both methods give good results.

**Ridged waveguide theory**

The important characteristics of ridged waveguide are the cutoff frequency, characteristic impedance, power handling capability, insertion loss, and bandwidth. This summary, which is based on previously published

material [3]-[5],[8], reviews these features, concentrating on those topics of importance to the combiner design.

A cross section of ridged rectangular waveguide, with the equivalent circuit at cutoff, is shown in Figure 7. This structure has lower cutoff frequency than rectangular waveguide with the same cross section dimensions. Using the transverse resonance method, the cutoff wavelength is given by the transcendental equation

$$1 - \frac{Z_2}{Z_1} \tan \phi_1 \cdot \tan \phi_2 - BZ_2 \cdot \tan \phi_2 = 0 \tag{14}$$

where  $Z_1$  and  $Z_2$  are the characteristic impedances of the parallel-plate lines of heights  $(b - d)$  and  $b$ , respectively. The variables  $\phi_1$  and  $\phi_2$  are the electrical lengths associated with these lines, as defined by

$$\phi_1 = \frac{s\pi}{\lambda_c} \tag{15}$$

and

$$\phi_2 = \frac{(a - s)\pi}{\lambda_c} \tag{16}$$

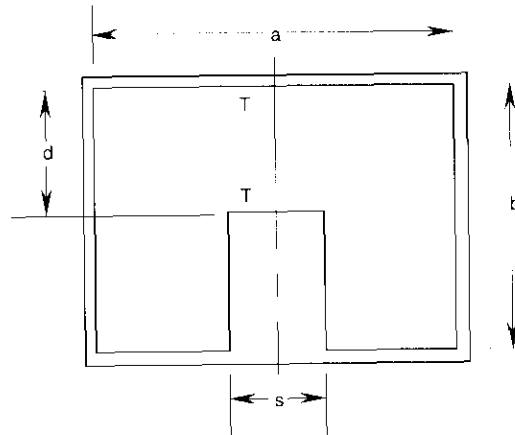
The normalized discontinuity susceptance,  $B$ , is given by

$$B = \frac{2\pi vC}{\lambda_c} \tag{17}$$

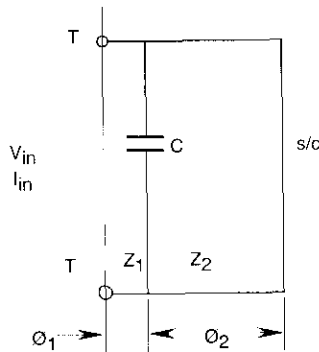
where  $C$  is a discontinuity capacitance dependent on the height of the ridge, and represents the effect of modes of higher order than the fundamental TEM mode. The higher order modes have been introduced by the presence of the ridge and, together with the fundamental TEM mode, give the field configuration for ridged rectangular waveguide. The variable  $v$  is the velocity of propagation of an electromagnetic wave in the medium of the guide. Equation (17) is a transcendental equation in  $\lambda_c$ , which may be solved for  $\lambda_c$  by suitable computer programming.

The discontinuity susceptance,  $BZ_2$ , for a step ratio  $a = d/b$  between parallel-plate lines has been obtained by Marcuvitz [4] and is accurate to 1 percent in the range  $b < \lambda_c$ . Marcuvitz's expression contains two terms: a DC term,  $T_1(\lambda_c/4b)$ , which is predominant and is given by

$$T_1 \frac{\lambda_c}{4b} = \ln \left[ \left( \frac{1 - \alpha^2}{4\alpha} \right) \cdot \left( \frac{1 + \alpha}{1 - \alpha} \right)^{1/2} \cdot \left( \alpha + \frac{1}{\alpha} \right) \right] \tag{18}$$



(a) Single Ridged Cross Section



(b) Equivalent Circuit at TT

Figure 7. Equivalent Transverse Circuit of Single Ridged Rectangular Waveguide at  $TE_{10}$  Mode Cutoff

and a frequency-dependent term,  $T_2(\lambda_c/4b)$ , which is given by

$$T_2 \frac{\lambda_c}{4b} = \frac{4b}{\lambda_c} \left[ 2 \left( \frac{A + A^1 + 2C}{AA^1 + C^2} \right) + \left( \frac{2b}{4\lambda_c} \right)^2 \left( \frac{1 - \alpha}{1 + \alpha} \right)^{4\alpha} \left( \frac{5\alpha^2 - 1}{1 - \alpha^2} + \frac{4\alpha^2 C}{3A} \right)^2 \right] \quad (19)$$

where 
$$A = \left( \frac{1 + \alpha}{1 - \alpha} \right)^{2\alpha} \left[ \frac{1 + \sqrt{1 - (2b/\lambda_c)^2}}{1 - \sqrt{1 - (2b/\lambda_c)^2}} \right] - \frac{1 + 3\alpha^2}{1 - \alpha^2}$$

$$A^1 = \left( \frac{1 + \alpha}{1 - \alpha} \right)^{2\alpha} \left[ \frac{1 + \sqrt{1 - (2d/\lambda_c)^2}}{1 - \sqrt{1 - (2d/\lambda_c)^2}} \right] - \frac{3 + \alpha^2}{1 - \alpha^2}$$

$$C = \left( \frac{4\alpha}{1 - \alpha^2} \right)^2$$

The discontinuity susceptance for a step ratio  $a = d/b$  between two infinite parallel-plate lines of heights  $d$  and  $b$  is given by

$$BZ_2 = T_1 + T_2 \quad (20)$$

Solving these transcendental equations for  $\lambda_{c10}$  and  $\lambda_{c30}$  shows that the bandwidths depend on the normalized ridged dimensions and are maximum for  $s$  equal to approximately half  $a$  and as  $(b - d)$  approaches zero.

The characteristic impedance of the ridged waveguide as a function of the physical dimensions and the cutoff wavelength is given by

$$Z_0 = \frac{Z_{0\infty}}{\sqrt{1 - (\lambda_0/\lambda_c)^2}} \quad (21)$$

where  $Z_{0\infty}$  is the characteristic impedance at an infinite frequency. Using the voltage-current ( $V$ - $I$ ) definition, Cohn [9] has developed a formula for characteristic impedance which is given by

$$Z_{0\infty} = \frac{120\pi^2 d}{\lambda_c \left[ \sin \phi_2 + \frac{d}{b} \cos \phi_2 \tan \left( \frac{\phi_1}{2} \right) \right]} \quad (22)$$

Based on a voltage-power definition, Hopfer [8] has developed the following formula for characteristic impedance:

$$Z_{0\infty} = \frac{d^2}{10 \left(\frac{d}{a}\right) \left(\frac{\lambda_c}{a}\right)} \cdot \frac{1}{W} \quad (23)$$

where  $W = \left\{ \frac{4\beta}{k} \cdot \cos^2\left(\frac{\pi\gamma}{k}\right) \cdot \text{Inscs}\left(\frac{\pi d}{2b}\right) + \frac{\pi\gamma}{2k} + \frac{1}{4} \sin\left(\frac{2\pi\gamma}{k}\right) + \frac{d \cos^2 \pi\gamma k}{b \sin^2 2\pi\delta k} \left[ \frac{\pi\delta}{k} - \frac{1}{4} \sin\left(\frac{4\pi\delta}{k}\right) \right] \right\}$

and where  $\gamma = s/a$   
 $k = \lambda_c/a$   
 $\beta = d/a$   
 $\delta = [1 - (s/a)]/2$

Equations (22) and (23) show that characteristic impedance is also dependent on the ridged dimensions.

The insertion loss and power handling capability of the combiner also depend on the ridge dimensions. If the spacing between the ridge and the top wall is reduced, the insertion loss increases and power handling capability is reduced.

**Parallel-plate impedance calculation**

The parallel-plate capacitance can be divided into three components—ridge capacitance, fringing capacitance, and parallel-plate capacitance—as shown in Figure 8a. The relationship between characteristic impedance and capacitance is given by

$$Z_T = \frac{(\mu \cdot \epsilon)^{1/2}}{C_T} \quad (24)$$

where  $C_T = C_1 + C_2 + C_3$ , as shown in the figure.

Using equation (16) or Collin [10], the DC component for fringing capacitance  $C_3$  is given by

$$BZ_2 = \frac{2b}{\lambda} \left[ 2 \ln \left( \frac{1 - \alpha^2}{4\alpha} \right) + \left( 1 + \frac{1}{\alpha} \right) \ln \left( \frac{1 + \alpha}{1 - \alpha} \right) \right] \quad (25)$$

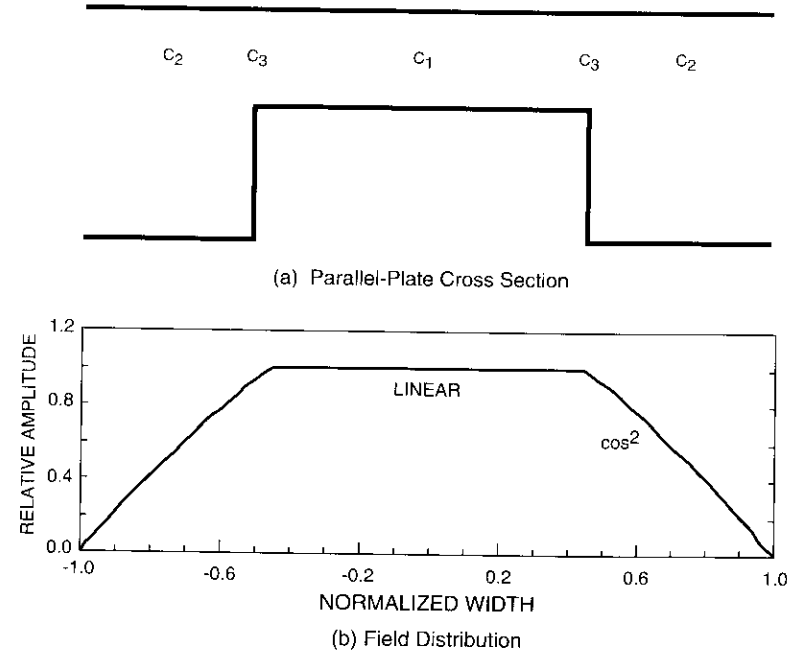


Figure 8. Parallel-Plate Field Distribution

where  $\lambda_c$  in equation (16) has been replaced by  $\lambda$ , and where

$$Z_2 = (\mu/\epsilon)^{1/2} \cdot b \quad (26)$$

and

$$B = 2\pi \cdot v \cdot \frac{C_3}{\lambda} = \frac{2\pi \cdot C_3}{(\mu \cdot \epsilon)^{1/2} \cdot \lambda} \quad (27)$$

From equations (25) through (27), the fringing capacitor is

$$C_3 = \frac{\epsilon}{\pi} \left[ 2 \ln \left( \frac{1 - \alpha^2}{4\alpha} \right) + \left( 1 + \frac{1}{\alpha} \right) \ln \left( \frac{1 + \alpha}{1 - \alpha} \right) \right] \quad (28)$$

For the two parallel-plate sections, the capacitors are given by

$$C_1 = \frac{\epsilon \cdot A_1}{d} \quad (29)$$

and

$$C_2 = \frac{\epsilon \cdot A_2}{b} \tag{30}$$

If the field distribution along the parallel-plate cross section (Figure 8b) is taken into account, the characteristic impedance,  $Z_T$ , is given by

$$Z_T = \frac{(\mu \cdot \epsilon)^{1/2}}{C_T} \tag{31}$$

where  $C_T = C_1 + 2 \cdot K \cdot C_2 + 2 \cdot C_3$  and  $0 < K < 1$ .

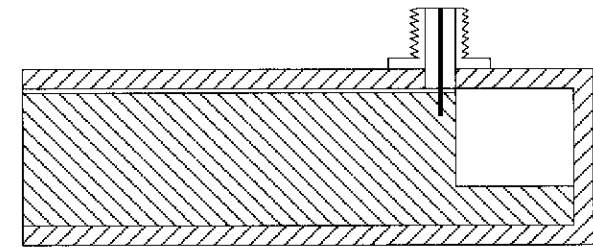
The variable  $K$  is a constant parameter that depends on the field distribution across the cross section of the parallel plates. The field distribution across the ridge was taken as constant, while that across the parallel plates was taken as  $\cos^2 x$ , where  $x$  is the cross section dimension from the center of the ridge, as shown in the figure. Calculations reveal that, for this field distribution,  $K = 0.442$ .

**Waveguide-to-coaxial-line transition design**

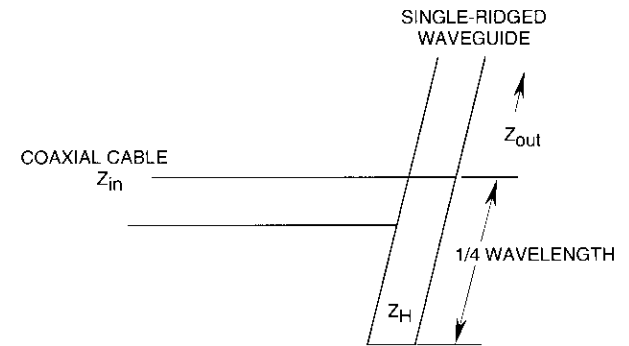
The top-wall waveguide-to-coaxial-line transition is very well known in the literature [11], while the end-launch waveguide-to-coaxial-line transition is much less well known [5]. The following will explain how the top-wall transition can be converted to an end-launch transition.

The top-wall ridged waveguide-to-coax transition and its circuit model are shown in Figure 9. The transition is built from 50-Ω coaxial cable, single ridged waveguide with 50-Ω characteristic impedance at center frequency, and shorted-end waveguide that is one-quarter wavelength long and has a characteristic impedance of  $Z_H$ . The equivalent circuit shows this junction to be equivalent to a continuous length of 50-Ω transmission line with a shorted length of  $Z_H$ -Ω line shunted to it. As long as the shunt line has a large reactance compared to 50 Ω, the standing wave ratio (SWR) of the junction will be low. The SWR is also affected by the fact that the waveguide characteristic impedance can be 50 Ω at only one frequency. An efficient means of increasing the transition bandwidth is to increase the characteristic impedance of the shorted shunt waveguide.

The procedure for replacing a top-wall transition with an end-launch transition is shown schematically in Figure 10. First, the top-wall transition with the shorted-end waveguide (Figure 10a) is bent, as shown in Figure 10b. Because the shorted  $\lambda/4$  section is larger than the waveguide height, the section is bent



(a) Waveguide-to-Coax Transition



(b) Circuit Model

Figure 9. Top-Wall Waveguide-to-Coax Transition

again to stay within the same waveguide dimensions. The final transition is depicted in Figure 10c. The characteristic impedance of the folded waveguide from the coaxial center pin is the same as that of the rest of the waveguide. The shorted waveguide characteristic impedance is as high as possible.

Figure 11 shows a circuit model of the final end-launch-to-coax transition. The bend in the shorted section is modeled by a series inductor, and the coupling between the wall and the ridged waveguide is represented by a capacitor.

**Divider/combiner design**

The key element in this combiner design (refer to Figure 1) is the sectored radial ridged waveguide with the two-dimensional tapered transition from 800-Ω characteristic impedance at the center to 50-Ω characteristic impedance at each peripheral port. Based on ridged waveguide theory, the combiner width and ridged dimensions were chosen so that the power combiner

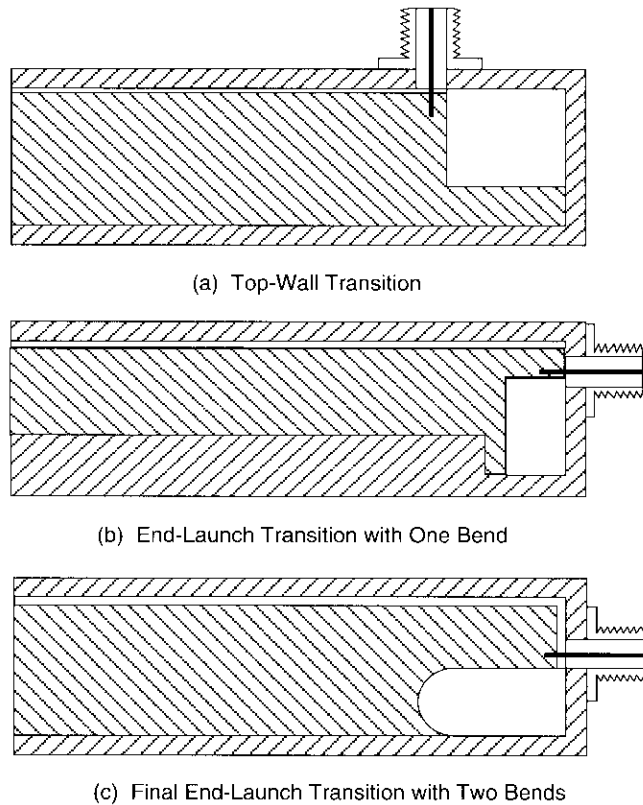


Figure 10. Replacement of a Top-Wall Transition With an End-Launch Transition

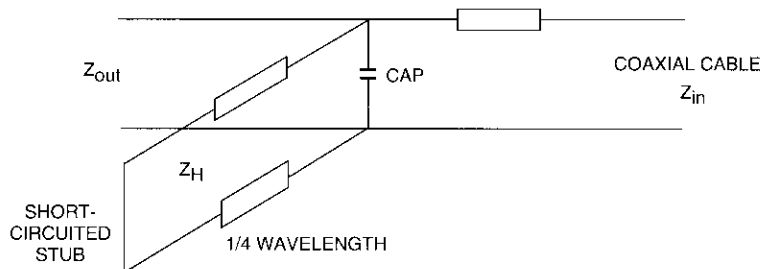


Figure 11. Circuit Model of the End-Launch Transition

bandwidth meets the specifications. The two-dimensional tapered transition is three-quarter wavelength at center frequency, and the transition between the combiner input and the rectangular waveguide is based on the new end-launch waveguide-to-coax transition. The center probe, which feeds 16 radially distributed ridges with 800- $\Omega$  waveguide impedance, was designed experimentally.

The calculated dimensions of the combiners are based on the theory discussed above. The peripheral and center-port ridged dimensions were calculated using equations (22) and (24), which employ the  $V-I$  definition for the characteristic impedance. In equation (22), the cutoff wavelength,  $\lambda_c$ , is determined by the sector boundary, and  $\lambda$  is the wavelength at the center of the band. The calculated dimensions for the peripheral ports are accurate in both equations; however, the dimensions for the center port were not accurate due to coupling between adjacent ridges and with the center port, and experimental compensation was needed.

The length of the end-launch transition is quarter-wavelength, measured from the center of the pin to the short on a curved line. The gap where the pin is located has the same dimensions as the space between the ridged waveguide and the top wall, such that the characteristic impedance will be the same as the ridged impedance at the peripheral port. The characteristic impedance,  $Z_{II}$ , of the folded ridged waveguide section is as high as possible within the limitations of the ridged dimensions and the combiner width.

The measured performance shows that the end launch bandwidth [6] and the impedance transformer bandwidth [5] are wide. The bandwidth is limited by the center probe. Using the equivalent circuit model without the center probe gives similar results.

**Equivalent circuit model**

A simple equivalent circuit description (Figure 12) was used to analyze the 16-way radial combiner circuit. The center probe is represented by a coaxial transmission line, an ideal transformer, and two shunt capacitors. The individual radial ridged waveguide with the two-dimensional taper is represented in the model by a cascade of short microstrip tapers, each with a different substrate thickness to simulate the taper. The end-launch waveguide-to-coax transition is represented by a short coaxial transmission line in parallel with a series short-circuited stub, as well as an inductor and a capacitor.

Using TOUCHSTONE™ software for the calculations, it was found that the circuit is quite broadband. The center frequency and the bandwidth are fundamentally determined by the diameter and length of the center probe,

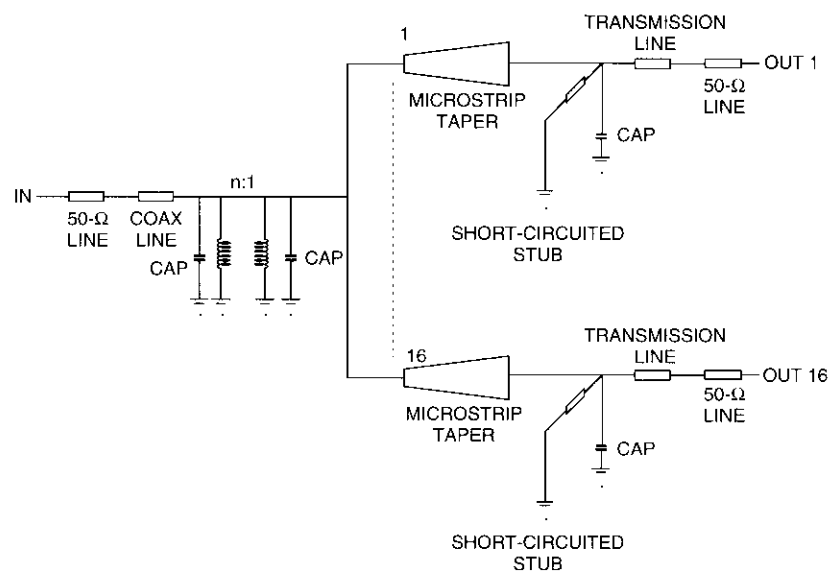


Figure 12. Equivalent Circuit for the Combiner

which also determine the resonant frequency and coupling between the center probe and the radial ridges. The predicted insertion loss and return loss are shown in Figure 13.

**Divider/combiner results**

The divider/combiner built using the above procedure has been tested with a Hewlett-Packard HP-8510 network analyzer. The parameters measured were the center port return loss and the amplitude and phase from the center port to each of the peripheral ports. From these measurements, the amplitude flatness, amplitude tracking, and insertion loss were plotted as shown in Figure 14, while Figure 15 is a plot of the port-to-port phase tracking characteristics. The isolation was measured by defining one of the peripheral ports as an input port and measuring the transmission from this port to the other 15 peripheral ports to obtain the combiner isolation. The isolation between the peripheral ports was shown in Figure 6, and the insertion loss measured for a divider/combiner back-to-back is plotted in Figure 16. Table 1 summarizes the performance of the combiner.

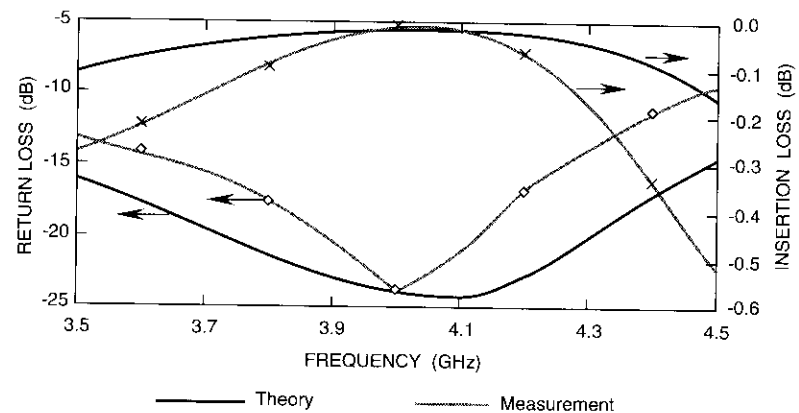


Figure 13. Normalized Insertion Loss and Return

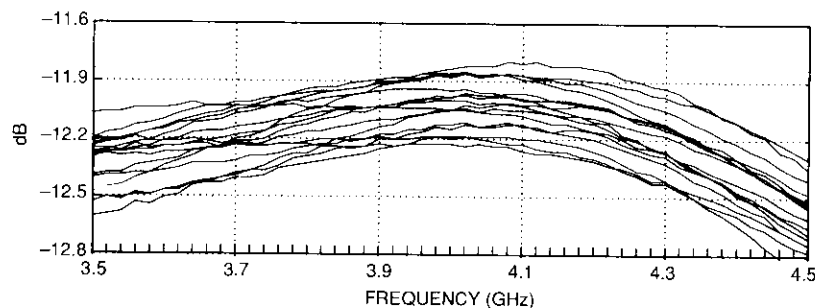


Figure 14. Combiner Amplitude Characteristics

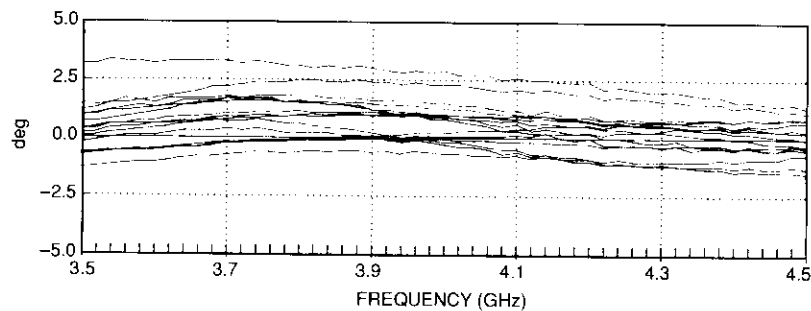


Figure 15. Phase Tracking as a Function of Frequency

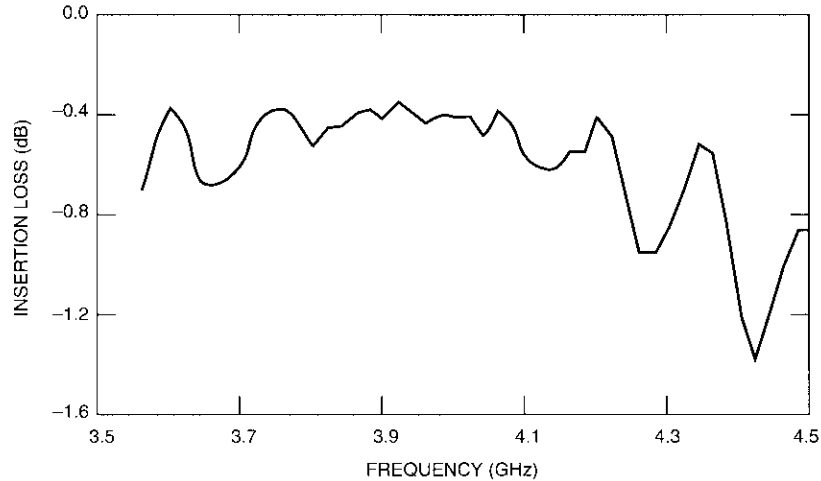


Figure 16. Insertion Loss for Divider/Combiner Back to Back

TABLE I. COMBINER PERFORMANCE SUMMARY

CHARACTERISTIC	PERFORMANCE
Bandwidth	3.7–4.2 GHz
Overall Combining Insertion Loss	0.2 dB max
Amplitude Flatness	$\pm 0.1$ dB max
Center Port SWR	1.3:1 max
Amplitude Tracking	$\pm 0.15$ dB max
Phase Tracking	$\pm 2.5^\circ$ max
Calculated Combining Loss due to Phase Imbalance (for $M/N = 1/2$ and $5^\circ$ phase imbalance)	0.01 dB (99.8 %)
Minimum Isolation Between Two Ports	8 dB
Median Isolation Between Two Ports	16 dB

Comparison of the calculated and measured combiner parameters shows good agreement between theory and experiment for the insertion loss and center port return loss. The amplitude and phase imbalance are as expected for the machining tolerances. The discrepancy noted in the isolation between any two peripheral ports is attributed to coupling between the ridges.

## Conclusions

Because it has the ability to combine large numbers of amplifiers with very low loss over relatively broad bandwidths, the radial combiner is a viable approach for many high-power applications. The ridged waveguide-based approach described here, along with the broadband coax/waveguide end-launch technique, make this an attractive solution for many power combining applications. Its basic limitations depend on the tolerances that can be maintained in machining the center of the combiner. The combiner can be designed for frequencies up to the millimeter-wave range. For higher frequencies, the peripheral ports and center port can be replaced by waveguide.

## References

- [1] K. J. Russell, "Microwave Power Combining Techniques," *IEEE Transactions on Microwave Theory and Techniques*, Vol. MTT-27, No. 5, May 1979, pp. 472–478.
- [2] M. Oz, "Wideband Double-Ridged 8-Way Radial Combiner," 14th European Microwave Conference, Liège, Belgium, September 1984, *Proc.*, pp. 317–322.
- [3] J. R. Pyle, "The Cutoff Wavelength of the  $TE_{10}$  Mode in Ridged Rectangular Waveguide of Any Aspect Ratio," *IEEE Transactions on Microwave Theory and Techniques*, Vol. MTT-14, No. 4, April 1966, pp. 175–183.
- [4] N. Marcuvitz, *Waveguide Handbook*, Massachusetts Institute of Technology Radiation Laboratory Series, New York: McGraw-Hill, 1951, Vol. 10, pp. 399–402.
- [5] G. L. Matthaei, L. Young, and E. M. T. Jones, *Microwave Filters, Impedance-Matching Networks, and Coupling Structures*, New York: McGraw-Hill, 1964, Ch. 6.
- [6] E. Gazit, "Wide Band End Launcher Feed for Ridged Waveguide," 15th Conference of Electrical and Electronic Engineers, Israel, April 1987, *Proc.*, p. 2.3.7.
- [7] J. M. Schellenberg, "Transistor Combinatorial Techniques," U.S. Air Force Avionics Laboratory, Technical Report No. AFAL-TR-77-205, November 1977.
- [8] S. Hopfer, "The Design of Ridged Waveguide," *IRE Transactions on Microwave Theory and Techniques*, Vol. MTT-3, No. 4, October 1955, pp. 20–29.
- [9] S. B. Cohn, "Properties of Ridge Wave Guide," *Proc. IRE*, Vol. 35, August 1947, pp. 783–788.
- [10] R. E. Collin, *Field Theory of Guided Waves*, New York: McGraw-Hill, 1960, p. 364.
- [11] S. B. Cohn, "Design of Broad-Band Wave-Guide-to-Coaxial-Line Junction," *Proc. IRE*, Vol. 35, September 1947, pp. 920–926.



*Moshe Oz received the B.Sc. degree from Ben-Gurion University, Beer-Sheva, Israel, in 1971. He then joined RAFAEL, Haifa, Israel, where as a Research Engineer he was involved in the development of microwave antennas, filters, multiplexers, amplifiers, and sources. In 1976, he became head of the transmitting and receiving group working on RF communications systems. From 1981 to 1983 he was on sabbatical with the RCA Laboratories Microwave Technology Center, where he was involved in the development of microwave components for T/R modules and active antenna arrays. He was then named head of the transmitting*

*and receiving section of RAFAEL, where he was involved in the design and development of communications systems, frequency synthesizers, and VHF/UHF receivers.*

*From 1990 to 1991, Mr. Oz was on sabbatical at COMSAT Laboratories, where he was involved in the design of a high-efficiency, high-power amplifier, and an active antenna array for satellite communications. He is currently involved in designing communications systems at RAFAEL.*

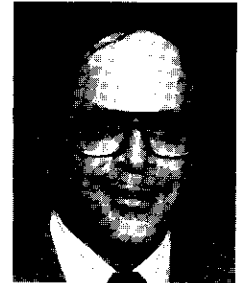
*Bernard D. Geller received a B.S. in electrical engineering from the Johns Hopkins University in 1967, and an M.S.E.E. from the University of Maryland in 1974. From 1967 to 1979, he was involved in the development of both passive and active microwave and millimeter-wave circuits at the Westinghouse Advanced Technology Laboratory in Baltimore, Maryland. After a short period at Fairchild Space and Electronics Company during which he designed satellite earth station components, he joined COMSAT Laboratories in November 1979. He is currently Manager of the Microwave Circuits Department and has been involved with the design of monolithic microwave integrated circuits (MMICs), high-efficiency power amplifiers, and other advanced MICs and packaging techniques. He is a Senior Member of IEEE.*



*Peggy Cline is an Associate Staff Member in the Microwave Electronics Division. Prior to joining COMSAT in July 1980, she served in the U.S. Army Communication Command where she was involved in operating and maintaining a satellite earth station. She has conducted assembly and testing on a TDMA satellite switch matrix, and on high-efficiency solid-state amplifiers using both silicon motherboard and conventional approaches, and has performed device characterization. She is currently working toward a degree in engineering.*

*Ilan Yogeve received his B.Sc. in mechanical engineering in 1976, and his M.Sc. from the Technion Israel Institute of Technology in 1985. In 1976, he joined RAFAEL as a Research Engineer and was involved in mechanical design, analysis, and development of advanced communications systems, including antennas and stabilized platform systems. He worked on the mechanical packaging of complex flight electronics (RF and digital components), including performance and evaluation during environmental testing.*

*Mr. Yogeve joined COMSAT Laboratories in 1989, on a 2-1/2 year sabbatical from RAFAEL, as a Member of the Technical Staff in the Satellite Technologies Division. During this period, he was responsible for the mechanical design of the ITALSAT In-Orbit Test Transponder (IOTT) and other RF components, such as the LNB for the DBS flat-plate antenna. He is currently involved in developing an advanced C-band phased-array antenna system for future communications satellites.*



## ***Translations of Abstracts***

### ***Conception de la plate-forme de l'INTELSAT VI***

L. R. DEST, J-P. BOUCHEZ, V. R. SERAFINI, M. SCHAVIETELLO  
ET K. J. VOLKERT

#### **Sommaire**

Cet article décrit la plate-forme du satellite stabilisé par rotation INTELSAT VI, et passe en revue les impératifs de conception et les divers sous-systèmes. Le satellite pèse environ 4 500 kg au lancement et sa masse est de 2 570 kg en début de vie. Sa masse sèche en fin de vie est de 1 905 kg. Il se compose d'une section rotative et d'une section contrarotative reliées par un ensemble de roulements et de transfert d'énergie. La section contrarotative abrite la charge utile de télécommunications (répéteurs et antennes) et assure les fonctions de télécommande, de télémessure et de thermorégulation. La section rotative renferme les sous-systèmes de commande d'attitude, d'alimentation, de propulsion et de thermorégulation. Les structures secondaires déployables, qui comprennent les antennes et un panneau solaire télescopique, sont commandées par plusieurs mécanismes.

### ***Système de commande d'attitude de l'INTELSAT VI***

L. I. SLAFER ET V. L. SEIDENSTUCKER

#### **Sommaire**

Cet article décrit le système de stabilisation et de commande d'attitude du satellite de télécommunications géosynchrone INTELSAT VI. Il passe en revue la conception de ce satellite à double rotation, le déroulement des opérations entre le lancement et la mise sur orbite finale, ainsi que la technique de la super-rotation, mise au point pour stabiliser le satellite lorsqu'il passe de l'orbite de transfert à l'orbite de géosynchronisme. La conception fonctionnelle, la réalisation et la performance du système de commande à microprocesseur sont exposées en détail. Autres sujets importants : la commande de pointage de précision de la plate-forme contrarotative (qui utilise soit un détecteur d'horizon terrestre et un capteur solaire maintenus en rotation, soit un récepteur de balise radioélectrique de poursuite), la stabilisation active de la nutation au moyen de boucles de pointage de la charge utile, les nombreuses mesures de protection contre les dérangements dans les processeurs, et le niveau élevé d'autonomie des systèmes de commande, qui comprennent les dispositifs de bord permettant la détermination et la commande d'orientation de l'axe de rotation, la commande à bord des manoeuvres de maintien de poste et le traitement d'ordres mémorisés.

### **Diseño y funcionamiento del subsistema SS-TDMA a bordo del INTELSAT VI**

R. K. GUPTA, J. N. NARAYANAN, A. M. NAKAMURA, F. T. ASSAL  
Y B. GIBSON

#### **Abstracto**

Se describe el diseño y funcionamiento del subsistema de acceso múltiple por distribución en el tiempo (SS-TDMA) a bordo del satélite INTELSAT VI. Se presenta un breve resumen del equipo y posibilidades de este subsistema, seguido de una discusión de las características clave del diseño de la matriz de conmutación de microondas (MSM), la unidad de control de distribución (DCU) y la fuente de temporización del subsistema SS-TDMA, así como de la forma en que se instaló su equipo. Luego se examina el diseño de las configuraciones de redundancia destinadas a aumentar la fiabilidad, así como el restablecimiento después de averías una vez identificadas estas. Se ha diseñado una probabilidad de supervivencia de 10 años superior a 0,99, que se logra incluyendo una redundancia de 10 por 6 en el trayecto de entrada para la MSM, de 2 por 1 para la DCU, y de 3 por 1 para la fuente de temporización. También se describen los conceptos fundamentales en que se basa el extenso programa de pruebas adoptado para el subsistema SS-TDMA, desde la concepción del diseño hasta la integración a gran escala del satélite.

### **Combinador radial de potencia de gran eficiencia, de 16 modos y un solo resalte interno**

M. OZ, B. D. GEILLER, P. K. CLINE Y I. YOGEV

#### **Abstracto**

Se ha desarrollado un nuevo combinador radial de potencia de gran eficiencia, de 16 modos y un solo resalte interno, para banda C. El diseño utiliza la teoría de guíaondas de resaltes internos para calcular la anchura de banda y la impedancia, así como una nueva transición al final de la transferencia de energía de un guíaonda a un cable coaxial. El combinador de potencia tiene una pérdida media de inserción de 0,1 dB a través de la banda de 3,7 a 4,2 GHz (una eficiencia de combinación del 98 por ciento), una relación de onda estacionaria menor de 1,35 a 1, un seguimiento de amplitud de  $\pm 0,2$  dB y un seguimiento de fase de  $\pm 2,5^\circ$ . La uniformidad de amplitud es  $\pm 0,1$  dB, y el aislamiento de apertura a apertura es superior a 8 dB a través de la banda.

## **Author Index, CTR 1990**

The following is a cross-referenced index of articles that appeared in *COMSAT Technical Review* for 1990. The code number at the end of each entry is to be used for ordering reprints from: Corporate Records, COMSAT Corporation, 22300 Comsat Drive, Clarksburg, MD 20871-9475.

- ALLNUTT, J. E.,\* see Rogers, D. V. [CTR90/355].  
 BROWN, M. P., Jr.,\* R. W. Duesing,\* L. N. Nguyen,\* W. A. Sandrin, and J. A. Tehrani,\* "INTELSAT VI Transmission Design and Associated Computer System Models for FDMA Services," *COMSAT Technical Review*, Vol. 20, No. 2, Fall 1990, pp. 373-399 [CTR90/362].  
 CAMPANELLA, S. J., G-P. Forcina,\* B. A. Pontano, and J. L. Dicks,\* "SS-TDMA System Considerations," *COMSAT Technical Review*, Vol. 20, No. 2, Fall 1990, pp. 335-371 [CTR90/361].  
 CAMPANELLA, S. J., see Garlow, R. K. [CTR90/353].  
 CANTARELLA, G. P.,\* and G. Porcelli,\* "Specifying the Spacecraft Bus," *COMSAT Technical Review*, Vol. 20, No. 2, Fall 1990, pp. 309-333 [CTR90/360].  
 CARLSON, H. E., see Chang, E. Y. [CTR90/352].  
 CHANG, E. Y., F. R. Phelleps, T. Smith, P. Laux, H. E. Carlson, R. J. Porter, T. C. Ho, and K. Pande, "Effect of Argon Plasma Cleaning on GaAs FET Passivation," *COMSAT Technical Review*, Vol. 20, No. 1, Spring 1990, pp. 1-20 [CTR90/352].  
 COTNER, C. B., see Layer, D. H. [CTR90/354].  
 DICKS, J. L.,\* see Campanella, S. J. [CTR90/361].  
 DUESING, R. W.,\* see Brown, M. P. [CTR90/362].  
 FAINE, E. A., see Perillan, L. B. [CTR90/358].  
 FORCINA, G-P.,\* see Campanella, S. J. [CTR90/361].  
 GARLOW, R. K., and S. J. Campanella, "RF/Optical Interface Design for Optical Intersatellite Links," *COMSAT Technical Review*, Vol. 20, No. 1, Spring 1990, pp. 21-61 [CTR90/353].  
 HO, T. C., see Chang, E. Y. [CTR90/352].  
 KAPPES, J. M., see Layer, D. H. [CTR90/354].  
 KEMP, L. W., "Geostationary Satellite Log for Year-End 1989," *COMSAT Technical Review*, Vol. 20, No. 1, Spring 1990, pp. 105-215 [CTR90/356].  
 LAUX, P., see Chang, E. Y. [CTR90/352].  
 LAYER, D. H., J. M. Kappes, and C. B. Cotner, "140-Mbit/s COPSK Modem Laboratory Tests and Transatlantic Field Trials," *COMSAT Technical Review*, Vol. 20, No. 1, Spring 1990, pp. 63-96 [CTR90/354].  
 LEE, L-N., and Rhodes, S., "Offset-QPSK Modulation for Maritime Satellite Communications," *COMSAT Technical Review*, Vol. 20, No. 2, Fall 1990, pp. 401-417 [CTR90/363].  
 MAHLE, C. E., see Pontano, B. A. [CTR90/359].

\* INTELSAT author.

- NGUYEN, L. N.,\* see Brown, M. P. [CTR90/362].  
 PANDE, K., see Chang, E. Y. [CTR90/352].  
 PERILLAN, L. B.,\* W. R. Schnicke, and E. A. Faine, "INTELSAT VI System Planning," *COMSAT Technical Review*, Vol. 20, No. 2, Fall 1990, pp. 247-269 [CTR90/358].  
 PHELLEPS, F. R., see Chang, E. Y. [CTR90/352].  
 PODRACZKY, E. I.,\* and W. R. Schnicke, "The Process for Success—INTELSAT VI," *COMSAT Technical Review*, Vol. 20, No. 2, Fall 1990, pp. 231-246 [CTR90/357].  
 PONTANO, B. A., A. I. Zaghoul, and C. E. Mahle, "INTELSAT VI Communications Payload Performance Specifications," *COMSAT Technical Review*, Vol. 20, No. 2, Fall 1990, pp. 271-308 [CTR90/359].  
 PONTANO, B. A., see Campanella, S. J. [CTR90/361].  
 PORCELLI, G.,\* see Cantarella, G. P. [CTR90/360].  
 PORTER, R. J., see Chang, E. Y. [CTR90/352].  
 RHODES, S., see Lee, L-N. [CTR90/363].  
 ROGERS, D. V., and J. E. Allnutt,\* "Results of a 12-GHz Radiometric Site Diversity Experiment at Atlanta, Georgia," *COMSAT Technical Review*, Vol. 20, No. 1, Spring 1990, pp. 97-103 [CTR90/355].  
 SANDRIN, W. A., see Brown, M. P. [CTR90/362].  
 SCHNICKE, W. R., see Perillan, L. B. [CTR90/358] and Podraczky, E. I. [CTR90/357].  
 SMITH, T., see Chang, E. Y. [CTR90/352].  
 TEHRANI, J. A.,\* see Brown, M. P. [CTR90/362].  
 ZAGHLOUL, A. I., see Pontano, B. A. [CTR90/359].

\* INTELSAT author.

## **Index of 1990 Publications by COMSAT Authors**

The following is a list of 1990 publications by authors at COMSAT Corporation. The list is cross-referenced based on COMSAT authors (only). Copies of these publications may be obtained by contacting the COMSAT authors at: COMSAT Corporation, 22300 Comsat Drive, Clarksburg, MD 20871-9475.

- ANDERSON, W. T.,\* A. R. Knudson,\* A. Meulenber, H-L. Hung, J. A. Roussos,\* and G. Kiriakidis,\* "Heavy Ion Total Fluence Effects in GaAs Devices," *IEEE Transactions on Nuclear Science*, Vol. 37, No. 6, December 1990, pp. 2065-2070.  
 ASSAL, F. T., see Zaghoul, A. I. (two papers); Potukuchi, J. R.; and Gupta, R.  
 ATIA, A. E., S. M. Day, and L. Westerlund, "Communications Satellite Operations in Inclined Orbit—The COMSAT Maneuver," AIAA 13th International Communication Satellite Systems Conference, Los Angeles, CA, March 1990, *A Collection of Technical Papers*, Pt. 2, pp. 452-455.  
 BONETTI, R. R., and A. E. Williams, "A Hexa-Mode Bandpass Filter," IEEE MTT-S International Microwave Symposium, Dallas, TX, May 1990, *Digest*, Vol. 1, pp. 207-210.  
 BONETTI, R. R., and A. E. Williams, "An Octave-Band MMIC Active Filter," IEEE MTT-S International Microwave Symposium, Dallas, TX, May 1990, *Digest*, Vol. 2, pp. 823-826.  
 BONETTI, R. R., and A. E. Williams, "Preliminary Design Steps for Thin-Film Superconducting Filters," IEEE MTT-S International Microwave Symposium, Dallas, TX, May 1990, *Digest*, Vol. 1, pp. 273-276.  
 BONETTI, R. R., and A. E. Williams, "State-of-the-Art and Future Trends in Satellite Communication Filters" (Abstract), ESA/ESTEC Workshop on Microwave Filters for Space Applications, Noordwijk, The Netherlands, June 1990, *ESTEC Book of Abstracts*, Session 2, p. 1.  
 BONETTI, R. R., see Williams, A. E.  
 CAMPANELLA, S. J., B. A. Pontano, and D. M. Chitre, "A Users Perspective of the ACTS Hopping-Beam Satellite," AIAA 13th International Communication Satellite Systems Conference, Los Angeles, CA, March 1990, *A Collection of Technical Papers*, Pt. 2, pp. 484-489.  
 CAMPANELLA, S. J., S. Sayegh, and M. Elamin,\* "A Study of On-Board Multicarrier Digital Demultiplexers for a Multi-Beam Mobile Satellite Payload," AIAA 13th International Communication Satellite Systems Conference, Los Angeles, CA, March 1990, *A Collection of Technical Papers*, Pt. 2, pp. 638-648.  
 CARLSON, H., see Gupta, R.  
 CARVER, W., and C. B. Cotner, "International Satellite Communications for the 1990s and Beyond—A Resource for the Military User," 5th Annual Pacific International Defense Electronics Conference and Symposium, Honolulu, HI, November 1990, *Proc.*, Paper No. 2.

\* Non-COMSAT author.

- CHITRE, D. M., and P. C. H. Redman, "Network Architectures for Satellite ISDN," AIAA 13th International Communication Satellite Systems Conference, Los Angeles, CA, March 1990, *A Collection of Technical Papers*, Pt. 1, pp. 143-153.
- CHITRE, D. M., and H. Lee, "Operation of Higher Layer Data Communication Protocols Over Satellite Links," *Proc. IEEE*, Vol. 78, July 1990, pp. 1289-1294.
- CHITRE, D. M., see Campanella, S. J.
- CLINE, P., see Geller, B.
- CORCORAN, F. L., see Dimolitsas, S.
- CORNFELD, A., see Hung, H-L. A., and Metzke, G.
- COTNER, C. B., see Carver, W.
- DAY, S. M., see Atia, A. E.
- DIMOLITSAS, S., and F. L. Corcoran, "Facsimile Compression for Transmission Over 800 bit/s to 2400 bit/s Digital Mobile Circuits," IEEE Military Communications Conference (MILCOM '90), Monterey, CA, September 1990, *Conf. Rec.*, Vol. 2, Paper 23.2, pp. 502-505.
- EVANS, J. V., and C. Mahle, "Research Into Advanced Satellite Technology at COMSAT Laboratories," AIAA 13th International Communication Satellite Systems Conference, Los Angeles, CA, March 1990, *A Collection of Technical Papers*, Pt. 2, pp. 798-806.
- EZZEDDINE, A., H-L. A. Hung, and H. C. Huang, "An MMAC C-Band FET Feedback Power Amplifier," *IEEE Transactions on Microwave Theory and Techniques*, Vol. 38, No. 4, April 1990, pp. 350-357.
- EZZEDDINE, A. K., and H-L. A. Hung, "A Novel Power Combiner for MIC and MMIC Amplifiers," IEEE International Microwave Symposium, Dallas, TX, May 1990, *Digest*, pp. 479-482.
- FAINE, E. A., D. K. Garlow, and R. W. Gruner, "Demonstration of a Low-Cost Tracking Mechanism for C-Band VSAT Applications," 12th Annual Conference of the Pacific Telecommunications Council, Honolulu, HI, January 1990, *Proc.*, pp. 397-403.
- FAINE, E. A., S. Matsomoto,\* M. Saito,\* M. Mikulicz,\* and A. Meyers,\* "First International HDTV Digital Transmission via INTELSAT," 12th Annual Conference of the Pacific Telecommunications Council, Honolulu, HI, January 1990, *Proc.*, pp. 53-61.
- FAINE, E. A., "International HDTV Service via INTELSAT," 4th International Colloquium on Advanced Television Systems, Ottawa, Canada, June 1990, *Proc.*, pp. 4B.2.3-4B.2.13.
- FAINE, E. A., and W. R. Schnicke, "International HDTV Service via INTELSAT," *HDTV World Review*, Vol. 1, No. 4, Fall 1990, pp. 176-184.
- FARIS, F., see Pontano, B. A.
- GARLOW, D. K., see Faine, E. A.
- GEILING, J. I., and K. E. Rasmussen, "Côte d'Ivoire Satellite Transmission System," AIAA 13th International Communication Satellite Systems Conference, Los Angeles, CA, March 1990, *A Collection of Technical Papers*, Pt. 1, pp. 410-414.

\* Non-COMSAT author.

- GELLER, B., J. Tyler, L. Holdeman, F. Phelleps, P. Cline, and G. Laird, "Integration and Packaging of GaAs MMIC Subsystems Using Silicon Motherboards," IEEE GaAs IC Symposium, New Orleans, LA, October 1990, *Digest*, pp. 85-88.
- GELLER, B. D., see Upshur, J. I.
- GRUNER, R. W., see Faine, E. A.
- GUPTA, R., F. Assal, and T. Hampsch, "A Microwave Switch Matrix Using MMICs for Satellite Applications," IEEE MTT-S International Microwave Symposium, Dallas, TX, May 1990, *Digest*, Vol. 2, pp. 885-888.
- GUPTA, R., L. Holdeman, H. Carlson, J. Potukuchi, K. Hogan, and K. Pande, "Manufacturing Technology and Yield Studies for MMIC 5-bit Digital Attenuators and Phase-Shifters," IEEE GaAs IC Symposium, New Orleans, LA, October 1990, *Digest*, pp. 305-308.
- GUPTA, R., "Single- and Dual-Gate FET Switch Elements for Microwave Switch Matrix Applications," International Conference on Millimeter Waves and Microwaves, New Delhi, India, December 1990, *Proc.*, pp. 111-114.
- GUPTA, R. K., see Potukuchi, J. R.
- HAMPSCH, T., see Gupta, R.
- HEGAZI, G., see Ho, T. (two papers), and Hung, H-L. A.
- HEMMATI, F., R. Marshalek, and D. Paul, "A Study of Forward Error Correction in Free-Space Laser Communications Systems," Conference on Free-Space Laser Communication Technologies II, Los Angeles, CA, January 1990, *Proc. SPIE*, Vol. 1218, D. L. Begley and B. D. Seery, eds., pp. 336-347.
- HO, T., F. Phelleps, G. Hegazi, K. Pande, and H. Huang, "A Monolithic mm-Wave GaAs FET Power Amplifier for 35-GHz Secker Applications," *Microwave Journal*, Vol. 30, No. 8, August 1990, pp. 113-121.
- HO, T., F. Phelleps, G. Hegazi, K. Pande, and H. Huang, "35-GHz Monolithic GaAs FET Power Amplifiers," IEEE Military Communications Conference (MILCOM '90), Monterey, CA, September 1990, *Conf. Rec.*, pp. 184-186.
- HO, T. C., see Metzke, G.
- HOGAN, K., see Gupta, R.
- HOLDEMAN, L., see Geller, B. and Gupta, R.
- HUANG, H. C., see Ezzeddine, A. K.; Ho, T. (two papers); and Hung, H-L. A.
- HULLEY, M. A., "Handling the RF Output of High-Power TWTAs in Spacecraft," IEEE Military Communications Conference (MILCOM '90), Monterey, CA, September 1990, *Conf. Rec.*, Vol. 1, Paper 6.2, pp. 188-192.
- HUNG, H-L. A., A. I. Zaghoul, J. Singer, G. Hegazi, F. Phelleps, G. Metzke, T. Lee, and A. Cornfeld, "Monolithic Integrated Circuits for Millimeter-Wave Phased-Array Applications," IEEE International Symposium on Antennas and Propagation, Dallas, TX, May 1990, *Digest*, Vol. 4, pp. 1409-1412.
- HUNG, H-L. A., T. Smith, and H. C. Huang, "FET: Power Applications," *Handbook of Microwave and Optical Components*, Ch. 10, New York: John Wiley, 1990.
- HUNG, H-L. A., see Ezzeddine, A. K. (two papers); Anderson, W. T.; Lee, C. H.; and Li, M. G. (three papers)

\* Non-COMSAT author.

- KELLY, W. H., and J. H. Reisenweber, "Conceptual Thermal Design for a Spacecraft Employing a High-Power Multibeam Phased Array," AIAA/ASME 5th Joint Thermophysics and Heat Transfer Conference, Seattle, WA, June 1990. AIAA Paper No. 90-1670.
- KNIGHT, I. N., "Committee T-1 Telecommunications in the '90s," Symposium on Telecommunication Standards '90, Tokyo, July 1990, *Proc.*, pp. 56-65.
- LAIRD, G., see Geller, B.
- LAUX, P. E., see Metz, G.
- LEE,\* C. H., M. G. Li,\* E. A. Chauchard,\* and H-L. Hung, "Microwave Phase Locking With Picosecond Laser Pulses," IEEE Princeton David Sarnoff Symposium, Princeton, NJ, March 1990, *Digest* (unpaginated).
- LEE, H., see Chitre, D. M.
- LEE, T., see Hung, H-L. A.
- LI, M. G.,\* E. A. Chauchard,\* C. H. Lee,\* and H-L. A. Hung, "Microwave Modulation of Optical Signal by Electro-Optic Effect in GaAs Microstrips," IEEE International Microwave Symposium, Dallas, TX, May 1990, *Digest*, pp. 948-951.
- LI, M. G.,\* E. A. Chauchard,\* C. H. Lee,\* and H-L. A. Hung, "Microwave Phase Locking Using Electro-Optic Harmonic Mixer," *Ultrafast Phenomena VII*, C. B. Harris, E. P. Ippen, G. A. Mourou, and A. H. Zewail, eds., New York: Springer-Verlag, May 1990, pp. 212-214.
- LI, M. G.,\* E. A. Chauchard,\* C. H. Lee,\* and H-L. A. Hung, "Intermixing Optical and Microwave Signals in GaAs Microstrip for Phase-Locking Applications," *IEEE Transactions on Microwave Theory and Techniques*, Vol. 38, No. 12, December 1990, pp. 1924-1931.
- LOMAS, N. S., and P. R. Schrantz, "An Evaluation of Low-Frequency Shock Spectrum Testing for INTELSAT V/Ariane Compatibility," International Symposium on Environmental Testing for Space Programmes—Test Facilities & Methods, ESTEC, Noordwijk, The Netherlands, June 1990, *Proc.*, pp. 341-346.
- MAHLE, C., see Evans, J. V.
- MARSHALEK, R., and D. Paul, "Mass, Prime Power, and Volume Estimates for Reliable Optical Intersatellite Link Payloads," Conference on Free-Space Laser Communication Technologies II, Los Angeles, CA, January 1990, *Proc. SPIE*, Vol. 1218, D. L. Begley and B. D. Seery, eds., pp. 30-40.
- MARSHALEK, R., see Hemmati, F.
- METZE, G., A. B. Cornfeld, P. E. Laux, T. C. Ho, and K. P. Pande, "A Dielectric-Assisted Liftoff Technique for the Formation and Monolithic Integration of Electronic and Optical Devices," *Applied Physics Letters*, Vol. 57, No. 24, December 1990, pp. 2576-2578.
- METZE, G., see Hung, H-L. A.
- MEULENBERG, A., see Anderson, W. T.
- MOTT, R. C., see Potukuchi, J. R., and Zaghoul, A. I.

\* Non-COMSAT author.

- OSPINA, S., "Space Law and Satellite Communications in Latin America" (in Spanish), Pan-American Conference on Space, San José, Costa Rica, March 1990, *Proc.*, pp. 316-331.
- OSPINA, S., "Economic and Legal Aspects of Project CONDOR" (in Spanish), 3rd Meeting of the Permanent Technical Committee, CITEL, Montevideo, Uruguay, April 1990, *Proc.* (unpaginated).
- OSPINA, S., "International Regulation of Satellite Telecommunications" (in Spanish), 3rd Meeting of the Legal Committee, Asociación Hispanoamericana de Centros de Investigación y Empresas de Telecomunicaciones (AHCJET), San José, Costa Rica, July 1990, *Proc.* (unpaginated).
- OSPINA, S., "International Telecommunications by Satellite" (in Spanish), 3rd Symposium on Electronics and Communication, ITES de Monterrey, Mexico City, September 1990, *Proc.* (unpaginated).
- OSPINA, S., "International Regulation of Satellite Communications" (in Spanish), Asociación Hispanoamericana de Centros de Investigación y Empresas de Telecomunicaciones (AHCJET), Madrid, Spain, October-December 1990, *Proc.*, Vol. 8, No. 43, pp. 13-25.
- PANDE, K., see Gupta, R.; Ho, T. (two papers); and Metz, G.
- PAUL, D. K., and R. A. Greenwell,\* "Introduction to the Proceedings of the SPIE," Conference on Fiber Optics Reliability: Benign and Adverse Environments IV, San Jose, CA, September 1990, R. A. Greenwell and D. K. Paul, eds., *Proc. SPIE*, pp. viii-x.
- PAUL, D., see Marshalek, R., and Hemmati, F.
- PHELLEPS, F., see Geller, B.; Ho, T. (two papers); and Hung, H-L. A.
- PONTANO, B. A., P. DeSantis,\* L. White, and F. Faris, "On-Board Processing Architectures for International Communications Satellite Applications," AIAA 13th International Communication Satellite Systems Conference, Los Angeles, CA, March 1990, *A Collection of Technical Papers*, Pt. 2, pp. 655-668.
- PONTANO, B. A., see Campanella, S. J.
- POTUKUCHI, J. R., R. C. Mott, A. I. Zaghoul, R. K. Gupta, F. T. Assal, and R. M. Sorbello, "MMIC Insertion in a Ku-Band Active Phased Array for Communications Satellites," IEEE MTT-S International Microwave Symposium, Dallas, TX, May 1990, *Digest*, Vol. 2, pp. 881-884.
- POTUKUCHI, J. R., see Zaghoul, A. I., and Gupta, R.
- RASMUSSEN, K. E., see Geiling, J. I.
- REDMAN, P. C. H., see Chitre, D. M.
- REISENWEBER, J. H., see Kelly, W. H.
- SAYEGH, S., see Campanella, S. J.
- SCHNICKE, W. R., see Faine, E. A.
- SCHRANTZ, P. R., see Lomas, N. S.
- SHERWOOD, P. G., see Tzeng, F. F.

\* Non-COMSAT author.

- SINGER, J., see Hung, H-L. A.  
 SMITH, T., see Hung, H-L. A.  
 SORBELLO, R. M., see Potukuchi, J. R., and Zaghoul, A. I. (two papers)  
 TONEY, P. A., "Fault Avoidance in Space Power Distribution Topologies," AIAA 13th International Communication Satellite Systems Conference, Los Angeles, CA, March 1990, *A Collection of Technical Papers*, Pt. 1, pp. 52-58.  
 TYLER, J., see Geller, B.  
 TZENG, F. F., "An Analysis-by-Synthesis Linear Predictive Model for Narrowband Speech Coding," IEEE International Conference on Acoustics, Speech, and Signal Processing, Albuquerque, NM, April 1990, *Proc.*, Vol. 1, pp. 209-212.  
 TZENG, F. F., "Near-Optimum Linear Predictive Speech Coding," IEEE Global Telecommunications Conference, San Diego, CA, December 1990, *Conf. Rec.*, Vol. 2, pp. 508.1.1-508.1.5.  
 TZENG, F. F., and P. G. Sherwood, "Error Protection for Low Rate Speech Transmission Over a Mobile Satellite Channel," IEEE Global Telecommunications Conference, San Diego, CA, December 1990, *Conf. Rec.*, Vol. 3, pp. 902.3.1-902.3.5.  
 TZENG, F. F., "Analysis-by-Synthesis Linear Predictive Speech Coding at 4.8 kbps and Below," *Advances in Speech Coding*, Norwell, MA: Kluwer Academic Publishers, 1990, pp. 135-143.  
 UPSHUR, J. I., and B. D. Geller, "Low-Loss 360° x-Band Analog Phase Shifter," IEEE MTT-S International Microwave Symposium, Dallas, TX, May 1990, *Digest*, Vol. 1, pp. 487-490.  
 WESTERLUND, L., see Atia, A. E.  
 WHITE, L., see Pontano, B. A.  
 WILLIAMS, A. E., and R. R. Bonetti, "Narrowband Active MMIC Filters," 3rd Asia-Pacific Microwave Conference, Tokyo, September 1990, *Proc.*, pp. 967-970.  
 WILLIAMS, A. E., see Bonetti, R. R. (four papers)  
 WILLIAMS, H. B., see Zaghoul, A. I.  
 ZAGHLOUL, A. I., R. C. Mott, J. R. Potukuchi, R. M. Sorbello, F. T. Assal, and H. B. Williams, "Measurement/Prediction Comparison of Ku-Band MMIC Active Phased Array," IEEE International Symposium on Antennas and Propagation, Dallas, TX, May 1990, *Digest*, Vol. 3, pp. 1158-1161.  
 ZAGHLOUL, A. I., Y. Hwang,\* R. M. Sorbello, and F. T. Assal, "Advances in Multibeam Communications Satellite Antennas," *Proc. IEEE*, Special Issue on Satellite Communications, Vol. 78, No. 7, July 1990, pp. 1214-1231.  
 ZAGHLOUL, A. I., see Hung, H-L. A., and Potukuchi, J. R.

## Papers Scheduled for Publication in the CTR INTELSAT VI Series

### COMSAT TECHNICAL REVIEW Volume 20 Number 2, Fall 1990

#### FOREWORD

**J. D. Hampton AND I. Goldstein**

#### EDITORIAL NOTE

**S. B. Bennett AND G. Hyde**

#### *INTELSAT VI: The Communications System*

##### THE PROCESS FOR SUCCESS—INTELSAT VI

**E. I. Podraczky AND W. R. Schnicke**

##### INTELSAT VI SYSTEM PLANNING

**L. B. Perillan, W. R. Schnicke AND E. A. Faine**

##### INTELSAT VI COMMUNICATIONS PAYLOAD PERFORMANCE SPECIFICATIONS

**B. A. Pontano, A. I. Zaghoul AND C. E. Mahle**

##### SPECIFYING THE SPACECRAFT BUS

**G. P. Cantarella AND G. Porcelli**

##### SS-TDMA SYSTEM CONSIDERATIONS

**S. J. Campanella, G-P. Forcina, B. A. Pontano AND J. L. Dicks**

##### INTELSAT VI TRANSMISSION DESIGN AND ASSOCIATED COMPUTER SYSTEM MODELS FOR FDMA SERVICES

**M. P. Brown, Jr., R. W. Duesing, L. N. Nguyen, W. A. Sandrin AND J. A. Tehrani**

\* Non-COMSAT author.